INVESTIGATING THE EMERGENT PROPERTIES OF AN AUTOPHAGY PROTEIN IN LIVING CELLS

By

Lewis J. Kraft

Dissertation
Submitted to the Faculty of the
Graduate School of Vanderbilt University
in partial fulfillment of the requirements
for the degree of

DOCTOR OF PHILOSOPHY
in

CHEMICAL AND PHYSICAL BIOLOGY

August, 2014

Nashville, TN

Approved:
Professor David W. Piston
Professor Albert H. Beth
Professor Todd R. Graham
Professor M. Shane Hutson

To my family

ACKNOWLEDGMENTS

"No man is an island". The list of the many people who have helped me along my journey through graduate school is long. I will start with my mentor, Anne Kenworthy, who gave me a compass to find my way to the new frontiers of science. Anne has been a huge source of inspiration, encouragement, and support. Not to mention she provided me with opportunities to see a little bit of the world. I will not forget your efforts, and moving forward I will not let you down. I owe special gratitude to my fantastic colleagues in the Kenworthy laboratory, in particular, Bing Han and Jake Dowler. We had many good times, and I will always remember you. I was fortunate enough to have had several fruitful collaborations at Vanderbilt with Caroline Hanson, Charlie Day, and Jessi Mazerik, and outside Vanderbilt with Tuan Nguyen and Steve Vogel at the NIH. I feel truly fortunate to have been able to work with you, as our collaborations helped me grow both as a scientist and as a man. I am grateful for being awarded a Vanderbilt dissertation enhancement award, as this gave me the opportunity to travel to the NIH to carry out experiments. I am thankful to have had a great group of scientists who served as members of my thesis committee. And, of course, these acknowledgments would not be complete without thanks to Jonathan McMurry, who gave me my start in science, and has been a continued source of support and encouragement.

TABLE OF CONTENTS

Page

LIST OF TABLES

LIST OF FIGURES

LIST OF ABBREVIATIONS

Atg	Autophagy related gene
Cdk1	Cyclin-dependent kinase 1
DFCP1	Zinc finger, FYVE domain containing 1
Dvl2	Dishevelled segment polarity protein 2
ER	Endoplasmic reticulum
FCS	Fluorescence correlation spectroscopy
FIP200	RB1-inducible coiled-coil 1
FRAP	Fluorescence recovery after photobleaching
FRET	Förster resonance energy transfer
FYCO1	FYVE and coiled-coil domain containing 1
GABARAP	Gamma-aminobutyric acid receptor-associated protein
GATE-16	Golgi-associated ATPase enhancer of 16 kDa
GFP	Green fluorescent protein
HCS	High content screen
HDAC6	Histone deacetylase 6
KEAP1	Kelch-like ECH-associated protein 1
KIR	KEAP1 interacting region
LAMP1	Lysosomal-associated membrane protein 1
LAMP2	Lysosomal-associated membrane protein 2
LC3	Microtubule-associated protein 1 light chain 3
LC3-I	Soluble LC3
LC3-II	Lipid modified LC3
LIR	LC3 interacting region
MAP1A	Microtubule-associated protein 1A
MAP1B	Microtubule-associated protein 1B
mTOR	Mechanistic target of rapamycin
NES	Nuclear export signal
NLS	Nuclear localization signal
PE	Phosphatidylethanolamine
PI3P	Phosphatidylinositol 3-phosphate
SPT	Single particle tracking
SQSTM1	Sequestosome 1

TP53INP1	Tumor protein p53 inducible nuclear protein 1
UBA	Ubiquitin-associated
UBL	Ubiquitin-like
ULK	unc like autophagy activating kinase
UVRAG	UV radiation resistance associated gene
Vps15	Phosphoinositide-3-kinase, regulatory subunit 4
Vps34	Phosphatidylinositol 3-kinase, catalytic subunit type 3
ZZ	ZZ-type zinc finger

CHAPTER I

Introduction

The scale of life is large – from humans down to the size of cells and molecules over one billion times smaller at the nanometer scale. Understanding molecules requires us to delve into a strange world from the perspective of a human observer. At this scale, the Reynolds number is small, that is to say, molecules live in a viscous world where there is essentially no momentum. Imagine yourself trying to swim in a pool full of molasses! You are throwing your arms and legs forward and backward up and down, but low Reynolds number means there will be no momentum to move you forward, only friction slowing you down. The world at this scale is strange indeed.

It is the monotonous, random heat energy that drives a nanometer sized molecule from one place to another. This type of motion is known as diffusion, or sometimes referred to as Brownian motion after the famous botanist Brown who made detailed observations of the random motion of pollen grains in year 1827. Diffusion is fundamental to life. It is an irreversible process leading to a net increase in the entropy of a system. Yet, the diffusive spreading out of molecules over time is what is largely responsible for the transfer of material and information from one place to another at the scale of a cell. Nearly every molecular process relies on diffusion, from the diffusional exchange of oxygen and carbon dioxide in the human lungs to the diffusional search of transcription factors for their gene targets. The nature of molecular diffusion, and thus the activity of molecules is highly dependent on environment. Yet, studies of the properties of molecules often lacks the context of a complex living system.

The focus of this dissertation is on studying the properties of molecules that emerge in the context of a living cell. In this chapter, historical perspectives on the problem of understanding life's complexity and emergent properties are described. A review of the literature on the autophagy pathway in general and the protein called LC3 in particular is then given. Introductions to the topics of modern experimental approaches for studying molecules in living cells using fluorescence microscopy will be given. Finally, an overview of the specific questions that are investigated is provided.

I.1 Historical perspectives

From antiquity, life was described as "animated matter". The Latin word for anima means soul, that is, life has a soul, distinct from the observable chemical and physical forces. Much has changed, over the last 100 years – dozens of natural laws have been discovered. Although many mysteries about life remain, the properties of life are now being explored in the terms of natural physical and chemical processes. In 1944 Erwin

Schrödinger set out to define in detail two such properties of life, in his highly influential, and provocatively titled book *What is Life?*. Firstly, Schrödinger highlighted the importance of what was Boltzmann's laws of thermodynamics, that all things tend toward disorder, but that life has the ability to overcome this natural fact, because it can collect energy from its environment through processes collectively known as metabolism. Life therefore is said to be a dissipative system. Secondly, Schrödinger went on to highlight the problem of information transfer. How does life transfer its blueprints from generation to generation with such exquisite fidelity? At the time, Schrödinger hypothesized the existence of a molecule, probably some aperiodic crystal, that was responsible. We now understand a great deal about the underlying mechanisms of information transmission thanks in no small part to the work of Watson and Crick in the 1950's. Their discovery, an aperiodic crystal, is what is now famously known as DNA (deoxy-ribo-nucleic-acid), and is one of the critical pieces of the puzzle of information transmission. But it is not enough to have mechanisms of acquiring energy and transferring information.

Life emerged in the form of a cell – a membrane bound compartment that separates inside from outside. The cell is the smallest recognizable unit of life and is a building block for higher order organisms. The first cell was observed with the aid of a microscope in the year 1665 by Robert Hooke. Although the molecules that make up cells are bounded by a protective membrane, they are far from fully shielded from their environment. The environment is full of damaging agents – UV rays from the sun, pathogens, etc. – for which the cell's membrane provides little protection. A struggle for any cell is to resist the natural tendency toward disorder. Remarkably, healthy cells are robust and capable of maintaining their normal condition in the face of endless perturbations from their environment (a phenomenon known as cellular homeostasis). On the other hand, diseased cells show signs of dysfunction in their homeostatic mechanisms. Cancerous cells survive in the relatively harsh conditions of a tumor where they otherwise should not. Beta cells in pancreatic islet of a diabetic patient unexpectedly die under conditions of oxidative stress induced by a poor diet. How is it that a normal cell's homeostatic mechanisms become dysfunctional? For many of the most important diseases affecting humans we do not know the answer. However, we do know the problem ultimately lies in the inner workings of the cell.

I.2 Emergence

The cell is far from equilibrium, and its molecules undergo dynamic self-assembly to form ordered structures on a scale from nanometers to tens of microns [1]. Some proteins function as isolated monomeric enzymes continuously processing substrates into products, while many others function as very large, labile multicomponent complexes. Function (and dysfunction), patterns, and behaviors of a cell ultimately emerge from the collective behaviors of its molecules and assemblies. Emergent complexity occurs at every physical scale of the universe. Emergent properties arise when numerous interacting components produce collective patterns or behaviors that are not attainable by the individual components themselves [2]. Life is rich with examples of emergent properties at the scales of populations, organisms, organs, tissues, cells, genes, all the way down to molecules and atoms. Insect colonies organize into wondrously complicated structures. Patterns form on the furs and shells of animals. The collective force of molecules in specialized muscle cells leads to contraction. Molecules collectively carry out tasks of unimaginable complexity such as gene replication, and cell division – all displaying properties of emergent complexity.

I.3 Autophagy

The autophagy pathway is an example of a metabolic process that displays stunning complexity, and that has exceptional relevance to human health and disease. Autophagy is a major catabolic pathway whereby cytoplasmic components including proteins, lipid droplets, glycogen, organelles, and even invading pathogens are sequestered and degraded via the lysosome. The term autophagy (from the Greek words for "self" and "eating") was coined by Christian de Duve in 1963 [3]. Autophagy is a conserved pathway in eukaryotes, and is vitally important for normal human health, development, and the prevention of disease [4].

A defining feature of the autophagy pathway is the formation of a peculiar double membrane vesicular intermediate known as an autophagosome, which is responsible for engulfing regions of cytoplasm. The autophagosome is subsequently trafficked to the lysosome, where the outer membrane of the autophagosome subsequently fuses with the lysosome thereby degrading its inner membrane and contents [5] (Figure I.1). The molecular mechanisms of autophagy are becoming more clear thanks to the discovery of a host of autophagy related genes (Atg) over the last two decades through genetic and proteomic studies [6–9].

I.3.1 Autophagy in human health and disease

Given autophagy's central role in eukaryotic cells, it is not surprising that the pathway has broad importance for human health. Early in life, at the stages of the oocyte to embryo transition, and the early neonatal period, catabolic autophagy plays a critical role in liberating energy and amino acid nutrients [11, 12]. In the development of red blood cells, autophagy plays important roles in cell remodeling via the selective removal of mitochondria [13]. In the pancreatic beta cells, autophagy is thought to play a role in protecting against oxidative injuries resulting from poor diets [14–16]. Similarly, autophagy is important for protecting the cells of the heart from stresses that ultimately lead to cardiovascular disease [17–23]. Autophagy is also relevant in cancer. It was suggested that dysregulated autophagy allows for the survival of a cancerous cell in the nutrient poor environment of the tumor. On the other hand, it was also proposed that autophagy could help prevent cancer by degrading damaged mitochondria that are generating free radicals [10, 24]. Recently,

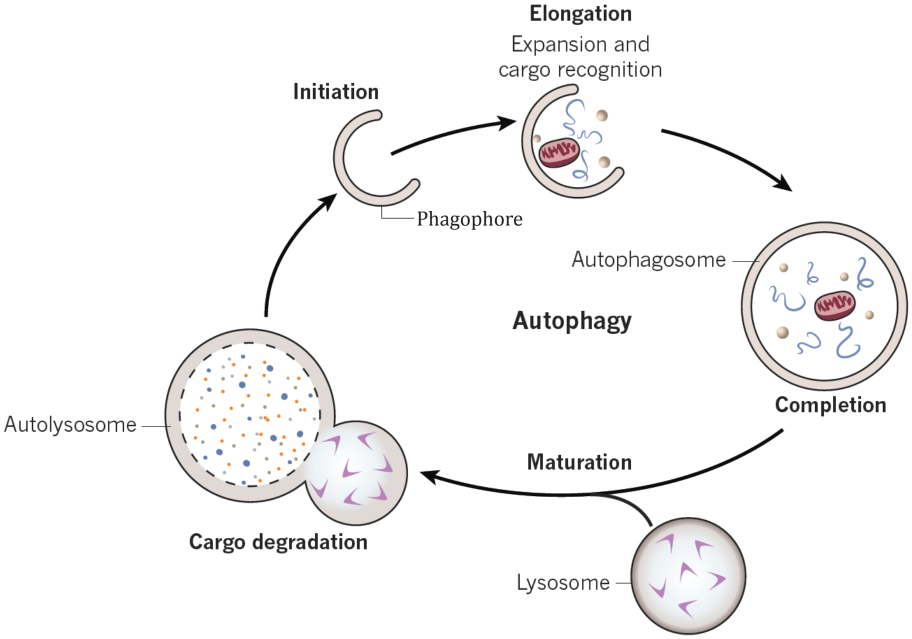

Figure I.1: Basic schematic of autophagosome formation. The autophagosome initiation site is referred to as the phagophore. As the autophagosome expands, cytosolic materials are captured in a double membrane bound vesicle called the autophagosome. The autophagosome is subsequently trafficked to the lysosome where it fuses leading to degradation and recycling of its contents. Adapted from Levine et al. [10].

there has also been intense focus on autophagy due to its connections with immunity, inflammation, and infection. As an example, it was shown that dysfunctional autophagy plays a major role in the development of Crohn's disease [25, 26]. Defects in autophagy have been implicated in many other diseases as well including Parkinson's disease, Alzheimer's disease, Huntington's disease, and Paget's disease of bone [24, 27–30]. Given autophagy's central importance in maintaining cellular homeostasis in eukaryotes, it is not surprising that autophagy has been implicated in nearly every major human disease. The molecular mechanisms that underlie autophagy and the factors that lead to its perturbation are currently unknown [31].

I.3.2 Autophagy regulation

Autophagy is constitutively active, and can occur either with or without substrate specificity, termed selective or macroautophagy respectively. Non-selective autophagy is thought to be a mechanism for bulk turnover of cytosolic components, and probably evolved as a mechanism to cope with conditions of starvation. On the other hand, in selective autophagy, a variety of cargo is specifically selected for degradation. Selective autophagy likely evolved as a mechanism to protect the cell against damaged molecules and organelles, as well as a mechanism of innate defense against invading pathogens [32].

Autophagosomes have been said to form de novo by their nucleation, growth, and fusion [33, 34]. The initial site of autophagosome formation, referred to as the phagophore, is a cup shaped membrane, which expands to encapsulate cargo. The source of the autophagosome membrane is currently hotly debated. A variety of different membrane sources have been implicated in the process. One hypothesis is that specialized regions of the endoplasmic reticulum (ER) called omegasomes might be the site of autophagosome formation. Zinc finger, FYVE domain containing 1 (DFCP1) is a phagophore marker, and was shown to associate with omegasomes [35]. Fluorescence microscopy studies identified another possible membrane source as the outer membrane of mitochondria [36]. Another set of studies showed that autophagosome membranes are derived from the plasma membrane via a clathrin dependent endocytic pathway [37]. Yet another hypothesis is that the cycling of the integral membrane protein, ATG9, between the Golgi complex and the site of autophagosomes could be a mechanism for phagophore expansion [38]. Finally, another study suggests the ER-Golgi intermediate compartment is a primary source of membrane for autophagosomes [39]. An intriguing question is whether autophagosomes formed from a particular membrane source are destined to capture specific cargoes.

The autophagy pathway is tightly regulated, and is under the control of the mechanistic target of rapamycin (mTOR) signaling pathway (Figure I.2). Autophagy is upregulated by perturbations in the levels of nutrients, hormones, molecular damage, and invasion of pathogens. By breakdown of already assembled macromolecules, autophagy thereby liberates basic building blocks like amino acids and free fatty acids, which can be used for producing energy or for building more essential molecules. Downstream of mTORC1, two main kinase complexes are involved in regulating the formation of autophagosomes. The first, is known as the unc like autophagy activating kinase (ULK) complex, and the second is known as the phosphatidylinositol 3-kinase, catalytic subunit type 3 (Vps34) complex [40]. In addition to ULK and Vps34 complexes, two other machineries have been identified as important for autophagosome formation - the ubiquitin like ATG12 and ATG8 conjugation systems.

ULK complex kinase activity is critical for autophagosome formation and the recruitment of other autophagic factors to the phagophore [41, 42]. The ULK complex is a multicomponent complex consisting of ULK1, ULK2, ATG13, RB1-inducible coiled-coil 1 (FIP200) , and ATG101. Under basal conditions, mTORC1 interacts with ULK complex to phosphorylate it thereby inhibiting its activity. When autophagy is upregulated mTORC1 dissociates from the ULK complex leading to activation of its kinase activity and targeting to phagophores [43]. The ATG8 family proteins play a scaffolding role in the assembly of the ULK complex [44, 45].

The Vps34 complex is also critical for autophagosome formation and the recruitment of autophagic factors to the phagophore. Like the ULK complex, the Vps34 complex is a multicomponent complex com-

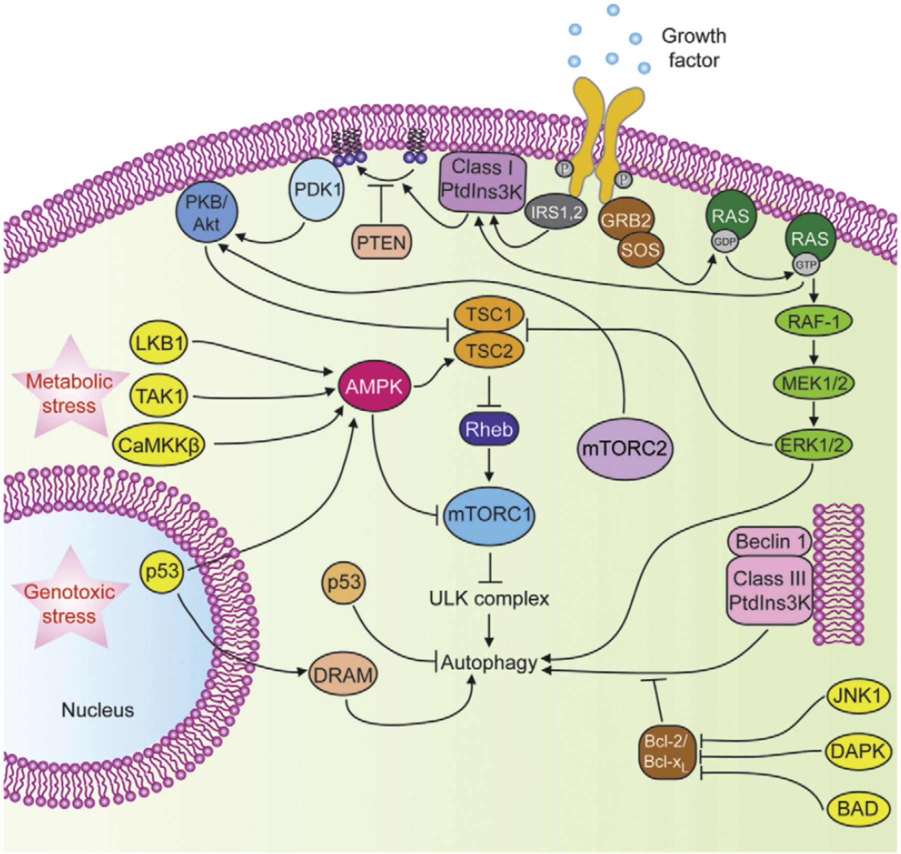

Figure I.2: Regulation of the autophagy pathway. Autophagy is negatively regulated by the mTOR signalling complex. The activity of autophagy is modulated by the levels of nutrients, the presence of growth factors, as well as genotoxic stress. The ULK complex and Vps34 complex (Class III PtdIns3K) are downstream regulators of autophagy. Adapted from Yang and Klionsky [40].

posed of Vps34, phosphoinositide-3-kinase, regulatory subunit 4 (Vps15) , phosphatidylinositol 3-phosphate (PI3P), Beclin-1 [46, 47], and ATG14 [40]. Many molecules regulate the assembly of the Vps34 complex including Bcl-2 [47], cyclin-dependent kinase 1 (Cdk1) [48], AMBRA1 [49], Bif-1 [50], UV radiation resistance associated gene (UVRAG) [51], and Rubicon [52, 53].

In macroautophagy, autophagosomes form randomly throughout the cytoplasm, and are subsequently trafficked toward the microtubule organizing center where lysosomes are clustered. Phagophores are immobile, while mature autophagosomes utilize bidirectional transport along microtubule tracks to arrive at their destination [54–57]. Minus end directed movement is mediated by the motor protein dynein [55, 56], whereas plus end directed movement is mediated by the motor protein kinesin-1, as well as Rab7, and FYVE and coiled-coil domain containing 1 (FYCO1) [58, 59]. Labile microtubules recruit early autophagic factors, while acetylated microtubules are associated with mature autophagosomes [58]. The spatial segregation of lysosomes and autophagosomes has been suggested to be an additional mechanism for regulating the autophagy pathway [38].

Knowledge of the mechanisms of fusion of autophagosomes with lysosomes is limited; however, several molecules are thought to be involved in the process. Histone deacetylase 6 (HDAC6) is involved in fusion processes related to the selective removal of ubiquitinated protein aggregates [60]. In addition, Rab7, lysosomal-associated membrane protein 1 (LAMP1) , and LAMP2 are all involved in fusion of autophagosomes with lysosomes [61, 62]. Recently, SNAREs have emerged as important mediators of fusion events [63–65]. More work needs to be done in this area to determine if there are any autophagy-specific factors involved.

I.3.3 Selective autophagy

Researcher's interest in autophagy was kindled by the discovery of selectivity for certain cargoes. In general, autophagy selectivity is achieved by first conjugating ubiquitin to specific substrates such as protein aggregates. Next, ubiquitin binding cargo receptor proteins associate with the ubiquitinated cargo. Finally, the cargo is captured in LC3-II labeled autophagosomes for degradation [32].

Autophagy cargo receptor proteins are a crucial component of the process of selective autophagy. Sequestosome 1 (SQSTM1) is a multifunctional scaffolding protein with functions in regulating signaling, receptor internalization, and proteasome mediated protein turnover [66]. SQSTM1 was first shown to interact directly with LC3 to degrade ubiquitinated protein aggregates by autophagy in the context of Huntington's disease [67, 68]. SQSTM1's domain structure consists of PB1, ZZ-type zinc finger (ZZ) , and Ub-associated (UBA) domains. The protein also contains two NLS signals, an NES signal, an LC3 interacting region (LIR) motif, and a KEAP1 interacting region (KIR) . The PB1 domain mediates SQSTM1 homo-oligomerization, the UBA domain is responsible for binding to ubiquitin chains, while the LC3 interacting region is involved in direct interactions with LC3 (reviewed in [32]). Additional selective autophagy receptors are known [69], and more are likely to be discovered.

Selective autophagy is not just limited to degrading protein aggregates. Specific proteins can be degraded as well, for example, ubiquitinated dishevelled segment polarity protein 2 (Dvl2) involved in the Wnt pathway is degraded by SQSTM1-mediated selective autophagy [70]. Organelles are also known to be selectively degraded. Examples include ubiquitinated mitochondria, ER, and peroxisomes [71–75]. Invading pathogens are also ubiquitinated and degraded by selective autophagy [76]. Interestingly, in yeast, ribosomes are selectively degraded [77], but it remains to be seen if ribosomes are also selectively degraded in higher eukaryotes. All of these components seem to be specifically degraded using a similar general mechanism. Interestingly, other specific proteins such as IKKβ in the NF-$\kappa\beta$ pathway are degraded using a slight variation of the theme. Instead of ubiquitination, IKKβ binds to kelch-like ECH-associated protein 1 (KEAP1), which then undergoes a specific interaction with SQSTM1 [78]. This suggests the selective autophagy mechanism may have the flexibility to degrade a very broad range of cargoes that may not necessarily be ubiquitinated.

I.3.4 LC3

The protein known as LC3 (also known as ATG8) plays a central role in the process of autophagosome formation. In yeast there is a single Atg8 gene, whereas in multicellular animals the Atg8 family consists of three distinct subfamilies. The mammalian LC3 family consists of 8 orthologs belonging to the subfamilies: microtubule-associated protein 1 light chain 3 (LC3), gamma-aminobutyric acid receptor-associated protein (GABARAP), and Golgi-associated ATPase enhancer of 16 kDa (GATE-16) [79]. Each LC3 subfamily is essential for autophagy [80]. LC3 genes are expressed in every human tissue [81], and the level of LC3 is upregulated in response to a variety of perturbations to the autophagy pathway [82, 83].

Studies have revealed that all of the ATG8 proteins share strong structural, but not sequence similarity with ubiquitin. Together with the fact that they undergo conjugation reactions resembling ubiquitination, they have fittingly been categorized as ubiquitin-like proteins [84, 85]. However, unlike ubiquitin, which is conjugated to other proteins, LC3 is conjugated to the head group of phosphatidylethanolamine (PE) [86]. LC3 is believed to function in autophagosome membrane expansion and elongation, and plays a role in cargo selection during selective autophagy. There are however also apparently autophagy-independent functions for LC3 that will be described further below.

Newly synthesized LC3 is processed by a cysteine protease called ATG4B, exposing its glycine residue at position 120 and priming it for lipid modification [86, 87] (Figure I.3). A large multimeric complex involving a second ubiquitin-like protein called ATG12 is believed to play important roles in specifying the

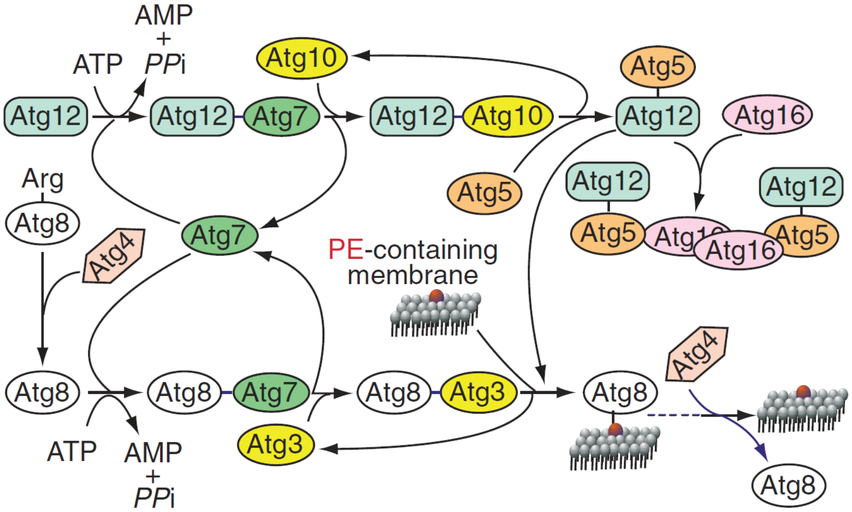

Figure I.3: The LC3 ubiquitin-like conjugation machinery. Newly synthesized LC3 (ATG8) is cleaved by ATG4B exposing a C-terminal glycine residue. LC3 is then conjugated to E1-like enzyme ATG7, followed by conjugation to E2-like enzyme ATG3. Finally, LC3 an isopeptide bond is formed between LC3's glycine residue and the amine head group of PE via E3-like enzyme ATG12-ATG5-ATG16. Adapted from Chen and Klionsky [31].

site of LC3 lipidation, as well as the conjugation reaction itself [88]. ATG12 is conjugated to ATG5 via intermediate reactions with E1-like and E2-like enzymes ATG7 and ATG10. The ATG12-ATG5 conjugate non-covalently associates with ATG16 to form a very large 400-800 kDa complex [89]. To date no ATG12-ATG5 deconjugation reaction has been identified. There is extensive overlap among the component involved in conjugating ATG12, and those involved in conjugating LC3. The C-terminal glycine residue on LC3 is conjugated to the head group of PE via an isopeptide bond by reactions with E1- and E2-like enzymes ATG7 and ATG3 [85]. The multimeric ATG12-ATG5-ATG16 is believed to function as an E3-like enzyme in the process [88]. LC3's lipidation with PE is reversible by a second cleavage reaction with ATG4B [87]. Cleaved LC3, known as LC3-I, is soluble, whereas lipid modified LC3, known as LC3-II, is tightly associated with autophagosomal membranes [90, 91]. LC3's role in autophagosome expansion was demonstrated by experiments showing the levels of ATG8 determine the size of autophagosome [92]. LC3 is thought to play a role in mediating membrane tethering and hemifusion [93, 94]. In addition, the evidence shows that different LC3 subfamilies are each essential, yet act differently in autophagosome biogenesis. The results indicate that the LC3 subfamily is involved in elongation of the phagophore, whereas the GABARAP and GATE16 subfamilies play a role later in the maturation of autophagosomes [80].

Recent studies have shown that LC3 can be post-translationally modified in at least two additional ways. First, LC3 was shown to be phosphorylated directly by protein kinase A [95]. Second, LC3 undergoes acetylation by the p300 acetyltransferase [96]. Interestingly, these additional post-translational modifications strongly regulate LC3's lipidation and activity in autophagy.

Each LC3 subfamily has a unique N-terminus, and it has been suggested that this may confer unique functionality to the different LC3 family members [97]. The LC3 N-terminus has been shown to play important functional roles. It was hypothesized that LC3 provides energy for membrane fusion events by homo-oligomerization via its N-terminus on opposing membranes [93]. GABARAP was crystallized in two distinct conformations suggesting LC3's N-terminus may be flexible [98]. There is some evidence to support the notion that lipidation of LC3 induces a conformational change in its N-terminus [93, 99]. This suggests a mechanism whereby LC3 lipidation could regulate LC3's interaction partners and thus its function. The N-terminus of LC3 was also shown to be important for recruitment of SQSTM1 into autophagosomes during selective autophagy [100].

LC3 forms several large complexes with the ubiquitin-like (UBL) conjugation machinery. First, LC3 forms a 2:1 complex with ATG4B. One LC3 is bound to the active site, while the other is bound to the N-terminus of ATG4B. It is unclear if binding to ATG4B's N-terminus plays a role in regulating LC3 lipidation. Alternatively, it may be an artifact of the crystallization environment [101]. More work needs to be done in order to determine if the 2:1 complex observed in the LC3 ATG4B crystal structure is physiologically relevant. A second large complex was observed during the transfer of LC3 from ATG7 to ATG3. ATG7 dimerizes and interacts with ATG3. ATG8 is transferred trans from ATG7 to ATG3 bound to the opposite ATG7 [102–104]. Finally, a third large complex is thought to form between LC3 and the E3-like ligase ATG12-ATG5-ATG16. ATG12-ATG5-ATG16 was found by size exclusion chromatography to have an exceptionally large size at 800 kDa. The ATG12-ATG5-ATG16 complex is thought to contain at least 4 subunits mediated by ATG16 homo-oligomerization [89].

There has, not surprisingly, been a great deal of interest surrounding LC3's possible homo-oligomerization. In addition to the proposal that LC3 oligomerization may promote membrane tethering and hemifusion [93], caution was raised about LC3's use as an autophagy marker by light microscopy, as it was shown to associate with protein aggregates independent of autophagosome membranes. It was speculated that LC3 may be prone to self aggregating [79, 105, 106]. The LC3 family member GABARAP was shown to oligomerize [107, 108]. However, the self association properties of LC3 have not been thoroughly examined in a physiological context.

LC3 is also seems to have apparently autophagy-independent functions. LC3 was originally characterized as a microtubule-associated protein where it interacts with microtubule-associated protein 1A (MAP1A) and MAP1B as well as microtubules assembled from purified tubulin [109]. LC3 was subsequently shown to interact with both polymerized and unpolymerized tubulin by surface plasmon resonance [110]. It also undergoes interactions with other cytoskeleton associated proteins such as caldendrin [111]. LC3 forms a large complex with MAP1B heavy (MAP1B-HC) and light chain (LC1) with an estimated stoichiometry of MAP1B-HC:LC1:LC3 of 1:2:0.2 [112]. The function of LC3 binding to microtubules is unclear, but several hypotheses have been proposed. It may play a role in increasing microtubule stability [113], or alternatively LC3 may link autophagosomes to the microtubule network [59]. LC3 family members are also known to be involved in membrane trafficking events. GATE16 interacts with the SNARE machinery in the Golgi complex in order to mediate membrane trafficking. [114]. GABARAP was shown to mediate ER to Golgi transport [115]. LC3 was proposed to regulate endocytic trafficking events through its interactions with Rab GAPs [116]. Interestingly, LC3 was also demonstrated to be an RNA binding protein via its triple arginine motif in the region of residues R68-R70. LC3 binds to fibronectin mRNA, and thus influences the expression of fibronectin protein [117–119]. There is also evidence for interplay between the autophagy and proteasomal degradation pathways [70].

Surprisingly, LC3 is found in the nucleus [120, 121]. This is an unexpected finding given that LC3 is primarily thought to function in the cytoplasm where autophagosomes form. This discovery thus raises the possibility that nuclear LC3 may have currently unknown functions in the autophagy pathway. A small number of studies have begun to examine LC3's potential functions in the nucleus. It was shown that LC3 interacts with the nuclear tumor suppressor tumor protein p53 inducible nuclear protein 1 (TP53INP1) and influences cell death by autophagy [122]. The interaction of LC3 with a TP53INP1 family member called diabetes and obesity regulated (DOR), also a nuclear protein, functions in the dual regulation of autophagy and thyroid hormone receptor transcription [123–125]. Recent studies suggest nuclear LC3 may also regulate signaling via interactions with ERK signaling cascade components [126]. More work needs to be done to determine what additional roles LC3 may play in the nucleus.

I.3.4.1 LC3's protein interaction network and the LIR motif

LC3 family members interact with a large network of over 65 different proteins with extensive overlap among family members [9]. The LC3 interacting region (LIR) motif W/F/Y-X-X-L/I/V has been identified as a common structural element used by proteins to interact specifically with LC3 [32, 45, 127]. Many LC3 interacting proteins bear this motif, and appear to interact with LC3 via its hydrophobic protein interaction surface in the region of residues F52, L53, and R70 [69, 128, 129]. Mutations to these key residues on LC3's hydrophobic protein interacting surface disrupt binding to tens of proteins, highlighting the importance of this region for engaging other proteins in productive binding [9, 69, 100, 127, 129, 130]. At this time it is unclear if LC3 family members associate with proteins in their network in a binary fashion, or if many proteins come together to form functional complexes. Using FRAP, our group recently showed that the soluble form of

LC3 diffuses unusually slowly for a cytoplasmic protein of its size under basal conditions [121]. Because the diffusion coefficient of a soluble, freely diffusing molecule is inversely related to its radius, this slower-than-expected-diffusion of LC3 could potentially reflect its association with macromolecular complexes comprised of LC3 and other components of the autophagy pathway. Alternatively, the slow diffusion of soluble LC3 could potentially arise from reversible binding to microtubules in cells or the incorporation of LC3 into homo-oligomers or aggregates or possibly membranes.

I.4 Investigating biopolymers *in vivo* with fluorescence microscopy

A common approach to understanding a cell's molecular machinery involves breaking open the cell and separating out its components, such that assays for structure and function can be carried out *in vitro*. This type of experimental approach is extremely powerful, but it carries some intrinsic limitations.

The function of a protein is highly dependent on context. Firstly, a molecule can have different functions depending on its subcellular localization. Second, post-translational modifications of molecule can regulate its involvement in a particular cellular function [90, 131]. Third, once in a dilute solution, labile multicomponent complexes begin to fall apart. Fourth, the cell is a crowded environment, and a dilute solution, by definition, may not accurately recapitulate this. Lastly, the dynamics of molecular transport processes like diffusion depend on the nature of the intracellular environment.

Fortunately, new developments in light microscopy are making it possible to overcome these limitations. Light microscopy is well suited to studying living cells, as the energy of visible light is minimally damaging to the components of a living cell. In addition, measurements with light microscopy are typically spatially resolved down to about 250 nm or half the wavelength of light. One fundamental limitation of light microscopy has been the lack of contrast between constituents with similar densities. However, the advent of green fluorescent protein (GFP) technologies led to dramatic improvements in contrast, and have fundamentally changed the limits of light microscopy. Today it is routinely possible to genetically fuse GFP to any protein of interest, and to incorporate this construct into a living cell for observation by light microscopy. There are currently a variety of different fluorescent proteins each with unique photophysical properties including a range of different colors from blue to far red. Likewise, parallel advances in modern microscopy instrumentation have led to the development of many sophisticated, quantitative experiments [132].

I.4.1 FRET

Fluorescent molecules are dipoles. When two dipoles become sufficiently close together, they can participate in a dipole-dipole interaction. This interaction results in non-radiative energy transfer from the donor molecule to an acceptor molecule. This photophysical energy transfer phenomenon was first observed in polarization experiments carried out in the 1920s, and was quantitatively explained by Theodor Förster in 1946 [133]. Paying homage to Förster's fundamental contributions to our understanding, the phenomenon has been named Förster Resonance Energy Transfer (FRET) .

Due to its very strong $1/r^6$ distance dependence, changes in FRET were soon exploited as a sort of molecular ruler [134]. The distance over which FRET occurs between a specific donor and acceptor is defined with respect to the Förster distance R_0. R_0 is a function of the relative dipole-dipole orientation, the refractive index, and the photophysical properties of the donor and acceptor fluorophores [135]. When the separation distance between fluorophores is close to R_0, small distance changes result in dramatic changes in the FRET efficiency, but this sensitivity quickly falls off at separation distances $< 0.5R_0$ or $> 1.5R_0$.

Direct protein-protein interactions bring proteins within close physical proximity of one another. If the two proteins are labeled with fluorescent molecules, this process can be monitored using FRET. Most common fluorescent labels have R_0 values of ~ 5 nm. This means that FRET can be used as means of detecting protein-protein interactions when their distance of separation is less than ~ 10 nm. A variety of fluorescent proteins can be used as FRET donors and acceptors [136]. One of the most common FRET pairs used is the cyan and yellow proteins Cerulean and Venus. Cerulean is used as the FRET donor, while Venus is the FRET acceptor. This FRET pair has an R_0 value of 5.4 nm [137].

I.4.2 Diffusion

I.4.2.1 Diffusion and its biological relevance

Diffusion, sometimes referred to as Brownian motion, is a fundamental transport phenomenon that occurs in nature. The theory of Brownian motion is well grounded thanks to the work of Albert Einstein in the early 1900s. Einstein envisioned a particle suspended in water, with thermal energy propelling individual water molecules in random directions, sometimes bombarding the particle more in one direction than in the others, with the net effect of causing the particle to be displaced along a random trajectory. Einstein's theory shows that a single particle undergoing stochastic Brownian motion can be described as having a mean squared displacement x that is directly proportional to time t and a constant coefficient of diffusion D,

$$< x^2 >= 2NDt \tag{I.1}$$

where N is the spatial dimensions. Einstein proceeded to relate the diffusion constant to physically measurable quantities such as the mobility of the particle μ and the temperature T,

$$D = \mu k_B T \tag{I.2}$$

where k_B is the Boltzmann constant. This relationship has been given the name, the Einstein-Smoluchowski relation, as Marion Smoluchowski independently arrived at the same conclusion in 1906. The relationship has both practical as well as theoretical significance, as it confirms that the second law of thermodynamics is a statistical law.

If the mean free path is large relative to the radius of the diffusing particle, as is the case in a dilute solution, one can combine Stokes' law with Einstein's relation to arrive at,

$$D = \frac{k_B T}{6\pi\eta r} \tag{I.3}$$

where η is the viscosity and r is the hydrodynamic radius of the diffusing species. This relationship, termed the Stokes-Einstein relation, allows one to clearly see the connections between the rate of particle diffusivity and the physical properties of the particle and the solution. For the purposes of studying protein complexes *in vivo* this relationship is very useful for directly measuring a particle's radius assuming knowledge of the solution properties.

Diffusion also has consequences for the rates of chemical reactions. The connection between the rate of diffusion and the rate of a chemical reaction was worked out by Smoluchowski in 1917. Smoluchowski imagined the diffusional encounters of two particles in the real world must be similar to an imaginary system in which one of the particles is immobilized, and the other is diffusing with a diffusion coefficient equal to the sum of the diffusion coefficients of the particles in the real system. In the imaginary system, one of the particles acts as sink for the mobile particle, and the reaction rate is defined as the steady-state flux of diffusing particles into the immobilized ones. Using this assumption, Smoluchowski determined, in the diffusion controlled limit, the rate at which two particles, A and B, interact,

$$\phi = C_A C_B 4\pi N_A d(D_A + D_B) \tag{I.4}$$

This relationship shows that the rate ϕ depends on the relative separation distance d the reaction partners must achieve to react, the concentrations of the reaction partners (C_A and C_B), and their diffusion coefficients (D_A and D_B). In the gas phase, where diffusion is relatively fast, the observed rates of reactions are usually due to a rate-limiting step somewhere along the reaction coordinate and not due to limitations in the frequency of reactant collisions. However, in solution – where the rates of particle diffusion are far slower – the observed reaction rate may be limited by the reactant collision frequency rather than some step along the reaction coordinate. Thus, we arrive at the very important realization that the diffusion rates of molecules that make up a living cell may, to a large extent, regulate the observable rates of reactions.

Experimentally, measuring diffusion in living cells using modern technology is now more accessible than ever before. Fluorescence based methods of measuring diffusion fall into the three main categories: Fluorescence Recovery After Photobleaching (FRAP), Fluorescence Correlation Spectroscopy (FCS), and Single Particle Tracking (SPT) . Although all of these methods rely on the underlying principles of diffusion, experimentally they are different approaches, and each method carries with it certain strengths and weaknesses.

FRAP was one of the first fluorescence microscopy experiments for quantitatively measuring molecular dynamics [138–140]. FRAP is carried out by irreversibly photobleaching a small population of molecules in a particular region of the sample and then monitoring the exchange of unbleached and bleached molecules over time. FRAP curves yield information about both the recovery kinetics and the fraction of molecules free to diffuse. Originally, FRAP measurements were performed using a focused, static laser beam to bleach molecules. A theoretical basis for the analysis of FRAP measurements of lateral diffusion by spot-photobleaching approaches for a static laser was established shortly after the development of FRAP [140]. The earliest applications of FRAP were predominantly confined to measurements of cell-surface proteins or lipids that could be fluorescently labeled by exogenous probes [139, 140]. The discovery of GFP and molecular techniques to tag proteins with GFP, or similar fluorescent proteins, has vastly expanded the number of proteins that can be studied by FRAP. Furthermore, technical advances in microscopes in the late 1980s to early 1990s have made this approach widely available to many researchers. One disadvantage of FRAP is that it is rarely sensitive enough to accurately quantify recoveries that are dominated by complicated scenarios such as the diffusion of different sized complexes [141]. FRAP has a major advantage over alternative methods however, in that it is capable of accurately measure the fraction of immobile molecules [132].

FCS approaches are another set of powerful tools for investigating molecular dynamics *in vivo*. In the modern FCS approach, particle fluctuations in a small, diffraction limited, observation volume are passively monitored with high temporal resolution. The average number of particles in the volume and the diffusivity of the particles are quantified by analysis of the fluctuation autocorrelation function [142]. FCS is exquisitely sensitive, allowing measurements on samples with concentrations in the pico- to nanomolar range [142, 143]. FCS works best when measuring the dynamics of faster moving molecules, as measurements of slower moving molecules may be confounded by photobleaching artifacts.

SPT measures diffusion by directly observing the trajectories of individual particles [144]. After data acquisition, the individual particle trajectories must be reconstructed from the set of coordinates of particles at each time point. This is a correspondence problem that can be particularly challenging, and thus a variety of approaches have been developed to solve it [145]. Next, the trajectories are typically analyzed in terms of their mean squared displacement [146]. The advantage of SPT is that it enables one to measure heterogeneity in a population of molecules. In addition, often the lifetime of a molecule as well as its lateral diffusion at the membrane can be quantified [147].

Given the assumptions that the particle is a sphere undergoing Brownian motion in a dilute solution, measuring diffusion might not seem to be a valid approach to determining the size of a protein or its binding reactions; however, recently this approach has been highlighted as a valuable way to at least get a first approximation. For example, Sprague et al. [148] used the Stokes-Einstein relation to quantify the binding of a transcription factor to DNA in living cells; Kang et al. [149] quantified the binding of a protein to membranes in living cells; and Drake et al. [121] used the approach to test if LC3 was a monomer in living cells. At this time, it remains unclear if the assumptions made explicit in the Stokes-Einstein relation are valid for measurements in living cells. To make matters worse, the technical approaches used to quantify diffusion in living cells are in their relative infancy, and there is a lack of a general consensus about the protocols to not only acquire, but also to analyze the data. Most of the assumptions either implicit or explicit in quantifying diffusion in living cells have already been acknowledged, but they still require more experimental evidence to determine the degree to which they may interfere with the interpretation of results.

I.5 Overview

Over the past two decades the importance of autophagy in human health and disease has come to the forefront. It is clear that discovery of new forms of treatment for human disease affecting such a complicating process as autophagy will require a greater understanding of the inner workings of the cell. The molecules involved in autophagy display emergent complexity, and to fully understand some of their properties will require their study in the living cell. The ubiquitin-like protein LC3 is a central component of the autophagy pathway. LC3 has an extensive network of interacting proteins, but little is known about their physiological regulation.

To begin, we sought to develop tools to make our FRAP approaches more broadly available to the biological community. Toward this end we developed a freely accessible software program called FRAP-Toolbox to perform quantitative FRAP analyses using the most up-to-date models for recoveries dominated by reactions, or diffusion. We also demonstrate how this software can be used to analyze actual FRAP. Next, in order to examine how the LC3 protein interaction network is regulated, we first characterized the size and stoichiometry of autophagosome independent LC3 in the cytoplasm of living cells and in cytoplasmic extracts and investigated how these properties are regulated by specific residues on LC3's hydrophobic protein binding surface as well its G120 residue required for lipid modification. In this study we found that individual soluble LC3 molecules associate with a $\sim 500\,\mathrm{kDa}$ complex and that residues on LC3's hydrophobic protein interaction surface are important for regulating its association with these complexes. We then sought to develop tools to study LC3 complex formation in live cells by analyzing the interactions of LC3 with a catalytically inert mutant form of ATG4B using FRET and FRAP. Here we found that our data are consistent with a model in which Atg4B(C74A) and LC3 not only directly interact, but also associate with a slowly diffusing complex in both the cytoplasm and nucleus of living cells. This complex could either have a relatively high molecular weight or be elongated in shape. In addition, our data suggest that the organization of LC3 within complexes in the nucleus may be different from that in the cytoplasm. Next, we developed an assay that can be more broadly used to study LC3 protein interactions using confocal microscopy. The method relies on quantifying LC3's nucleocytoplasmic ratio both with and without co-overexpression of potential LC3 interacting proteins. This method can be easily extended to a high throughput format. Lastly, in order to gain novel insights into the nature of nuclear LC3, I present several works in progress, and propose future directions. Through these studies, we have uncovered a wholly novel LC3 associated complex, and we have developed several tools that will aid in future investigations of LC3 and other proteins in the autophagy pathway more generally. The results in this dissertation also demonstrate the usefulness of fluorescence based microscopy methods for investigating protein dynamics in living cells.

CHAPTER II

FRAP-Toolbox: Software for the analysis of Fluorescence Recovery After Photobleaching

Fluorescence recovery after photobleaching (FRAP) reports on the mobility of fluorescently labeled molecules. FRAP is a powerful approach used to study the dynamic properties of proteins in their native environment - living cells. Questions of interest include quantifying reversible binding events, transport between cellular compartments, and intracompartmental diffusion. Although advances in microscope technologies have made this approach increasingly straightforward to carry out, quantitative data analysis using newly developed FRAP models currently requires training in computer programming and data analysis. It thus presents a significant barrier to its widespread use by the scientific community. In order to make analyzing FRAP data using newly developed FRAP models more accessible, we developed a modular software program called FRAP-Toolbox. This chapter begins by introducing the problem of measuring molecular mobility in living cells by FRAP. Next, the design of our open source software program to analyze FRAP data is described. In depth examples of how to use FRAP-Toolbox to analyze several test data sets is given. Finally, the usefulness of FRAP-Toolbox is demonstrated by analyzing the dynamics of the autophagy protein ATG5 in living cells. A webpage dedicated to all aspects of the development of FRAP-Toolbox can be accessed online at http://www.fraptoolbox.com.

II.1 Introduction

Mobility is a property of fundamental importance, which can control the availability of a molecule for reactions, and has even been proposed to contribute to the establishment of patterns in organism development [150]. One of the most useful tools for characterizing a molecule's mobility is fluorescence recovery after photobleaching (FRAP). FRAP is a widely accessible technique, which can be performed on virtually any modern fluorescence microscope, and is applicable to studies in both solution as well as living cells [132]. New FRAP methodology and quantitative FRAP models are greatly facilitating the use of this technology to make important advances in basic studies of biology [151, 152]. FRAP data is often analyzed qualitatively by making comparisons among FRAP curves collected under identical conditions [153, 154]; however, more sophisticated quantitative analysis strategies are available, but researchers often struggle with these methods due to a lack of simple to use software for image-processing and data analysis. Therefore, in order to facilitate obtaining quantitative information from FRAP experiments, we have developed an open source software

---

This manuscript was prepared for publication in *PLoS Comp Biol*.

program called FRAP-Toolbox, which provides automated batch image-processing and data analysis.

The FRAP method is carried out by irreversibly photobleaching a small population of fluorescent molecules within a defined region, and monitoring their recovery back to the steady-state (Figure II.1). FRAP reports on the fraction of molecules that are free to recover over the time scale of the experiment termed the mobile fraction (Mf), and the rate at which those molecules recover (related to the recovery halftime $\tau_{1/2}$). Typically, Mf is a readout of stable associations with immobile structures, while $\tau_{1/2}$ is a parameter related to the characteristic dynamics of the molecules such as directed flow, diffusion, and reversible reactions. $\tau_{1/2}$ is also affected by experiment specific parameters such as the size and geometry of the bleach region employed. Although $\tau_{1/2}$ and Mf can be used in comparative studies to make qualitative arguments for faster or slower dynamics, better quantitative FRAP approaches and models have been developed to gain even deeper insights into the nature of the underlying molecular dynamics. For example, models have been developed to specifically distinguish between recoveries dominated by the kinetics of a reaction, diffusion, flow, and even by a mixture of reactions and diffusion (discussed in more detail in the supplementary material) [140, 148, 149, 151, 155–160].

Despite the relative ease of acquiring robust FRAP data, an ongoing obstacle for subsequent quantitative analyses of FRAP experiments lies in the image processing and data analysis steps. In order to overcome this obstacle and help make these quantitative methods more broadly available to the biological community, several software tools have been developed. These software tools are all mostly freely available and have been developed to aid in normalizing FRAP data and non-linear least squares analysis using analytical one and two component reaction dominant FRAP models (Table II.1). However, the tools that have been developed generally lack one or more of the features in high demand such as: 1) easy-to-use integrated image processing; 2) analytical models for obtaining an instrument independent diffusion coefficient (D); and 3) a streamlined approach to batch processing many datasets.

In order to meet all of these needs, we have developed a freely accessible software program called FRAP Toolbox to perform quantitative FRAP analyses using the most up-to-date models for recoveries dominated by reactions or diffusion. We demonstrate how this software can be used to analyze actual FRAP data using Venus-ATG5 as a test case. FRAP-Toolbox can be accessed at https://www.fraptoolbox.com.

II.2 Design and implementation

II.2.1 Overview of the software

For an overview of the FRAP-Toolbox design refer to the schematic in Figure II.2. FRAP-Toolbox begins with a main GUI. The main GUI accepts several basic user inputs including a FRAP model selection. The user then has a choice: the user can a) preview their FRAP dataset, or b) proceed to the FRAP data analysis;

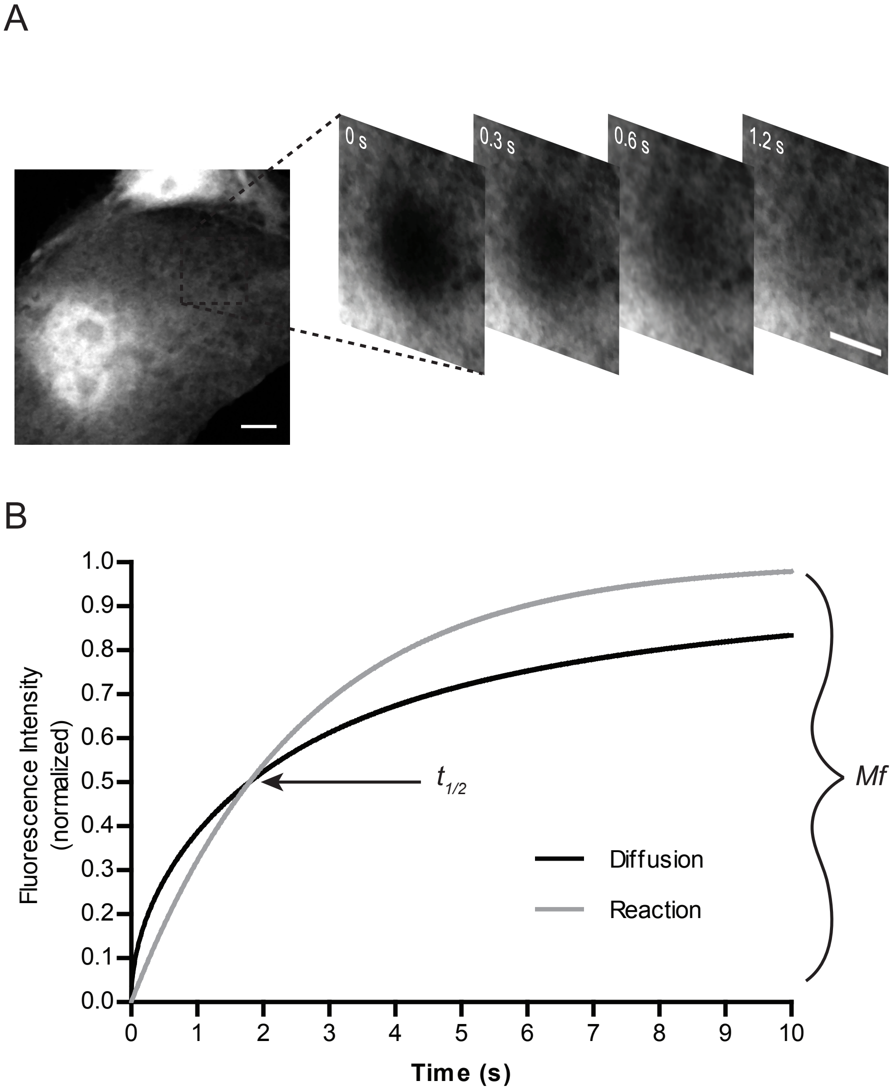

Figure II.1: Schematic of a typical FRAP experiment. (A) A region of a cell expressing a fluorescently labeled molecule is selectively photobleached. The recovery of fluorescence as unbleached molecules exchange with bleached molecules is followed over time. (B) The FRAP curve is the mean fluorescence in the bleach region versus time. The FRAP curve provides quantitative information about the mobility of the underlying molecules (qualitatively related to $t_{1/2}$), as well as the fraction of those molecules which are free to recover (the mobile fraction Mf). Note that different underlying physical processes result in differently shaped FRAP curves with identical $t_{1/2}$ values. Here is an example of recoveries dominated by diffusion (black line), and a first order reaction (gray line).

Table II.1: A comparison of software tools for the analysis of FRAP data and their features.

Software Name	FRAP-Toolbox	EasyFRAP	FRAPCalc	FRAPAnalyzer	Virtual FRAP	FRAP Analysis
Availability	Free	Free	Requires IgorPro	Free	Free	Free
Integrated Image Analysis	Yes	No	No	No	Yes	Yes
Observational photobleaching correction	Yes	Yes	Yes	Yes	No	No
1 comp. reaction model	Yes	Yes	Yes	Yes	No	No
2 comp. reaction model	Yes	Yes	Yes	Yes	No	No
1 comp. diffusion model	Yes	No	No	No	No	No
Numerical integration	No	No	No	No	Yes	No
Batch processing	Yes	Yes	Yes	No	No	No
URL	http://wwww.fraptoolbox.com	http://ccl.med.upatras.gr/index.php?id=easyfrap	http://cmci.embl.de/downloads/frap_analysis	http://actinsim.uni.lu/eng/Downloads	http://wiki.vcell.uchc.edu/twiki5/bin/view/VCell/VFRAP	http://imagejdocu.tudor.lu/doku.php?id=plugin:analysis:frap_analysis:start

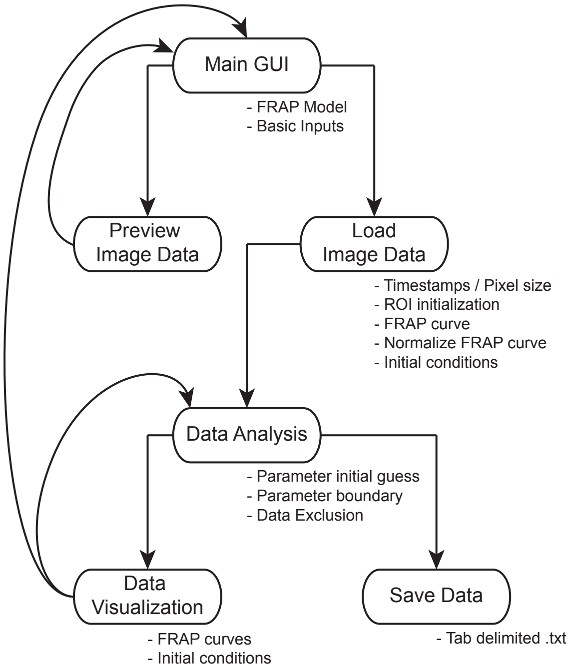

Figure II.2: An overview of the FRAP-Toolbox design.

however, before the user can perform the FRAP data analysis, FRAP-Toolbox will automatically load their image data from the raw microscope files using Bioformats [161] (an opensource java library for reading a variety of proprietary and non-proprietary life science image formats). During these steps, information is extracted from the metadata of the raw file including timestamps and pixel size; in addition, image analysis is performed to obtain FRAP curves and initial conditions (if applicable). Next, the user is presented with a data analysis and visualization window where they interact with the program and run the fitting routine. If these results are satisfactory, the user has the option to save the data generated by FRAP-Toolbox. In the sections below we explain in more detail each of the steps in the FRAP-Toolbox design.

II.2.2 Main GUI

The main GUI serves as a means of collecting seven basic pieces of information from the user.

1. Where are the raw FRAP datasets located?
2. Which FRAP model should be used for the analysis? Current choices are: Diffusion, Reaction 1, and Reaction 2 models.
3. What type of bleaching ROI was used in the experiment? Current choices are a circle and user defined.
4. Which frame number corresponds to the post-bleach image?

5. What is the background fluorescence intensity?

6. Should the data be normalized by the whole cell intensity?

7. How many pre-bleach images need to be used for normalizing the FRAP curve?

II.2.3 Preview image data

The first selected FRAP dataset in the list is loaded and displayed along with user defined circular ROIs. The user can scroll through the images in the FRAP dataset and verify that their basic inputs are correct.

II.2.4 Load image data

During this stage of the algorithm, each raw FRAP dataset from the microscope is read using Bioformats, and the relevant data extracted. Using the basic inputs from the user, bleaching ROIs, and cell ROIs are initialized. Next, image analysis is performed to obtain FRAP curves. Finally, the FRAP data are normalized to the pre-bleach steady-state intensity. Here the diffusion model deviates from the Reaction 1 and Reaction 2 models in that it requires the use of a circular bleach region; in addition, image analysis is performed to obtain radial post-bleach profiles that are used later to find the initial conditions for the diffusion equation.

II.2.5 Data Analysis

After the FRAP datasets are loaded, the user is directed to a data analysis and visualization GUI providing the user with an opportunity to supply inputs for the initial parameter guesses, lower and upper bounds on parameters, and the range of data to fit (for example, the user can exclude FRAP curve timepoints after reaching post-bleach steady-state). FRAP-Toolbox uses the trust-region reflective algorithm – a constrained non-linear least squares approach – to fit the data. The fitting routine finds the parameters x that solve the problems (where applicable),

$$\min \sum_{0}^{x} (I(x;t=0) - i(x;t=0))^2 \tag{II.1}$$

$$\min \sum_{0}^{x} \frac{(I(t) - i(t))^2}{t + \sum_0^t I(t)} \tag{II.2}$$

Here, $I(x;t=0)$ is the normalized post-bleach profile, and $i(x;t=0)$ is the analytical approximation. $I(t)$ is the normalized FRAP data, and $i(t)$ is the analytical FRAP model.

The FRAP-Toolbox currently supports three different models. The first model is called Diffusion. The Diffusion model is a series representation of a closed-form analytical FRAP equation describing free diffusion of unbleached molecules into a circular bleach ROI, which is applicable to data obtained on a laser scanning confocal microscope [158]. This equation corrects for the diffusion that occurs during the photobleaching event.

The second and third models are called Reaction 1 and Reaction 2 respectively. The Reaction 1 model describes FRAP recoveries that are dominated by pseudo-first order reaction kinetics, while the Reaction 2 model describes FRAP recoveries that are dominated by the sum of two independent first order reactions kinetics. Many physical-chemical situations are thought to be appropriately modeled using equations of this type. Some examples include the turnover kinetics of actin binding proteins [162] and the nucleocytoplasmic exchange of molecules [163].

II.2.6 Data visualization

For the purposes of examining the results of the fitting routine, theoretical FRAP curves using the optimized parameters are plotted along with the experimental data. In addition, the residuals are plotted so that the user can check for systematic deviations between the fit and the data. The optimized parameters are automatically uploaded into the table in the data analysis GUI.

II.2.7 Save data

Finally, once the user is satisfied with the results of their fitting routine the optimized parameters and processed data can be exported as a tab delimited text file for later use in downstream statistical analyses and the generation of publication quality figures.

II.3 Results

II.3.1 Published examples of the FRAP-Toolbox algorithms

The algorithms that underlie FRAP-Toolbox have been validated by measurements of the diffusion of EGFP in cells and solutions of known viscosity. D was shown to be independent of experimental conditions [158]. They also have been used to gain novel insights into biological problems. Previously, we quantitatively analyzed the diffusion rate of microtubule associated protein 1 light chain 3 beta (MAP1LC3B/LC3) *in vivo* and uncovered quantitative information about its effective hydrodynamic radius [164], as well as its interactions with ATG4B(C74A) in living cells [165].

II.3.2 Quantifying the effective size of Venus-ATG5 in living cells

In order to further demonstrate the usefulness of FRAP-Toolbox for this class of problems, in what follows, we examine the intracellular mobility of a GFP tagged form of the autophagy protein ATG5 (Venus-ATG5). We built our Venus-ATG5 construct by performing a BglII and EcoRI double restriction digest on the original GFP-ATG5 vector [166]. ATG5 ($\sim 30\,\text{kDa}$ monomer) is a key component of the autophagy pathway where

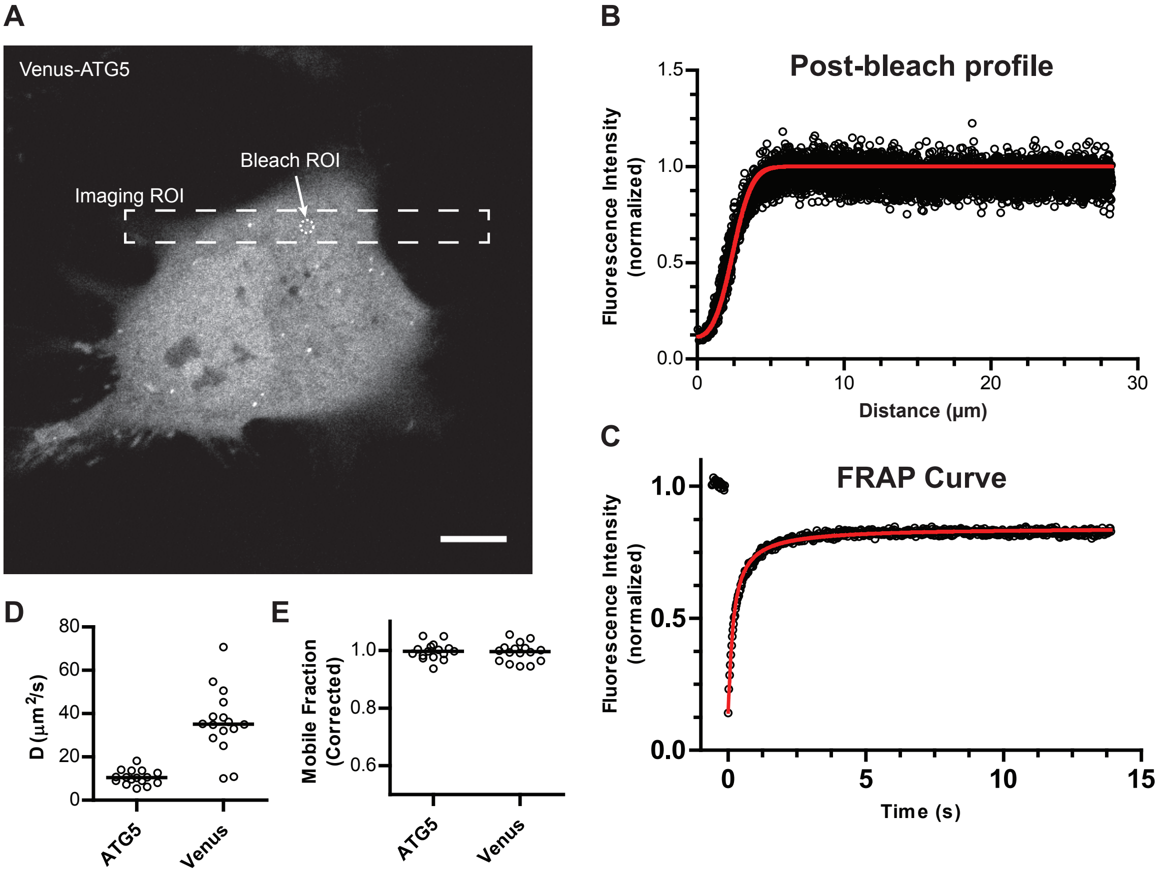

Figure II.3: The effective diffusion of Venus-ATG5 is slower than expected for a freely diffusing monomer. (A) A quantitative FRAP assay was carried out on HeLa cells expressing either Venus as a control for a 27 kDa monomer or Venus-ATG5. We selectively photobleached a small 1 μm bleach region placed in a region of the cytoplasm independent of puncta. (B) The initial conditions for the diffusion equation are obtained from the radial post-bleach profile. (C) The FRAP recovery was well fit by the FRAP-Toolbox Diffusion model. (D) Diffusion coefficients and (E) corrected mobile fractions from measurements on multiple cells. (N=15)

it is thought to contribute to the assembly of autophagosomes via formation of a membrane scaffold together with ATG12, ATG16, and ATG8 [167]. It is known that ATG5 forms a covalent complex with ATG12; this conjugate – together with non-convalent association with ATG16 – plays a role as an E3-like factor in the conjugation of ATG8 to phosphatidylethanolamine [168]. The ATG12-5-16 complex has been proposed to be in the range of $\sim$400 kDa–800 kDa based on in vitro chromatography experiments [89]. However, an analysis of the properties of ATG5 complexes within the context of living cells has not been carried out.

In the case of ATG5, we are motivated to understand if ATG5, independent of autophagosomes, normally behaves as if it is associated with an $\sim$400 kDa–800 kDa complex in living cells. In order to address this question we carried out a quantitative FRAP assay using a Zeiss LSM 510 confocal microscope. Our measurements were directed at the diffuse cytosolic pool of the protein independent of any visible fluorescent puncta, using a 1 μm radius circular bleach region (Figure II.3A). We expect this cytoplasmic form of ATG5 is largely independent of that associated with autophagic membranes, but may be constitutively associated with ATG12 and ATG16 to form freely diffusing ATG12-5-16 complexes. Figure II.3B shows an example of the postbleach radial fluorescence profile from our measurements that is fit to obtain the initial conditions for the diffusion FRAP model. The FRAP recovery curve for this diffuse cytoplasmic pool of Venus-ATG5 was well fit by the single component diffusion model in FRAP-Toolbox (Figure II.3C). The measurements were repeated for a number of different cells, and the diffusion coefficients and mobile fractions from the fits to the data are shown as scattered dot plots in (Figure II.3D and E).

Next, we estimated the effective size of the diffusing Venus-ATG5 species in order to test if Venus-ATG5's diffusion is consistent with its association with ATG12 and ATG16 in a $\sim 400\,\mathrm{kDa}$–$800\,\mathrm{kDa}$ complex. To accomplish this, we quantified the diffusion coefficient of Venus as a control for a monomer with a known molecular weight of $27\,\mathrm{kDa}$. Using the Stokes-Einstein relation (D is proportional to $MW^{-1/3}$), and the measured diffusion coefficient of Venus-ATG5, we estimate the size of the diffusing Venus-ATG5 is approximately $1100 \pm 500\,\mathrm{kDa}$ assuming a spherical geometry. This is consistent with the hypothesis that ATG5 constitutively associates with ATG12 and ATG16 to form a large multiprotein complex rather than existing as a freely diffusing monomer in the cytosol of living cells.

II.3.3 Quantifying the nucleocytoplasmic exchange rate of ATG5 in living cells

Interestingly, in a putatively autophagy independent role, ATG5 was proposed to translocate into the nucleus where it promotes apoptosis [169]. In our own experiments, we noticed Venus-ATG5 was, in fact, localized in the nucleus as well as in the cytoplasm where it is thought to function in autophagy (Figure II.4A). However, relatively little is known about the dynamics of ATG5 nucleocytoplasmic transport.

In order to further investigate this, we carried out a quantitative FRAP assay where we selectively photobleached Venus-ATG5 in the nuclear compartment and monitored its recovery over time in order to quantify the rate of nucleocytoplasmic transport (Figure II.4A and C). We carried out this set of FRAP experiments using a Nikon Eclipse Ti laser scanning confocal microscope. Our FRAP curves for Venus-ATG5 nucleocytoplasmic transport, and a Venus control are shown in Figure II.4B. While the nucleocytoplasmic recovery for Venus was well fit by a one component exponential function, the Venus-ATG5 recovery required the sum of two independent exponential components. We attribute the faster component of the ATG5 recovery to intracompartmental diffusion, as this rate ($1.8 \pm 0.2 \times 10^{-2}\,\mathrm{s}^{-1}$) is consistent with our measured diffusion coefficient, whereas the slower component of the ATG5 recovery is due to nucleocytoplasmic exchange. The rate we obtained from our measurements of Venus nucleocytoplasmic exchange was $9.7 \pm 0.4 \times 10^{-3}\,\mathrm{s}^{-1}$. This is very close to what was previously measured for passive diffusion of GFP through nuclear pores in

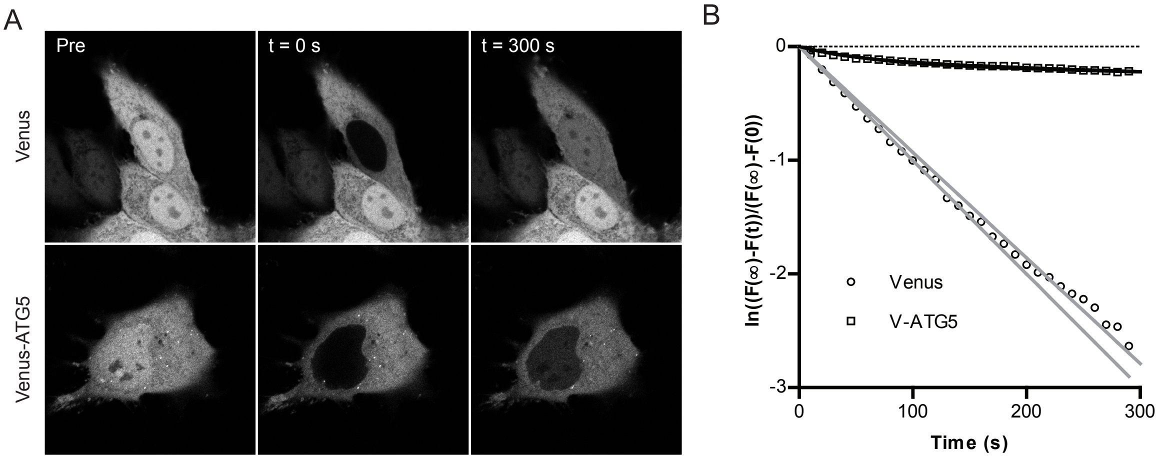

Figure II.4: The nucleocytoplasmic exchange rate of Venus-ATG5 is slower than expected for a monomer undergoing passive diffusion. (A) A quantitative FRAP assay was carried out on HeLa cells expressing either Venus as a control for a (2 nm monomer or Venus-ATG5. We selectively photobleached the entire nuclear region, and monitored the recoveries of fluorescence. Shown are representative examples of the experiment just prior to the bleach (pre), just after the bleach ($t = 0\,\mathrm{s}$), and after a significant amount of time had elapsed ($t = 300\,\mathrm{s}$)). (B) The recoveries from 2 different cells were averaged together and plotted according to the following transformation: $\ln\left(\frac{I(\infty)-I(t)}{I(\infty)-I(0)}\right)$. The 95 % confidence intervals for the fit to Venus are shown as solid gray lines, while those for Venus-ATG5 are shown as solid black lines.

COS7 cells [170]. On the other hand, the rate we obtained from our measurements of Venus-ATG5 nucleocytoplasmic exchange was $2.7 \pm 0.5 \times 10^{-4}\,\mathrm{s}^{-1}$. That is about 30 fold slower than Venus. This result is not at all surprising given our measured D for ATG5 is quite slow suggesting Venus-ATG5 is bound to a very large complex. Our results are consistent with a model whereby the binding of Venus-ATG5 to a large $\sim 1000\,\mathrm{kDa}$ complex may be hindering its ability to undergo passive nucleocytoplasmic exchange.

II.3.4 Summary

Many biological hypotheses are experimentally untestable without the use of *in vivo* techniques such as FRAP due to the complexity of purifying and reconstituting the molecular components. The power of FRAP is in quantifying the nature and rate of molecular mobility in living cells. Here, we provide two examples of important biological processes for which a detailed understanding of the underlying molecular mobility is crucial. Most modern confocal microscopes have out-of-the-box capability to perform FRAP experiments in simple and complex geometries. In addition, there have been many advances in the theoretical analysis of FRAP experiments with the addition of methods and models to quantify, for example Brownian motion. However, a remaining hurdle for the widespread adoption and use of FRAP among the scientific community is that quantitative FRAP analysis requires handling of large datasets, and programming of complicated data fitting routines using consensus approaches. Our solution to these problems is the development of an open source software program called FRAP-Toolbox.

II.4 Availability and future directions

We have created a website dedicated to all aspects of the development of FRAP-Toolbox and consensus FRAP methods at http://www.fraptoolbox.com. The source codes for FRAP-Toolbox can be downloaded at https://github.com/kraftlj/frap-toolbox.

II.5 Supplementary Material

II.5.1 Installation

The user has two options to run FRAP-Toolbox:

1. Using the source files and a full installation of MATLAB
2. As a standalone application by first installing the royalty-free MATLAB Compiler Runtime.

The standalone application and information about where to find the source files can found on our download page at http://www.fraptoolbox.com/Download.

II.5.1.1 System requirements

FRAP-Toolbox has been tested on a PC running 32 bit Windows XP and 64 bit Windows 7, as well as a MAC running OS X 10.9. The installation requirements for MATLAB 2013 can be found at http://www.mathworks.com/support/sysreq/current_release/.

II.5.1.2 FRAP-Toolbox using source code

In MATLAB, navigate to the FRAP−Toolbox directory containing the source files. Open and run MainGUI.m.

II.5.1.3 FRAP-Toolbox as a standalone application

Instructions for a PC

1. Move the folder FRAP−Toolbox to a suitable location, e.g. C:\FRAP−Toolbox, on your hard drive.
2. Install the MATLAB Compiler Runtime by double clicking on the MCR_R2013a_win32_installer.exe file, and following the on screen instructions.
3. Open `classpath . txt` for editing. By default this file is located in C:\Program Files\MATLAB\MATLAB Compiler Runtime\v81\toolbox\local\classpath.txt. You need to first give yourself administrative

privileges for editing *classpath.txt* by right clicking the file, click properties, click Security, click Edit, and giving Full control to Users. Press OK to save the changes giving you rights to edit classpath . txt. On a new line, at the end of the file, append the text file with, C:\FRAP−Toolbox\loci_tools.jar. Save the changes before closing.

4. You can now run FRAP-Toolbox by double clicking the FrapToolbox.exe file. Note: you can place the FRAP−Toolbox directory in any desired location on your hard drive, but be sure to add the correct path to loci_tools . jar in classpath . txt.

Instructions for a MAC

1. Move the folder FRAP−Toolbox to the location, / Applications /FRAP−Toolbox, on your hard drive. / Applications /FRAP−Toolbox can be accessed by selecting Applications in finder and then navigating to the FRAP-Toolbox folder.
2. Install the MATLAB Compiler Runtime by double clicking on the MCR_R2013b_maci64_installer.zip file, and following the on screen instructions.
3. Open classpath . txt for editing. This file can be found in / Applications /MATLAB_R2013b/toolbox /local/classpath.txt. You may need to right-click the MATLAB_R2013b icon in your Applications folder and select "Show Package Contents" in order to navigate there. You may need to give yourself administrative privileges. On a new line, at the end of the file, append the text file with, / Applications /FRAP−Toolbox/loci_tools.jar. Save the changes before closing.
4. You can now run FrapToolbox_Mac.app located in / Applications /FRAP−Toolbox. Note: you can place the FRAP−Toolbox directory in any desired location on your hard drive, but be sure to add the correct path to loci_tools . jar in classpath . txt.

II.5.2 Supported image formats

FRAP-Toolbox directly opens raw image formats by integrating with Bio-Formats a standalone Java library for reading and writing life science image file formats [161]. For a full list of the supported image formats by Bio-Formats see http://www.openmicroscopy.org/site/support/bio-formats4/supported-formats.html. We have verified FRAP-Toolbox correctly reads .lsm and .nd2 raw image formats from Zeiss and Nikon microscopes.

II.5.3 Using FRAP-Toolbox

FRAP-Toolbox begins with a main window (Figure II.5) that requires the user to provide several basic inputs. The first input is the location where raw FRAP data is stored. The files in the selected directory appear in a right hand panel, which allows the user to select one or more files. In the example (Figure II.5) we selected 10 FRAP datasets, which were acquired with a Zeiss LSM 510, and have the raw file extension .lsm. For these datasets we photobleached a circular region in the nucleus of COS7 cells expressing the Venus fluorescent protein. Next, the user must enter a set of basic inputs including the model to use for the data analysis, the geometry of the bleaching ROI, the image frame number of the bleaching event, a constant background intensity (experimentally determined with unlabeled controls), an option to correct the fluorescence intensity using the mean intensity of the whole cell, as well as the number of pre-bleach images that should be used for normalization purposes. Finally, the user will either choose to preview their settings by loading and visualizing the first FRAP data set, or the user will press the next button to proceed to data fitting and data saving.

Pressing the image preview button on the main window will load the first FRAP data set selected in the list of files (Figure II.6). The previewing window includes a scroll bar at the bottom to allow previewing of each image in the image stack, and will also plot a user defined bleaching ROI. If instead the user proceeds to data fitting and data saving by pressing the next button, FRAP-Toolbox will load all of the selected FRAP data sets using the Bio-Formats library for reading and writing life sciences image file formats [161]. A new data analysis and visualization window will pop-up after the data is finished loading (Figure II.7). In this example, we chose to use the FRAP-Toolbox diffusion model, and loaded all 10 FRAP data sets as was shown in Figure II.5. The data analysis and visualization window (FigureII.7) consists of three parts. The first part allows the user to provide several basic inputs to the fitting process, namely, initial guesses on fitting parameters, boundaries on fitting parameters, and an option to exclude data points (for example, the fitting can be constrained to early time points).

Next, the user will press the Run button to fit the FRAP data. As the software finishes the fitting routine, several windows will automatically pop-up to provide the user with the ability to visually inspect the results of the fitting routine (Figure II.8). For the case of the diffusion model, the initial conditions are plotted, as well as the diffusion model fits to the FRAP curves. The optimized parameters from the fitting routine are automatically uploaded in tabular form (Figure II.7). These optimized parameters, the raw FRAP data, as well as the processed FRAP data, and fits to the FRAP data may now be conveniently saved to text files by pressing the save button in the data analysis and visualization window (Figure II.7). Thus, with a few steps, the FRAP-Toolbox provides users with easy access to the latest advancements in quantitative FRAP

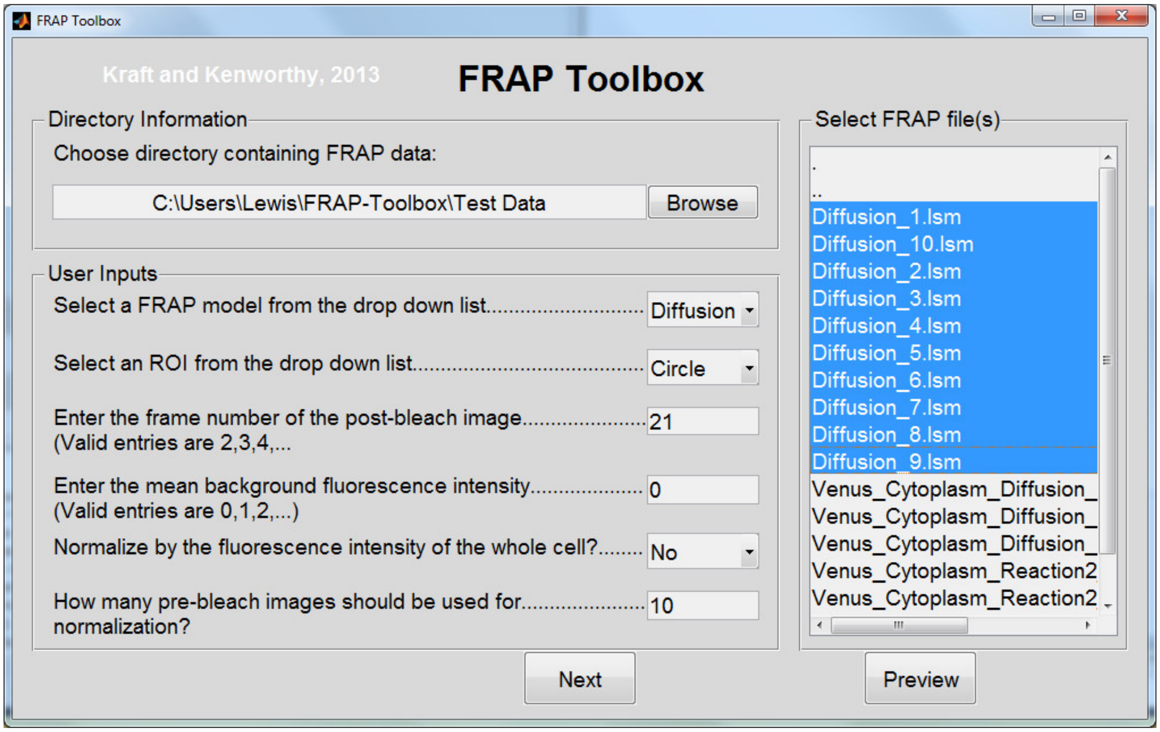

Kraft and Kenworthy, 2013

FRAP Toolbox

Directory Information

Choose directory containing FRAP data:

C:\Users\Lewis\FRAP-Toolbox\Test Data

User Inputs

Select a FRAP model from the drop down list.......................... Diffusion

Select an ROI from the drop down list....................................... Circle

Enter the frame number of the post-bleach image..................... 21
(Valid entries are 2,3,4,...

Enter the mean background fluorescence intensity.................... 0
(Valid entries are 0,1,2,...)

Normalize by the fluorescence intensity of the whole cell?........ No

How many pre-bleach images should be used for..................... 10
normalization?

Select FRAP file(s)

.
..
Diffusion_1.lsm
Diffusion_10.lsm
Diffusion_2.lsm
Diffusion_3.lsm
Diffusion_4.lsm
Diffusion_5.lsm
Diffusion_6.lsm
Diffusion_7.lsm
Diffusion_8.lsm
Diffusion_9.lsm
Venus_Cytoplasm_Diffusion_
Venus_Cytoplasm_Diffusion_
Venus_Cytoplasm_Diffusion_
Venus_Cytoplasm_Reaction2
Venus_Cytoplasm_Reaction2

Figure II.5: FRAP Toolbox begins with a main window requesting several basic inputs from the user. First, the user must navigate to the location of saved FRAP datasets on their computer or network (these are raw microscope files, in this case named 1.lsm, 2.lsm, 3.lsm, ...). The user can select one or more of these files at a given time depending on whether they wish to process them all at once or one at a time (Note: batch processing requires all datasets to have the same structure.) Next, the user must select a suitable model for data fitting, the geometry of the bleaching ROI, the frame number for the first post-bleach image, background fluorescence intensity, as well as options for data normalization. Finally, the user can either preview their settings and dataset using the preview button, or proceed to the data analysis screens.

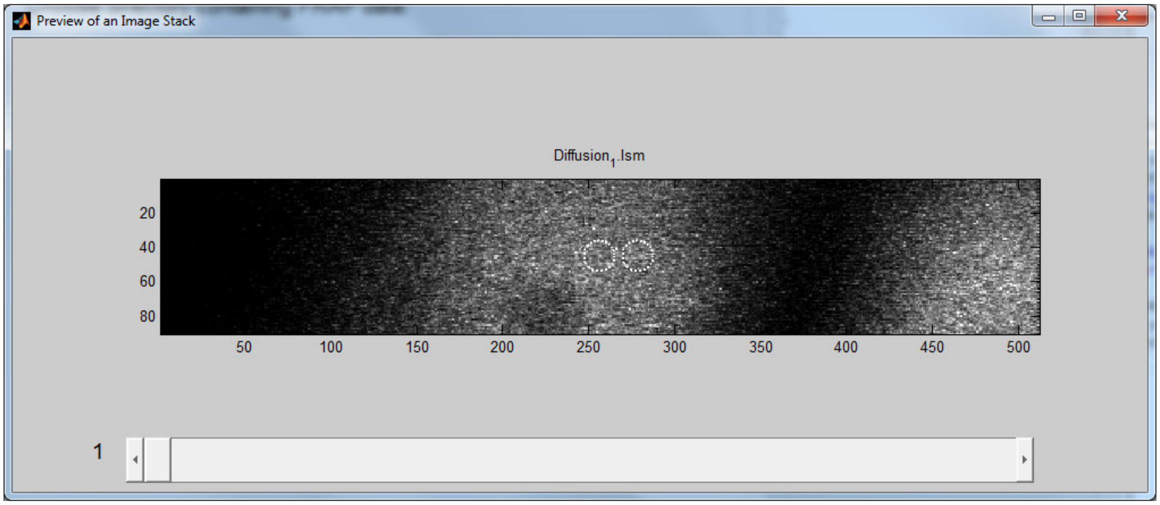

Figure II.6: Previewing a FRAP dataset allows the user to verify the correctness of basic inputs.

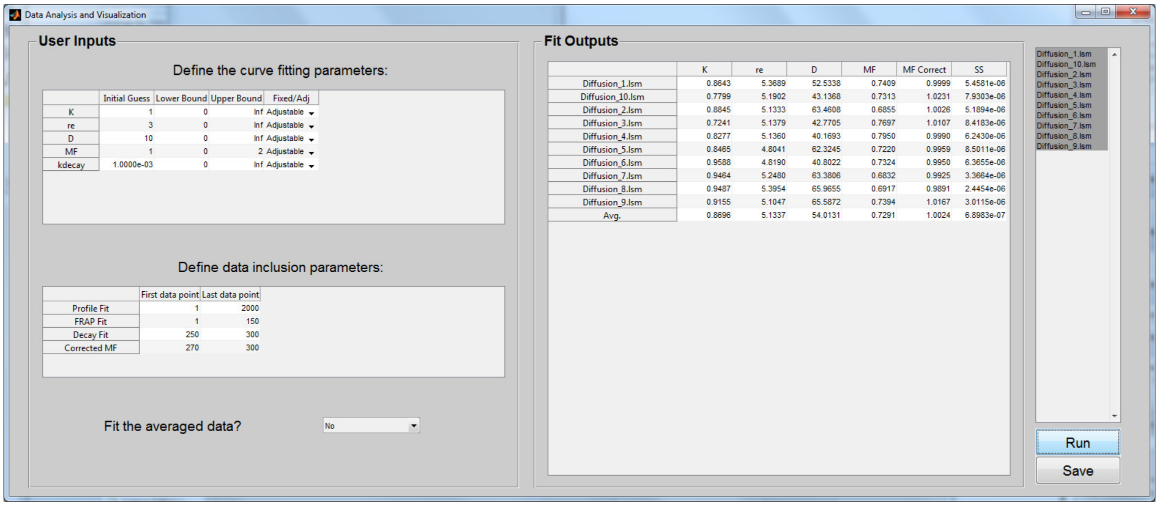
Data Analysis and Visualization

User Inputs

Define the curve fitting parameters:

	Initial Guess	Lower Bound	Upper Bound	Fixed/Adj
K	1	0	Inf	Adjustable
re	3	0	Inf	Adjustable
D	10	0	Inf	Adjustable
MF	1	0	2	Adjustable
kdecay	1.0000e-03	0	Inf	Adjustable

Define data inclusion parameters:

	First data point	Last data point
Profile Fit	1	2000
FRAP Fit	1	150
Decay Fit	250	300
Corrected MF	270	300

Fit the averaged data? No

Fit Outputs

	K	re	D	MF	MF Correct	SS
Diffusion_1.lsm	0.8643	5.3689	52.5338	0.7409	0.9999	5.4581e-06
Diffusion_10.lsm	0.7799	5.1902	43.1368	0.7313	1.0231	7.9303e-06
Diffusion_2.lsm	0.8845	5.1333	63.4608	0.6855	1.0026	5.1894e-06
Diffusion_3.lsm	0.7241	5.1379	42.7705	0.7697	1.0107	8.4183e-06
Diffusion_4.lsm	0.8277	5.1360	40.1693	0.7950	0.9990	6.2430e-06
Diffusion_5.lsm	0.8465	4.8041	62.3245	0.7220	0.9959	8.5011e-06
Diffusion_6.lsm	0.9588	4.8190	40.8022	0.7324	0.9950	6.3655e-06
Diffusion_7.lsm	0.9464	5.2480	63.3806	0.6832	0.9925	3.3664e-06
Diffusion_8.lsm	0.9487	5.3954	65.9655	0.6917	0.9891	2.4454e-06
Diffusion_9.lsm	0.9155	5.1047	65.5872	0.7394	1.0167	3.0115e-06
Avg.	0.8696	5.1337	54.0131	0.7291	1.0024	6.8983e-07

Figure II.7: The data analysis and visualization window allows the user to customize their fitting routine, as well as view and save the results. In the left panel the user has the option of inputting specific initial guesses, and lower and upper bounds for the fitting parameters. In addition, the user has the ability to specifically control how many data points should be fit (often the user will not want to include data points after the fluorescence has plateaued.) The user can specify if all of the FRAP data sets should be fit individually or if the FRAP data sets should be averaged together before fitting. In the right panel the optimal parameters returned by the fitting routine are displayed in table form. In addition, the user can choose to exclude certain datasets by toggling them on and off in the far right panel. After the user is satisfied with the results of the fitting routine there is a button which will save the data as a tab delimited text file.

data analysis. For more information about potential uses for FRAP, acquiring FRAP data, and quantitative analysis we refer the user to recent literature on the topic [164, 165, 171].

II.5.4 Considerations for designing FRAP experiments

II.5.4.1 Diffusion

The user must:

1. Use a circular bleach ROI, record the (x,y) center of the ROI, and its radius (units are in pixels).
2. Record the frame number of the post-bleach image.
3. Independently measure the mean background intensity from unlabeled samples. Often background fluorescence can be approximated as zero.
4. Acquire images that capture the entire cell within the frame if normalizing the FRAP curve by the mean intensity of the whole cell.
5. Acquire at least one pre-bleach image so that the FRAP curves can be normalized.

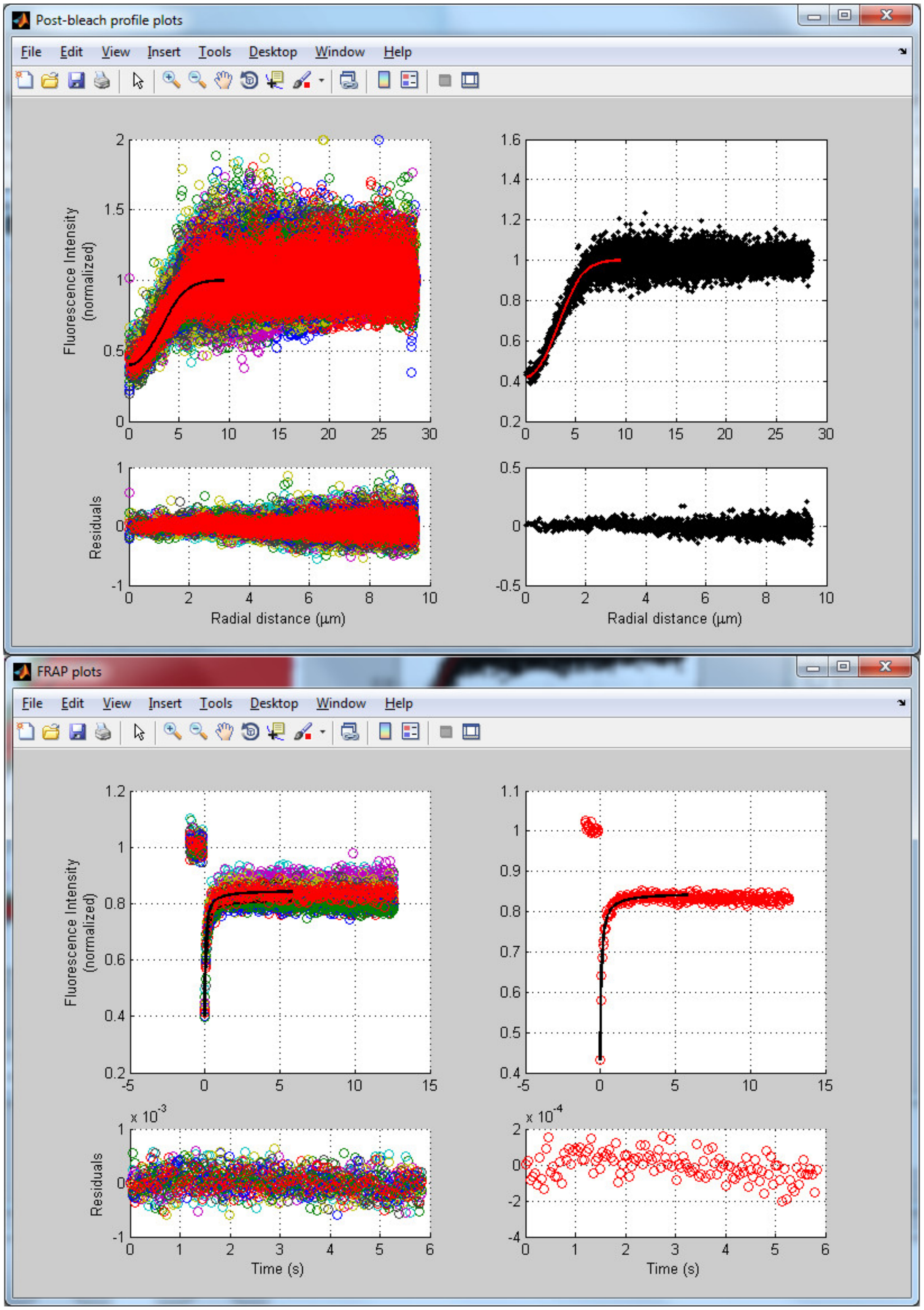

Figure II.8: Diffusion model pop-up windows allow easy inspection of the curve fitting results. (A) In the left panel the radial post-bleach profiles and fits from each individual data set are displayed along with fits and residuals. In the right panel the average post-bleach profile for all datasets and fit is displayed. (B) In the left panel the normalized FRAP curves from each individual data set are displayed along with fits and residuals. In the right panel is the average FRAP curve for all datasets and optimized model with residuals.

Note: Decay due to imaging, and loss of fluorescence in a compartment due to the bleaching event are both inherently corrected if the images are normalized by the mean intensity of the cell. If the FRAP curves are not normalized by the mean intensity of the whole cell, the rate of unintentional photobleaching must be taken into account. FRAP-Toolbox can model this slow decay as a single exponential if the user carries out the recovery for a period of time after again reaching steady-state. Alternatively, the user can measure the decay due to imaging using independent control samples, and input a decay constant as a fixed parameter in FRAP-Toolbox.

II.5.4.2 Reaction 1 and Reaction 2 models

The user must:

1. Use a circular bleach ROI or a user defined polygon, If the bleach geometry is circular, record the (x,y) center of the ROI, and its radius (units are in pixels).
2. Record the frame number of the post-bleach image.
3. Independently measure the mean background intensity from unlabeled samples. Often background fluorescence can be approximated as zero.
4. Acquire images that capture the entire cell within the frame if normalizing the FRAP curve by the mean intensity of the whole cell.
5. Acquire at least one pre-bleach image so that the FRAP curves can be normalized.

II.5.5 FRAP Models and their Applications

II.5.5.1 Diffusion

The Diffusion model is useful for simulating FRAP recoveries dominated by single component Brownian motion. The Diffusion model is a closed form analytical equation for extracting an instrument independent diffusion coefficient [158]. The model has several assumptions: 1) a homogeneous distribution of molecules; 2) a complete bleach through the sample in the z-direction such that diffusion occurs in two dimensions; 3) infinite boundary conditions; and 4) a single diffusing component.

Denote the mean fluorescence intensity within the bleach region as, $I(t)$. $I(t)$ is normalized to the pre-bleach steady-state intensity. The diffusion coefficient D and mobile fraction Mf are found by fitting the data to the FRAP model,

$$I(t) = I_0 \left(\sum_{m=0}^{m=20} \frac{-K^m r_e^2}{m![r_e^2 + m(8Dt + r_n^2)]} \right) Mf + (1 - Mf)I(0) \tag{II.3}$$

where I_0 is 1 for a normalized FRAP curve, and r_n is the nominal radius of the bleaching ROI. This is a modified form of the Axelrod equation [140] where the laser is assumed to be a Gaussian, and the parameters r_e and K take into account the initial conditions for the solution of the diffusion equation. We determine re and K by fitting the normalized radial post-bleach profile, $I(x;t=0)$, to an analytical approximation,

$$I(x;t=0) = I_0 \exp\left(-K \exp\left[-\frac{2x^2}{r_e^2}\right]\right) \tag{II.4}$$

where $I0$ is 1 for a normalized post-bleach profile, and x is the radial distance from the center of the bleaching ROI [155]. D is a coefficient that is related to the physical properties of the diffusing species, and the surrounding medium. Consider spherical molecules undergoing Brownian motion where the relationship is as follows:

$$D = \frac{k_B T}{6\pi\eta R} \tag{II.5}$$

Here, k_B is Boltzmanns constant, T is the absolute temperature, η is the viscosity of the medium, and R is the radius of the diffusing sphere.

The Mf quantifies the percentage of molecules that are free to diffuse.

Corrections

To correct for unintentional photobleaching during the imaging and loss of fluorescence in the compartment due to the bleaching event, we divide by the integrated intensity of the whole cell. Alternatively, unintentional photobleaching can be corrected by approximating it as a single exponential decay process at time points after the fluorescence has once again reached steady-state,

$$I(t) = e^{-k_{decay}t} \tag{II.6}$$

k_{decay} is the unintentional photobleaching rate constant.

The loss of fluorescence in the compartment due to the bleach leads to misleading mobile fractions less than 1 unless this is corrected. To do this we measure the intensity inside an ROI adjacent to the bleach region and correct by,

$$Mf_{correct} = 1 - (I_{adjacent}(t) - I(t)) \tag{II.7}$$

Curve Fitting Parameters

Initial conditions: K and r_e

Diffusion model: D and Mf

II.5.5.2 Reaction 1

The Reaction 1 model simulates FRAP recoveries that can be modeled using a single component exponential function with the following form:

$$I(t) = a - be^{-ct} \tag{II.8}$$

There are a variety of physical problems where this model is appropriate. As an example, consider molecules that are either free to diffuse f_1, or bound in an immobile complex c_1,

$$f_1 \longleftrightarrow c_1 \tag{II.9}$$

Assuming f_1 equilibrates rapidly in the bleach region, $f_1 = F_{eq}$, and the differential equation governing the change in the concentration of complex over time is,

$$\frac{dc_1}{dt} = k_{on}^{*} F_{eq} - k_{off} c_1 \tag{II.10}$$

k_{on}^{*} and k_{off} are the pseudo-on-rate and off-rate for complex formation respectively. In this case, the FRAP curve is modeled using,

$$I(t) = I(\infty) - [I(\infty) - I(0)] C_{eq} e^{-k_{off} t} \tag{II.11}$$

where $C_{eq} = \frac{k_{on}^{*}}{k_{off}} F_{eq}$ from the equilibrium expressions. Therefore, for this example, in equation II.8, $a = I(\infty)$, $b = [I(\infty) - I(0)]$, and $c = k_{off}$.

Curve Fitting Parameters

a, b, and c

II.5.5.3 Reaction2

The Reaction 2 model simulates FRAP recoveries that can be modeled using a two component exponential function with the following form:

$$I(t) = a - be^{-ct} - de^{-ft} \tag{II.12}$$

Again, this model is appropriate for a variety of physical problems. As an example, consider molecules that are either free to diffuse f_1, or bound in an immobile complex c_1, or a second immobile complex c_2,

$$
\begin{aligned}
&f_1 \longleftrightarrow c_1 \\
&f_1 \longleftrightarrow c_2
\end{aligned}
\tag{II.13}
$$

In the same fashion as in the example presented for the Reaction 1 model, assuming f_1 equilibrates rapidly in the bleach region, $f_1 = F_{eq}$, and the differential equations governing the change in the concentration of complex over time is,

$$
\begin{aligned}
\frac{dc_1}{dt} &= k^*_{1on} F_{eq} - k_{1off} c_1 \\
\frac{dc_2}{dt} &= k^*_{2on} F_{eq} - k_{2off} c_2
\end{aligned}
\tag{II.14}
$$

where k^*_{1on} and k^*_{2on}, k_{1off} and k_{2off}, and c_1 and c_2 are the pseudo-on rates the off rates, and the concentrations for the first and second complexes. In this case, the FRAP curve is modeled using,

$$
\begin{aligned}
I(t) = I(\infty) - [I(\infty) - I(0)]C_{1eq}e^{-k_{1off}} \\
-[I(\infty) - I(0)]C_{2eq}e^{-k_{2off}}
\end{aligned}
\tag{II.15}
$$

where $\frac{1}{C_{1eq}} = 1 + \frac{k_{1off}}{k^*_{1on}}(1 + \frac{k^*_{2on}}{k_{2off}})$, and $\frac{1}{C_{2eq}} = 1 + \frac{k_{2off}}{k^*_{2on}}(1 + \frac{k^*_{1on}}{k_{1off}})$ from the equilibrium expressions. Therefore, for this example, in equation II.12, $a = I(\infty)$, $b = [I(\infty) - I(0)]C_{1eq}$, $c = k_{1off}$, $d = [I(\infty) - I(0)]C_{2eq}$, and $f = k_{2off}$.

Curve fitting parameters

a, b, c, d, and f

II.5.6 Test Data

You will find fully documented examples of how to work with each of the FRAP-Toolbox models along with links to download the test datasets in what follows.

II.5.6.1 Diffusion

Using a Zeiss LSM 510 confocal microscope we photobleached a small 1 µm circular region in the cytoplasm of HeLa cells expressing the fluorescent protein Venus or Venus-ATG5. We found the recoveries of these FRAP datasets are fit well by the FRAP-Toolbox diffusion model.

1. Download the test datasets at http://fraptoolbox.com/DownloadFiles/Diffusion.zip.
2. Open FRAP-Toolbox.
3. Select the “Diffusion” model from the dropdown list of models, select “Circle” for the ROI, the post-bleach image is “21”, the mean background intensity is “0”, Do not normalize by the whole cell, and

Table II.2: Curve fitting parameters for the Diffusion test data

	Initial Guess	Lower Bound	Upper Bound	Fixed/Adj
K	1	0	Inf	Adjustable
r_e	3	0	Inf	Adjustable
D	10	0	Inf	Adjustable
Mf	1	0	2	Adjustable
k_{decay}	1e-3	0	Inf	Adjustable

	First Data Point	Last Data Point
Profile Fit	1	5626
FRAP Fit	1	600
Decay Fit	500	600

use “10” pre-bleach images for the normalization.

4. Select all of the test datasets with names “Venus_Cytoplasm_∗.lsm”. in the right hand panel.

5. Click the next button. FRAP-Toolbox will display a prompt requesting more information about the bleaching ROI. Enter “256 23” for the center of the bleach ROI, and “9” for the radius of the bleach ROI before pressing ok. Next, FRAP-Toolbox will ask you if you would like to calculate a corrected mobile fraction. Choose “yes”. After the program loads the test datasets, the data analysis and visualization window will appear.

6. Define the curve fitting parameters as shown in Table II.2. Select “No”, do not fit the averaged data. Make sure all of the data sets in right hand panel are selected, and press Run.

7. As FRAP-Toolbox finishes the parameter optimization routine, two windows will automatically pop-up to visualize the results. The first window is the initial conditions of the FRAP experiment. This is the radially averaged intensity versus distance from the center of the bleaching ROI calculated from the first image after the bleaching event. The second window is the FRAP curves. This is the integrated intensity inside the bleaching ROI versus time. In both windows you will find the individual datasets plotted on the left with optimized fits, and the average of all of the datasets plotted on the right with the fit calculated by averaging the optimized parameters from the individual fits. Below each of these plots you will find the residuals, which is the difference between the FRAP data and the optimized fit.

8. The optimized parameters from the fits are automatically uploaded into the table in the data analysis and visualization window. See Table II.3 for a summary of these results.

9. In order to save these optimized parameters to a tab delimited $.txt$ file, click the save button and enter a descriptive tag-name for the files such as Venus_Cytoplasm. FRAP-Toolbox will append $*$

_Diffusion_Fit_Parameters .txt, ∗_Diffusion_FRAP_datasets.txt, and ∗ _Diffusion_Postbleach_profiles .txt on the end of your tag-name. This will help you keep track of the model these save files came from. You will notice that the optimized parameters, the optimized FRAP curves, and the optimized post-bleach profiles all have their own .txt files.

That's all! With a few easy clicks, one can extract quantitative diffusion coefficients, and mobile fractions from raw image files using FRAP-Toolbox. We also included the Venus-ATG5 datasets, which should be analyzed using the same procedure that was outlined above for Venus.

Table II.3: Optimized Curve fitting parameters for the Diffusion test data

FileNames	k	re	D	MF	MF Corrected	SS
Venus_Cytoplasm_1.lsm	1.49227	3.52497	10.71	0.778875	0.944335	1.50E-06
Venus_Cytoplasm_10.lsm	1.50518	3.92221	31.2611	0.798046	1.00502	6.80E-07
Venus_Cytoplasm_11.lsm	1.24909	4.24756	69.1622	0.82531	0.990743	1.56E-06
Venus_Cytoplasm_12.lsm	1.625	3.56148	28.1604	0.907764	0.951867	3.61E-07
Venus_Cytoplasm_13.lsm	1.42082	3.62627	37.9302	0.842007	0.963113	1.97E-06
Venus_Cytoplasm_14.lsm	1.43272	3.9784	38.5733	0.835316	0.998234	1.27E-06
Venus_Cytoplasm_15.lsm	1.37271	3.86398	32.2078	0.794803	0.944473	1.70E-06
Venus_Cytoplasm_2.lsm	1.41287	3.89225	34.0451	0.78997	1.00995	8.89E-07
Venus_Cytoplasm_3.lsm	1.23637	4.32865	34.7806	0.795314	1.00073	1.73E-06
Venus_Cytoplasm_4.lsm	1.13864	4.49717	49.0692	0.868395	1.04124	4.70E-07
Venus_Cytoplasm_5.lsm	1.34346	3.90619	35.1196	0.808686	1.0077	2.00E-06
Venus_Cytoplasm_6.lsm	1.25745	4.1467	24.0467	0.962918	1.02806	1.99E-06
Venus_Cytoplasm_7.lsm	1.21802	4.05839	37.3884	0.857001	1.05485	1.80E-06
Venus_Cytoplasm_8.lsm	1.19425	4.21281	47.7528	0.86983	0.963787	9.31E-07
Venus_Cytoplasm_9.lsm	1.40613	3.99158	24.7671	0.87384	0.992741	6.77E-07
Avg.	1.35366	3.98391	35.665	0.840538	0.993123	1.40E-07
Venus-Atg5_Cytoplasm_1.lsm	2.13326	3.03023	12.3554	0.760985	0.960108	2.87E-06
Venus-Atg5_Cytoplasm_10.lsm	2.1835	2.99236	8.77951	0.901954	1.01935	3.03E-06
Venus-Atg5_Cytoplasm_11.lsm	1.9164	3.25953	13.375	0.866339	1.04926	3.25E-06
Venus-Atg5_Cytoplasm_12.lsm	2.08378	2.95893	10.5893	0.848098	1.00169	3.66E-06
Venus-Atg5_Cytoplasm_13.lsm	2.08839	3.0656	10.1128	0.790749	0.984935	2.99E-06
Venus-Atg5_Cytoplasm_14.lsm	2.59773	2.83641	5.36561	0.759974	0.994943	8.72E-07
Venus-Atg5_Cytoplasm_15.lsm	1.91945	3.14534	17.8351	0.80017	0.978091	3.13E-06
Venus-Atg5_Cytoplasm_2.lsm	2.29892	3.0424	8.89663	0.805056	0.982664	2.08E-06
Venus-Atg5_Cytoplasm_3.lsm	2.02854	3.13199	13.7669	0.824206	1.00859	3.04E-06
Venus-Atg5_Cytoplasm_4.lsm	2.20468	2.89709	13.3891	0.808597	1.01588	3.59E-06
Venus-Atg5_Cytoplasm_5.lsm	2.30317	2.82927	7.96808	0.769746	0.936311	2.46E-06
Venus-Atg5_Cytoplasm_6.lsm	2.29612	2.92836	7.18344	0.844084	0.9718	1.25E-06
Venus-Atg5_Cytoplasm_7.lsm	2.09037	3.10371	10.4623	0.854266	1.04887	2.11E-06
Venus-Atg5_Cytoplasm_8.lsm	2.20337	2.90907	9.52221	0.821008	0.990787	2.71E-06
Venus-Atg5_Cytoplasm_9.lsm	2.01298	3.13327	6.02719	0.858868	1.0058	1.96E-06
Avg.	2.15738	3.01757	10.3752	0.82094	0.996604	2.50E-07

Table II.4: Curve fitting parameters for the Reaction 1 test data

	Initial Guess	Lower Bound	Upper Bound	Fixed/Adj
a	1	0	Inf	Adjustable
b	1	0	Inf	Adjustable
c	1	0	Inf	Adjustable
k_{decay}	1e-3	0	Inf	Adjustable

	First Data Point	Last Data Point
Profile Fit	1	130
Decay Fit	135	185

II.5.6.2 Reaction 1

Using a Nikon Eclipse Ti confocal microscope we photobleached Venus in the nuclear region of HeLa cells using a user defined bleaching ROI. We found the recoveries of these FRAP datasets are fit well by the FRAP-Toolbox Reaction 1 model.

1. Download the test datasets at http://fraptoolbox.com/DownloadFiles/Reaction1.zip.
2. Open FRAP-Toolbox.
3. Select the “Reaction 1” model from the dropdown list of models, select “User Defined” for the ROI, the post-bleach image is “6”, the mean background intensity is “0”, Do normalize by the whole cell, and use “5” pre-bleach images for the normalization.
4. Select all of the test datasets with names “Venus_∗.nd2” in the right hand panel.
5. Click the next button. FRAP-Toolbox will display a prompt requesting the user to draw the bleaching ROI. The user must draw an ROI in the nuclear regions as shown in Figure II.9A. Next, FRAP-Toolbox will ask the user to draw the whole cell ROI. The user must draw an ROI around the whole cell as shown in Figure II.9A. After the program loads the test datasets, the data analysis and visualization window will appear.
6. Define the curve fitting parameters as shown in Table II.4. Select “No”, do not fit the averaged data. Make sure all of the data sets in right hand panel are selected, and press Run.
7. As FRAP-Toolbox finishes the parameter optimization routine, a single window will automatically pop-up to visualize the results. Inside this window is the plotted FRAP curves. This is the integrated intensity inside the bleaching ROI versus time. In both windows you will find the individual datasets plotted on the left with optimized fits, and the average of all of the datasets plotted on the right with

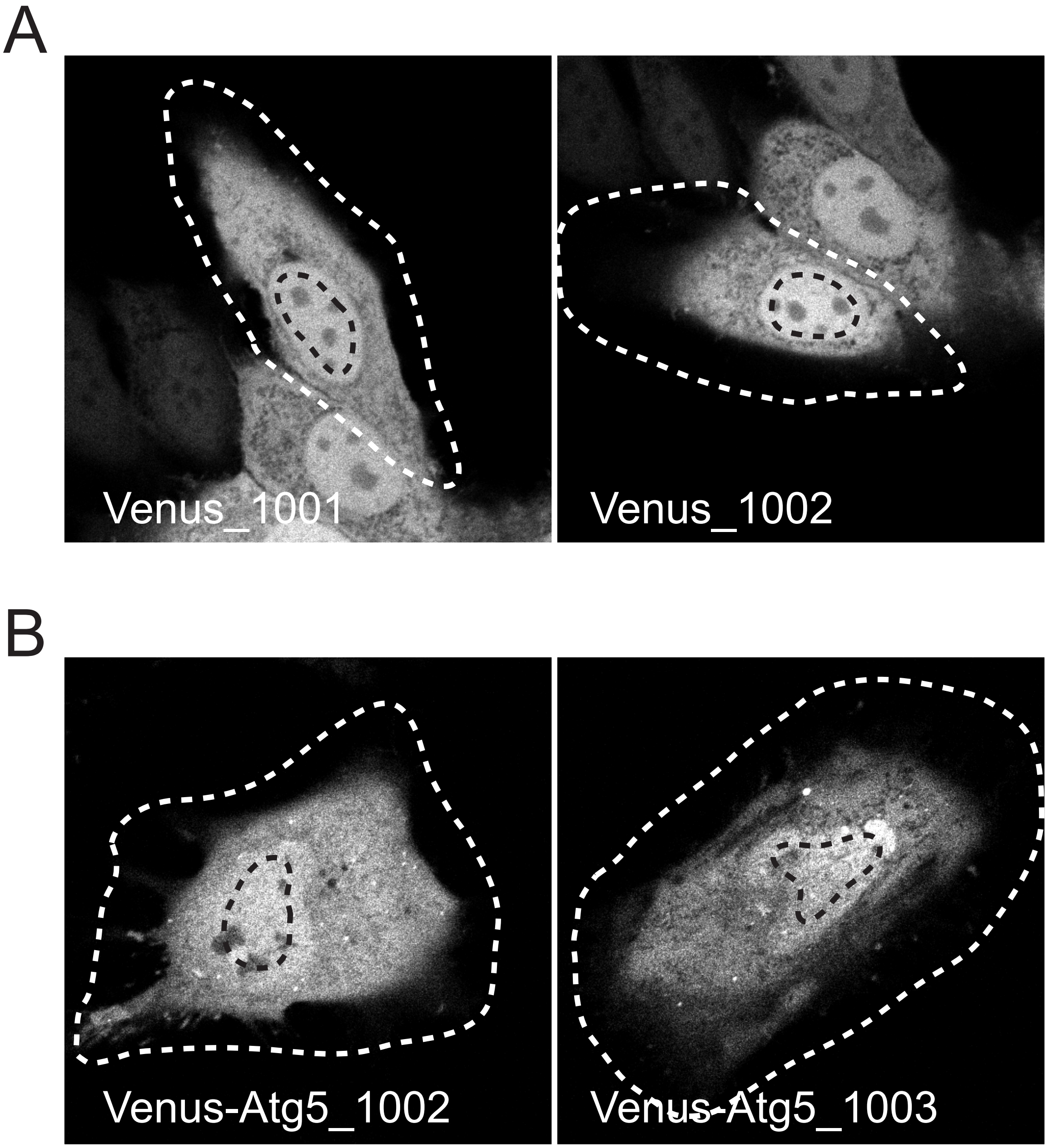

Figure II.9: User Defined ROIs for Reaction 1 and Reaction 2 test data. (A) Reaction 1 test data consists of Venus_1001.nd2 and Venus_1002.nd2. (B) Reaction 2 test data consists of Venus−Atg5_1002.nd2 and Venus −Atg5_1003.nd2. The bleach ROIs are shown as dashed black lines, and the whole cell ROIs are shown as dashed white lines.

the fit calculated by averaging the optimized parameters from the individual fits. Below each of these plots you will find the residuals, which is the difference between the FRAP data and the optimized fit.

8. The optimized parameters from the fits are automatically uploaded into the table in the data analysis and visualization window. See Table II.5 for a summary of these results (note that due to the user input in the process of drawing ROIs these parameters may not be exactly the same, but should be very close).

9. In order to save these optimized parameters to a tab delimited $.txt$ file, click the save button and enter a descriptive tag-name for the files such as Venus_NCTransport. FRAP-Toolbox will append $*$ $_$Reaction_Fit_Parameters $.txt$, and $*$_Reaction_FRAP_datasets$.txt$ on the end of your tag-name. This will help you keep track of the model these save files came from. You will notice that the optimized parameters, and the optimized FRAP curves all have their own $.txt$ files.

That's all! With a few easy clicks, one can extract quantitative kinetic data from raw image files using the Reaction 1 model in FRAP-Toolbox.

Table II.5: Optimized Curve fitting parameters for the Reaction 1 test data

FileNames	a	b	c	SS
Venus_1001.nd2	0.873656	0.762292	0.00844	8.33E-08
Venus_1002.nd2	0.855588	0.753077	0.015899	6.70E-08
Avg.	0.864622	0.757685	0.01217	2.10E-07

II.5.6.3 Reaction 2

Using a Nikon Eclipse Ti confocal microscope we photobleached Venus-ATG5 in the nuclear region of HeLa cells using a user defined bleaching ROI. We found the recoveries of these FRAP datasets are fit well by the FRAP-Toolbox Reaction 2 model.

1. Download the test datasets at http://fraptoolbox.com/DownloadFiles/Reaction2.zip.

2. Open FRAP-Toolbox.

3. Select the "Reaction 2" model from the dropdown list of models, select "User Defined" for the ROI, the post-bleach image is "6", the mean background intensity is "0", Do normalize by the whole cell, and use "5" pre-bleach images for the normalization.

4. Select all of the test datasets with names "Venus$-$Atg5_$*$.nd2" in the right hand panel.

Table II.6: Curve fitting parameters for the Reaction 2 test data

	Initial Guess	Lower Bound	Upper Bound	Fixed/Adj
a	1	0	Inf	Adjustable
b	0.5	0	Inf	Adjustable
c	0.05	0	Inf	Adjustable
d	0.5	0	Inf	Adjustable
f	5e-4	0	Inf	Adjustable
k_{decay}	1e-3	0	Inf	Adjustable

	First Data Point	Last Data Point
Profile Fit	1	185
Decay Fit	135	185

5. Click the next button. FRAP-Toolbox will display a prompt requesting the user to draw the bleaching ROI. The user must draw an ROI in the nuclear regions as shown in Figure II.9B. Next, FRAP-Toolbox will ask the user to draw the whole cell ROI. The user must draw an ROI around the whole cell as shown in Figure II.9B. After the program loads the test datasets, the data analysis and visualization window will appear.

6. Define the curve fitting parameters as shown in Table II.6. Select "Yes", fit the averaged data. Make sure all of the data sets in right hand panel are selected, and press Run.

7. As FRAP-Toolbox finishes the parameter optimization routine, a single window will automatically pop-up to visualize the results. Inside this window is the plotted FRAP curves. This is the integrated intensity inside the bleaching ROI versus time. In both windows you will find the individual datasets plotted on the left with optimized fits, and the average of all of the datasets plotted on the right with the fit calculated by averaging the optimized parameters from the individual fits. Below each of these plots you will find the residuals, which is the difference between the FRAP data and the optimized fit.

8. The optimized parameters from the fits are automatically uploaded into the table in the data analysis and visualization window. See Table II.7 for a summary of these results (note that due to the user input in the process of drawing ROIs these parameters may not be exactly the same, but should be very close).

9. In order to save these optimized parameters to a tab delimited .txt file, click the save button and enter a descriptive tag-name for the files such as Venus−Atg5_NCTransport. FRAP-Toolbox will append *_Reaction_Fit_Parameters.txt, and *_Reaction_FRAP_datasets.txt on the end of your tag-name. This will help you keep track of the model these save files came from. You will notice that the optimized parameters, and the optimized FRAP curves all have their own .txt files.

That's all! With a few easy clicks, one can extract quantitative kinetic data from raw image files using the Reaction 2 model in FRAP-Toolbox.

Table II.7: Optimized Curve fitting parameters for the Reaction 2 test data

FileNames	a	b	c	d	f	SS
Venus-Atg5_1002.nd2						
Venus-Atg5_1003.nd2						
Avg.	1.4704	0.228479	0.0207795	1.12884	0.000442516	1.78E-07

II.5.7 Troubleshooting

FRAP-Toolbox has several built-in warning dialogs that will display when it detects potential errors. For example, when batch processing, all of the datasets must have been acquired using identical settings; otherwise, FRAP-Toolbox will halt and display the appropriate error dialogue. If a user comes across bugs they are encouraged to report these by following the instructions on our Bug Reporting page at http://www.fraptoolbox.com/BugReporting.

CHAPTER III

Size, stoichiometry, and organization of soluble LC3-associated complexes

Although LC3 is known to associate with tens of proteins, relatively little is known about soluble LC3 aside from its interactions with the LC3 lipid conjugation machinery. In previous studies we found autophagosome-independent GFP-LC3B diffuses unusually slowly for a protein of its size, suggesting it may constitutively associate with a high molecular weight complex, form homo-oligomers or aggregates, or reversibly bind microtubules or membranes. In this chapter we begin with an introduction to the problem. We then go on to examine the source of LC3's slow diffusion by characterizing the size, stoichiometry, and organization of autophagosome-independent LC3B in living cells and in cytoplasmic extracts using fluorescence recovery after photobleaching (FRAP) and fluorescence polarization fluctuation analysis (FPFA). The details of our FRAP assay were described in Chapter II. These findings provide new insights into the nature of soluble LC3B and illustrate the power of FRAP and FPFA to investigate the emergent properties of protein complexes in the autophagy pathway.

III.1 Introduction

Autophagy is a major pathway for the capture and degradation of cytosolic materials via the lysosome. A distinctive feature of the pathway is the formation of a double membrane bound vesicle called the autophagosome [31]. Autophagosome membrane expansion, fusion and substrate selection are carried out, in part, by a family of ATG8 proteins [32, 67, 80, 92–94, 127, 172, 173]. Despite these proposed major roles for ATG8 proteins in autophagy, there are still many open questions in regard to how ATG8 proteins carry out these tasks [174].

ATG8 proteins share high structural (but not sequence) homology with ubiquitin, and thus have been termed ubiquitin-like proteins [79]. Interestingly, unlike ubiquitin, which is conjugated to other proteins, ATG8 proteins are conjugated to the head group of the lipid phosphatidylethanolamine [84]. In mammals, the best-studied ATG8 family member, MAP1LC3B (LC3), exists in both soluble (LC3-I), as well as lipid modified form (LC3-II) [90]. Under conditions of stress or starvation, LC3 lipid modification becomes upregulated, in turn targeting the protein to autophagosome membranes [91]. LC3 is released from autophagosome membranes by the cysteine protease activity of ATG4B [87].

LC3 and other members of the ATG8 protein family have numerous interacting proteins, suggestive of

---

This chapter is adapted from the published manuscript: Kraft et al. [164]

their possible participation in multi-protein complexes [9, 44, 59, 69, 116, 122–124, 129]. In addition, many LC3 interacting proteins contain a consensus LC3 interacting motif (W/F/Y-X-X-L/I/V) for efficient binding to a hydrophobic surface on LC3 in the region of residues F52/L53 and R70 [32, 45, 127]. Mutations to these key residues on LC3's hydrophobic protein interacting surface disrupt binding to tens of proteins, highlighting the importance of this region for engaging other proteins in productive binding [9, 69, 100, 127, 129, 130]. Importantly, it is unknown if soluble LC3 interacts with its protein partners in a binary fashion or if instead it constitutively associates with multi-protein or other multicomponent complexes to accomplish its varied functions in autophagy.

Using confocal FRAP, our group recently showed that the soluble form of LC3 diffuses unusually slowly for a cytoplasmic protein of its size under basal conditions [121, 165]. Because the diffusion coefficient of a soluble, freely diffusing molecule is inversely related to its radius, this slower-than-expected-diffusion of LC3 could potentially reflect its association with macromolecular complexes comprised of LC3 and other components of the autophagy pathway. Alternatively, the slow diffusion of soluble LC3 could potentially arise from reversible binding to microtubules in cells[109] or the incorporation of LC3 into homo-oligomers or aggregates or possibly membranes [93, 105, 106].

To address these possibilities, in the current study, we investigate the size, stoichiometry, and organization of LC3-containing protein complexes using two complementary fluorescence based approaches, confocal Fluorescence Recovery After Photobleaching (FRAP) and Fluorescence Polarization Fluctuation Analysis (FPFA). The first of these methods, FRAP, is a powerful and versatile tool for measuring the ensemble dynamics of molecules. The instrumentation for FRAP is now widely accessible in many laboratories, and by analyzing FRAP data with recently described models it is now possible to accurately measure diffusion coefficients, as well as quantify reversible interactions [149, 158, 175]. FRAP also has the unique ability to quantify the extent of irreversible interactions and very slow turnover on the timescale of the measurements as reflected in the mobile fraction. The second approach, FPFA, is a newly developed experimental method combining Fluorescence Correlation Spectroscopy (FCS) and Time Resolved Fluorescence Anisotropy (TRFA) [176]. Like FRAP, FCS reports on the diffusional mobility of molecules. However, FCS has exceptional sensitivity enabling measurements of the concentrations of fluorescent proteins in the pM to nM range and is capable of resolving the diffusion coefficients of multiple diffusing species, and their molecular brightness [142]. By combining FCS and TRFA into a single measurement, FPFA enables the simultaneous measurement of translational and rotational mobility, concentration, brightness, and homo-FRET [176]. Thus, FPFA is a tool that can be used to simultaneously investigate a protein's mobility, stoichiometry, and organization.

Our FRAP and FPFA measurements reveal that under basal conditions, soluble Venus-LC3 diffuses as if it associates with a complex with an effective molecular weight of approximately 500 kDa in size, and each complex contains on average a single LC3. Similar complexes were observed in living cells and in cytoplasmic extracts depleted of intact microtubules. In addition, we show that the size and stoichiometry of complexes containing LC3 are altered by mutational disruption of LC3's hydrophobic binding surface, but not mutational disruption of LC3's lipid modification. The effective size of the LC3 associated complexes only modestly changes after perturbations to the autophagy pathway with rapamycin or chloroquine treatments. These findings provide new insights into the nature of soluble LC3 and illustrate the power of confocal FRAP and FPFA to provide novel insights into the emergent properties of protein complexes in the autophagy pathway.

III.2 Results

III.2.1 Effect of mutations of the hydrophobic binding interface and lipid modification site on the subcellular distribution of LC3.

In previous studies, we found GFP-LC3 and Venus-LC3 diffuse more slowly in the cytoplasm of cells than expected for a monomer using confocal FRAP, suggesting LC3 may associate with a high molecular weight complex [121, 165]. Given many LC3 interacting proteins interact with a hydrophobic interaction surface on LC3 using a W/F/Y-X-X-L/I/V motif,[32] we asked whether disruption of specific residues in this region on LC3 will disrupt its association with the putative high molecular weight complexes. To address this question, we focused on two sets of mutations, R70A and F52A/L53A. These mutations were shown to disrupt binding to at least 18 and 9 binding partners respectively [9]. Several of the disrupted binding partners are involved in activities ranging from LC3's lipid modification to autophagy substrate specificity [9, 59, 69, 129]. For comparison, we also examined a G120A mutant of LC3, which is unable to undergo lipid modification [106].

We first examined the effects of the R70A, F52A/L53A, and G120A mutations on the subcellular distribution of LC3 in HeLa cells. As previously described, Venus-LC3 was found in a diffuse cytoplasmic form as well as in discrete 0.5 µm–2 µm puncta in the cytoplasm corresponding to LC3 labeled autophagosomes as well as autophagosome independent substrates and aggregates [105]. Some diffuse Venus-LC3 was also observed in the nucleus, consistent with our previous findings quantifying the amount of GFP tagged LC3 in the nucleus (Fig. III.1A) [121].

Like wild type Venus-LC3, a substantial fraction of diffuse Venus-LC3(F52A/L53A), Venus-LC3(R70A), and Venus-LC3(G120A) was present in both the cytoplasm and nucleoplasm of live HeLa cells (Fig. III.1B-D). However, on average about two fold fewer puncta were present in cells expressing Venus-LC3(R70A) than in cells expressing Venus-LC3 ($p < 0.008$; Bonferonni corrected t-test), and even fewer puncta were positive for Venus-LC3(F52A/L53A) or Venus-LC3(G120A) ($p < 0.008$; t-tests) (Fig. III.1E). These findings are consistent with the idea that LC3's hydrophobic binding surface regulates protein-protein interactions,

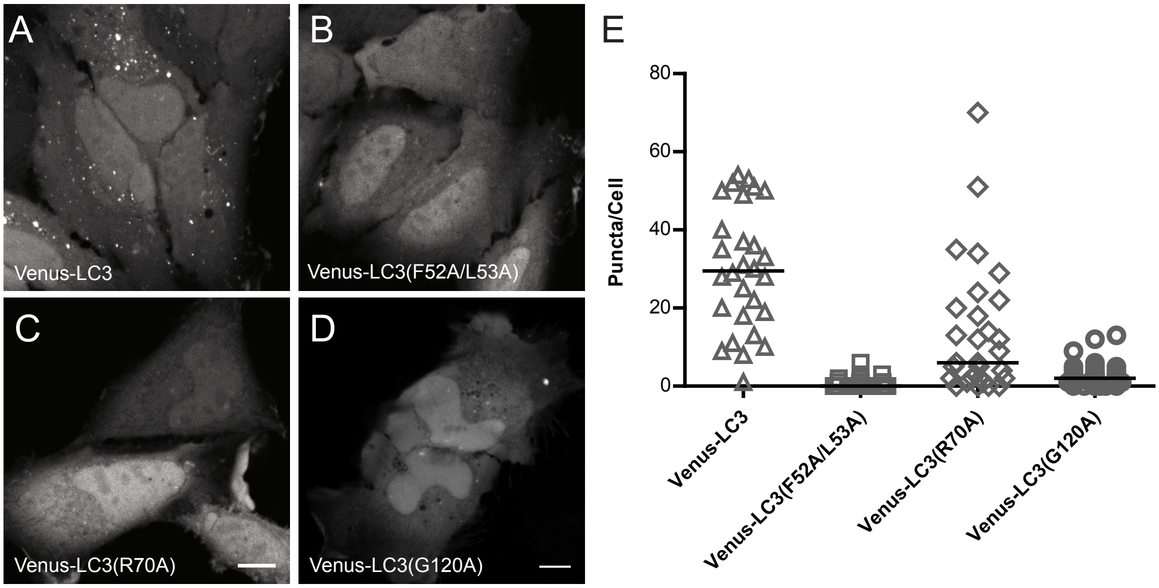

Figure III.1: Venus-LC3(F52A/L53A) and Venus-LC3(R70A) show a reduced association with cytoplasmic puncta compared to wild type Venus-LC3. (A) Venus-LC3, (B) Venus-LC3(F52A/L53A), (C) Venus-LC3(R70A), and (D) Venus-LC3(G120A) were expressed individually in HeLa cells and imaged live under basal conditions (complete media, 37 °C) using confocal microscopy. Scale bar is 10 µm. (E) The numbers of ~ 0.5 µm–2 µm punctate spots per cell cytoplasm were counted for each of the indicated constructs. Bars represent the median. One-way ANOVA test $p < 1 \times 10^{-4}$. Pairwise comparisons between all of the constructs were made using Bonferonni corrected t-tests as described in the text.

including SQSTM1/p62 binding, which facilitate targeting LC3 to autophagy-independent puncta [130]. In addition, they suggest that the F52A/L53A and G120A mutants are more strongly defective in their ability to bind to cytoplasmic puncta than is the R70A mutant of LC3.

III.2.2 LC3 retains the ability to associate with autophagosomal membranes upon disruption of its hydrophobic binding interface.

Since the Venus-LC3(F52A/L53A), Venus-LC3(R70A), and Venus-LC3(G120A) mutants have defects in the numbers of puncta present under steady-state conditions, we wanted to determine if these mutants retain their ability to associate with autophagosomal membranes. To test this, we monitored their accumulation on autophagosomal membranes after inhibition of lysosomal acidification with chloroquine. After treatment with chloroquine, both Venus-LC3(F52A/L53A) and Venus-LC3(R70A) accumulated on autophagosomal membranes, similar to wild type Venus-LC3 (Fig. III.2A-F). This result is consistent with what was previously reported for a GFP-LC3(F52A) mutant after treatment with both starvation and Bafilomycin A1 [100]. In contrast, no changes to the localization of Venus-LC3(G120A) were observed after treatment with chloroquine (Fig. III.2G,H). This is consistent with the inability of the G120A mutant to be targeted to autophagosomes by lipid modification of this residue [106].

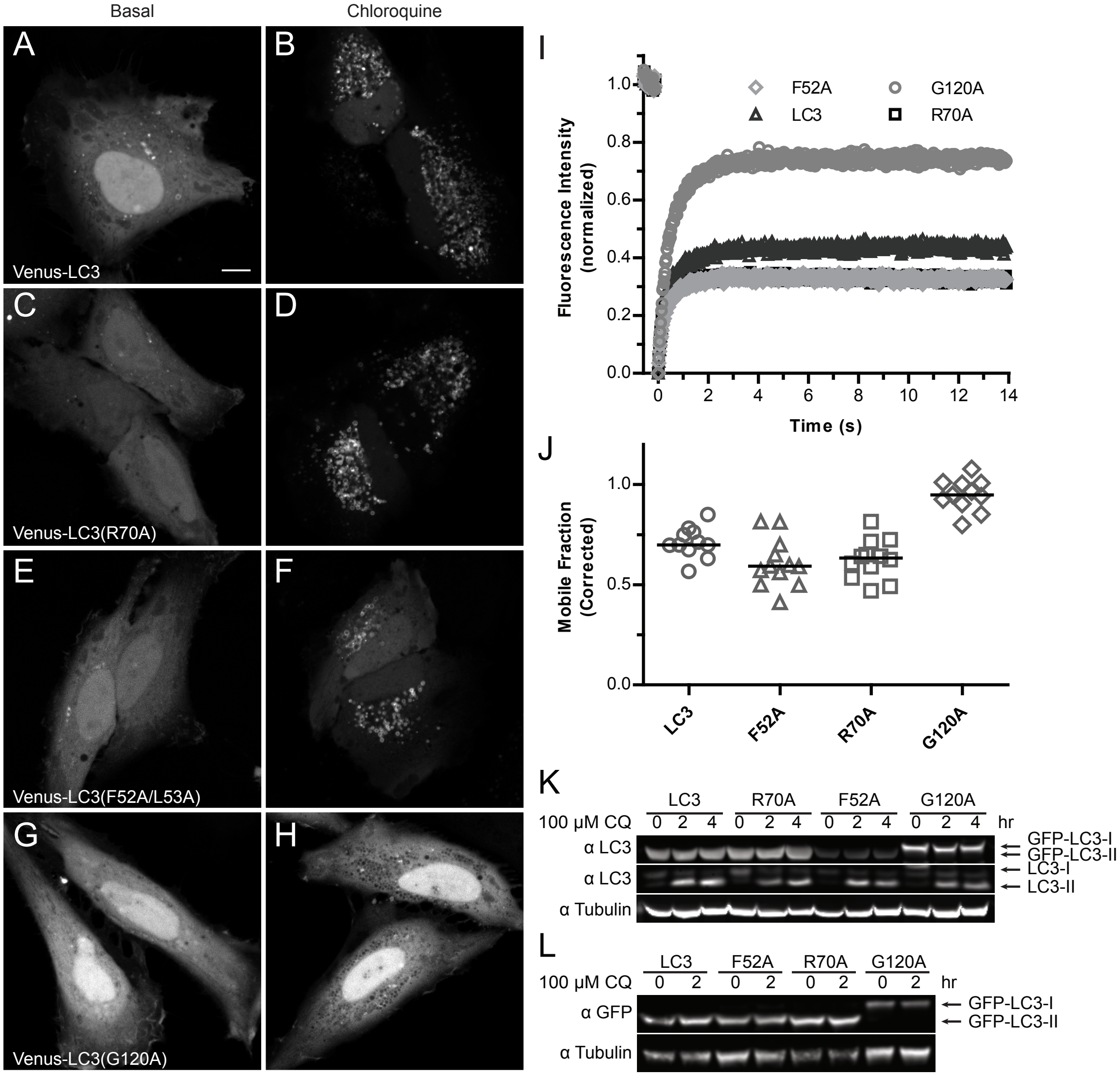

Figure III.2: Venus-LC3(F52A/L53A) and Venus-LC3(R70A), like wild type Venus-LC3, accumulate on lysosomal membranes after treatment with chloroquine. Cells expressing (A,B) Venus-LC3, (C,D) Venus-LC3(R70A), (E,F) Venus-LC3(F52A/L53A), or (G,H) Venus-LC3(G120A) were imaged under basal conditions (A,C,E,G) or after a 2 hour incubation with 100 μM chloroquine (B,D,F,H). Scale bar is 10 μm. The steady-state localization of LC3, R70A, and F52A/L53A on autophagosomal membranes is upregulated after blocking lysosome function with chloroquine. In contrast, G120A was not targeted to autophagosomal membranes under these conditions. (I) Individual spots as seen in (B,D,F,H) were selectively photobleached using a 1 μm radius Bleach ROI revealing a slow turnover rate for membrane associated LC3, R70A, and F52A/L53A puncta in contrast with the faster turnover rate of substrate associated G120A puncta. The differences in the recovery of membrane associated LC3 versus substrate associated LC3 are reflected in the mobile fractions quantified in (J). Symbols for the R70A recovery are underneath the symbols for the F52A/L53A recovery. (K,L) SDS-PAGE and western blot for LC3-I versus LC3-II under basal conditions and after chloroquine treatment. (K) Antibodies against LC3 show there are no major defects in the formation of GFP-LC3-II for LC3, R70A, or F52A/L53A, in contrast with the negative control G120A. (L) Similar to (K), except the electrophoresis was carried out for a longer period of time in order to obtain better resolution of the higher molecular weight GFP-LC3-I versus GFP-LC3-II bands and blotting was performed using an anti-GFP antibody. Antibodies against tubulin were used as loading controls.

Table III.1: Predicted molecular weights and mobile fractions for Venus, Venus-LC3, and Venus-LC3 mutants based on the FRAP diffusion measurements in live HEK 293 cells using under basal conditions.

Construct	Monomer MW (kDa)	ξ FRAP Predicted MW (kDa)	FRAP Mobile Fraction (%)
Venus	27	N/A	100 ± 1 (34)
Venus-LC3	45	500 ± 200 (30)	99 ± 1 (30)
Venus-LC3 (F52A/L53A)	45	1200 ± 400 (30)	100 ± 1 (30)
Venus-LC3(R70A)	45	130 ± 50 (30)	102 ± 2 (30)

ξ calculated assuming diffusing species has a spherical shape; mean ± 95 % CI (N = #cells)

It was recently shown, using selective photobleaching of GFP-LC3 associated puncta, that LC3 incorporated into autophagosomal membranes turns over much more slowly than GFP-LC3 associated with autophagy substrates [153]. We used this method to further characterize the nature of the LC3-positive puncta present after incubation with chloroquine (Fig. III.2I). The FRAP analysis revealed that while Venus-LC3, Venus-LC3(R70A) and Venus-LC3(F52A/L53A) puncta had very large immobile fractions, Venus-LC3(G120A) had a relatively high mobile fraction indicative of more rapid turnover (Fig. III.2J). This is consistent with the notion that R70A and F52A/L53A mutants of LC3 retain their ability to become lipid modified and subsequently incorporated into the membranes of autophagosomes, whereas the LC3(G120A) mutant does not. In order to further verify that there are no defects in the LC3-I to LC3-II processing of the R70A and F52A/L53A mutants we performed SDS-PAGE and western blotted for LC3 (Fig. III.2K) and GFP (Fig. III.2L) both under basal conditions and after treatment with chloroquine. This experiment showed that there are no defects in the LC3-I to LC3-II processing of Venus-LC3, Venus-LC3(F52A/L53A), or Venus-LC3(R70A) in stark contrast with the GFP-LC3(G120A) negative control [106].

III.2.3 Disruption of LC3's hydrophobic binding interface changes the effective diffusion of LC3-associated complexes in living cells.

Next, we tested the effect of the R70A and F52A/F53A mutations on the diffusional mobility of soluble cytoplasmic LC3 in living cells using a quantitative confocal FRAP assay [158, 175]. As shown in (Fig. III.3A), this experiment was aimed towards quantifying the diffusion of the diffuse pool of LC3, and excludes any LC3 associated with puncta. As an internal control, we performed FRAP experiments of Venus, a soluble, freely diffusing protein. The Venus FRAP curve was well fit by a single component model for Brownian motion with a diffusion coefficient of $41 \pm 4\,\mu m^2/s$ and a mobile fraction of 100 % in HEK 293 cells (Fig. III.2B,C, Table III.1). Next, we carried out FRAP experiments on Venus-LC3 in the cytoplasm. Consistent with our previous findings[121, 165], we found Venus-LC3 had an approximately two and half fold slower D compared to that of Venus, much slower than the predicted diffusion coefficient for monomeric Venus-

Table III.2: Predicted molecular weights and mobile fractions for Venus, Venus-LC3, and Venus-LC3 mutants based on the FRAP diffusion measurements in live HeLa cells under basal conditions, after incubation with 100 µM chloroquine (CQ) for 2 hours, and after incubation with 200 nM rapamycin (Rp) for 2 hours.

Construct	Monomer MW (kDa)	ξ Basal Predicted MW (kDa)	ξ CQ Predicted MW (kDa)	ξ Rap Predicted MW (kDa)	ξ NZ Predicted MW (kDa)	Basal Mobile Fraction (%)	CQ Mobile Fraction (%)	Rap Mobile Fraction (%)
Venus	27	N/A	N/A	N/A	N/A	99.5 ± 0.7 (30)	99.2 ± 0.7 (80)	99.5 ± 0.8 (30)
Venus-LC3	45	500 ± 100 (30)	900 ± 200 (60)	800 ± 200 (30)	500 ± 100 (20)	100.5 ± 0.8 (30)	99 ± 1 (60)	99 ± 1 (30)
Venus-LC3 (F52A/L53A)	45	1200 ± 300 (35)	1400 ± 300 (60)	1600 ± 500 (30)	900 ± 300 (20)	98 ± 1 (35)	99 ± 1 (60)	100 ± 1 (30)
Venus-LC3 (R70A)	45	110 ± 40 (30)	190 ± 40 (60)	160 ± 40 (30)	80 ± 30 (20)	99.2 ± 0.8 (30)	99 ± 1 (60)	100 ± 1 (30)
Venus-LC3 (G120A)	45	400 ± 100 (30)	1000 ± 200 (40)	900 ± 200 (30)	700 ± 200 (20)	99 ± 1 (30)	99 ± 1 (40)	100.4 ± 0.7 (30)

ξ calculated assuming diffusing species has a spherical shape; mean ± 95 % CI (N = #cells) ; chloroquine (CQ); rapamycin (Rap); nocodazole (NZ)

LC3 ($p \leq 0.008$; t-test) (dashed line in Fig. III.3C). This corresponds to an effective molecular weight of $\sim 500\,\text{kDa}$ (Table III.1). We found similar results in HeLa cells ($p \leq 0.008$; t-test) (Fig. III.3D, Table III.2).

After establishing baselines for diffusion comparisons, next, we measured the diffusion of soluble Venus-LC3(F52A/L53A) and Venus-LC3(R70A) by confocal FRAP. We found that their mobile fractions were also both approximately 100 % (Tables III.1,III.2), similar to that of soluble Venus-LC3 itself (ns; $p > 0.008$; t-tests). However, their diffusion coefficients differed from that of one another as well as from that of Venus LC3. Interestingly, in HEK 293 cells, D for Venus-LC3(F52A/L53A) ($11.6 \pm 0.7\,\mu\text{m}^2/\text{s}$) was slower than that of wild type Venus-LC3 ($15 \pm 2\,\mu\text{m}^2/\text{s}$) ($p \leq 0.008$; t-test), while D for Venus-LC3(R70A) ($24 \pm 2\,\mu\text{m}^2/\text{s}$) was faster than Venus-LC3, but still not to the level expected for a Venus-LC3 monomer ($p \leq 0.008$; t-test) (Fig. III.3). Similar results were obtained in HeLa cells (Fig. III.3D). Assuming the slow diffusion of the proteins reflects their association with spherical complexes, their predicted molecular weights would be $\sim 1.2\,\text{MDa}$ for Venus-LC3(F52A/L53A) and $\sim 130\,\text{kDa}$ for Venus-LC3(R70A) (Tables III.1,III.2).

III.2.4 The slow diffusion of LC3 is not due its lipid modification or association with autophagosome membranes

Although our FRAP experiments were directed towards the soluble pool of LC3, it is formally possible that LC3's slow diffusion is a result of a small fraction of lipid modified LC3 incorporated into sub-diffraction vesicles or autophagosomes. This seemed unlikely, because, theoretically, $\sim 250\,\text{nm}$ radius vesicles would be expected to diffuse ~ 100 fold slower than Venus ($D1/D2 = 2\,\text{nm}/250\,\text{nm}$), whereas, experimentally, Venus-LC3 diffused only ~ 2.5 fold slower. However, our FRAP measurements do not have the resolution to adequately test this possibility without additional experimental information [141]. Therefore, to address this question we performed FRAP measurements on Venus-LC3(G120A), since this mutation of LC3 prevents its lipid modification and subsequent incorporation into autophagosomal membranes [86]. As shown in Fig. III.3D, Venus-LC3(G120A) diffuses similarly to wild type Venus-LC3 (ns; $p > 0.005$; t-test). These data support the notion that the slow diffusion of LC3 is not the result of its association with autophagosomes or interactions with other molecules that depend on lipid modification of the protein. Rather, the slow diffusion could reflect the association of LC3 with other molecules.

III.2.5 The effective size of putative LC3 associated complexes are modestly affected by autophagy modulators

In order to gain further insights into how these complexes are modulated by perturbations to the autophagy pathway, we extended our analysis of the diffusion of LC3 under basal conditions to two additional conditions known to modulate the autophagy pathway. The first condition was to inhibit autophagy by incubating

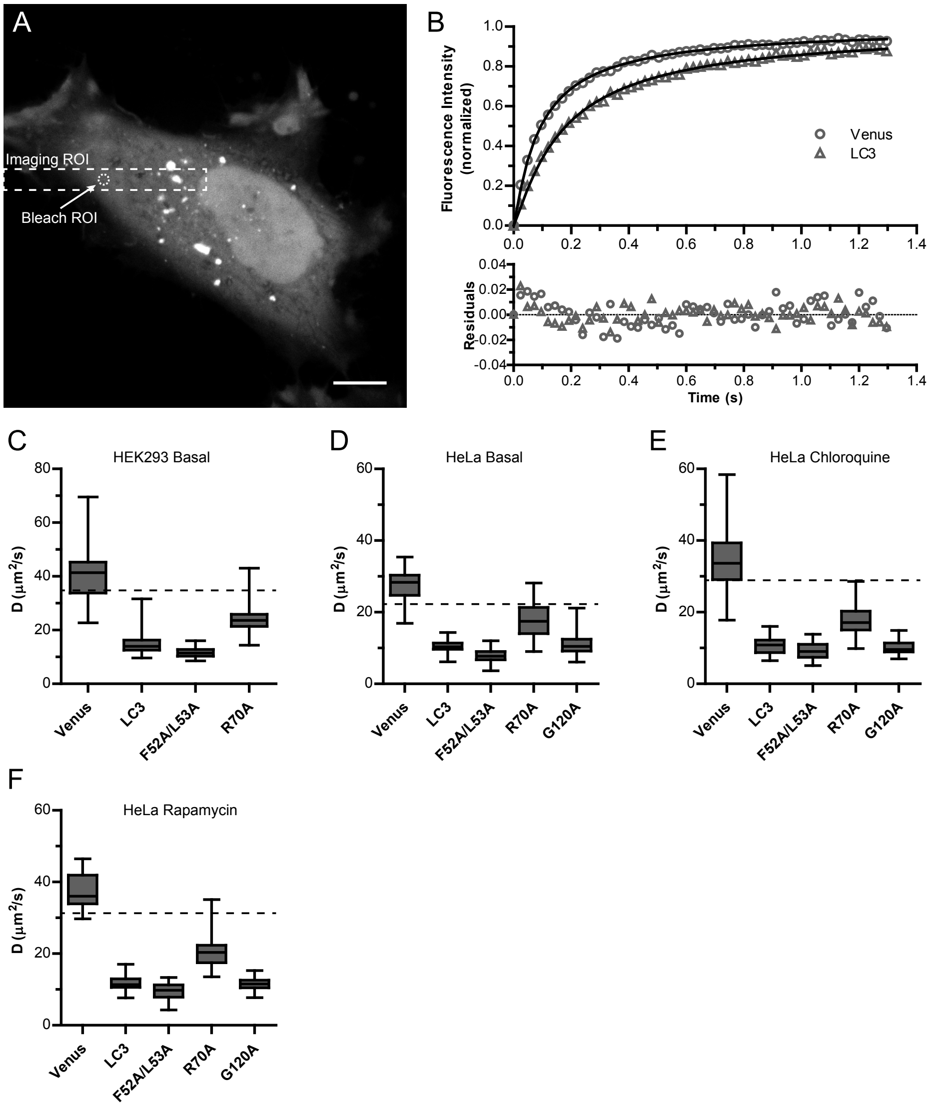

Figure III.3: Mutations to LC3's hydrophobic protein interaction surface at residues R70 or F52/L53 change the diffusional mobility of Venus-LC3 in the cytoplasm of living cells. (A) Cells expressing Venus, Venus-LC3, Venus-LC3(R70A, Venus-LC3(F52A/L53A), or Venus-LC3(G120A) were photobleached using a 1 µm radius Bleach ROI placed in the cytoplasm such that puncta were avoided. Dashed lines designate the typical Imaging ROI and Bleach ROI used in these experiments. (B) Comparison of the mean FRAP data from approximately 30 HeLa cells expressing either Venus or Venus-LC3 (symbols) were well fit by a Brownian diffusion model (solid lines). The data are normalized between 0 and 1 using $(F(t) - F(0)) / (F(\infty) - F(0))$ to more clearly demonstrate the differences in their recovery rates. (C, D, E, F) Box plots of the diffusion coefficients obtained from FRAP experiments on either HEK 293 cells or HeLa cells. While experiments summarized in (C) and (D) were carried out under basal conditions those in (E) were obtained from HeLa cells pre-treated for 2 hours with 100 µm chloroquine, and those in (F) were obtained from HeLa cells pre-treated for 2 hours with 200 nM rapamycin. The ratio of D for the monomeric Venus control to LC3, F52A/L53A, R70A, or G120A is a quantitative indicator of their effective sizes. Whiskers represent the minimum and maximum. N can be found in Table III.1. The dashed horizontal lines in (C, D, E) are the predicted diffusion coefficients for a 45 kDa Venus-LC3 monomer assuming both Venus and Venus-LC3 are spherical. For (C, D, E) One-way ANOVA test $p \leq 1 \times 10^{-4}$. Pairwise comparisons between all of the constructs were made using Bonferonni corrected t-tests as described in the text.

the cells with 100 μM chloroquine for 2 hours, and the second condition was to stimulate autophagy by incubating the cells with 200 nM rapamycin for 2 hours before performing FRAP measurements. We found that rapamycin and chloroquine treatments produced similar changes in the diffusion of the constructs shown in Fig. III.3. At first glance, the trends between the constructs appear to be maintained. However, after normalization to the diffusion of Venus, using the Stokes Einstein relationship as before, we found that the effective molecular weights for the LC3 associated complexes were modestly upregulated approximately two fold compared to basal conditions ($p \leq 0.005$; t-tests; see Table III.2 for a summary). These data suggest that the effective sizes of the soluble LC3 associated complexes are only modestly affected by perturbations to the autophagy pathway with rapamycin and chloroquine in vivo.

III.2.6 Disruption of LC3's hydrophobic binding interface but not of its lipidation site changes the effective diffusion of LC3-associated complexes in cytoplasmic extracts.

In order to test if the complexes observed in cells are intrinsically stable, or if they require cellular components, such as microtubules, we next examined the properties of the LC3 constructs in cytoplasmic extracts. In principle, it is possible to measure the diffusion of LC3 in cytoplasmic extracts using confocal FRAP; however, we wished to obtain additional information about the putative complexes, such as whether multiple types of complexes were present and how many LC3 molecules were present in each complex. Therefore, we turned to another technique that is sensitive to protein mobility and stoichiometry, FPFA[176], to analyze the LC3 associated complexes cytoplasmic extracts. To carry out FPFA measurements on the fluorescently labeled proteins in our cytoplasmic extracts, we utilized a recently described custom-built FPFA instrument with two-photon excitation to define the focal volume [176]. HEK cells expressing Venus or Venus-LC3 were extracted using passive lysis buffer and clarified by a brief high speed spin before the FPFA measurements were performed.

In order to determine the diffusivity and molecular brightness of the species, FPFA macro-time measurements of orthogonally polarized fluorescence emission were cross-correlated. The cross-correlation curves for both Venus and Venus-LC3 were well fit by a single-component model for Brownian motion suggesting the absence of multiple diffusing species with large differences in their sizes (See Fig. III.4A for an example of one versus two component models). The diffusion coefficients from the fits to Venus and Venus-LC3 were 67 ± 2 and $25 \pm 2\,\mu m^2/s$, respectively (Fig. III.4B). Thus, the diffusion coefficient for Venus-LC3 in cell extracts was much slower than Venus alone (approximately 2.5 fold) as seen previously using FRAP in live cells, and much slower than predicted for a freely diffusing Venus-LC3 monomer ($p \leq 0.003$; t-tests). Making the simplifying assumption that the complexes containing Venus-LC3 are spherical, we calculated their predicted size is about 500 kDa (Table III.3).

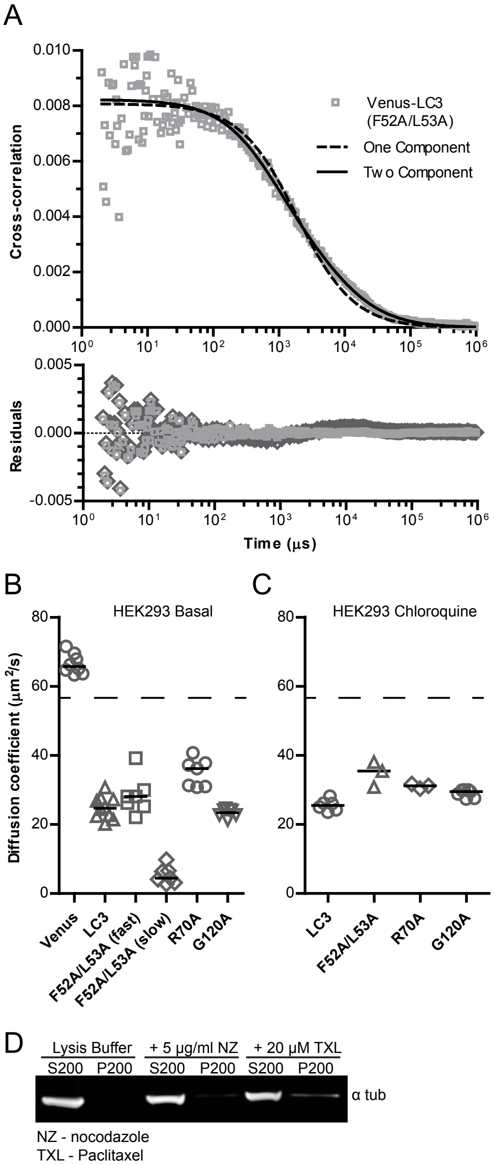

Figure III.4: Mutations to LC3's hydrophobic protein interaction surface at residues R70 or F52/L53 change the diffusional mobility of Venus-LC3 in cytoplasmic extracts. FPFA measurements were collected from cytoplasmic extracts of HEK 293 cells individually expressing Venus, Venus-LC3, Venus-LC3(F52A/L53A), Venus-LC3(R70A), or Venus-LC3(G120A); the macro time fluorescence fluctuations were cross-correlated and fit with diffusion models, see (A) for an example of one and two component fits to the Venus-LC3(F52A/L53A) data. In this case, the two component model was a better fit than the one component model. (B,C) Diffusion coefficients obtained from the fits to the data collected under basal conditions or after the cells were incubated for 2 hours in 100 µM chloroquine respectively. Compare the ratio of the Venus control to each of the constructs as an indicator of their effective sizes. The dashed lines are the predicted diffusion coefficients for a 45 kDa Venus-LC3 monomer assuming both Venus and Venus-LC3 are spherical. Bars represent the median. Samples are replicate measurements from 4-5 extract preparations. One-way ANOVA test $p \leq 1 \times 10^{-4}$. Pairwise comparisons between all of the constructs were made using Bonferonni corrected t-tests as described in the text. (D) Assay to quantify the amount of polymerized microtubules in the extract preparations. Unpolymerized tubulin remains in the supernatant (S200) after centrifugation at 2×10^5 RCF over a sucrose cushion, while polymerized microtubules pellet (P200). As controls, extracts were treated with nocodazole (NZ) to depolymerize microtubules or taxol (TXL) to stabilize microtubules. Note the buffer that was used for the extract preparations is not suitable for stabilizing polymerized microtubules.

Table III.3: Predicted molecular weights and rotational correlation times for Venus, Venus-LC3, and Venus-LC3 mutants based on the FPFA diffusion measurements in HEK 293 cell extracts under basal conditions, and after incubation with 100 µM chloroquine (CQ) for 2 hours.

Construct	Monomer MW (kDa)	ξ Basal Predicted MW (kDa)	ξ CQ Predicted MW (kDa)	Basal Percent Species (%)	Basal Rotational Correlation Time (ns)	CQ Rotational Correlation Time (ns)
Venus	27	N/A	N/A	N/A	12.3 ± 0.2 (4)	N/A
Venus-LC3	45	500 ± 100 (10)	480 ± 90 (6)	N/A	24.9 ± 0.6 (10)	25.0 ± 0.3 (6)
Fast Venus-LC3 (F52A/L53A)	45	300 ± 100 (7)	190 ± 70 (3)	70 ± 4 (4)	25.6 ± 0.3 (7)	25.5 ± 0.1 (4)
Slow Venus-LC3 (F52A/L53A)	45	$(5 \pm 5) \times 10^4$ (7)	N/A	30 ± 4 (4)	N/A	N/A
Venus-LC3 (R70A)	45	190 ± 50 (7)	260 ± 30 (3)	N/A	24.3 ± 0.6 (7)	23.9 ± 0.1 (3)
Venus-LC3 (G120A)	45	600 ± 90 (7)	330 ± 40 (7)	N/A	24.8 ± 0.3 (7)	25.3 ± 0.5 (7)

ξ calculated assuming diffusing species has a spherical shape; mean ± 95 % CI (N = #cells); chloroquine (CQ)

After establishing baselines for diffusion comparisons, next, we performed FPFA measurements of the Venus-LC3(R70A) and Venus-LC3(F52A/L53A) mutants in cytoplasmic extracts. Interestingly, the cross-correlation curve for Venus-LC3(F52A/L53A) was not well described by a single component model (Fig. III.4A). It was, however, fit well by a two component diffusion model where approximately three quarters of the molecules have a diffusion coefficient of $28 \pm 4\,\mu\text{m}^2/\text{s}$ while the remainder have a diffusion coefficient of $5 \pm 2\,\mu\text{m}^2/\text{s}$ (Fig. III.4A,B). The diffusion coefficient for the faster diffusing Venus-LC3(F52A/L53A) species was similar to that of Venus-LC3 ($p > 0.003$; t-test), while the diffusion coefficient for the slower diffusing species was much slower than Venus-LC3 ($p \leq 0.003$; t-test). The cross-correlation curve for Venus-LC3(R70A) on the other hand was well fit by a single component diffusion model with a diffusion coefficient of $35 \pm 3\,\mu\text{m}^2/\text{s}$, which was statistically faster than Venus-LC3 ($p \leq 0.003$; t-test) (Fig. III.4B). Assuming the complexes have a spherical geometry, the predicted sizes of the Venus-LC3(F52A/L53A) associated complexes are about 300 kDa and 50 MDa (note however that we observed relatively high variability in the measurements of the F52A/L53A construct), and the predicted size of Venus-LC3(R70A) associated complexes is about 190 kDa (Table III.3). These values are in agreement with those measured by confocal FRAP in live cells, assuming the D measured for Venus-LC3(F52A/L53A) by FRAP reflects the contributions of two diffusing species detected by FPFA.

In order to directly test if LC3's incorporation into protein complexes is regulated by its lipid modification we performed FPFA measurements on Venus-LC3(G120A). The diffusion coefficient for Venus-LC3(G120A), $23.4 \pm 0.9\,\mu\text{m}^2/\text{s}$, was identical to wild type Venus-LC3 (ns; $p > 0.003$; t-test), further supporting our conclusion based on the FRAP results that the slow diffusion of Venus-LC3 is not due to its lipid modification (Fig. III.4B). In addition, these data further suggest that LC3's lipid modification is not a major factor in regulating the effective size of the LC3 associated complexes.

Our in vivo results revealed the effective sizes of complexes are modestly upregulated by perturbations to the autophagy pathway. We next explored the possibility that the effective sizes of these soluble LC3 associated complexes under chloroquine conditions are maintained in vitro. We prepared cytoplasmic extracts from cells incubated in 100 μM chloroquine for 2 hours before cell lysis. We found that in cells treated with chloroquine, there was little effect on the sizes of the wild type Venus-LC3, Venus-LC3(R70A), and Venus-LC3(G120A) associated complexes compared to basal conditions (ns; $p > 0.003$; t-test) (Fig. III.4C). The diffusion of the Venus-LC3(F52A/L53A) complex under chloroquine conditions was primarily fit with a single component model. These results differed slightly from what we observed in living cells, and suggest that some of the components of the soluble LC3 associated complexes present after treatment with chloroquine were not maintained in vitro. These results further support the conclusion that the complexes we are detecting are independent of lipid modified LC3 incorporated in autophagosomal membranes, as this would have shown up as a component with a diffusion coefficient approximately two orders of magnitude slower than Venus.

III.2.7 Interactions of LC3 with polymerized microtubules are not responsible for the slow diffusion of soluble LC3.

It is formally possible that LC3's slow diffusion could be due to interactions with microtubules given that LC3 was originally identified as a microtubule associated protein [109]. To address this possibility we specifically tested for the presence of polymerized microtubules in the cytoplasmic extracts by sedimentation at a relatively high centrifugal force [177]. We were unable to detect significant levels of polymerized microtubules under the conditions of our experiments (Fig. III.4D). This suggests that the slow diffusion of Venus-LC3 detected by FPFA is not the result of reversible binding to polymerized microtubules. We further tested this possibility in vivo, by performing FRAP experiments on cells depleted of polymerized microtubules by treatment with nocodazole for 15 minutes on ice followed by 1 hour at 37 °C. We observed that the effective sizes of the complexes were maintained in live cells treated with nocodazole (Table III.2), further supporting the notion that reversible interaction with polymerized microtubules is not responsible for LC3's slow diffusion.

III.2.8 There is no evidence of homo-FRET between Venus-LC3, Venus-LC3(F52A/L53A), Venus-LC3(R70A), or Venus-LC3 (G120A).

Our diffusion measurements indicate soluble LC3 is constitutively associated with a high molecular weight complex; however, it is possible the complexes we detect by diffusion may correspond to small aggregates of LC3. We previously tested for oligomerization of puncta independent LC3 in vivo using Cerulean-LC3 and Venus-LC3 as FRET donors and acceptors. FRET microscopy failed to detect significant levels of energy transfer, suggesting soluble LC3 is unlikely to homo-oligomerize or aggregate [165]. However, unfavorable dipole-dipole orientation may have prevented energy transfer, even between fluorophores in close proximity [178, 179]. Thus, LC3's oligomerization state remains unclear.

In order to test if there are multiple LC3 molecules within FRET proximity in our cytoplasmic extracts, next, we examined our FPFA measurements for evidence of homo-FRET. Homo-FRET analysis provides information about the proximity of Venus fluorophores, and thus may be able to detect homo-oligomerization of Venus-LC3 or the Venus-LC3 mutants. For the purpose of performing an analysis of homo-FRET, our FPFA micro-time measurements of orthogonally polarized fluorescence emission were used to calculate time-resolved fluorescence anisotropy decay curves. The decay of fluorescence anisotropy can be due to several factors including rotational diffusion and the presence or absence of FRET [178]. In the absence of FRET, we expect the fluorescence anisotropy curve will exhibit a single exponential decay as was previously measured for Venus, and in the presence of FRET we expect the fluorescence anisotropy curves will exhibit a multi component exponential decay as was previously measured for a series of positive controls consisting of Venus molecules separated by short linkers [176].

We found the fluorescence anisotropy decay curves for both Venus and Venus-LC3 were well fit using a single exponential decay model, indicating little, if any, homo-FRET was occurring in these samples (Fig. III.5A). This result is consistent with a previous study in which we found no significant FRET occurs between soluble Cerulean-LC3 and Venus-LC3 in the cytoplasm of living cells [165]. The single exponential decay rates of the fluorescence anisotropies for Venus and Venus-LC3 are related to the rotational diffusion of the Venus fluorophore attached to LC3 by a flexible linker (Table III.3) [180]. However, because of the flexible nature of the linker it is not possible to use these values to calculate the size of the Venus-LC3-associated complexes based on their rotational correlation times alone.

Next, we examined our FPFA measurements of Venus-LC3(F52A/L53A), Venus-LC3(R70A), and Venus-LC3(G120A) for evidence of homo-FRET in order to determine if these mutations resulted in a change in the proximity of multiple LC3 molecules. In both cases, the anisotropy decay curves were fit by a single exponential, with similar rotational correlation times to that of wild type Venus-LC3 (Fig. III.5A, Table III.3). This suggests the Venus proteins attached to the LC3 mutants are also, to some extent, free to rotate independently of LC3, and that no detectable homo-FRET occurs in either case.

III.2.9 There is on average only one soluble Venus-tagged LC3 protein per complex, and disruption of LC3's hydrophobic binding interface changes the stoichiometry of LC3-associated complexes.

A negative FRET result cannot conclusively rule out the presence of multiple Venus-LC3's per complex, as the Venus fluorophores may be positioned such that their proximity or their average relative dipole orientations does not satisfy the FRET requirements [178]. Fortunately, FPFA measurements provide an additional opportunity to gain insights into the stoichiometry of a protein by quantifying its molecular brightness. Fluorescence brightness is extracted from the statistics of fluorescence intensity fluctuations using a method that has been termed brightness analysis [142]. The principle behind the interpretation of our data lies in the idea that a Venus labeled molecule with a stoichiometry of two will have twice the brightness compared to Venus alone, and it follows that higher order oligomerization states will have quantized brightness values of Venus as was previously measured using a series of positive controls [176].

After establishing the Venus baseline for brightness comparisons, next, we investigated the brightness of Venus-LC3 using our FPFA measurements. We found Venus-LC3 has a normalized brightness of 1.16 ± 0.09, which is approximately 16 % brighter than Venus ($p \leq 0.008$; t-test) (Fig. III.5B). These data strongly suggest the majority of Venus-LC3 does not extensively oligomerize or aggregate in solution. Instead, they suggest

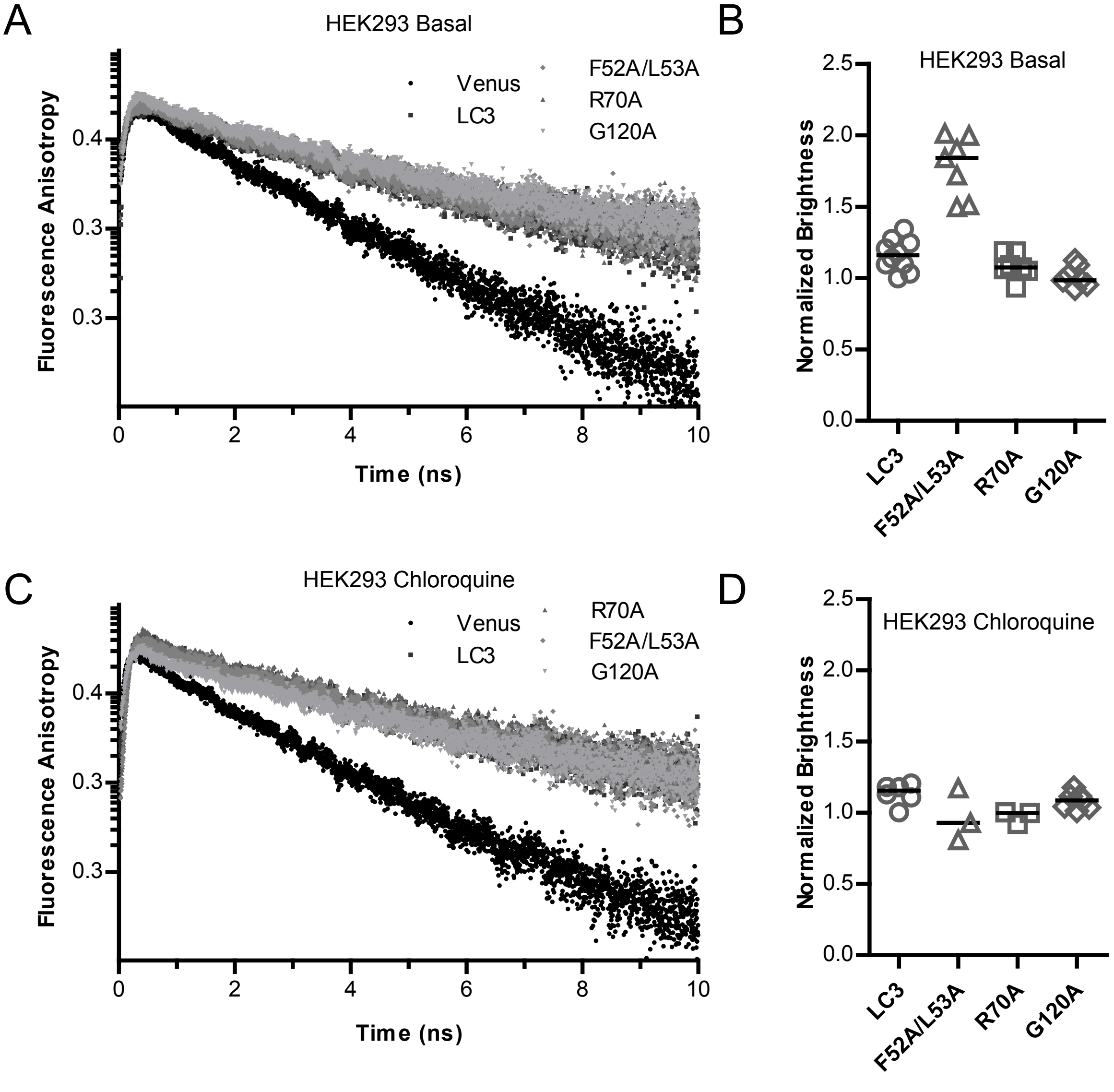

Figure III.5: The majority of complexes contain one soluble Venus-LC3, and mutations to LC3s hydrophobic surface at residues F52/L53 but not R70 alter the stoichiometry of LC3 in complexes. Time Resolved Fluorescence Anisotropy analysis was performed using the microtime FPFA measurements collected from cytoplasmic extracts of HEK 293 cells individually expressing Venus, Venus-LC3, Venus-LC3(F52A/L53A), Venus-LC3(R70A), or Venus-LC3(G120A) under (A) basal conditions, or (C) after incubation in 100 µM chloroquine for 2 hours. The decays are single exponential (linear on a semilog plot) indicating no detectable homo-FRET in all cases. Brightness analysis was performed using the macrotime from the FPFA measurements under (B) basal conditions or (D) after incubation in 100 µM chloroquine for 2 hours. Anisotropy correlation times from replicate measurements can be found in Table III.3. Brightness data is normalized to the average brightness of Venus. Bars represent the median. One-way ANOVA test $p \leq 1 \times 10^{-4}$ for the brightness measurements from either condition. Pairwise comparisons between all of the constructs under either condition were made using Bonferonni corrected t-tests as described in the text.

Venus-LC3 primarily has a stoichiometry of close to one in cytoplasmic complexes.

Finally, in order to gain additional information about the stoichiometry of the mutant LC3 proteins, we performed brightness analysis using our FPFA measurements of Venus-LC3(F52A/L53A), Venus-LC3(R70A), and Venus-LC3(G120A). Assuming the brightness values of the two Venus-LC3(F52A/L53A) species with distinct diffusion times are the same, the normalized brightness of the Venus-LC3(F52A/L53A) complexes is about 1.8 ± 0.1. This brightness value was approximately twice that of Venus, suggesting either one or both of the Venus-LC3(F52A/L53A) complexes has a stoichiometry of two ($p \leq 0.008$; t-test) (Fig. III.5B). On the other hand, the brightness values obtained from the Venus-LC3(R70A), and the Venus-LC3(G120A) FPFA data, were both similar to Venus-LC3. Venus-LC3(R70A) had a normalized brightness of 1.1 ± 0.1, or about 10 % brighter than Venus ($p > 0.008$; t-test), and Venus-LC3(G120A) had a normalized brightness of 1.0 ± 0.1 which was indistinguishable from that of Venus (ns; $p > 0.008$; t-test) (Fig. III.5B). Thus, like wild type Venus-LC3, these data suggest only one Venus-LC3(R70A) and only one Venus-LC3(G120A) molecule is associated with a given complex.

Given the effective sizes of complexes appear to change upon treatment with chloroquine, we reasoned there may also be changes in LC3's stoichiometry or organization under these conditions. We tested for these changes by examining the time resolved anisotropy and the molecular brightness from our FPFA measurements of the LC3 constructs, after treatment with chloroquine, in cytoplasmic extracts. However, we found the anisotropy decays for the constructs were similar to basal conditions (Fig. III.5C), and the molecular brightness values were also similar to basal conditions (Fig. III.5D). On the other hand, the Venus-LC3(F52A/L53A) construct's brightness became more similar to Venus at 1.0 ± 0.2. These data suggest soluble LC3 does not have a propensity to aggregate or homo-oligomerize either under basal conditions or after treatment with chloroquine.

III.3 Discussion

In this study, we analyzed the size and stoichiometry of puncta independent LC3 in the cytoplasm of living cells and in cytoplasmic extracts and examined how these properties are regulated by specific residues on LC3's hydrophobic protein binding surface as well its G120 residue required for lipid modification. On the basis of our findings, we suggest the following working model for the basal organization of LC3 (Fig. III.6). A single soluble Venus-LC3 protein associates with a cytoplasmic complex with a molecular weight about an order of magnitude greater than expected for a spherical monomer. Similarly slow diffusion for puncta independent LC3 was detected in HeLa, COS7, and HEK293 cells ([121, 165] and current study), suggesting this is a general feature of LC3 in the cytoplasm.

We also find that disruption of specific residues on LC3's hydrophobic protein binding surface alters

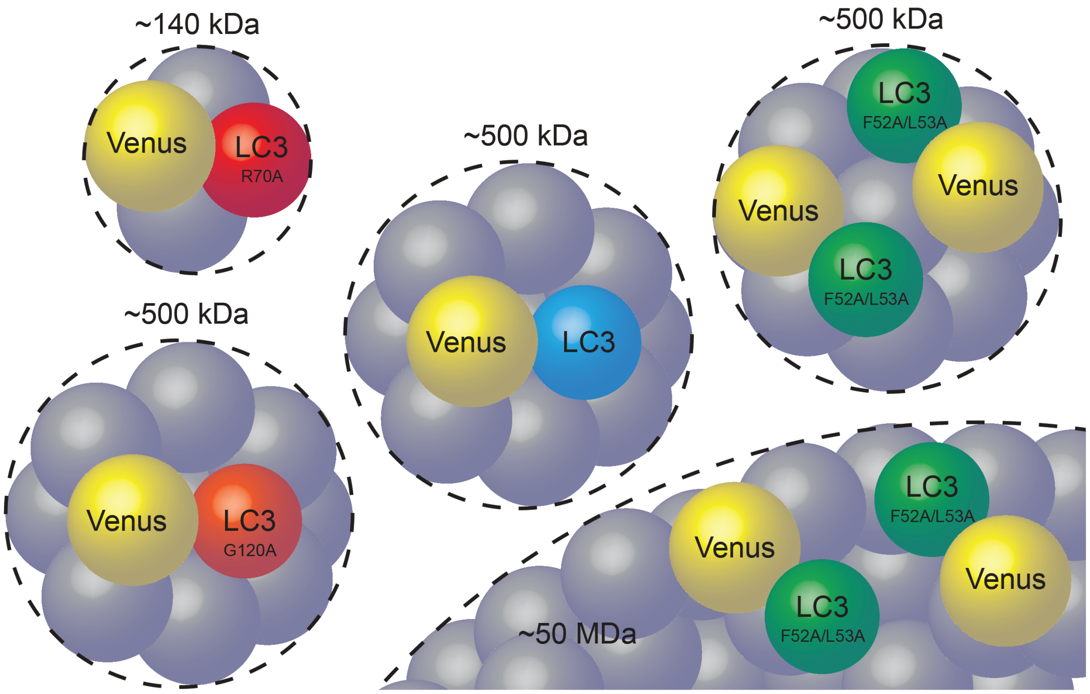

Figure III.6: Working model of the size, stoichiometry and organization of cytoplasmic LC3 associated complexes. On average one soluble Venus-LC3 is constitutively bound to an approximately 500 kDa complex of unknown composition. Mutating LC3 residue R70 to an alanine disrupts LC3s association with the large complex. Mutating LC3 residues F52/L53 to alanines results in altered stoichiometry and binding to a second, ~ 50 MDa, complex. Mutating LC3 residue G120 to an alanine does not change its effective size or stoichiometry.

both the hydrodynamic radius and stoichiometry of LC3-associated complexes (Fig. III.6). We studied two mutants known to disrupt the interaction of multiple proteins with LC3. The first is an F52A/L53A double mutation to LC3 that has been reported to disrupt the interaction of LC3 with several important protein binding partners including SQSTM1 and NBR1, cargo adaptor proteins involved in targeting substrates for autophagic degradation [9, 69, 100, 129, 130]. The second, an R70A mutation to LC3, is also known to disrupt interactions with important binding partners such as SQSTM1 and NBR1, but also additional proteins including FYCO1, a RAB7 effector mediating microtubule plus-end directed vesicular transport [9, 59, 69, 129].

Both Venus-LC3(F52A/L53A) and Venus-LC3(R70A) were poorly targeted to puncta in the cytoplasm under steady state conditions, but showed no dramatic defects in their accumulation on autophagosomal membranes, consistent with the idea that these residues are important for the interactions of LC3 with cargo adaptors, but not autophagosomal membranes [69, 100, 129]. Remarkably, however, the R70A and F52A/L53A mutations had dramatically different effects on LC3's rate of diffusion. Venus-LC3(F52A/L53A) diffused more slowly than Venus-LC3, indicating the complexes it associates with become larger, rather than smaller. The predicted size of the larger Venus-LC3(F52A/L53A) associated complex is exceptionally large, with a predicted molecular weight on the order of 50 MDa. This corresponds to an effective Stoke's radius of $\sim 25\,\mathrm{nm}$; although, we note there is large variability in this estimate. For comparison, the measured hydrodynamic radius of the 70 S ribosome is between $\sim 12\,\mathrm{nm}$–$15\,\mathrm{nm}$ [181, 182]. Furthermore, the Venus-LC3(F52A/L53A) mutant appears to associate with at least two discrete complexes, in which one or both contain multiple copies of LC3(F52A/L53A). The Venus-LC3(F52A/L53A) data provides an excellent example of how FPFA can overcome the limitations of FRET by simultaneously providing information about molecular brightness. In particular, we found no evidence of homo-FRET, but the brightness indicated a stoichiometry of approximately two suggesting the two Venus-LC3(F52A/L53A) proteins are part of the same complex, but further than 10 nm apart. Although it is appealing to imagine the larger Venus-LC3(F52A/L53A) complex revealed by FPFA might serve as a sink for many LC3 proteins, this is not supported by the molecular brightness data.

In contrast to F52A/L53A, the R70A mutant largely disrupted LC3's slow diffusion. In addition, the measured stoichiometry of LC3 in complexes containing the R70A mutant is one, similar to Venus and wild type Venus-LC3. Thus, the R70A mutation decreases the size of LC3 associated complexes, while the F52A/L53A increases the size LC3 associated complexes as well as the number of LC3 molecules in the complexes (Fig. III.6). This was unexpected, since both mutants were reported to be less efficient at binding to numerous important LC3 interacting proteins compared to wild type [9]. If the residues on LC3's hydrophobic protein interaction surface were all required for its association with a high molecular weight complex, we would have predicted that both mutants would have smaller hydrodynamic radii compared to wild type LC3. The data taken together raise the possibility that F52A/L53A mutations to LC3 may change the properties of the protein such that it is sequestered in an entirely new complex, whereas the R70A mutation to LC3 nearly completely disrupts its ability to associate with the complex altogether. Furthermore, the complexes appeared to change upon treatment of cells with rapamycin or chloroquine, suggesting they could be modulated by perturbations to the autophagy pathway.

The identity of the components of these soluble LC3 associated cytoplasmic complexes and their function(s) in the regulation of autophagy or autophagy-independent processes remain to be determined. Given that both the F52A/L53A and R70A mutations interfere with the binding of LC3 to SQSTM1 and NBR1, it seems unlikely that binding to cytoplasmic cargo adaptors, and thus sub-diffraction aggregates could account for the composition of the complexes. Instead, we speculate that these complexes may consist of other LC3 interacting proteins or LC3 interacting protein complexes that may be disrupted due to the R70A mutation. At first glance, the LC3 lipid conjugation machinery is an obvious candidate given ATG7 is known to homo-oligomerize and form a complex with ATG3 to carry out E1- and E2-like LC3 processing reactions [102]. The ATG12, ATG5, and ATG16L1 proteins form complex as large as $\sim 800\,\mathrm{kDa}$[89], which is thought to function as an E3-like ubiquitin ligase for LC3 lipid modification[168] and direct LC3 to the site of autophagosome formation [88]. However, our observation that the diffusion of the LC3(G120A) mutant is similar to the wild type protein, despite the fact that it fails to interact with the LC3 ubiquitin-like conjugation machinery[106], suggests the possibility that puncta independent LC3 constitutively associates with the ATG12/ATG5/ATG16L1 complex is unlikely. There are however, several other proteins whose binding to LC3 is completely disrupted by mutation of LC3's residue R70 that would make for prime candidates [9]. Future work will be required to determine whether the $\sim 500\,\mathrm{kDa}$ LC3 associated complexes consist of these other known autophagy related proteins, or perhaps include others of the recently identified LC3 interacting proteins [9]. One approach that can be used in the future to test for the presence of specific multi-protein complexes in cells is through the combined use of FRET and FRAP, as we illustrated previously for the case of complexes containing LC3 and ATG4B(C74A) [165]. The study of the interaction of LC3 and ATG4B(C74A) validated these approaches as a useful means for characterizing the properties of protein complexes under physiological conditions. Intriguingly, LC3 has also been reported to associate with the 3 UTR of fibronectin mRNA[117], and this interaction depends on a triple arginine motif (residues 68-70) which overlaps with the R70A mutant analyzed in our current study. Thus, LC3-associated complexes detected in our experiments could also potentially represent mRNA-containing complexes.

Our findings also allow us to rule out several alternative models that could account for the slow diffusion of Venus-LC3. First, we found that the measured diffusion of Venus-LC3(G120A) was indistinguishable from wild type LC3. This implies that neither lipidation of LC3 nor its ability to bind to autophagosomal membranes contribute to its slow diffusion. Second, we compared the diffusion of Venus-LC3 in live cells under control conditions and following microtubule disruption, as well in cytoplasmic extracts under conditions that are unfavorable for the maintenance of polymerized microtubules in order to determine if its diffusion is slowed as the result of reversible binding to microtubules. We observed no difference in LC3's diffusion in cells following microtubule disruption, and very close agreement between our in vivo measurements and our in vitro measurements for the diffusion of LC3. This suggests that microtubule binding is not responsible for the slow diffusion of LC3, at least under basal conditions. Finally, our homo-FRET and brightness results strongly suggest that the slowly diffusing complexes of LC3 do not represent either homo-oligomers[93] or aggregates[105] of LC3. These findings imply that if LC3 homo-oligomerization is involved in contributing energy to membrane fusion events in autophagy[93], this event must be limited to autophagosomal membranes.

In this study we utilized two complementary fluorescence-based approaches, FRAP and FPFA to characterize the properties of soluble LC3 associated complexes. The FPFA and FRAP results were in excellent agreement, lending confidence in the conclusions of our studies. However, like any method, each approach has some limitations. First, both FRAP and FPFA rely on measurements of exogenous, fluorescently tagged versions of the protein of interest. This could have several possible consequences on the interpretation of our findings. Our experiments were carried out under conditions where Venus-LC3 is overexpressed, and thus other LC3 binding partners could potentially become limiting for complex formation. Under these conditions one might expect to find excess monomeric Venus-LC3, but our data suggest this is unlikely given the combination of our FRAP and FCS measurements failed to show any evidence for such a scenario. On the other hand, one advantage of over-expressing Venus-LC3 is that it is in excess over the endogenous protein, and thus it is likely that the complexes we detect contain primarily the tagged form of the protein. This increases the likelihood that our measurements accurately report the effective size, stoichiometry, and organization of LC3 associated complexes.

Second, both FRAP and FPFA interpretation requires the fitting of models which carry with them certain a priori assumptions. Often, several competing models can fit a particular dataset equally well, e.g. a small percentage of LC3 associating with membranes or a fraction of LC3 reversibly binding to a microtubule network. Therefore, additional experiments are required to distinguish between competing models, such as the use of mutants, drug treatments, or comparisons of in vivo versus in vitro results as we have done here. Even with such information in hand, there are still circumstances which different models cannot be resolved by an analysis of diffusion alone. For example, although our FRAP and FPFA data were well fit by single component diffusion models, we cannot conclusively rule out the possibility that there are multiple distinct complexes of similar size present. Similar assumptions are inherent in our modeling of the FPFA brightness measurements; in the case of a mixture of complexes, as we detected for F52A/L53A, we cannot rule out the possibility that the two fold increased brightness may have originated from one of the complexes in particular and not both.

Third, although FPFA can potentially provide information about rotational diffusion, and thus yield insights into the size and shape of the diffusing species, our current data cannot be quantitatively analyzed in this way. This is because in our experiments, the Venus label is not rigidly attached to LC3 allowing it to undergo rotational motion independently of LC3 or the LC3 associated complexes. In addition, the lifetime of the Venus fluorophore (on the order of a few nanoseconds) is not long enough to allow accurate quantitation of rotational diffusion for slowly rotating complexes [180]. Thus, our rotational diffusion measurements should not be expected to match our translational diffusion measurements. A rigidly attached fluorophore with a much longer lifetime would be a better choice for measuring the rotational mobility of large complexes.

Lastly, the details of our experimental design should be considered carefully as they also constrain our conclusions in several ways. Our FRAP measurements were specifically designed to avoid LC3 in puncta, and instead focus on the diffuse pool of LC3 independent of bright puncta. Under certain conditions, upregulation of the autophagy pathway for example, the cytoplasm may become full with large numbers of puncta making it difficult or impossible to avoid puncta with a 1 µm radius bleach region. Although this was not a problem under the conditions examined in our study, in the future, methods of analysis may need to be devised in order to extend the range of conditions which can be analyzed by FRAP, for example, the application of reaction and diffusion models[149] to accurately quantify autophagy protein turnover rates on puncta. Similarly, our method of cellular extract preparation should be taken into consideration when interpreting our FPFA findings; we prepared them in such a way that LC3-II incorporated into autophagosomal membranes was either solubilized by detergent and/or excluded from the extract by centrifugation. In the future, FPFA measurements could be performed on LC3-II in autophagosomes using an alternative extraction procedure or using an in vivo configuration in order to test if lipid modified LC3 homo-oligomerizes on autophagosomal membranes and to follow up on previous stoichiometry determinations for ATG proteins on autophagosomes [183].

In summary, our data suggest that in the cytoplasm, individual soluble LC3 molecules associate with a $\sim 500\,\mathrm{kDa}$ complex and that residues on LC3's hydrophobic protein interaction surface are important for regulating its association with these complexes. In the future, we anticipate FRAP and FPFA will become valuable methods for uncovering the emergent properties of protein complexes in the autophagy pathway.

III.4 Materials and Methods

III.4.1 cDNA constructs

GFP-LC3 was the kind gift of T. Yoshimori [173]. Cerulean and Venus tagged versions of LC3 were as previously described [165]. Venus-LC3(R70A), Venus-LC3(F52A/L53A), and Venus-LC3(G120A) mutations were constructed using the Stratagene's QuikChange site- directed mutagenesis kit (Agilent Technologies, Inc.; 200523). For LC3(R70A) the forward and reverse primers were 5'catcaagataattagaagggccctgcagctcaatgctaac3' and 5'gttagcattgagctgcagggcccttctaattatcttgatg3' respectively. For LC3(F52A/L53A) the forward and reverse primers were 5'gtcctggacaagaccaaggcccttgtacctgatcacgt3' and 5'acgtgatcaggtacaagggccttggtcttgtccaggac3' respectively. For
LC3(G120A) the forward and reverse primers were 5'caggagacgttcgcgacagcactggct3' and 5'agccagtgctgtcgcgaacgtctcctg3' respectively.

III.4.2 Cell culture and transfections

HeLa cells and HEK 293T cells (American Type Culture Collection; CCL-2 and CRL-1573) were maintained in Dulbecco's Modified Eagle Medium (DMEM) containing 10 % fetal bovine serum (Life Technologies; 10437028), 1 % PenStrep, and phenol red or High Glucose DMEM containing L-Glutamine, sodium pyruvate, 10 % fetal bovine serum, 1 % PenStrep, and phenol red respectively at 37 °C, 5 % CO_2.

For our live cell imaging experiments, on the day prior to transfection, HeLa cells were plated in MatTek 35 mm No. 1.5 glass bottom culture dishes (Ashland; P35G-1.5-10-C). On the following day the cells (50 to 80 % confluent monolayer) were transfected with described mammalian expression constructs using FuGENE 6 transfection reagent according to the manufacturer's recommended protocol (Promega Corp.; E2691). HEK 293T cells were plated and transfected similarly, except the MatTek chambers were first coated with poly-D-lysine (Sigma-Aldrich; P7886). On the day of the experiment (24 hours after transfection) cell culture medium was rinsed and replaced with phenol red-free DMEM supplemented with 10 % fetal calf serum, 1 % PenStrep, and 25 mM HEPES. The cells were allowed to come to equilibrium at 37 °C for ~ 5 min before transferring to the temperature-controlled microscope stage and objective set to 37 °C.

For our FPFA measurements in cytoplasmic extracts, on the day prior to measurements, plasmid DNA (typically $1\,\mu g/2.5 \times 10^5$ cells) were transfected using electroporation (Digital Bio/BTX MicroPorator). On the following day, the cells were harvested and lysed using passive lysis buffer (Promega; E1941) containing 1 % Protease & Phosphatase Inhibitor Cocktail (Thermo Fisher Scientific Inc.; 78440). The homogenates were centrifuged at 2×10^4 RCF for 15 minutes, and the supernatants were diluted ~ 20 fold with purified water for FPFA to yield a photon count rate between ~ 25 kcps and 100 kcps (> 30 x the dark count rate) to avoid TCSPC pile-up artifacts.54 The clarified homogenates were then loaded into 35 mm glass bottom dishes for measurements at 25 °C.

III.4.3 Analysis of LC3-I to LC3-II processing

The LC3-I to LC3-II processing assay was performed by lysing cells plated in 6 well culture dishes using CellLytic M reagent (Sigma-Aldrich Co. LLC; C2978) as per the manufacturer's instructions; spinning down at 1.3×10^4 RCF for 20 minutes; followed by SDS-PAGE of the supernatant. We blotted using antibodies against beta-tubulin (Developmental Studies Hybridoma Bank; E7), GFP (JL-8) (Clontech; 632380), and LC3 (Novus Biologicals; NB100-2220).

III.4.4 Drug Treatments

In order to block lysosomal degradation of LC3 or upregulate the autophagy pathway we incubated the cells with either 100 µM chloroquine (Sigma-Aldrich Co. LLC; C6628) or 200 nM rapamycin (Sigma-Aldrich; R8781) for 2 hours at 37 °C before performing live cell imaging or preparing cell extracts. In order to disrupt microtubules in live cells, we incubated the cells on ice with 5 µg/ml nocodazole (Sigma-Aldrich Co. LLC; M1404) for 15 minutes before transferring to 37 °C for an additional hour. The cells were imaged in the continued presence of nocodazole.

III.4.5 Microtubule pelleting assay

We examined the extent of polymerized microtubules in our cytoplasmic extracts using a microtubule pelleting assay [177]. The cytoplasmic extracts were loaded onto a 40 % sucrose cushion and spun at 2×10^5 RCF for 20 minutes at 25 °C. Fractions from the pellet and supernatant were analysed by SDS-PAGE. Although the conditions of the passive lysis buffer are not suitable for maintenance of polymerized microtubules in vitro, we attempted to further depolymerize microtubules or repolymerize tubulin by incubating our extracts with nocodazole (5 µg/ml) for 15 minutes on ice or with paclitaxel (20 µM) at 37 °C for 15 minutes before the pelleting assay.

III.4.6 Laser scanning confocal microscopy and quantification of LC3-associated puncta

Cells were imaged live using a Zeiss LSM 510 confocal microscope (Carl Zeiss MicroImaging Inc., Thornwood, NY) equipped with an Argon/2 30 mW laser (458, 488, 514 nm) using an oil immersion 40x 1.3 N.A. Zeiss Plan-Neofluar objective. The total numbers of bright, Venus-LC3 labeled spots ($\sim$ 0.5 µm–2 µm) obtained in single confocal sections (1 Airy unit) were manually counted in the cytoplasm of each cell and reported as the mean number of cytoplasmic spots per cell.

III.4.7 FRAP methods

Confocal FRAP measurements were performed using a Zeiss LSM 510 confocal microscope (Carl Zeiss MicroImaging Inc.) equipped with an Argon/2 30 mW laser (458, 488, 514 nm) using an oil immersion 40x 1.3 N.A. Zeiss Plan-Neofluar objective. Confocal FRAP data were obtained using 512 X 45 pixel images at 4X digital zoom using a 1 Airy unit pinhole at a rate of 42 frames per second. Venus was irreversibly photobleached by iteratively scanning a 514 nm laser (30 mW nominal power) 10 times in a circular ROI with a nominal radius r_n of 0.99 µm, centered in the imaging window. Imaging of the prebleach steady state fluorescence and the postbleach recovery was carried out using a much lower nominal laser power of 0.06 mW. In order to separate excitation and emission light sources we employed several standard filter sets for the Zeiss LSM 510 (HFT 458/514, and LP 530). A total of 600 images were acquired for each recovery ($\sim$ 15 seconds), and the bleaching event required 129 ms before acquisition of the postbleach image under our conditions.

To analyze the confocal FRAP data we utilized a recently developed analytical equation for simple Brownian motion to extract an instrument independent diffusion coefficient [158]. The first step in the approach is to plot the mean fluorescence intensity within the bleach region as a function of time to yield a FRAP curve, $I(t)$. We next normalize $I(t)$ by dividing by the pre-bleach steady-state fluorescence and correct for any unintentional photobleaching encountered during normal imaging. To do this we fit the last 50 data points, at a time sufficiently long enough after the bleach to reach diffusional steady-state, of $I(t)$ to a first order decay process,

$$I(t) = \exp(-k_{decay}t) \tag{III.1}$$

where t is time, and kdecay is the unintentional photobleaching rate constant. $I(t)$ is corrected by dividing by the exponential decay [157]. Next, the diffusion coefficient D and mobile fraction Mf were found by fitting the data to a one component FRAP model for Brownian motion with infinite boundary conditions,

$$I(t) = I_0 \left(\sum_{m=0}^{m=200} \frac{-K^m r_e^2}{m![r_e^2 + m(8Dt + r_n^2)]} \right) Mf + (1 - Mf)I(0) \tag{III.2}$$

where I_0 is 1 for a normalized FRAP curve, and *rn* is the nominal radius of the bleaching ROI [158]. This is a modified form of the Axelrod equation[140] where the laser is assumed to be a Gaussian, and the parameters *re* and K take into account the initial conditions for the solution of the diffusion equation. The FRAP model assumes a homogenous distribution of molecules were bleached along the Z-axis resulting in diffusional exchange along the X and Y axes. We determined *re* and K by fitting the normalized radial post-bleach profile, $I(x;t=0)$, to an analytical approximation,

$$I(x;t=0) = I_0 \exp\left(-K \exp\left[-\frac{2x^2}{r_e^2}\right]\right) \tag{III.3}$$

where I_0 is 1 for a normalized post-bleach profile, and x is the radial distance from the center of the bleaching ROI [155].

For comparison, we also analyzed a subset of the data using a newly described simplified FRAP equation for Brownian motion [175]. In this approach, $I(x;t=0)$ was further approximated as,

$$I(x;t=0) = 1 - K \exp\left(-\frac{2x^2}{r_e^2}\right) \tag{III.4}$$

resulting in the simplified FRAP model,

$$I(t) = I_0 \left(1 - K\left[1 + \frac{r_n^2}{r_e^2} + \frac{8Dt}{r_e^2}\right]^{-1}\right) Mf + (1 - Mf) I(0) \tag{III.5}$$

A comparative analysis of these two analytical FRAP models (Equations III.2 and III.5) revealed no significant differences in D or Mf with the level of noise present in our data. This means using Equation III.5 is the preferred method of extracting diffusion coefficients and mobile fractions, as it greatly reduces the complexity in programming a non-linear fitting routine. Furthermore, if there is a priori knowledge that the fluorescence recovery is dominated by Brownian motion rather than reaction kinetics, and the system was allowed to relax back to a steady-state one could use linear interpolation to find the half time of the recovery ($\tau_{1/2}$) and resultant D without any fitting required using

$$D = \frac{r_e^2 + r_n^2}{8\tau_{1/2}} \tag{III.6}$$

where indicated, D values were used to calculate the Stokes radius using the Stokes-Einstein equation:

$$D = \frac{k_B T}{6\pi\eta r} \tag{III.7}$$

where k_B is Boltzmann's constant, T is temperature, r is the Stokes radius, and η is viscosity. The apparent molecular weight MW was then calculated as follows (assuming a spherical geometry):

$$MW = MW_{GFP} \left(\frac{D_{GFP}}{D}\right)^3 \tag{III.8}$$

where MW_{GFP} is the molecular weight of GFP (27 kDa) and D_{GFP} is the measured diffusion coefficient of the GFP control.

In principle, a freely diffusing control such as Venus should be 100 % mobile on the time scale of our experiments as indicated by Mf. However, under the conditions of our experiments a significant fraction of molecules in the cytoplasm were irreversibly destroyed during the experiment resulting in Mf values less than 1. In order to correct for the significant loss of fluorescence in the compartment due to the bleaching event, we calculated the true mobile fraction ($Mf_{correct}$) by,

$$Mf_{correct} = 1 - (I_{adjacent}(t) - I(t)) \tag{III.9}$$

where $I_{adjacent}(t)$ is the intensity inside an ROI placed adjacent to the bleaching ROI.

III.4.8 FPFA methods

An 80 MHz, 200 fs mode locked Ti:sapphire laser (Coherent Chameleon Ultra-2) operated at 950 nm provided pulsed two-photon excitation. The excitation beam, passed through a power attenuator, a spatial filter system (KT310, Thorlabs), a near-IR linear polarizer (100,000:1 extinction ratio, Thorlabs), and finally a multiphoton short-pass dichroic beamsplitter (FF670-SDi01-25x36, Semrock) was used to reflect the excitation beam to a Zeiss 63x 1.2 N.A. water objective (back aperture slightly overfilled). This setup focused the beam to a diffraction-limited spot (~ 0.4 µm in diameter). The excitation power was kept low (typically ~ 10.2 mW at the focal point) to avoid bleaching during acquisition (150-200 s).

Fluorescence collected from the observation volume in the sample was guided through a BG39 filter (to block residual near-IR photons), a high throughput band-pass filter (FF01-540/50-25, Semrock), and finally a polarizing beam splitter (Thorlabs) augmented with two orthogonally oriented linear polarizers (Thorlabs) to increase the extinction ratio. At the beam splitter, parallel and perpendicular emitted photons were separated and focused onto two HPM-100-40 hybrid detectors (Becker & Hickle). The dark count rate for these detectors was typically 200-750 cps at 25 °C. Photons detected by each detector were processed by a SPC-132 TCSPC card (Becker & Hickle). For synchronization between excitation pulses and detected photons, a small fraction of the excitation beam was extracted and focused onto a high-speed photodetector (DET10A, Thorlabs) powered by a battery to avoid crosstalk. Note that all optics used in the excitation pathway were selected to minimize group delay dispersion.

For each homogenate, three to five replicate measurements were performed and these were averaged for each point. All measurements were performed at room temperature.

SPCM software (Becker & Hickle) running in FIFO mode was used to calculate time-resolved fluorescence and cross-correlation functions. Time-resolved anisotropy was calculated based on fluorescence decay of parallel and perpendicular channels using the following equation[180, 184]:

$$r(t) = \frac{I_{\parallel}(t) - gI_{\perp}(t)}{I_{\parallel}(t) + 2gI_{\perp}(t)} \tag{III.10}$$

where $I_{\parallel}(t)$ and $I_{\perp}(t)$ are the fluorescence intensity of parallel and perpendicular channels (dark noise subtracted) respectively, and g is an instrument correction factor which for our microscope had a value of 0.96 as determined by tail fitting calibration measurements of fluorescein.

For FPFA, independently measured emission events detected in the parallel and perpendicular light paths were cross-correlated, $G(\tau)$. The time dependence of these curves were initially fit using a single component three-dimensional (3D) diffusion equation to estimate the value of $< N >$, the average number of fluorescent molecules in the excitation volume, and τ_D, the correlation time (the average time that a molecule spends in the detection volume) for each sample:

$$G(\tau) = \frac{\gamma}{< N >} \frac{1}{1+(\tau/\tau_D)} \frac{1}{\sqrt{1+(\omega/z)(\tau/\tau_D)}} \tag{III.11}$$

where ω and z, are the radial and axial beam waists respectively calculated from calibration experiments, and the constant γ has a value of 0.35 for a three-dimensional Gaussian PSF [142]. The molecular brightness b is the average number of photon emitted per second per molecule (cpsm)

$$b = \frac{< k >}{< N >} \tag{III.12}$$

where $< k >$ is the average photon count rate recorded during data acquisition.

To model a mixture of two species having the same brightness but independent diffusion times:

$$\begin{aligned} G(\tau) = & \frac{\gamma}{(< N_1 > + < N_2 >)^2} \\ & \left(< N_1 > \frac{1}{1+(\tau/\tau_{D1})} \frac{1}{\sqrt{1+(\omega/z)(\tau/\tau_{D1})}} + < N_2 > \frac{1}{1+(\tau/\tau_{D2})} \frac{1}{\sqrt{1+(\omega/z)(\tau/\tau_{D2})}} \right) \end{aligned} \tag{III.13}$$

In this case,

$$b_1 = b_2 = \frac{< k >}{< N_1 > + < N_2 >} \tag{III.14}$$

With two-photon excitation the relationship between correlation time τ_D and D is given by61:

$$\tau_D = \frac{\omega^2}{8D} \tag{III.15}$$

III.4.9 FPFA Calibrations

The instrument correction factor g for calculating time-resolved anisotropy (Equation III.10) was measured using tail-fitting[180] of fluorescein samples and found to be 0.96. The value of ω/z for our microscope (used in Equations III.11 and III.13) was 0.1 at an excitation power of 10.2 mW (at 950 nm) using calibration standards of fluorescein in water at pH 9.5 [176]. Assuming fluorescein has a diffusion coefficient of 300 μm^2/s, using the measured correlation time of 75 ± 9 µs, the value of ω was 424 ± 30 nm. The validity of this calibration procedure was confirmed by measuring the diffusion coefficient of Venus monomers under identical conditions. Using $\omega/z = 0.1$, the measured correlation time for Venus monomers with 10.2 mW excitation power was 343 ± 17 µs ($n = 3$). This corresponds to a diffusion coefficient for Venus monomers in solution of 65.5 ± 8.6 μm^2/s ($n = 3$), in good agreement with the diffusion coefficient measured for GFP [185].

III.5 Curve fitting and statistics

IGOR Pro software (Version 6.22) was used for fitting of time-resolved anisotropy, cross-correlation curves, and for global fitting of calibration standards. FRAP data was fit using custom routines written in MATLAB based on the trust-region-reflective algorithm (The MathWorks; R2010B). The errors reported throughout the text are 95 % confidence intervals unless otherwise stated. To test the hypothesis that two group means are not different, under circumstances where there were multiple groups being compared, we used the Bonferonni method to control the overall type-I error rate such that for all pairs of comparisons the familywise significance level was 0.05. For example, if 4 groups are being compared the total number of comparisons is 6, thus the p value cutoff is $0.05/6 = 0.008$.

III.6 Acknowledgments

We are grateful for the constructive criticism and advice from the other members of the Kenworthy laboratory and to Dr. Christian Behrends for helpful discussions. This work was funded by grant NSF/DMS 0970008 from the National Science Foundation, by the intramural program of the National Institutes of Health, National Institute on Alcohol Abuse and Alcoholism, Bethesda, MD 20892, and utilized the core(s) of the Vanderbilt Diabetes Research and Training Center funded by grant DK020593 from the National Institute of Diabetes and Digestive and Kidney Disease. The funding sources had no role in the study design, collection, analysis or interpretation of data, writing the report, or the decision to submit the paper for publication.

CHAPTER IV

Imaging protein complex formation in the autophagy pathway: analysis of the interaction of LC3 and Atg4B(C74A) in live cells using Förster Resonance Energy Transfer and Fluorescence Recovery After Photobleaching

In Chapter III we discovered that the slow diffusion of autophagosome independent LC3 is due to its association with a $\sim 500\,\mathrm{kDa}$ complex. This raises the question: what are the other components in the complex with LC3? In the current study, we aimed to develop FRET and FRAP based methods to investigate protein complexes in the autophagy pathway. This chapter begins with a brief introduction. As a model system for studying protein complex formation we investigated the interactions of LC3 with Atg4B(C74A), a catalytically inactive mutant of the cysteine protease involved in lipidation and de-lipidation of LC3. These FRET and FRAP studies suggest Atg4B(C74A) and LC3 form a larger than expected complex in the cytoplasm of live cells, consistent with the size and shape of a recent crystal structure for the interaction. We conclude that the FRET and FRAP methods can be useful tools for studying the properties of protein complexes in the autophagy pathway.

IV.1 Introduction

The influx of information about protein-protein interactions from bioinformatics and proteomics analyses has shifted the bottleneck to discovery towards a more thorough characterization of these interactions within the context of living cells [132, 186–188]. Fortunately, recent advances in live cell imaging are making it possible to quantitatively characterize the spatial and temporal regulation of green fluorescent protein (GFP) tagged proteins in the complex environment of the living cell. For example, protein-protein interactions are readily monitored through the use of FRET microscopy [178, 189–193], and the dynamics of individual proteins and protein complexes can be quantitatively characterized using techniques sensitive to mobility such as confocal fluorescence recovery after photobleaching (FRAP) and fluorescence correlation spectroscopy (FCS) [121, 140, 148, 149, 155, 157, 194–199].

One example of an intracellular pathway whose function depends on the coordinated effort of a network of interacting proteins is macroautophagy (referred to here as autophagy) [9]. The process of autophagy is activated in response to stress signals such as low nutrient availability, and up-regulation of the pathway leads to the capture of cytosolic materials in a double membrane structure termed the autophagosome that is

---

This chapter is adapted from the published manuscript: Kraft and Kenworthy [165] subsequently trafficked to the lysosome for degradation and recycling [5, 10, 24]. LC3 (ATG8 in yeast) plays a central role in the autophagy pathway[9, 10, 24] facilitating the formation of autophagosomes [84, 85, 200]. Under basal conditions LC3 is known to exist in a soluble form termed LC3-I, and upon upregulation of the autophagy pathway LC3 is converted to a lipidated form termed LC3-II that associates with autophagosomal membranes [90].

Recently, a large-scale proteomics screen of the human autophagy pathway revealed LC3 and orthologs interact with a network of 67 proteins [9]. In independent studies, our group discovered soluble EGFP-LC3 diffuses much more slowly than predicted for a freely diffusing monomer in both the cytoplasm and nucleus of live cells [121]. This raises the possibility that LC3 may constitutively associate with a high molecular weight complex containing multiple proteins, perhaps comprised of one or more LC3-interacting proteins identified in the large scale proteomics screen [9]. Importantly, constitutive association of LC3 with a multi-protein complex could be a potential mechanism for regulating the autophagy pathway. However, it is unclear how many of these proteins come together in live cells to perform the diverse functions associated with autophagy related proteins, or how these complexes are regulated.

In the current study, we sought to develop tools to further investigate protein complex formation in the autophagy pathway. As a test case, we examined the properties of the complex formed between LC3 and Atg4B(C74A), a catalytically inactive mutant of the cysteine protease known to play important roles in both the lipidation and de-lipidation of LC3 [201]. Previous studies reported over-expression of wild type Atg4B reduces LC3 lipidation as well as LC3 membrane localization [173]. Fujita et al. demonstrated this effect was likely the result of Atg4B non-productively binding to LC3. In their study, they showed expression of a protease inactive mutant, Atg4B(C74A), has similar effects, and proposed the use of this construct as a tool for studying autophagy [173]. Given the strong biochemical evidence that shows Atg4B(C74A) directly interacts with LC3 to form a stable complex, we used this pair of proteins as a model for developing FRET and diffusion based methods to characterize protein complexes in living cells. The basis for using FRET to analyze protein-protein interactions lies in the distance dependence of near field non-radiative energy transfer between two suitable fluorophores known as the donor and acceptor,

$$E = \frac{1}{1+(r/R_0)^6} \tag{IV.1}$$

where the energy transfer efficiency E varies with the inverse sixth power of the separation distance r between them[135, 202, 203], and the Förster distance R_0 is the distance between a given pair of donor and acceptor fluorophores at which $E = 50\,\%$. R_0 is $\sim 5\,\text{nm}$ for commonly used donors and acceptors used in microscopy-based FRET experiments, such as the GFP variants Cerulean and Venus [204]. Considering the lengthscale of a typical protein-protein interaction, FRET can be used to determine if two fluorescently labeled proteins are either directly interacting or are close together in a complex. Live cell FRET measurements can be carried out in a number of ways by fluorescence microscopy, for example by measurements of sensitized acceptor emission, analysis of fluorescence lifetime, or quantification of donor dequenching following acceptor photobleaching [135, 191, 202, 203].

While FRET is clearly a powerful tool for mapping protein-protein interactions in the cell, diffusion-based measurements can provide complementary information about the nature of protein complexes. A commonly used technique to measure the diffusion of fluorescently labeled molecules in single living cells is FRAP. In recent years, FRAP has become a popular technique to study the dynamics of GFP-tagged proteins in intracellular compartments using confocal microscopes [132, 194, 195, 197]. In these experiments, cells expressing a fluorescently tagged protein of interest are visualized by fluorescence microscopy. In order to probe the underlying motions of the proteins, an intense pulse of laser light is directed to a defined region of interest in the cell, inducing permanent photobleaching of the fluorophores within that region. Subsequently, unbleached molecules from the surrounding regions exchange with the bleached molecules (termed recovery). The rate at which exchange occurs reveals useful information about the state of the underlying molecules of interest, including the translational diffusion coefficient D and the fraction of mobile molecules, commonly referred to as the mobile fraction or Mf. For the case of simple diffusion of soluble proteins, D is related to the size and shape of the diffusing species, the viscosity η of the medium and the absolute temperature T. The precise relationship is given by the Stokes-Einstein relation,

$$D = \frac{k_B T}{6\pi\eta R} \tag{IV.2}$$

for spherical molecules with radius R, where k_B is Boltzmanns constant. Thus, the diffusion coefficients for two soluble proteins within the same multi-protein complex should be identical, and correspond to the size and shape of the complex itself.

To obtain this information from FRAP data, it is necessary to quantitatively analyze the recovery curves to obtain an accurate measurement of D. In a classic paper, Axelrod et al. described an analytical solution for FRAP involving a circularly symmetric stationary focused laser beam that can be used to extract D [140]. However, several of the assumptions underlying derivation of this equation do not hold when applied to FRAP data obtained using confocal microscopes, such as the assumption that the bleaching event occurs rapidly relative to the characteristic recovery time. Recently, our lab described an approach that generalizes the Axelrod equation to a form that can be applied to data obtained using a laser scanning confocal microscope [140, 158]. Here, we use FRET microscopy and confocal FRAP as complementary methods to characterize the properties of LC3 and Atg4B(C74A) complexes in single living cells.

IV.2 Results

IV.2.1 The subcellular localization of LC3 is altered upon co-expression of Atg4B(C74A).

The interaction of Atg4B(C74A) with LC3 has been reported to cause a shift in the subcellular localization of LC3, leading to its sequestration in the cytoplasm [121, 173]. To confirm this shift in localization occurs under the conditions of our experiments, we compared the subcellular distribution of Venus and Cerulean-tagged forms of LC3 and Atg4B(C74A) expressed individually versus under conditions where they were co-expressed using confocal microscopy (Figure IV.1). COS-7 cells were used as a model system for these studies, and as a control, we confirmed Venus itself is evenly distributed between the nucleus and cytoplasm (Figure IV.1A).

When expressed on its own, Venus-LC3 was found localized in both the cytoplasm and nucleoplasm, but was notably enriched in the nucleoplasm (Figure IV.1B). Venus-Atg4B(C74A) expressed individually was also localized in both the cytoplasm and nucleus; however, unlike Venus-LC3, Venus-Atg4B(C74A) was enriched in the cytoplasm over the nucleus (Figure IV.1C). We next compared the distribution of Venus-LC3 and Cerulean-Atg4B(C74A) when the two proteins were co-expressed in the same cells. Under these conditions, Cerulean-ATG4B(C74A) was further concentrated in the cytoplasm, and almost completely absent from the nucleus (Figure IV.1E). Similarly, a significant shift in the distribution of Venus-LC3 out of the nucleus was observed in cells co-expressing Cerulean-ATG4B(C74A) (Figure IV.1D).

These findings show Venus and Cerulean tagged versions of these proteins behave as expected, consistent with a previous study where we showed by quantitative image analysis that the levels of EGFP-LC3 are significantly higher in the nucleus relative to the cytoplasm, and that co-expression of Strawberry-ATG4B(C74A) with EGFP-LC3 results in a redistribution of EGFP-LC3 out of the nucleus [121, 173].

IV.2.2 ATG4B(C74A) and LC3 are within FRET proximity in living cells.

Catalytically inactive Atg4B mutants were previously shown to constitutively bind to LC3 [101, 173]. In addition, a recent crystal structure shows two molecules of LC3 bind to catalytic and regulatory domains on a single molecule of Atg4BC74S [101]. These findings suggest LC3 and ATG4B(C74A) should be within FRET proximity in living cells. To test this prediction, we performed acceptor photobleaching FRET microscopy measurements, using Cerulean and Venus as the FRET donor and acceptor, respectively.

To establish conditions for the FRET assay, we measured a series of FRET standards consisting of Cerulean and Venus separated by 5, 17, or 32 amino acids as positive controls [205]. The measured en-

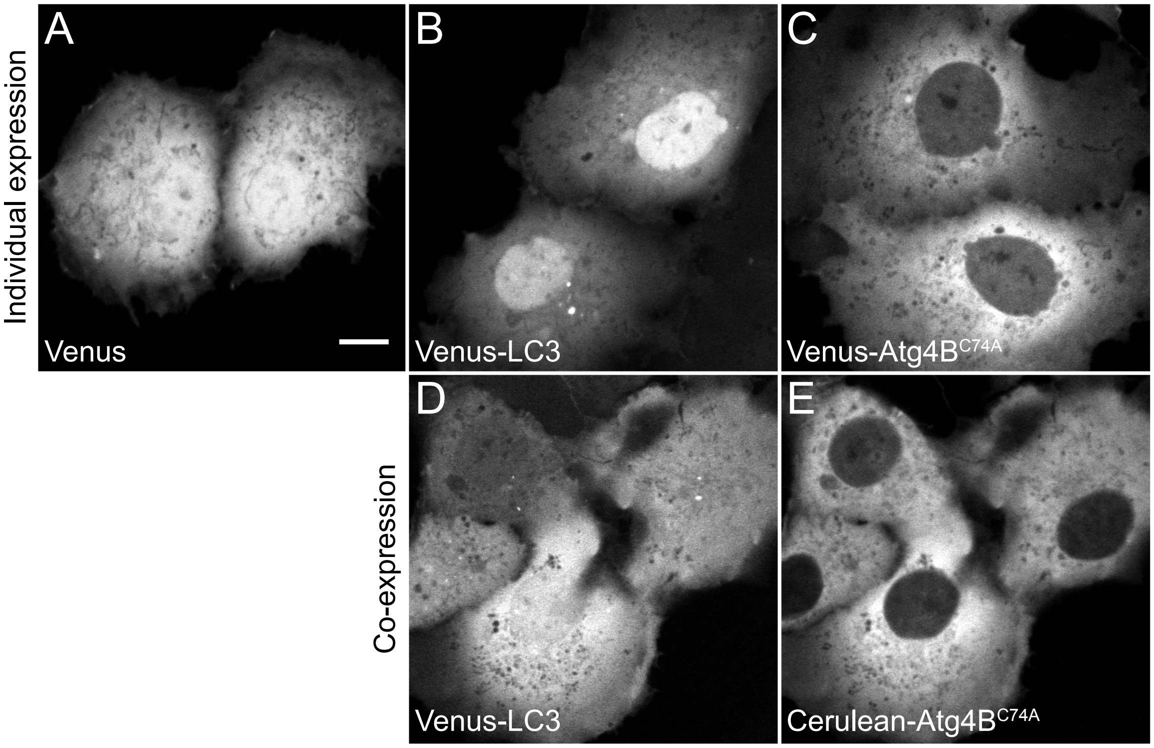

Figure IV.1: Subcellular localization of Venus and Cerulean-tagged versions of Atg4B(C74A) and LC3 when expressed individually or in combination. COS-7 cells were transiently transfected with the indicated constructs and imaged live. (A) Venus is evenly distributed between the cytoplasm and nucleus. (B) Venus-LC3 is enriched in the nucleus relative to the cytoplasm. (C) Venus-Atg4B(C74A) is enriched in the cytoplasm relative to the nucleus. (D) In cells co-expressing Venus-LC3 and Cerulean-Atg4B(C74A), LC3 is pulled out of the nucleus. The relative distribution of LC3 between the nucleus and cytoplasm varies between cells depending on levels of Atg4B(C74A) present (not shown). (E) In cells co-expressing Venus-Atg4B(C74A) and Cerulean-LC3, Atg4B(C74A) is further enriched in the cytoplasm, compared to its distribution in cells expressing Venus-Atg4B(C74A) alone. Bar, 10 µm.

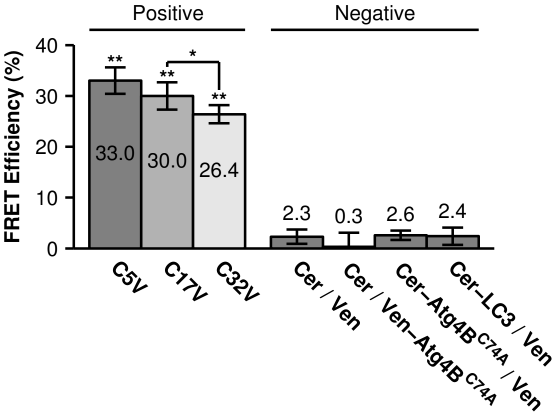

Figure IV.2: Controls for FRET microscopy. (A) Mean percent energy transfer efficiency for positive FRET controls consisting of Cerulean and Venus linked by 5, 17, or 32 amino acids, and negative FRET controls (cells co-expressing Cerulean and Venus, Cerulean and Venus-Atg4B(C74A), Cerulean-Atg4B(C74A) and Venus measured from the mean of a whole cell. Error bars represent 95 % CI with $N \geq 11$ cells from at least two independent experiments.

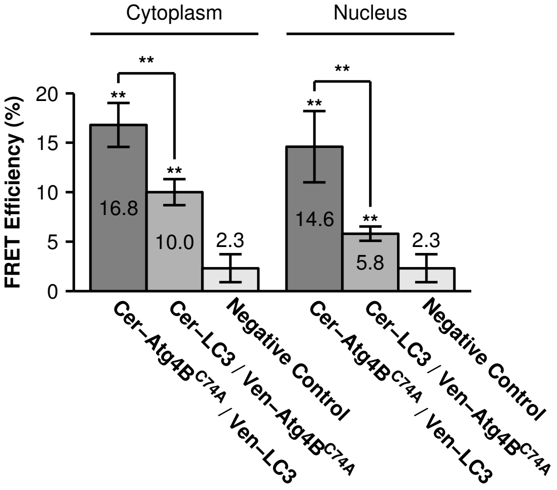

Figure IV.3: FRET is detected between LC3 and Atg4B(C74A) in both the cytoplasm and nucleus of living cells. FRET efficiency between Cerulean- LC3 and Venus-Atg4B(C74A), or Cerulean-Atg4B(C74A) and Venus-LC3 as measured using acceptor photobleaching FRET. Data are shown for measurements in both the cytoplasm and the nucleus. FRET efficiencies between the negative control Cerulean and Venus are shown for comparison. Error bars represent 95 % CI with $N \geq 16$ COS-7 cells from at least two independent experiments.

ergy transfer efficiencies (E) under our conditions (Figure IV.2) were slightly less than the values previously reported, possibly due to a small population ($< 5\,\%$) of acceptor remaining after bleaching [205]. However, the relative trend between samples was identical. As negative controls, we measured FRET in cells co-expressing Cerulean and Venus-LC3, Cerulean and Venus-ATG4B(C74A), Cerulean-LC3 and Venus, and Cerulean-ATG4B(C74A) and Venus. For these constructs, the mean E ranged from $\sim 0\,\%$–$2.6\,\%$ (Figure IV.2).

We measured significant FRET in the cytoplasm and nucleus of cells co-expressing either Cerulean-LC3 and Venus-ATG4B(C74A) or Cerulean-ATG4B(C74A) and Venus-LC3 (Figure IV.3). Additionally, the measured FRET efficiencies were $\sim$ 2–3 times larger when the FRET acceptor, Venus, was attached to LC3 compared to when Venus was attached to ATG4B(C74A) in the cytoplasm and nucleus (Figure IV.3). These results show ATG4B(C74A) and LC3 are within FRET proximity in the cytoplasm of living cells, in agreement with previous biochemical evidence showing the two proteins constitutively interact in solution (32). In addition, our results suggest LC3 and ATG4B(C74A) also interact in the nuclear compartment.

Both ATG4B(C74A) and LC3 diffuse more slowly than freely diffusing monomers as measured by confocal FRAP. In a previous study, we found EGFP-LC3 diffuses more slowly than expected for a freely diffusing monomer, suggesting it may be part of a multi-protein complex [121]. This raises the possibility that other proteins known to interact with LC3 may also be part of this complex, and diffuse similarly to LC3. Since ATG4B(C74A) is predicted to interact with endogenous LC3, we hypothesized ATG4B(C74A) may also diffuse as if it is part of a much larger complex, rather than a freely diffusing monomer.

To test this, we performed measurements of Venus-ATG4B(C74A) using confocal FRAP to obtain a translational diffusion coefficient which is related to its size assuming a particular geometry, such as a sphere or rod. Although a monomer and a dimer are difficult to discern from one another using this approach, molecules that exhibit large differences in molecular weight or shape from one another can be distinguished. As internal controls, we performed parallel FRAP studies for Venus and Venus-LC3, where Venus serves as an inert reporter of free diffusion [148]. Soluble proteins like Venus diffuse rapidly, making it technically challenging to analyze their diffusional mobility because they recover completely within seconds following a photobleaching event. Because a laser scanning confocal microscope takes ~ 1 s to acquire a full frame (512 x 512) image, it is not possible to resolve the early time points of the recovery curve while collecting images of this size. Therefore, to analyze the diffusional mobility of these proteins, we bleached a small circular region of interest located either in the nucleoplasm or the cytoplasm, and imaged only the area immediately surrounding the bleach ROI during the recovery (Figure IV.4A-B) [155]. Under these conditions, we were able to acquire images every 0.0451 s.

We bleached a 0.99 μm circular bleach ROI positioned in either the cytoplasm or nucleus by scanning 10 iterations of a higher intensity laser light, requiring approximately 0.15 s (Figure IV.4A-B). Because the bleaching event is not instantaneous and soluble proteins diffuse rapidly, some diffusion of the protein from the bleached region to the surrounding area occurs in the time it takes to acquire the post-bleach image. This is evidenced by the presence of bleached molecules outside of the user-defined bleach ROI (Figure IV.4B). It is important to take this into account, because the intensity profile of the bleach spot defines the initial conditions to solve Ficks second law in the derivation of the FRAP equation (Eq. IV.6) [155, 158]. This is accomplished by fitting the post-bleach profile to obtain parameters K and r_e (Figure IV.4C) (Eq. IV.5) [155]. With the parameters K and r_e in hand, the corrected FRAP data is fit with equation IV.6 to obtain parameters D and Mf (Figure IV.4D) [158]. The value of the diffusion coefficient D obtained for this example is 17.1 μm^2/s, and the mobile fraction Mf is 0.82. However, because a significant fraction of fluorophores is lost as the result of the photobleaching event, this does not reflect the true fraction of mobile molecules. To obtain a more accurate estimate of Mf (0.99 ± 0.01, 95 % CI $N = 30$), we compared the fluorescence intensity inside an ROI positioned adjacent to the bleach regions after the fluorescence had completely recovered [206].

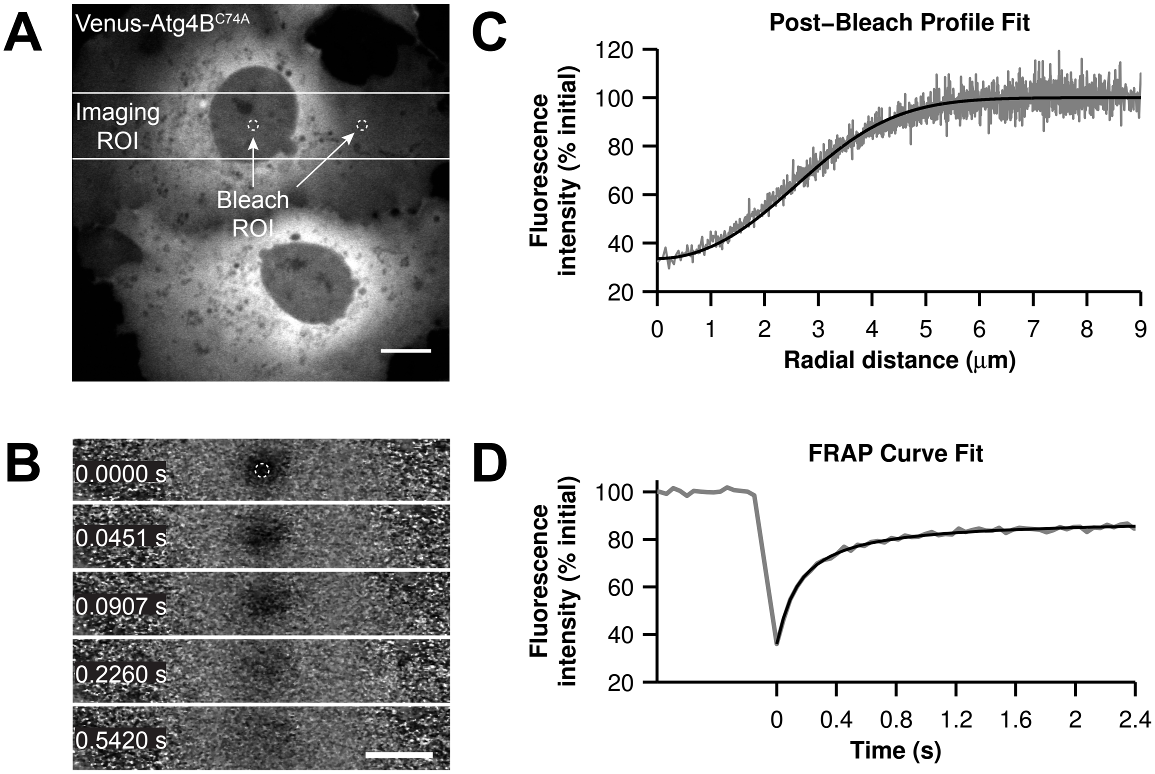

Figure IV.4: Confocal FRAP assay. (A) Example of the imaging ROI used for confocal FRAP experiments, and the position and size of bleach ROI's used to perform FRAP in the nucleus and cytoplasm. The image is representative of COS-7 cells expressing Venus-Atg4B(C74A). Bar, 10 μm. (B) Normalized images of selected time points from a representative FRAP experiment on Atg4B(C74A) in the nucleus. The white circle shows the nominal bleach ROI. Bar, 10 μm. For visualization purposes a 1 pixel median filter was applied to the images. (C) Representative example of a fit (black line, Eq. IV.5) to the mean post-bleach profile of Venus-Atg4B(C74A) in the nucleus (gray line, $N = 30$ cells) obtained from images such as in B at $t = 0$. The bleach depth ($K = 1.09$) and effective radius ($r_e = 3.9$) parameters from the post-bleach profile fit provide an empirical estimate of the initial conditions for the diffusion equation. The normalized post-bleach fluorescence intensity was obtained as described in the Materials and Methods. (D) Representative example of the mean confocal FRAP data from Venus-Atg4B(C74A) in the nucleus (gray line, $N = 30$) fit with a theoretical FRAP curve assuming a single diffusing species (Eq. IV.6).

Table IV.1: Mobile fractions (Mf) for Venus-LC3 and Venus-Atg4B(C74A)

Protein	Cytoplasm	Nucleus
Venus	0.99 ± 0.02 (30)	0.99 ± 0.01 (30)
Venus-LC3	0.98 ± 0.01 (30)	0.99 ± 0.01 (30)
Venus-Atg4B(C74A)	0.99 ± 0.01 (30)	0.99 ± 0.01 (30)
Venus-LC3 (+ Cerulean-Atg4B(C74A))	0.99 ± 0.01 (30)	0.99 ± 0.01 (30)
Venus-Atg4B(C74A) (+ Cerulean-LC3)	1.00 ± 0.02 (20)	N/A

Values are the mean ± 95 % CI (N = #cells)

Table IV.2: Comparison of the experimentally determined apparent molecular weights to the expected molecular weights for Venus-Atg4B(C74A) and Venus-LC3.

		*Apparent MW (kDa)	
Protein	Expected MW (kDa)	Cytoplasm	Nucleus
Venus-Atg4B(C74A)	72	250 ± 80 (30)	600 ± 200 (30)
Venus-LC3	45	500 ± 100 (30)	1800 ± 600 (30)
Venus-LC3 (+ Cerulean-Atg4B(C74A))	117	400 ± 200 (30)	2500 ± 800 (30)
Venus-Atg4B(C74A) (+ Cerulean-LC3)	117	400 ± 100 (30)	N/A

Values are the mean ± 95 % CI (N = #cells). *Calculated assuming a spherical geometry

By comparison of the mean FRAP curves we found Venus-LC3 and Venus-ATG4B(C74A) both diffuse more slowly than Venus in the cytoplasm (Figure IV.5A) as well as in the nucleus (Figure IV.5B). We measured mobile fractions close to 100 % for all of these proteins on the timescale of our experiments (Table IV.1). To obtain D values, the FRAP curves for Venus, Venus-LC3, and Venus- ATG4B(C74A) were fit with a one component diffusion model (Eq. IV.6). This model fit the recovery curves effectively in both the cytoplasm (Fig. IV.5C-E) and nucleus (data not shown). The mean D from fits to Venus-LC3 and Venus-ATG4B(C74A) FRAP curves were 2.6 ± 0.3 and 2.1 ± 0.2 times smaller respectively than the mean D for Venus in both the cytoplasm and nucleus (95 % CI, $N = 30$) (Figure IV.5F).

Using the Stokes-Einstein relation ($D \propto MW^{-1/3}$, with Venus as a standard for MW)[148] we determined Venus-LC3 diffuses with an apparent molecular weight of 500 ± 100 kDa, and Venus-ATG4B(C74A) diffuses slightly faster with an apparent molecular weight of 250 ± 80 kDa in the cytoplasm assuming a spherical geometry (95 % CI, $N = 30$). In the nucleus we see a similar trend; Venus-LC3 diffuses with an apparent molecular weight of 1800 ± 600 kDa, and Venus-ATG4B(C74A) diffuses with an apparent molecular weight of 600 ± 200 kDa (95 % CI, $N = 30$). Importantly, these molecular weights are much larger than the expected molecular weights for monomeric Venus-LC3 (45 kDa) and Venus-ATG4B(C74A) (72 kDa) (Table IV.2).

The above estimates of the size of the putative complex containing ATG4B(C74A) and LC3 assume a spherical geometry. Given the crystal structure of the LC3-Atg4B complex appears roughly rod shaped[101], if we estimate a fluorescently labeled complex is ~ 22 nm long, and ~ 5 nm wide the expected diffusion coefficient is $\sim 17\,\mu m^2/s$ [207], consistent with our diffusion measurements in the cytoplasm. However, in

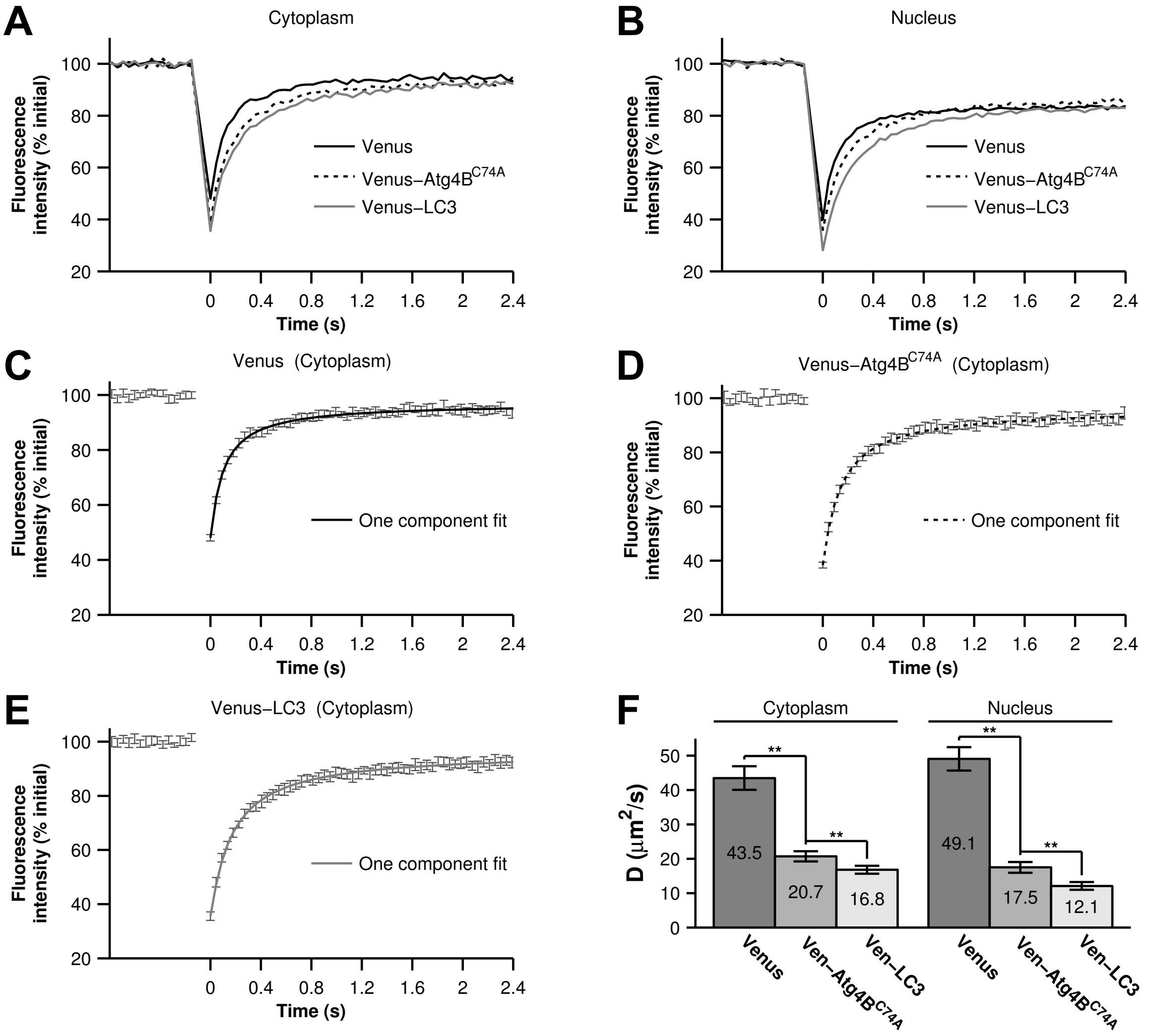

Figure IV.5: The diffusional mobilities of Venus-LC3 and Venus-Atg4B(C74A) in both the cytoplasm and nucleus are significantly slower than that of Venus as assessed by confocal FRAP. (A) Comparison of mean FRAP curves for Venus, Venus-LC3, and Venus-Atg4B(C74A) in the cytoplasm. ($N = 30$ cells from 3 independent experiments). (B) Comparison of mean FRAP curves for Venus, Venus-LC3, and Venus-Atg4B(C74A) in the nucleus. ($N = 30$ cells from 3 independent experiments). (C-E) Representative examples of fits using a one component diffusion model to the experimentally determined recovery curves for Venus (C), Venus-LC3 (D), or Venus-Atg4B(C74A) (E) in the cytoplasm (Error bars represent 95 % CI $N = 30$ cells from 3 independent experiments). (F) Diffusion coefficients for Venus, Venus-LC3, and Venus-Atg4B(C74A) in the cytoplasm and nucleus. Error bars represent 95 % CI $N = 30$ cells from 3 independent experiments.

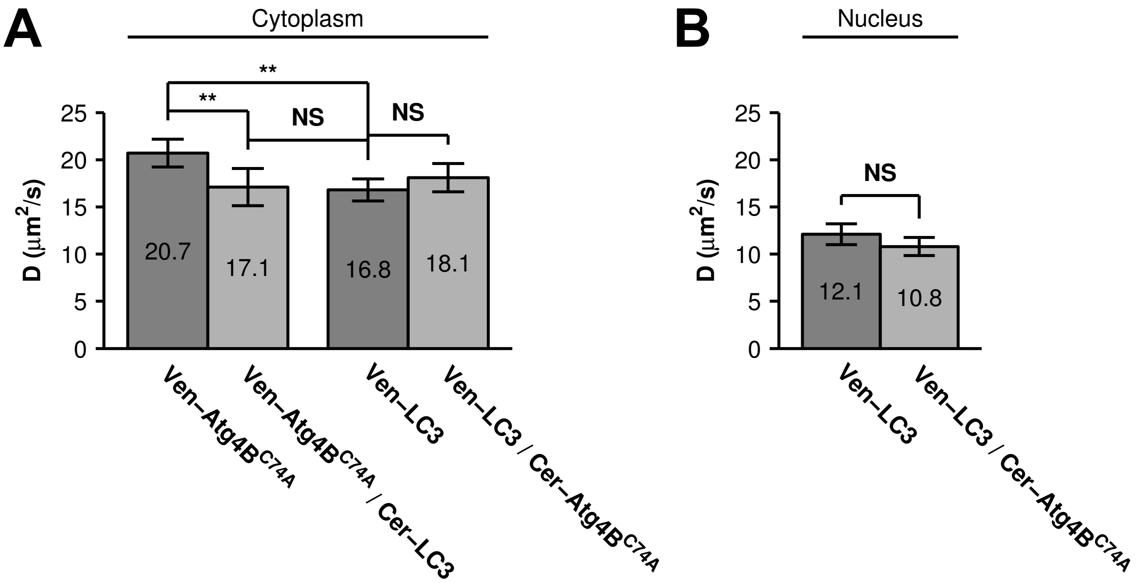

Figure IV.6: The diffusional mobility of Venus-Atg4B(C74A) is significantly slower upon co-expression with Cerulean-LC3, whereas no significant change was observed for the mobility of Venus-LC3 upon co-expression with Cerulean-Atg4B(C74A). (A) Mean diffusion coefficients for Venus-Atg4B(C74A) and Venus-Atg4B(C74A) co-expressed with Cerulean-LC3 in the cytoplasm ($N > 20$ COS-7 cells). (B) Mean diffusion coefficients for Venus-LC3 and Venus-LC3 co-expressed with Cerulean Atg4B(C74A) in the cytoplasm and nucleus. Error bars represent 95 % CI with $N = 30$ COS-7 cells.

the nucleus the measured diffusion coefficient of LC3 is significantly smaller suggesting the formation of a higher molecular weight complex or a much more anisotropic complex in this compartment.

IV.2.3 ATG4B(C74A) and LC3 co-expression slows ATG4B(C74A) diffusion as measured by confocal FRAP.

If ATG4B(C74A) and LC3 are bound to the same complex, we expect the diffusion coefficients for these proteins should be identical, and correspond to the size and shape of the complex. However, we determined D for Venus-ATG4B(C74A) is $21 \pm 1\,\mu\text{m}^2/\text{s}$ while D for Venus-LC3 is slightly slower at $17 \pm 1\,\mu\text{m}^2/\text{s}$ in the cytoplasm (95 % CI $N = 30$) (Figure IV.5F). A simple explanation for this finding is that there may be different fractions of bound and unbound forms of LC3 and ATG4B(C74A). For example, 100 % of Venus-ATG4B(C74A) may not be bound to LC3 if endogenous LC3 levels are limiting. Thus, the recoveries for Venus-ATG4B(C74A) may contain contributions from both rapidly diffusing unbound protein and slowly diffusing bound protein. If this is the case, we reasoned it may be possible to drive additional complex formation by transiently expressing additional LC3. Therefore, we next performed confocal FRAP measurements of Venus-ATG4B(C74A) in cells co-expressing additional Cerulean-LC3 (Figure IV.6). As a control, we also measured the diffusional mobility of Venus-LC3 in cells co-expressing additional Cerulean-ATG4B(C74A).

The FRAP curves for Venus-ATG4B(C74A) and Venus-LC3 in cells co-expressing either Cerulean-LC3 or Cerulean-ATG4B(C74A) respectively were, again, effectively fit by a pure diffusion model in both the cytoplasm and nucleus (data not shown). Under these conditions, essentially 100 % of the molecules were mobile on the timescale of our experiments (Table 1). The mean D for Venus-LC3 co-expressed with Cerulean-ATG4B(C74A) was identical within error to that obtained for Venus-LC3 expressed alone (Figure IV.6). This suggests excess Cerulean-ATG4B(C74A) binding to Venus-LC3 does not significantly influence the size or dynamics of the putative macromolecular complex containing Venus-LC3. In contrast, the mean D for Venus-ATG4B(C74A) in the cytoplasm of cells co-expressing Cerulean-LC3 was significantly slower at $17 \pm 2\,\mu\text{m}^2/\text{s}$ compared to cells expressing Venus-ATG4B(C74A) on its own, and is identical to that of LC3 itself (95 % CI, $N = 20$).

Using the Stokes-Einstein relation ($D \propto MW^{-1/3}$, with Venus as a standard for MW)[148], we determined the apparent molecular weight of Venus-LC3 diffusing in cells co-expressing Cerulean-ATG4B(C74A) is 400 ± 200 kDa in the cytoplasm, and 2500 ± 800 kDa in the nucleus, which is statistically identical to Venus-LC3 expressed on its own (95 % CI, $N = 30$). This is also identical to the apparent molecular weight of 400 ± 100 kDa for Venus-ATG4B(C74A) diffusing in the cytoplasm of cells co-expressing Cerulean-LC3 (95 % CI, $N = 20$) (Table IV.2). These results indicate the levels of LC3 in the cytoplasm of cells is an important determinant of the diffusional mobility of ATG4B(C74A) when LC3 concentrations are limiting, and suggests not only are LC3 and ATG4B(C74A) likely directly interacting in live cells, but they are also part of the same multi-protein complex. As discussed above, if we assume the complex has a rod shape instead of spherical, the actual MW may be smaller than estimated here.

IV.2.4 LC3 and LC3 are within FRET proximity in the nucleus, but not the cytoplasm of living cells.

The results of the above experiments suggest both LC3 and ATG4B(C74A) are part of the same multi-protein complex in cells. However, it is unclear whether these complexes contain multiple copies of LC3 or ATG4B(C74A). Furthermore, it was reported an LC3 homolog, GABARAP, forms homo-oligomers [107, 108]. Therefore, the formation of large homo-oligomers of Venus-LC3 could possibly explain LC3s slower than expected diffusional mobility. To test for the presence of homo-oligomers, as well as to test if multiple copies of LC3 may be present within the same high molecular weight complex, we performed acceptor photobleaching FRET experiments on cells co-expressing Venus-LC3 and Cerulean-LC3. We detected no significant difference between E for cells co-expressing Venus-LC3 and Cerulean-LC3 in the cytoplasm and E for negative controls ($p > 0.05$, $N = 18$) (Figure IV.7). However, we observed a small, but significant amount of energy transfer (6 ± 2 %) in the nucleus of cells expressing Venus-LC3 and Cerulean-LC3 compared to the negative control (2 ± 1 %) (95 % CI, $N = 18$) (Figure IV.7). These results suggest LC3 either

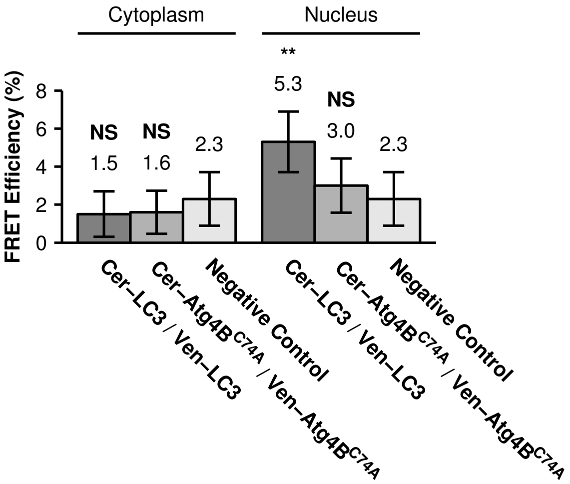

Figure IV.7: FRET occurs between donor and acceptor-labeled LC3 in the nucleus but not the cytoplasm of living cells, whereas no FRET is detected between donor and acceptor-labeled Atg4B(C74A) in either the cytoplasm or nucleus. FRET efficiency between Cerulean-LC3 and Venus-LC3, or Cerulean-Atg4B(C74A) and Venus-Atg4B(C74A) as measured using acceptor photobleaching FRET. Data are shown for measurements in both the cytoplasm and the nucleus. FRET efficiencies between the negative control Cerulean and Venus are shown for comparison. Error bars represent 95 % CI with $N \geq 18$ COS-7 cells from at least two independent experiments.

homo-oligomerizes, or more than one LC3 is in close proximity within a multi-protein complex in the nucleus, but not the cytoplasm of live cells.

IV.2.5 ATG4B(C74A) and ATG4B(C74A) are not in FRET proximity in both the cytoplasm and nucleus of living cells.

We also considered the possibility that ATG4B(C74A) forms homo-oligomers or that multiple copies of ATG4B(C74A) may be present within the same multi-protein complex. To test this, we performed acceptor photobleaching FRET experiments on cells co-expressing Venus-ATG4B(C74A) and Cerulean-ATG4B(C74A). The energy transfer efficiencies between Venus-ATG4B(C74A) and Cerulean-ATG4B(C74A) were identical within error to values obtained for the negative controls (Figure IV.7). These results demonstrate that if multiple copies of ATG4B(C74A) are present in the same multi-protein complex, they are not close enough to yield detectable FRET.

IV.3 Discussion

In the current study, we used FRET and FRAP to characterize the properties of a protein complex formed by the interaction of LC3 with a catalytically inert mutant form of Atg4B, the protease responsible for both lipidation and delipidation of LC3. Our findings reveal several novel properties of the complex formed between ATG4B(C74A) and LC3, as well as each of these molecules individually.

As a starting point for our study, we confirmed co-expression of Cerulean-ATG4B(C74A) with Venus-LC3 results in a detectable shift in the subcellular localization of LC3 as reported previously [121, 173]. In particular, upon co-expression with ATG4B(C74A), LC3 is de-enriched from the nucleus and becomes sequestered in the cytoplasm. This suggests the localization of ATG4B(C74A) is dominant over that of LC3.

Why this is the case has not been established. However, a predictive sequence analysis for nuclear export signals indicates ATG4B(C74A) contains a putative consensus leucine rich (LxxLxL) NES at residues 225-230 [208]. Thus, it is possible ATG4B(C74A) is actively exported from the nucleus, leading to the accumulation of both LC3 and ATG4B(C74A) in the cytoplasm. LC3 was also predicted to have an NES; however, this NES does not appear to be functional under steady state conditions [121]. Therefore, a functional NES on Atg4B may control the nucleocytoplasmic distribution of both Atg4B and LC3.

Our FRET measurements provide supporting evidence that LC3 and ATG4B(C74A) likely directly interact in the cytoplasm of living cells. The observation that these two proteins are in FRET proximity is in good agreement with previous biochemical evidence showing these two proteins form a stable complex [101, 173]. We also show here the interaction of LC3 and ATG4B(C74A) is not exclusively confined to the cytoplasm, where the lipidation and de-lipidation of LC3, and autophagosome formation are known to occur. Instead, they interact within the nucleus as well, indicating either LC3 or Atg4B, or both may have currently unidentified functions in the nucleus, consistent with our previous findings showing soluble LC3 itself is enriched in the nucleus relative to the cytoplasm [121].

In addition, we observed a significant increase in energy transfer efficiency when the acceptor LC3 is labeled with the acceptor as opposed to when ATG4B(C74A) is labeled with the acceptor. In our experiments, the manner in which Cerulean or Venus is attached to LC3 and Atg4B is identical. Assuming the average relative orientation of transition dipole moments in a complex between LC3 and Atg4B is the same regardless of which protein is labeled with Cerulean or Venus, the only variable in a comparison of FRET experiments where the donor and acceptors are switched is the relative amount of donor to acceptor. Based on the recent crystal structure for the interaction, it is plausible two molecules of acceptor labeled LC3 are within close proximity of a single donor labeled ATG4B(C74A) providing significantly more opportunity for energy transfer to occur [101, 178]. This suggests the ATG4B(C74A)-LC3 complex may not only occur under crystallographic conditions, but also in the native environment of live cells, and may represent an important mechanism for regulating LC3 post-translational modification. However, slight structural differences in the two different fluorescent protein labels could lead to differences in the average relative orientation of transition dipole moments when bound in the complex [179]. For this reason, brightness analysis or time-resolved fluorescence anisotropy could be used in the future to further validate a 2:1 stoichiometry for the LC3-ATG4B(C74A) complex in live cells [202, 209].

In a previous study, we found the mobility of LC3 is much slower than expected for a free monomer in the cytoplasm and nucleus consistent with that of a high molecular weight complex [121]. The actual molecular weight of this complex is currently unknown, as the relationship between D and MW is dependent on the geometry of the complex, and for anisotropic molecules D will be dominated by the longest dimension of the molecule. Since ATG4B(C74A) should bind to endogenous LC3, we speculated it may also become incorporated into a slowly diffusing complex as the result of this interaction. Here, we tested this possibility by performing quantitative FRAP experiments using a laser scanning confocal microscope. If the transport process leading to recovery of fluorescence after photobleaching is simple diffusion, quantitative analysis of a FRAP curve yields the diffusion coefficient of the diffusing species, which is related to the temperature and viscosity of the medium, as well as the size and shape of the diffusing species. To obtain quantitative estimates of the diffusion coefficients from FRAP data we utilized a recently developed analytical FRAP model applicable to laser scanning confocal microscopes (Eq. IV.6) [158]. The model is a generalized form of the classical Axelrod equation which assumed a stationary Gaussian laser profile, but takes into account diffusion which occurs before acquisition of the first image in the time series, by determining the initial conditions from the post-bleach image intensity profile (Figure IV.4B-C) [155].

Our FRAP measurements revealed the diffusion coefficient of ATG4B(C74A) expressed in live cells was much slower than expected for a freely diffusing monomer according to the Stokes-Einstein relation. Although it is difficult to distinguish a monomer from a dimer using this method, a monomer is readily discernible from a much larger or more anisotropic complex. Thus, our finding strongly suggests ATG4B(C74A) does not exist as a monomer, but rather is incorporated into a larger complex in live cells. However, we noted *D* for ATG4B(C74A) was slightly faster than *D* for LC3. We hypothesized the difference in *D* between these proteins expressed individually could be due to limiting concentrations of endogenous LC3 resulting in a larger fraction of ATG4B(C74A) unbound from the complex. To test this, we co-expressed LC3 in an attempt to drive additional complex formation, and reduce the fraction of unbound ATG4B(C74A). Interestingly, the *D* for Venus-ATG4B(C74A) in cells expressing additional LC3 became significantly slower to match that of LC3 itself. These results complement our conclusions based on the FRET data, and further suggest LC3 and Atg4B are likely directly interacting to form a complex in live cells.

As a control, we also expressed additional ATG4B(C74A) and looked for changes in *D* for Venus-LC3. Interestingly, *D* for Venus-LC3 was unchanged in cells co-expressing additional ATG4B(C74A). These results suggest there was little LC3 unbound from the complex, and that expression and binding of ATG4B(C74A) to LC3 does not interfere with the size or dynamics of the LC3 interacting complex normally slowing its diffusion. FCS could be used in future experiments to further validate these findings based on its ability to readily resolve multiple diffusing components.

Given the approximate rod shape of the complex between LC3 and Atg4BC74S as observed from a recent crystal structure[101] we examined the possibility that LC3 and ATG4B(C74A) may be diffusing as a rod shaped complex in live cells. We found our diffusion measurements for LC3 and ATG4B(C74A) were consistent with their incorporation into a complex of this size and shape in the cytoplasm, but fluorescence anisotropy measurements could potentially be used to further validate this finding. Interestingly, we observed LC3 diffuses much slower in the nucleus implying LC3 may constitutively associate with a larger or more anisotropic complex with currently unknown composition in this compartment.

Our FRAP measurements from cells expressing LC3 alone, ATG4B(C74A) alone, as well as cells co-expressing the two proteins all displayed mobile fractions $\geq 99\,\%$ in the regions of the cells where we performed our measurements. This suggests the majority of LC3 and ATG4B(C74A) does not stably associate with cellular superstructures e.g. microtubules or DNA which are essentially immobile on the time scale of our FRAP experiments. We deliberately avoided bright punctate ($\sim 0.5\,\mu$m) structures, which presumably represent autophagosome vesicles. The large vesicles are also effectively stationary on the time scale of our FRAP experiments. If these structures were selected for FRAP experiments, the mobile fractions would likely be less than $100\,\%$.

Since we found both LC3 and ATG4B(C74A) appear to diffuse as part of the same complex, this raised the possibility that the slower than expected diffusion may be the result of homo-oligomerization of LC3 or ATG4B(C74A), or that multiple copies of LC3 and ATG4B(C74A) may be contained within the same multi-protein complex. To test this possibility we performed acceptor photobleaching FRET measurements on cells co-expressing Venus and Cerulean tagged versions of LC3 and ATG4B(C74A). In the cytoplasm we found no evidence for the presence of LC3 or ATG4B(C74A) homo-oligomers. The absence of detectable FRET between LC3 and LC3, or between ATG4B(C74A) and ATG4B(C74A) implies if more than one copy of LC3 or ATG4B(C74A) is present in the same slowly diffusing complex, these molecules are positioned at distances greater than 10 nm from one another in the cytoplasm. However, due to the orientation requirements for FRET the absence of energy transfer efficiency cannot rule out the possibility of homo-oligomerization, or more than one LC3 in a complex. For example, if two LC3s are bound to Atg4B as seen in the crystal structure it is possible their N-terminal fluorescent protein labels are positioned on opposite sides of Atg4B ($r > \sim 10$nm) preventing a detectable amount of energy transfer from occurring.

Conversely, in the nucleus we observed a detectable level of energy transfer between Cerulean-LC3 and Venus-LC3 compared to negative controls. Therefore, in the nucleus, LC3 may either homo-oligomerize, or more than one LC3 molecule is present in close proximity within the same multi-protein complex. Further, this suggests the organization of LC3 within complexes in the nucleus may differ from that in the cytoplasm, bringing the proteins into sufficiently close proximity to give rise to FRET.

In summary, our data are consistent with a model in which ATG4B(C74A) and LC3 not only directly interact, but also associate with a slowly diffusing complex in both the cytoplasm and nucleus of living cells. This complex could either have a relatively high molecular weight or be elongated in shape. The identities of the components of the putative large complexes in the nucleus are not yet known, but are likely to involve other components of the conjugation machinery in the autophagy pathway. In addition, the organization of LC3 within complexes in the nucleus may be different from that in the cytoplasm, or alternatively LC3 may homo-oligomerize in the nucleus. These data also strongly suggest LC3 and Atg4B may both have currently undefined functions in the nucleus. Ultimately, these types of fundamental measurements of live cell protein diffusion and complex formation described here can be used to extend biochemical studies to the single living cell in order to better understand intracellular pathways such as autophagy.

IV.4 Materials and Methods

IV.4.1 Cell lines and constructs

COS-7 cells were obtained from ATCC (Manassas, VA) and cultured in DMEM supplemented with 10 % fetal calf serum, 1 % PenStrep, and phenol red. EGFP-LC3 and mStrawberry-Atg4B(C74A) were the gift of T. Yoshimori (Osaka University)[173]. Cerulean and Venus were the gift of D. Piston (Vanderbilt University)[204]. Cerulean and Venus tagged versions of LC3 and Atg4B(C74A) were constructed as follows: cDNA for Cerulean and Venus were inserted into Clonetech pEGFP-C1 vectors by AgeI and BsrGI double restriction digestion resulting in pCerulean-C1 and pVenus-C1 vectors. Next, we inserted LC3 and Atg4B(C74A) cDNA into the pCerulean-C1 and pVenus-C1 multiple cloning sites by BglII and EcoRI double restriction digestion.

IV.4.2 Microscope and cell preparation for live cell imaging

All FRET and FRAP microscopy experiments were carried out on a Zeiss LSM 510 confocal microscope (Carl Zeiss MicroImaging, Inc., Thornwood, NY) using an Argon/2 30 mW laser (458, 488, 514 nm), oil immersion 40X 1.3 N.A. Zeiss Plan-Neofluar objective, and 1 Airy Unit pinhole.

COS-7 cells were plated on the day before transfection in either MatTek (Ashland, MA) 35 mm No. 1.5 glass bottom culture dishes, or Lab-Tek II 4-well No. 1.5 glass bottom chamber slides (Thermo Fisher Scientific, Rochester, NY). On the following day the cells (50 %–80 % confluent monolayer) were transfected with the described mammalian expression constructs using FuGENE 6 (Roche Applied Science, Indianapolis, IN) transfection reagent according to the manufacturer's recommended protocol.

On the day of the experiment (24 hours after transfection) cell culture medium was rinsed and replaced with phenol red-free DMEM supplemented with 10 % fetal calf serum, 1 % PenStrep, and 25 mM HEPES. The cells were allowed to come to equilibrium at 37 °C $\sim$ 5 min before transferring to the temperature controlled microscope stage set to 37 °C.

IV.4.3 Acceptor photobleaching FRET data acquisition

When FRET occurs the intensity of fluorescence emission from the donor is quenched and fluorescence emission from the acceptor is stimulated. The FRET efficiency can be determined by quantifying the relative intensity of fluorescence emission from the donor in the presence and absence of the acceptor. A form of FRET microscopy known as acceptor photobleaching directly measures these quantities on a single sample by irreversibly photobleaching the acceptor. If donor and acceptor are undergoing FRET this procedure results in an increase in the intensity of fluorescence emission from the donor called dequenching [191, 203, 210]. Of the various methods available to experimentally measure FRET in single cells using fluorescence microscopy, the acceptor photobleaching method is a straightforward approach that avoids many of the technical difficulties involved in measuring FRET accurately. A limitation of acceptor photobleaching is that it only provides a single time point steady-state measurement of FRET [203].

To perform acceptor photobleaching FRET experiments the microscope was configured for time lapse imaging, and several images were collected: first, a 12 bit 512 X 512 (146 nm/pixel) image of the donor at 3X digital zoom using 0.375 mW 458 nm excitation followed by acquisition of a second image of the acceptor using 0.075 mW 514 nm excitation (pre-bleach images). Next, we bleached the acceptor from the entire cell using 30 iterations of 15 mW 514 nm excitation. Finally, we collected another set of images using the same settings as described for the pre-bleach images (post-bleach images). With these settings, ~ 3 seconds were required to acquire a single image of the donor and acceptor, and ~ 47 seconds were required to bleach the acceptor. To separate the excitation and emission wavelengths we used an HFT 458/514 dichroic, followed by an NFT 515 dichroic. In addition, a 470-500 band pass filter was positioned before the donor channel detector, and a LP 530 filter was positioned before the acceptor channel detector.

IV.4.4 Acceptor photobleaching FRET data analysis

We defined freehand ROIs outlining the cytoplasm and nucleus of each cell using ImageJ (NIH), as well as a background ROI in a similar manner for unlabeled cells. Next, we measured the mean intensity inside the ROIs for the pre-bleach images in the donor (I_{Dpre}) and acceptor channels (I_{Apre}) followed by the mean intensities inside the same ROIs for the post-bleach images in the donor (I_{Dpost}) and acceptor ($I_{A}post$) channels. The background fluorescence levels were estimated by examining the mean intensity in the background ROI from the post-bleach images in the donor channel (I_{bkgd}). In control experiments we found the background intensity from unlabeled cells was very low, and was statistically identical to the background measured in the media adjacent to the cell under the conditions of our experiments. In addition, we verified the background intensity in the donor channel was identical before and after a mock acceptor bleaching experiment, indicating no bleaching of other fluorophores in the media was occurring. Although under the conditions of our experiments the background fluorescence was identical in media and unlabeled cells, for situations where cells express lower levels of fluorescent proteins or have higher autofluorescence, the intensity measured within unlabeled cells would be a more appropriate measure of the background. The percent FRET efficiency E was calculated for each cell,

$$E = \left[\frac{\left(I_{Dpost} - I_{bkgd}\right) - \left(I_{Dpre} - I_{bkgd}\right)}{I_{Dpost} - I_{bkgd}} \right] 100 \tag{IV.3}$$

we collected data from multiple cells over several different experiments and report the mean E ±95 % confidence interval for the total number of cells. To ensure significant bleaching of the acceptor we verified,

$$\left(\frac{I_{Apost} - I_{bkgd}}{I_{Apre} - I_{bkgd}} \right) 100 < 5\,\% \tag{IV.4}$$

IV.4.5 Confocal FRAP data acquisition

The microscope was configured for time-lapse imaging of a 12-bit 512 X 90 pixel (110 nm/pixel) imaging ROI at 4X digital zoom. We defined a circular bleaching ROI (9 pixel radius, 0.99 µm) centered at pixel (x = 256, y = 45) within the imaging ROI. Imaging was performed using 0.15 mW 514 nm excitation, and bleaching was performed by scanning 10 iterations of 30 mW 514 nm excitation throughout the bleaching ROI. We utilized bi-directional rastering, and maximized the scan speed of our microscope. Under these conditions, 45.1 msec were required to acquire a single image, and 150.1 msec were required to bleach the circular ROI and acquire the next image. We collected 20 pre-bleach images followed by 280 post-bleach images to monitor recovery after the bleach.

IV.4.6 Quantitative FRAP data analysis

In this study we analyzed the diffusion of fast moving proteins such as soluble Venus which have been a challenge to quantitatively measure in cells by confocal FRAP [121, 148, 157, 158]. Under our experimental conditions a significant amount of diffusion occurred during the time it took to perform the bleach step (0.1501 sec). In order to quantitatively analyze the FRAP curve to obtain D, the initial conditions to solve the diffusion equation in the derivation of the FRAP model must be empirically determined from the intensity profile of the image collected immediately after photobleaching (post-bleach profile)[155],

$$I(x;t=0) = I_0 \exp\left[-K \exp - \left(\frac{2x^2}{r_e^2} \right) \right] \tag{IV.5}$$

where $I_0 = 1$ for a normalized post-bleach profile, K is a bleaching parameter, x is the radial displacement from the center of the bleaching ROI, and r_e is the effective radius. K and r_e reflect the diffusion that occurs in the time it takes to bleach and acquire the post-bleach image.

In a previous study, we collected line profiles from the post-bleach image and averaged them for multiple cells to obtain the mean r_e [121]. This was necessary because line profiles are inherently noisy. Here, we determined r_e on a cell-by-cell basis by increasing the signal to noise of the experimentally determined post-bleach profiles as follows. First, we normalized the image acquired immediately after bleaching a circular bleach ROI (post-bleach image) to the mean of 10 images acquired immediately prior to the post-bleach image (pre-bleach images). Next, we calculated the radial displacement for each pixel in the image from the center of the circular bleach ROI (x = 28.16 µm, y = 4.95 µm). The symmetry of a circular bleach ROI allows us to reduce the dimensions of the post-bleach profile by plotting the intensity of a pixel in the normalized post-bleach image vs. its radial displacement from the center of the circular bleaching ROI, $I(x;t=0)$.

To calculate D, we utilized a series representation of a closed-form analytical FRAP equation describing free diffusion of unbleached molecules into a circular bleach ROI which is applicable to data obtained on a laser scanning confocal microscope[158],

$$I(t) = I_0\left(\sum_{m=0}^{m=200}\frac{-K^m r_e^2}{m![r_e^2+m(8Dt+r_n^2)]}\right)Mf+(1-Mf)I(0) \tag{IV.6}$$

where $I_0 = 1$ for a normalized FRAP curve, t is time, D is the diffusion coefficient, and Mf is the mobile fraction. This equation is a modified form of the Axelrod equation[140] where a Gaussian laser profile, and an approximation for the diffusion of molecules that occurred before acquisition of the post-bleach image is taken into account by incorporation of K and r_e parameters from the post-bleach profile [158]. To obtain a good match between K from the post-bleach profile, and K from the FRAP data we numerically evaluated K using Eq. IV.6 at $t = 0$.

To obtain an experimental FRAP curve we measured the mean intensity inside the circular bleaching ROI ($rn = 0.99$ µm) at the location defined during data acquisition for each image in the time-lapse data set $I(t)$. Next, we normalized $I(t)$ by the mean of $I(t)$ for ten pre-bleach images.

Under our experimental conditions, there was a small amount of unintentional photobleaching that occurred throughout FRAP data acquisition. We verified this decay could be approximated by a first order exponential rate equation,

$$I(t) = \exp(-k_{decay}t) \tag{IV.7}$$

where k_{decay} is the first order rate constant for the decay. To correct the experimental curves we acquired time-lapse data significantly longer than required for complete recovery after photobleaching, and used $I(t)$

at these later time points to estimate k_{decay} [157]. The corrected FRAP curve is then,

$$I_{corr}(t) = \frac{I(t)}{I_{decay}(t)} \tag{IV.8}$$

By fitting the corrected data to equation IV.6 we obtain the parameters D and Mf. However, because a significant fraction of fluorophores are irreversibly lost as the result of the photobleaching event, Mf is underestimated by this approach. To determine the true fraction of immobile fluorophores on the time scale of our FRAP experiments, we calculated the difference between $I(t)$ and the mean intensity inside an adjacent circular ROI, $I_{adjacent}(t)$, at time points after the recovery was complete [206].

IV.4.7 Other data analysis

Image analysis was performed using ImageJ (NIH), and non-linear least squares analysis was performed using custom routines written in MATLAB (MathWorks; Natick, MA). All scatter plots and bar graphs were created using MATLAB and Adobe Illustrator (Adobe Systems Incorporated; San Jose, CA).

IV.5 Acknowledgments

We sincerely thank M Kang for assistance with FRAP data analysis, and J Greer for technical assistance with cloning. We also thank the other members of the Kenworthy lab for helpful discussions about the project. We thank S Vogel for providing the FRET standards, T Yoshimori for providing the EGFP-LC3 and mStrawberry-ATG4B(C74A) constructs, and D Piston for providing the Cerulean and Venus constructs. Supported by R01 GM073846, 3R01 GM73846-4S1, and NSF/DMS 0970008. The funding sources had no role in the study design, collection, analysis or interpretation of data, writing the report, or the decision to submit the paper for publication.

CHAPTER V

Fluorescence-based assays to probe for LC3 interacting proteins in living cells

Multiple proteins interact with LC3 to assist with its roles in cargo selection and autophagosome assembly. Most LC3 interacting proteins have been identified using biochemical approaches. In Chapter IV we described how FRET and FRAP can be used to gain insights into the nature of LC3 associated complexes in living cells. In this chapter, we describe how an additional fluorescence microscopy assay based on quantifying LC3's nucleocytoplasmic (N/C) ratio, together with FRET and FRAP, can be used to detect the interaction of specific proteins with LC3 in living cells. To validate these methods, we monitored the interaction of LC3B and p62/sequestosome1 (SQSTM1), a well-known LC3 interacting protein involved in selective autophagy. We verified the specificity of these techniques by demonstrating that interactions of SQSTM1 with LC3B were inhibited by F52A and L53A mutations of LC3Bs hydrophobic protein binding interface as reported by all three methods. Importantly, these assays take advantage of widely available technologies and offer a complementary approach to existing methods to detect protein interactions with LC3. They can also be readily adapted to characterize other protein complexes in the autophagy pathway, as illustrated here through the analysis of soluble SQSTM1 homo-oligomers.

V.1 Introduction

Autophagy is a major degradation pathway whereby cytoplasmic contents are sequestered for degradation via the lysosome [5]. A conserved pathway in eukaryotes, autophagy is vitally important for normal health, development, and the prevention of disease [211]. Upregulation of autophagy leads to the formation of a double membrane vesicular intermediate known as an autophagosome that is responsible for engulfing regions of cytoplasm. The outer membrane of the autophagosome subsequently fuses with the lysosome thereby degrading its inner membrane and contents [5]. Autophagy can occur either with or without substrate specificity, termed selective or macroautophagy, respectively. In selective autophagy, a ligand - usually ubiquitin - is conjugated to specific substrates such as protein aggregates. Next, receptors and adaptors bind to the ubiquitinated substrate, and target it to autophagosome associated ATG8 proteins [32, 38, 69]. The autophagosome is subsequently trafficked to the lysosome for degradation and recycling of its contents.

Members of the ATG8 protein family are central to the autophagy pathway and are best known for their role in autophagosome formation [80]. Human ATG8 proteins consist of three subfamilies, MAP1LC3

This manuscript was prepared for publication in *Autophagy*.

(LC3), GABARAP, and GATE-16. The LC3 subfamily encompasses four genes, MAP1LC3A, MAP1LC3B, MAP1LC3B2, and MAP1LC3C [79]. Among these genes the most widely studied is Microtubule Associated Protein 1 Light Chain 3B (hereafter referred to as LC3B). The known functions of LC3 include contributions to autophagosome membrane expansion and fusion, and selective recruitment of cargo to the autophagosome [38]. LC3 is known to exist in at least two forms, a soluble form known as LC3-I, as well as lipid modified LC3-II [90, 91]. LC3-II consists of phosphatidylethanolamine covalently attached to a glycine residue on the C-terminus of LC3. The process of LC3 lipid modification is carried out through a series of enzymatic reactions resembling ubiquitination, and since LC3 itself is structurally similar to ubiquitin it has been dubbed an ubiquitin-like protein [79]. Soluble LC3 is found in the nucleoplasm as well as in the cytoplasm, and undergoes slow exchange between the two compartments by an unknown mechanism [121].

Consistent with their central role in the autophagy pathway, LC3 and other ATG8 family members interact with a large network of over 65 different proteins with extensive overlap among ATG8 family members [9]. Many of these interactions are mediated by a consensus LC3 interacting region (LIR) in the interacting proteins [212]. SQSTM1/p62 (sequestosome1) is one of the best characterized examples of an LC3-interacting protein [67, 213]. A homo-oligomer, SQSTM1 functions as a cargo receptor and together with ubiquitin and LC3 plays an important role in selective autophagy [32, 214]. The interactions of SQSTM1 and LC3 have been studied extensively using a combination of co-immunoprecipitation, pull down assays, structural analysis, mass spectrometry, and colocalization approaches [9, 67, 68, 100, 129, 130, 215]. The results of these studies have revealed that SQSTM1 interacts with LC3 via its LIR domain [68, 100, 129]. Interactions of SQSTM1 with LC3 are mediated by LC3s N-terminal domain as well as residues F52, L53, and R70 [9, 129, 214]. The interaction of SQSTM1 with LC3 does not depend on lipidation of LC3, as a G120A mutant of LC3 coimmunoprecipitates with it [100]. However, SQSTM1 binding to LC3 alone is not sufficient to target SQSTM1 for degradation by autophagy [129].

In parallel to biochemical approaches to study protein-protein interactions, in recent years a number of fluorescence-based approaches have emerged that enable the detection of protein complex formation in the context of living cells [188, 216–219]. One good example is Förster resonance energy transfer, or FRET [136, 178, 220, 221]. FRET is a photophysical process that occurs between a donor and acceptor fluorophore when they are brought into sufficiently close distances, typically $< 10\,\mathrm{nm}$ to each other. Because of its distinct distance dependence, FRET can be used to monitor the interactions of appropriately fluorescently labeled proteins. The distance over which FRET occurs between a specific donor and acceptor is defined with respect the to the Förster distance R_0. R_0 is a function of the average relative dipole-dipole orientation, the refractive index, and the photophysical properties of the donor and acceptor fluorophores. FRET occurs between a number of fluorescent protein pairs typically used to study protein localization in live cells, including Cerulean and Venus [136]. In FRET studies, Cerulean serves as the donor and Venus functions as the acceptor. For this FRET pair, R_0 is 5.4 nm [137].

The efficiency of energy transfer E between the donor and acceptor is a function of R_0 and r, the distance between the donor and acceptor. The functional relationship between E, r, and R_0 is given by

$$E = \frac{1}{1 + (r/R_0)^6} \tag{V.1}$$

Thus, when r = 5.4 nm, E will be 50 % for the Cerulean and Venus pair, and when $r > 10\,\text{nm}$, E will drop to $\sim 0\,\%$. Importantly, FRET can be directly measured using fluorescence microscopy using a number of methods, including sensitized acceptor fluorescence, acceptor photobleaching, fluorescence lifetime imaging, and anisotropy [203, 222–228]. Despite the power of FRET to detect protein-protein interactions, this method and related approaches have not yet gained widespread use in the autophagy field and to our knowledge have only been applied in a handful of studies [124, 153, 164, 165].

A second class of biophysical approaches that can be used to study protein-protein interactions relies on measurements of the diffusion of fluorescently labeled proteins. These include Fluorescence Recovery after Photobleaching (FRAP), photoactivation/photoconversion, fluorescence correlation spectroscopy (FCS), and single particle tracking [132, 218, 229–231]. Of these methods, FRAP is the most easily implemented, as it can be readily performed using confocal microscopes [148, 155, 158, 164, 165, 171, 175, 197, 232–234]. These approaches take advantage of the fact that molecules undergo constant motion in the form of Brownian diffusion. Diffusion is typically characterized in terms of a diffusion coefficient D, which provides a measure of the mean squared displacement of a diffusing particle per unit time. Importantly, for soluble proteins, the diffusion coefficient is related to the size of the diffusing species according to the Stokes-Einstein relation:

$$D = \frac{k_B T}{6\pi\eta r} \tag{V.2}$$

Here, the diffusion constant D is directly related to the absolute temperature T, and inversely related to the viscosity η and the hydrodynamic radius of the diffusing species r. k_B is Boltzmann's constant. Thus, measurements of D can be used provide an estimate of the size of soluble, freely diffusion proteins. Transient binding of proteins to immobile structures such as DNA will slow their diffusion [148, 206, 235]. When freely diffusing soluble proteins interact to form a complex, D can also decrease. Conversely, D for a multi-component complex will increase upon breakdown of the complex. In these cases, the magnitude of the change in D will depend on the differences in the hydrodynamic radius of the protein in the unbound state and that of the bound complex according to equation V.2 [165].

Using diffusion-based measurements, we previously showed that soluble LC3B diffuses slower than expected for a monomer [121]. We subsequently determined the slower than expected diffusion was the result of LC3 constitutively associating with complexes with an effective molecular weight of about 500 kDa in the cytoplasm of living cells and in cytoplasmic extracts by FCS [164]. Furthermore, we found that the size of these complexes is modulated by disruption of residues known to be important for LC3 to bind to other proteins [164]. However, the full potential of FRAP and related approaches to monitor the interactions of specific proteins with LC3 in the cellular environment has yet to be tested.

In the current study, we demonstrate how a combination of FRET, FRAP, and LC3 localization measurements can be used to monitor the specific interactions of proteins with LC3 in living cells. To validate these approaches, we studied the interaction of Cerulean-SQSTM1 with Venus-LC3B. We show that all three assays are capable of detecting interactions of overexpressed SQSTM1 and LC3, and verify the specificity of these interactions using LC3 mutants with decreased ability to bind LC3. Finally, we illustrate the broader applicability of these approaches to study protein complexes in the autophagy pathway by characterizing the properties of soluble SQSTM1-associated homo-oligomers.

V.2 Results

V.2.1 Proteins examined in this study

As a model system, we studied the interaction of fluorescent protein-tagged versions of SQSTM1 and LC3 in HeLa cells. To test for the specificity of binding, we utilized several mutant forms of LC3. These included a G120A mutant, which is unable to be properly lipidated [106]; R70A, a mutant that exhibits decreased binding to a subset of LC3-interacting proteins [9]; and F52A and L53A, another mutant that undergoes decreased binding to a subset of LC3-interacting proteins [9]. Previous studies have indicated that the LC3 mutants G120A and R70A mutants are capable of binding to SQSTM1, while the F52A and L53A shows greatly reduced binding [9, 69, 100, 129].

When transiently expressed in HeLa cells, both wild type and the mutant forms of Venus-LC3 were found in soluble forms in the cytoplasm and nucleus (Figure V.1A). Venus-LC3 was also found in perinuclear puncta. Fewer puncta were observed for the R70A mutant and G120A mutant, and very few puncta were seen for F52A and L53A (Figure V.1C). In comparison, transiently expressed Venus-SQSTM1 was primarily found in a soluble form in the cytoplasm. This is consistent with previous studies in HeLa cells reporting that under basal conditions less than 5 % of the cells have SQSTM1 inclusions [68], and its steady-state cytoplasmic localization is maintained by active nuclear export [236].

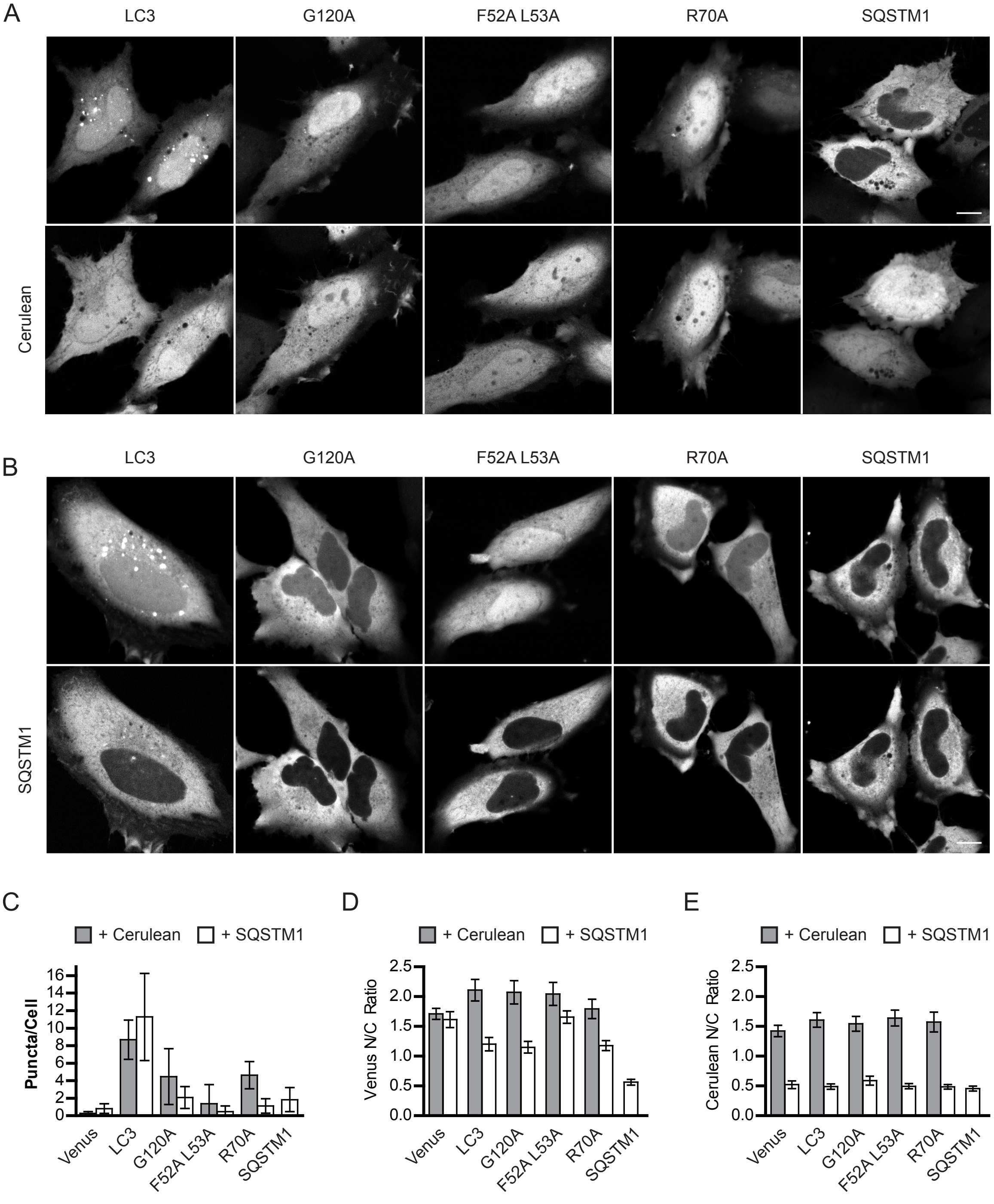

Figure V.1: The nucleo-cytoplasmic ratio of soluble LC3 is decreased in the presence of overexpressed SQSTM1. Representative confocal images of the localization of Venus-LC3, Venus-LC3(G120A), Venus-LC3(F52A and L53A), Venus-LC3(R70A), and Venus-SQSTM1 when transiently co-expressed with (A) Cerulean or (B) Cerulean-SQSTM1 in HeLa cells. Scale bars, 10 µm. An automated analysis routine was used to quantify (C) the numbers of puncta/cell and (D) the N/C ratio of the puncta independent Venus signals in cells coexpressing the indicated Venus-tagged constructs in combination with either Cerulean (gray boxes) or Cerulean-SQSTM1 (white boxes.) (E) N/C ratio of the puncta independent Cerulean signals from cells coexpressing the indicated Cerulean-tagged constructs in combination with either Venus or Venus-SQSTM1. In C-E, bars are the mean ± 95 % confidence interval; N=20 cells from 2 independent experiments.

V.2.2 The nucleocytoplasmic ratio of autophagosome independent LC3 is decreased in the presence of overexpressed SQSTM1

Previous studies have noted that the soluble LC3 is shifted out of the nucleus when co-expressed with ATG4B [165, 173]. This suggests the putative nuclear export signal on ATG4B dominates the nucleocytoplasmic distribution of LC3 when the two proteins form a complex. We thus sought to determine whether this could be used as a general method to quantify interactions of proteins with LC3.

To test this, we co-expressed Venus-LC3 or its mutants with Cerulean-SQSTM1. As a control, cells were instead co-transfected with Cerulean. Co-expression of SQSTM1 and Venus-LC3 proteins led to a dramatic shift in soluble Venus-LC3 out of the nucleus into the cytoplasm (Figure V.1). We used an automated image analysis routine to quantify this effect across multiple cells in terms of a nucleo-cytoplasmic ratio (N/C ratio in Figure V.1D). The Venus LC3 G120A mutant showed a similar decrease in N/C ratio, as did the R70A mutant. Co-expression of SQSTM1 with a Venus-LC3(F52A L53A) mutant also led to a significant decrease in the N/C ratio ($p \leq 0.003$; t-test). However, the magnitude of this decrease was much smaller than that seen for either wild type LC3 or the other mutants. These findings are consistent with previous reports that the F52A L53A mutant has a significantly decreased ability to bind to SQSTM1.

Because a significant fraction of LC3 is typically found in the nucleus, we wondered whether this nuclear pool of LC3 might be able to recruit SQSTM1. To address this question we measured the N/C ratio for SQSTM1 in these experiments. The N/C ratio of Cerulean-SQSTM1 remained essentially unchanged under all conditions examined (Figure V.1E). These findings suggest that under steady state conditions, the active nuclear export signal present in SQSTM1 will dominate the localization of LC3 when co-expression induces their interaction, similar to the effect of binding of ATG4B(C74A) to LC3.

V.2.3 FRET reports on the close physical proximity of SQSTM1 and LC3

Direct protein-protein interactions bring proteins within close physical proximity of one another and thus can be monitored using FRET [136, 178, 220, 228]. To measure FRET between Cerulean and Venus-tagged versions of LC3 and SQSTM1, we used acceptor photobleaching, a well-characterized method to quantify energy transfer by fluorescence microscopy [153, 165, 186, 203, 210, 237, 238]. This approach takes advantage of the fact that when energy transfer occurs, the fluorescence of the donor is quenched. Thus, fluorescence of the donor is higher in the absence of the acceptor than in its presence. This change in donor intensity can be measured experimentally on a single sample by photobleaching the acceptor.

An example of an acceptor photobleaching FRET experiment is shown in Figure V.2. In this approach, cells are cotransfected with donor and acceptor-labeled proteins. Images are collected of the donor and acceptor-labeled proteins before bleaching the acceptor. The acceptor fluorophore is then photobleached

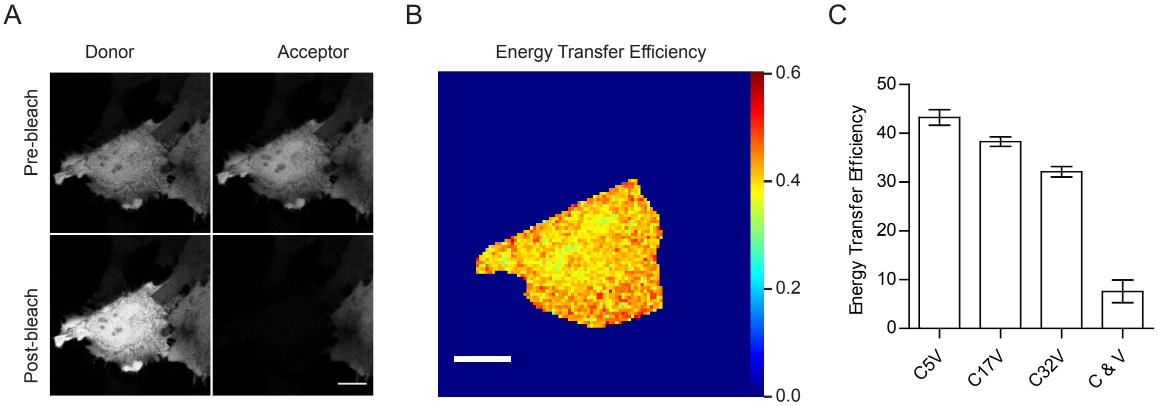

Figure V.2: Principles of acceptor photobleaching FRET experiment and positive and negative controls. HeLa cells were transfected with either positive FRET controls (C5V, C17V, C32V) or a negative FRET control (soluble Cerulean and Venus) and imaged using an acceptor photobleaching assay. (A) Representative donor and acceptor images before and after acceptor photobleaching from a FRET experiment on C5V. Scale bars, 10 µm. (B) Representative energy transfer efficiency image calculated from the images in (A). (C) Quantitation of the mean cytosolic FRET signals across multiple cells. N=20 cells from 2 indpendent experiments. Bars are the mean ± 95 % confidence intervals.

to near background levels by repetitively imaging it using high laser excitation intensity. Another set of images of the donor and acceptor labeled proteins are collected, using identical settings as the first pair of images (Figure V.2). The energy transfer efficiency E can then be calculated using the background-corrected fluorescence intensity of the donor fluorescence before D_{pre} and after photobleaching the acceptor D_{post} according to the following equation:

$$E = \frac{D_{post} - D_{pre}}{D_{post}} \tag{V.3}$$

This calculation can be performed either using mean fluorescence values obtained from regions of interest on the donor pre- and post-bleach images, or alternatively, energy transfer efficiency images can be calculated to yield spatially resolved FRET maps within the cell (Figure V.2B). In what follows, we report FRET efficiencies that are averaged over the whole cell unless otherwise noted.

To optimize conditions for our FRET experiments we first carried out control experiments. As a negative control, we co-expressed mCerulean and mVenus. Because these two proteins are monomeric they should not specifically interact, and at moderate concentrations, FRET between them should be minimal. Thus, FRET measurements between Cerulean and Venus can be used to define how much E is detected in the absence of specific FRET, and also to determine the level of noise inherent in the measurements. Acceptor photobleaching measurements of mCerulean and mVenus-coexpressing samples yielded E of 8 ± 1 % under the conditions of our experiments (Figure V.2C). As a positive control, we expressed constructs that exhibit intra-molecular FRET. These constructs consists of Cerulean and Venus separated by variable length linkers of amino acids [205]. E of $43 \pm 1\,\%$ was measured for C5V, $38 \pm 1\,\%$ for C17V, and $31 \pm 2\,\%$ for C32V was measured in HeLa cells (Figure V.2C).

Since SQSTM1 is known to homo-oligomerize [239, 240] we next asked if measurable FRET occurred between mCerulean-SQSTM1 and mVenus-SQSTM1 (Figure V.3F). FRET of $13 \pm 1\,\%$ was observed under these conditions, verifying that the method is capable of detecting homo-oligomers as expected. In contrast, when SQSTM1 was co-expressed with mCerulean, FRET levels were comparable to background measurements between Cerulean and Venus (Figure V.3F).

Next, we measured FRET between SQSTM1 and LC3 (Figure V.3). Co-expression of either wild type Venus-LC3 or Venus-LC3(G120A) with Cerulean-SQSTM1 gave rise to substantial FRET, E $13 \pm 1\,\%$ and $14 \pm 1\,\%$ respectively (Figure V.3C). A similar level of FRET was also detected between Cerulean-SQSTM1 and Venus-LC3(R70A), indicative of their close interaction ($12 \pm 1\,\%$. However, E measured between SQSTM1 and the Venus-LC3(F52A and L53A) mutant was near background levels at $7 \pm 1\,\%$. Similar results were obtained between mCerulean-tagged LC3 constructs and mVenus-SQSTM (Figure V.3D). These results confirm that as expected, SQSTM1 and LC3 are within close proximity of one another. It also verifies that this interaction does not require LC3's lipid modification with PE or residue R70, but does depend importantly on residues F52 and L53.

V.2.4 LC3's rate of diffusion changes when co-expressed with SQSTM1

We next asked whether binding of SQSTM1 to LC3 leads to a change in the size of LC3-associated protein complexes. Because SQSTM1 is a homo-oligomer and binds to polyubiquitinated proteins, it would be predicted to form a complex with LC3 that has a much larger hydrodynamic radius than that of unbound LC3. To address this question we took advantage of a quantitative confocal FRAP-based assay directed at the puncta independent pool of the proteins. In this assay we use a small circular 1 µm radius bleach region placed in a relatively homogeneous region of the cytoplasm as to avoid any bright puncta (Figure V.4A).

The exact size of the SQSTM1 complexes with which LC3 associates is not clear, as SQSTM1 is capable of interacting with a number of proteins as well as ubiquitinated substrates. However, by size exclusion chromatography, endogenous SQSTM1 runs as a heterogeneous series of complexes in the range of 0.4 MDa–5 MDa [241] suggesting they should be slowly diffusing. Thus, as a starting point for these experiments, we performed FRAP measurements of soluble Venus-SQSTM1 in the cytoplasm. As an internal control, we measured D for cytoplasmic Venus. In these experiments, Venus should diffuse as an inert protein with an expected MW of ~ 27 kDa. We obtained a D of $35 \pm 3\,\mu\text{m}^2/\text{s}$ for Venus, a result consistent with previous measurements [164]. Mf was near 100 % for Venus, as expected based on its ability to freely diffuse (Table V.1).

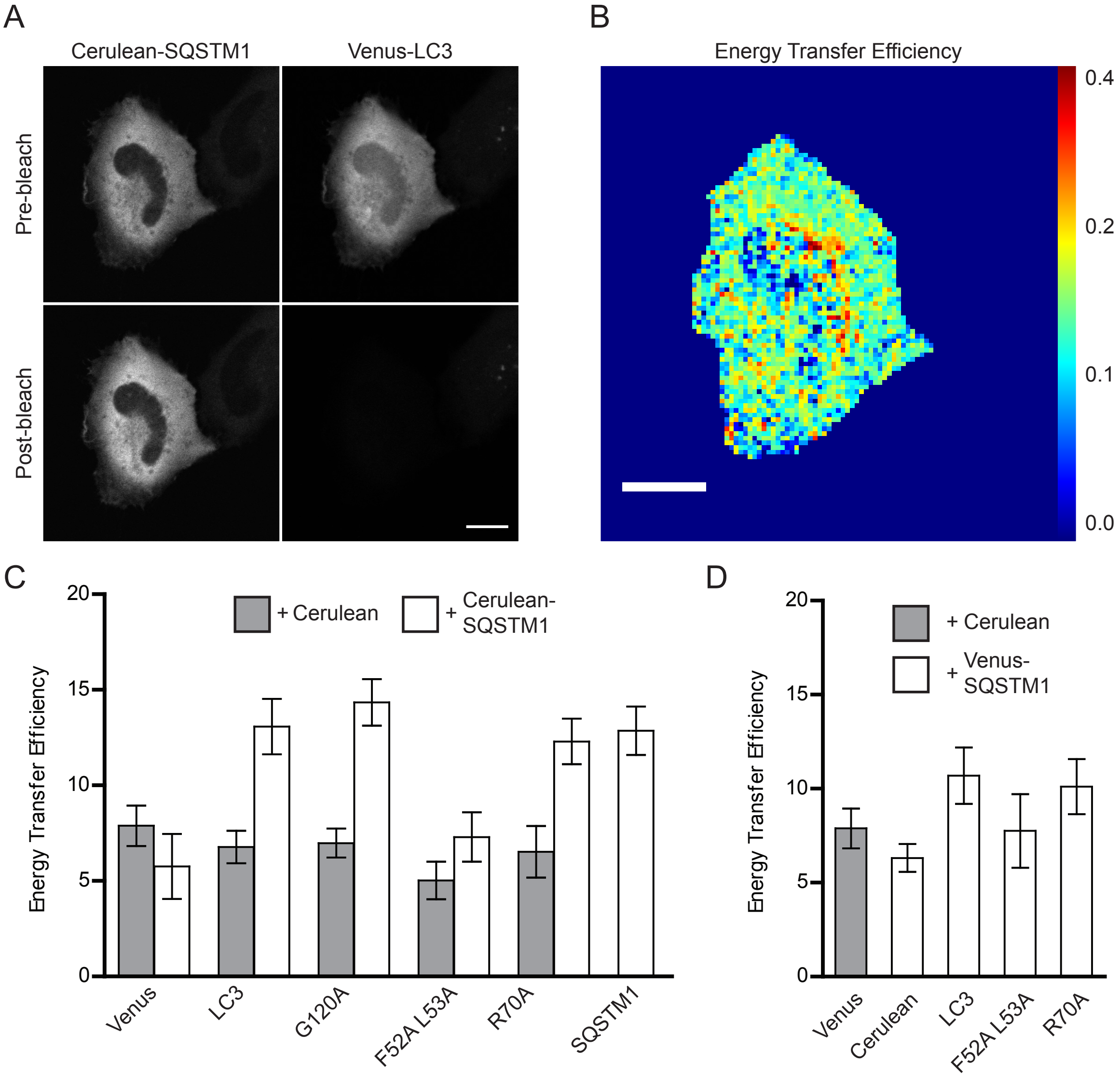

Figure V.3: FRET reports on the close physical proximity of SQSTM1 and LC3. (A) Representative donor and acceptor images from a FRET experiments on cells coexpressing Cerulean-SQSTM1 and Venus-LC3. Scale bars, 10 µm. (B) Representative energy transfer efficiency image from the images in (A). (C) FRET analysis was performed on cells coexpressing the indicated Venus-tagged constructs with either Cerulean or Cerulean-SQSTM1 and automatically analyzed across multiple cells. (D) FRET analysis was performed on cells coexpressing the indicated Cerulean-tagged constructs coexpressed with either Venus or Venus-SQSTM1. In panels C and D, bars show the mean ± 95 % confidence intervals; $N > 20$ cells from at least 2 independent experiments.

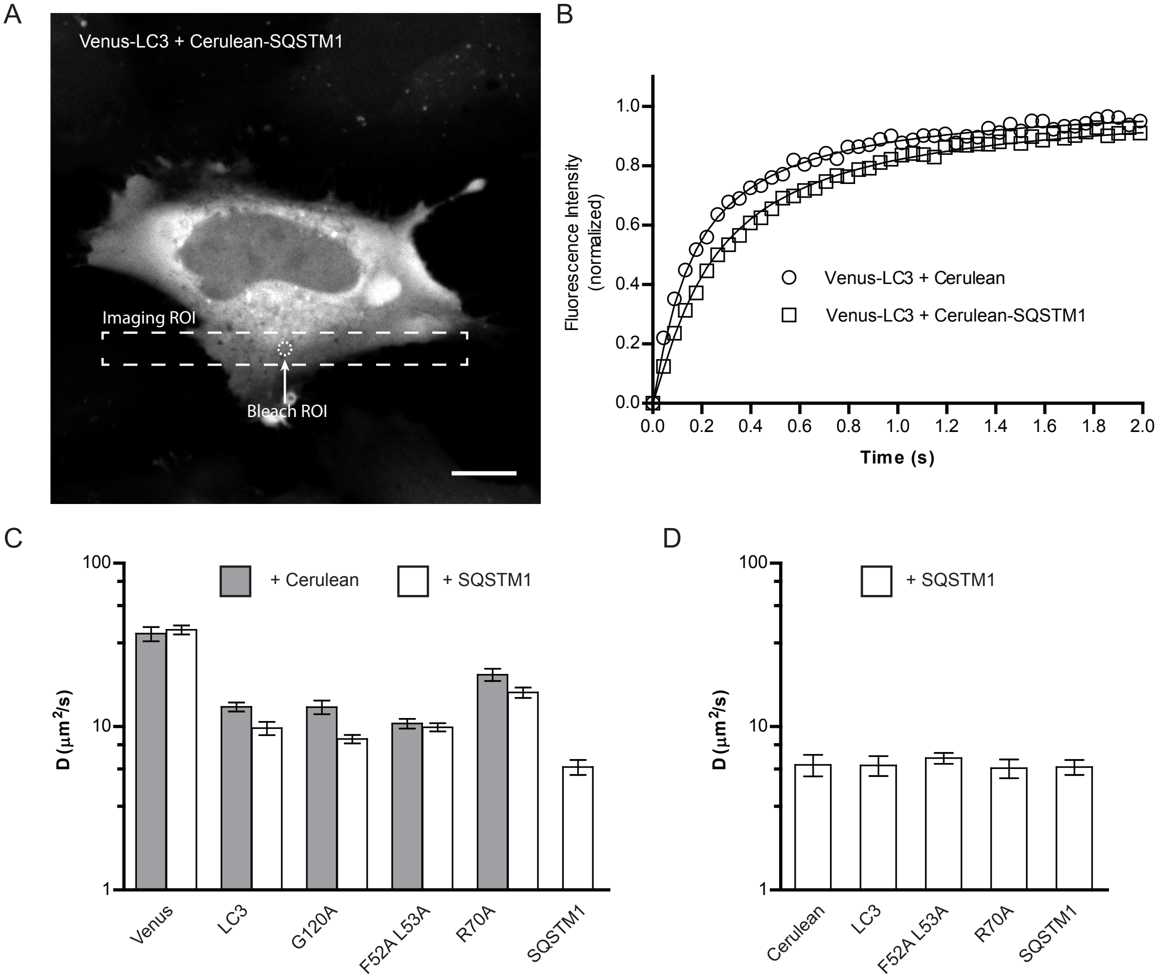

Figure V.4: LC3's rate of diffusion changes when co-expressed with SQSTM1. (A) A quantitative FRAP assay was carried out on cells coexpressing various Venus- and Cerulean-tagged constructs using a rectangular imaging ROI centered on the cytoplasm, and small circular bleach region (r_n=1 μm) placed in a region devoid of puncta. Scale bar is 10 μm (B) Examples of the averaged recoveries of Venus-LC3 coexpressed with Cerulean (circles) or with Cerulean-SQSTM1 (squares). The solid lines are fits to a single component diffusion model. (C) *D* values for Venus, Venus-LC3, Venus-LC3(G120A), Venus-LC3(F52A L53A), Venus-LC3(R70A), or Venus-SQSTM1 either coexpressed with Cerulean or Cerulean-SQSTM1. (D) *D* values for Venus-SQSTM1 coexpressed with Cerulean, Cerulean-LC3, Cerulean-LC3(F52A L53A), Cerulean-LC3(R70A), or Cerulean-SQSTM1. In C and D, bars show the mean ± 95 % confidence intervals; $N > 20$ cells from at least 2 independent experiments.

Next, we performed FRAP measurements for SQSTM1. The recovery for Venus-SQSTM1 was substantially slower than Venus with $D = 6 \pm 1\,\mu\text{m}^2/\text{s}$ ($p \leq 0.003$). We found that SQSTM1 was also 100 % mobile (Table V.1). Puncta-indpendent SQSTM1's diffusion is far slower than what we previously measured for Venus-LC3 [164]. Assuming a spherical geometry, this would correspond to a complex with an apparent size of ~ 6 MDa (Table V.1).

We next measured the diffusional mobility of Venus-LC3 and Venus-LC3 mutants in the presence of Cerulean in order to document inherent differences in the sizes of LC3-associated protein complexes. The results of these experiments revealed differences in the diffusional mobility of the different mutants, consistent with those recently reported [164]. Assuming spherical complexes, LC3 and G120A were both ~ 500 kDa, while R70A was much smaller at ~ 130 kDa, and F52A and L53A was larger at ~ 1000 kDa (Table V.1).

Given the large size of Venus-SQSTM1-containing complexes detected by the FRAP measurements, we hypothesized that the interaction of overexpressed Cerulean-SQSTM1 with Venus-LC3 would lead to the formation of a larger complex that diffused more slowly than LC3 itself. We further hypothesized that such changes should only be observed for LC3 mutants capable of binding to SQSTM1. FRAP measurements in cells coexpressing the two proteins confirmed this is indeed the case (Figure V.4. D for wild type Venus-LC3, G120A, and R70A were all significantly decreased in the presence of overexpressed Cerulean-SQSTM1 compared to cells co-expressing Cerulean (Figure V.4C $p \leq 0.003$). This is in good agreement with the results of the N/C measurements and FRET measurements, which also reported similar interactions between SQSTM1 and either wild type LC3, G120A, or R70A. On the other hand, the diffusional mobility of the F52A and L53A mutant was unchanged in the presence of overexpressed SQSTM1 (Figure V.4C $p > 0.003$). This also is consistent with findings from the N/C ratio and FRET assays. Assuming spherical geometries, we estimated the size of each of the Venus-LC3/Cerulean-SQSTM1-associated complexes using the Stokes-Einstein relation, as summarized in Table V.1.

In principle, the effective size of the SQSTM1 complexes may also change upon co-expression of SQSTM1 and LC3. To test this, we performed experiments in which we measured the diffusional mobility of Venus-SQSTM1 in the presence of overexpressed Cerulean-LC3 constructs (Figure V.4D). Surprisingly, no change in the diffusional mobility of Venus-SQSTM1 was observed upon co-expression with any of the Cerulean-LC3 constructs ($p > 0.003$). However, the diffusion of SQSTM1 suggests it is already associated with very large complexes (~ 6 MDa) when expressed individually, and therefore the binding of LC3 to the SQSTM1-associated complexes may result in too small of a change in the hydrodynamic radius of SQSTM1 to be detected using this approach.

Table V.1: Predicted molecular weights and mobile fractions for Venus, Venus-LC3, and Venus-LC3 mutants coexpressing either Cerulean or Cerulean-SQSTM1 based on the FRAP diffusion measurements in live HeLa cells under basal conditions.

Construct	Monomer MW (kDa)	ξ Predicted MW (kDa)	Mobile Fraction (%)
Venus + Cerulean	27	N/A	100 ± 1 (35)
Venus-LC3 + Cerulean	45	500 ± 200 (29)	100 ± 1 (29)
Venus-LC3 + Cerulean-SQTM1	120	1200 ± 500 (51)	99.9 ± 0.6 (51)
Venus-LC3(G120A) + Cerulean	45	500 ± 200 (30)	100 ± 1 (30)
Venus-LC3(G120A) + Cerulean-SQTM1	120	2000 ± 600 (50)	99.7 ± 0.8 (50)
Venus-LC3(F52A L53A) + Cerulean	45	1000 ± 300 (32)	100 ± 1 (32)
Venus-LC3(F52A L53A) + Cerulean-SQTM1	120	1200 ± 400 (60)	99.6 ± 0.8 (60)
Venus-LC3(R70A) + Cerulean	45	130 ± 40 (29)	100 ± 1 (29)
Venus-LC3(R70A) + Cerulean-SQTM1	120	280 ± 90 (50)	99.5 ± 0.8 (50)
Venus-SQSTM1 +Cerulean-SQSTM	150	6000 ± 2000 (20)	99 ± 2 (20)

V.3 Discussion

Given the important role of LC3 in the autophagy pathway, it is critical to develop new approaches to understand how the complexes between LC3 and LC3-interacting proteins are regulated. In the current study, we describe several complementary approaches to monitor the interaction of fluorescent protein chimeras of SQSTM1 and LC3 in living cells using fluorescence microscopy. We also demonstrate the broader applicability of these methods by showing they can detect the association of LC3 with slowly diffusing puncta independent SQSTM1 homo-oligomers.

The first assay quantifies changes in the nucleocytoplasmic distribution of Venus-LC3 in the presence of a putative interacting protein. This assay takes advantage of the fact that transiently overexpressed LC3 is found in both the cytoplasm and nucleoplasm. LC3 lacks both a functional NES or NLS and normally undergoes slow transport between the nucleus and cytoplasm by a mechanism that does not involve active nuclear export [121]. However, many LC3 interacting proteins have intrinsic NES and NLS signals that regulate their nucleo-cytoplasmic distribution. SQSTM1 has both NLS and NES signals, but its NES signal dominates its steady-state localization, causing it to be enriched in the cytoplasm and depleted from the nucleus [236]. Overexpression of SQSTM1 relative to endogenous LC3 binding proteins drives complex formation between LC3 and SQSTM1. Under these conditions, the localization of LC3 appears to be dominated by SQSTM1's CRM1-mediated NES. As a result, co-expression of Cerulean-SQSTM1 with Venus-LC3 leads to a dramatic shift in the subcellular distribution of Venus-LC3 out of the nucleus. Binding of LC3 to SQSTM1 thus provides LC3 with the new functionality of active nuclear export, and leads to a greater relative concentration of LC3 in the cytoplasm. This type of functionality may be quite common, as it has also been observed in the context of the nuclear protein DOR recruiting LC3 to cytoplasmic autophagosomes in response to autophagy activation [123, 124]. Remarkably, we found that this assay was highly sensitive to the presence of overexpressed SQSTM1, as well as mutations in LC3 that disrupt SQSTM1 binding (Figure V.5). This is important because this assay is extremely straightforward, and also has the potential to be easily converted to a high throughput format.

Our second assay utilized FRET to detect the close proximity between fluorescent proteins appended to LC3 and SQSTM1. Because FRET only occurs within distances of $< 10\,\text{nm}$, it is well suited to test for protein-protein interactions [136, 178, 220, 221]. Our FRET measurements revealed significant FRET occurred between Venus-LC3 and Cerulean-SQSTM1, indicating the two proteins are closely apposed. We also measured a high level of FRET between Venus-SQSTM1 and Cerulean-SQSTM1 consistent with the expected presence of homo-oligomers of SQSTM1. We focused primarily on using FRET as a semi-quantitative readout for the presence of specific protein-protein interactions. From a more quantitative perspective, the

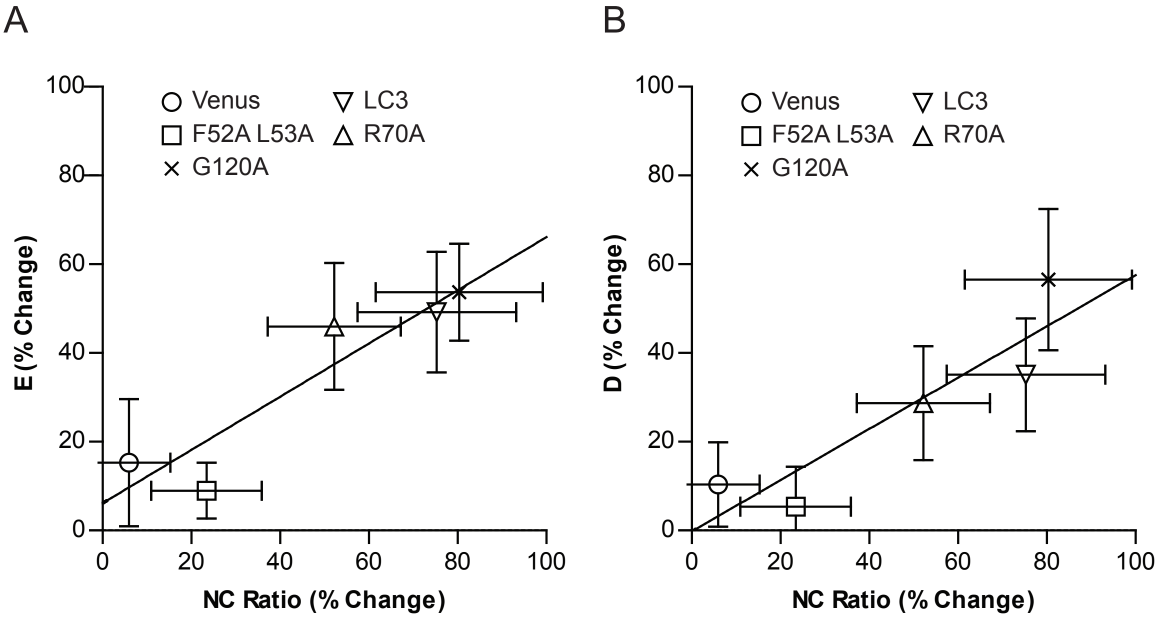

Figure V.5: A comparison of the N/C ratio, FRET, and FRAP assays for detecting LC3 interactions. (A) The percent change in *E* versus N/C ratio between cells expressing the Venus-LC3 constructs and Cerulean or Cerulean-SQSTM1. (B) The percent change in *D* versus N/C ratio between cells expressing the Venus-LC3 constructs and Cerulean or Cerulean-SQSTM1. The error bars are the propagated errors on the 95 % confidence intervals.

absolute magnitude of FRET is a function of the distance and orientation between the donor and acceptor fluorophore as well as the fraction of donors bound by acceptors. Using more sophisticated analysis that takes donor:acceptor ratios as well as protein expression levels into account it is in principle possible to obtain information about the stoichiometries of protein complexes using this approach [242–244]. It is also possible to directly couple FRET and diffusion measurements to assess the dynamics of protein interactions [190].

FRET microscopy has several advantages as a method to monitor specific protein-protein interactions. It can be used to generate spatially resolved maps of where FRET occurs intracellularly, and thus can obtain separate measurements for puncta, nucleus, and cytoplasm, or individual organelles. For example, it was recently used to demonstrate FRET between SQSTM1 and LC3 in puncta [153]. In our experiments, the vast majority of LC3 and SQSTM1 were present in a diffuse puncta independent form, and we did not observe substantial differences in FRET between different subcellular compartments. FRET can also be performed over time and has the potential of utilizing a wide range of fluorescent proteins as donors and acceptors [136]. However, FRET measurements have some potential pitfalls that should be considered carefully. One limitation of FRET is that a negative result does not exclude possible direct or indirect interactions, because the fluorophores may not have a favorable orientation, or may be greater than 10 nm apart in the same complex [178]. Thus, FRET signals can vary depending on the position of the fluorescent probes on the interacting proteins being tested. For example, recent studies showed that fluorescent proteins tagged at the N-terminus of SQSTM1 yield detectable FRET, whereas little FRET was observed between N-terminally and C-terminally tagged SQSTM1 constructs [153]. In addition, membranes are very crowded environments where FRET is often significant due to the random close proximity of molecules integrally or peripherally associated with membranes [245–247]. However, for soluble proteins, typically measurements of FRET efficiency are very low unless specific interactions are present [248].

FRET can be measured in a number of different ways, each with their own particular advantages and disadvantages [136, 249, 250]. In the current study we use the acceptor photobleaching FRET measurement approach [153, 165, 186, 203, 210, 237, 238]. This particular approach to FRET measurements is very straightforward and easily quantified. The disadvantage of acceptor photobleaching is that it requires photobleaching of the acceptor, and is typically not suitable for timelapse FRET imaging. Also, photoswitching of the acceptor to a donor-like state has been observed for some acceptor fluorophores which can give rise to a false positive FRET signal [251]. However, when acceptor photobleaching is coupled with the use of photoswitchable proteins, FRET can be performed over time. Use of photoswitchable proteins can also help overcome problems of low signal-to-noise when the FRET efficiency is small, for example when there is only a small fraction of interacting proteins [252]. Alternative strategies for FRET measurements include sensitized emission, spectral unmixing [191, 253], lifetime imaging [228] and polarization [191, 203, 222–228, 253]. Homo-FRET measurements using fluorescence anisotropy are also useful for studying homo-oligomers or clustering of like proteins [176, 184, 224, 254].

As a third approach, we used FRAP to test for changes in the hydrodynamic radius of LC3 as inferred from changes in the diffusion coefficient D for LC3 upon binding SQSTM1. As a starting point for these studies, we measured D for each protein expressed individually. In agreement with our previous studies, we found that the diffusional mobility of Venus-LC3 is consistent with that of a $\sim 500\,\mathrm{kDa}$ complex [164]. Here, we found that when expressed on its own, Venus-SQSTM1 is associated with a much larger complex, with a predicted MW of $\sim 6\,\mathrm{MDa}$. Upon coexpression of Cerulean-SQSTM1 and Venus-LC3, D for Venus-LC3 decreased. Nevertheless, the diffusion of Venus-LC3 was still faster than that of Venus-SQSTM1 alone. This suggests that not all of LC3 is bound to SQSTM1. If $100\,\%$ of the proteins were bound to each other we would expect their diffusion to become identical. This could mean that endogenous proteins compete for binding to Venus-LC3 and Cerulean-SQSTM1. Alternatively, the affinity of SQSTM1 for LC3 may be such that they will not be $100\,\%$ complexed under the conditions of our measurements, or LC3 may bind to a subset of SQSTM1-containing complexes with specialized composition and size. Interestingly, when we performed the converse experiment, we did not observe a slowing in the diffusion of Venus-SQSTM1 to match that of LC3's mobility. We speculate that the size of the SQSTM1 complex is so large that the addition of LC3 does not cause a detectable increase in size. This result also implies that binding of LC3 to SQSTM1's LIR does not outcompete SQSTM1 binding to the components that cause SQSTM1's very slow diffusion. This is in agreement with the notion that SQSTM1's domain architecture may help to segregate functions such as PKC binding, LC3 binding, ubiquitin binding and homo-oligomerization [255].

FRAP has several advantages over currently available methods to measure protein diffusion. First, it can be readily performed using most confocal microscopes. Second, FRAP data can be analyzed quantitatively to yield diffusion coefficients. For example, we have developed several approaches to carry out these measurements [158, 171, 175] and have developed freely available software for this purpose http://www.fraptoolbox.com). Third, FRAP has the advantage of being able to quantify very slowly moving molecules all the way down to those that are completely immobile. Because FRAP reports on changes in *D* that occur as the result of protein complex formation, this assay will be the most sensitive under conditions where the diffusional mobility of the smaller protein is measured (in this case, that of LC3). Importantly, FRAP provides information on the apparent size of the complex containing the diffusing proteins without requiring knowledge of what the other molecules in the complex are. This also means that changes in *D* may reflect remodeling of complexes that occur in response to binding, and not simply the additional mass due to the binding of the interacting protein. The rate of diffusion is also sensitive to the shape of the diffusing species. Thus, FRAP needs to be interpreted in the context of other assays. FRAP can also be used to study reaction-diffusion events [148, 149, 256]. FRAP typically does not have adequate resolution to distinguish multiple components, and thus provides a population average measure. Distinguishing bound and unbound fractions can potentially be accomplished using more sophisticated methods such as fluorescence correlation and cross-correlation spectroscopy [199, 229, 257].

Using the combination of assays described here, we recapitulated several key findings regarding the interactions of LC3 and SQSTM1 obtained previously using biochemical approaches. Our FRET measurements are in good agreement with previous studies showing that LC3 and SQSTM1 directly interact [68, 129], including recent FRET measurements between LC3 and SQSTM1 in puncta [153]. Our experiments also confirmed that the binding of LC3 to SQSTM1 depends on hydrophobic surface residues F52 and L53 [129], but does not depend on residue R70 [9]. In addition, our results indicate that disrupting LC3's lipid modification does not inhibit its interaction with SQSTM1. This is consistent with reports demonstrating LC3-I can be recruited to SQSTM1 inclusions, and that LC3(G120A) retains affinity for SQSTM1 by co-immunoprecipitation [100]. Indeed, under the conditions of our experiments, the majority of both LC3 and SQSTM1 were present with a localization that was puncta independent and diffusely distributed. Thus, the interactions between LC3 and SQSTM1 that we detected primarily occur independently of autophagosome binding and also do not correspond to insoluble protein aggregates.

Importantly, the combination of approaches we describe here can also be readily extended to study other protein complexes in the autophagy pathway. As illustrated here, our current findings have already begun to shed new light into the properties of SQSTM1-containing complexes. For example, SQSTM1 is thought to form homo-oligomers [67, 239–241], and our FRET measurements suggest that this is the case in living cells. Although we cannot infer the number of SQSTM1 monomers in each oligomer directly from FRET measurements alone, more specialized techniques such as FPFA or brightness analysis could be used to address this question in future studies [164, 176]. Our FRAP results also reveal that SQSTM1's diffusion coefficient is extremely slow for a soluble protein. This is consistent with the known association of the protein with high molecular weight complexes as detected by size exclusion chromatography of purified recombinant SQSTM1 homo-oligomers [240] or as measured in cell lysates [241]. The size of the complexes implied by our FRAP measurements is remarkably large. Assuming the SQSTM1-associated complexes are spherical, they are predicted to have a $\sim 10\,\text{nm}$ radius. This could correspond to very large complexes consisting of homo-oligomers of SQSTM1 bound to selective autophagy substrates. SQSTM1 is also known to associate with mTORC1 complexes [258]. This slowly diffusing SQSTM1 complexes inferred from our findings could potentially also be assiciated with large macromolecular structures such as the ribosome or proteasomes. For example, ribosomes have a large radius of about 15 nm [259]. The interaction of SQSTM1-containing complexes with ribosomes could potentially be related to ribophagy [260], or cotranslational quality control [261–263]. Alternatively, the slowly diffusing SQSTM1 complex could potentially be associated with proteasomes, structures measuring approximately 7 nm in radius on their longest dimension [264]. This is an attractive possibility given that in addition to its role in selective autophagy, SQSTM1 is involved in shuttling ubiquitinated cargo to the proteasome for degradation and has been shown to directly bind to the proteasome in the process [265]. Using the assays outlined here, it should be possible to distinguish between these and other models in future studies.

V.4 Materials and Methods

V.4.1 Cells and constructs

Venus-LC3 and Venus-LC3 mutants were as previously described [164]. Venus-SQSTM1 and Cerulean-SQSTM1 were constructed by BglII and EcoRI double restriction digestion of mVenus-C1, mCerulean-C1, and DsRed-SQSTM1 vectors (http://www.addgene.org/28024/). A series of positive FRET controls consisting of Cerulean and Venus separated by linkers of different lengths (C5V, C17V, C32V) was obtained from Dr. Steven Vogel [205].

HeLa cells (American Type Culture Collection; CCL-2) were maintained in Dulbeccos Modified Eagle Medium (DMEM) containing 10 % fetal bovine serum (Life Technologies; 10437028), 1 % PenStrep, and phenol red at 37 °C, 5 % CO2. For live cell imaging experiments, on the day prior to transfection, HeLa cells were plated in MatTek 35 mm No. 1.5 glass bottom culture dishes (Ashland; P35G-1.5-10-C). On the following day the cells (50 %–80 % confluent monolayer) were transfected with described mammalian expression constructs using FuGENE6 transfection reagent according to the manufacturers recommended protocol (Promega Corp.; E2691). Cells were imaged in phenol red free DMEM.

V.4.2 Confocal Microscopy

Microscopy was performed using a Zeiss LSM 510 laser scanning confocal microscope using a 40X 1.3 NA objective as previously described [164]. Cells were maintained at 37 °C using an objective heater and stage heater.

V.4.3 Quantification of nucleo-cytoplasmic ratio

Quantification of the nucleocytoplasmic ratio was performed using a custom MATLAB algorithm. Our MATLAB scripts for quantifying N/C ratios are open source and are freely available at https://github.com/kraftlj/LocalizeLC3. Just prior to imaging the cells were labeled with a far red DRAQ5 (Cell Signaling Technology, Inc; #4084) nuclear label. Confocal images were acquired for the CFP, YFP, and far red channels. Masks for the cell and nucleus were generated using a manually defined threshold intensity in either the YFP or the far red channel respectively. Masks for the puncta were generated by first subtracting the uneven diffuse cellular signal using a tophat filter. The cytoplasm mask was created by subtracting the nuclear and puncta masks from the cell mask. The nucleus mask was created by subtracting the puncta mask from the nuclear mask.

V.4.4 Acceptor Photobleaching FRET

Acceptor photobleaching FRET measurements were performed using a custom MATLAB algorithm which is essentially as previously described previously [44]. Our MATLAB scripts for quantifying FRET are open source and are available at https://github.com/kraftlj/abFRET. In brief, confocal images of the acceptor and donor before bleaching (A_{pre} and D_{pre} respectively) as well as after photobleaching the acceptor (A_{post} and D_{post} respectively) were acquired. Masks were defined for the cell and the background using a manually defined threshold intensity in the Acceptor channel. Masks were defined for the puncta by first subtracting the uneven diffuse cellular signal using a median filtering approach. Averaged energy transfer efficiency for the background subtracted cell (devoid of puncta) or punta was calculated according to equation V.3. Lateral movement of the donor images before and after photobleaching were corrected by crosscorrelation. The FRET efficiency images were calculated by first binning the images 5X to increase the signal/noise.

V.4.5 FRAP

FRAP measurements were performed as recently described [164]. In brief, a smaller rectangular imaging ROI was used for increased temporal resolution, and a small circular 1 μm radius bleach ROI was used for bleaching. FRAP data were analyzed using FRAP-Toolbox - a freely available software for the analysis of FRAP data available online at http://www.fraptoolbox.com. In particular, the diffusion model fit all of the FRAP curves in this study well.

V.4.6 Statistics

Values reported throughout the text are the mean ± 95 % confidence intervals. Statiscal comparisons were made we using a Bonferonni corrected t-test. Where multiple comparisons were made, we corrected the p-value threshold such that the overall type-I error rate for all pairs of comparisons was 0.05. For example if 15 pairs of comparisons were made among 6 different groups the p-value threshold was set to 0.003.

CHAPTER VI

The nucleocytoplasmic distribution and nuclear dynamics of LC3 are regulated by LC3's hydrophobic binding interface but not its ability to undergo lipidation

Although the formation of autophagosomes occurs in the cytoplasm, it is increasingly evident that several key proteins in the autophagy pathway shuttle in and out of the nucleus. LC3, a protein that participates in autophagosome formation and cargo selection in the cytoplasm, is also enriched in the nucleus in a slowly diffusing form. However, the mechanisms that retain LC3 in the nucleus and control its nuclear dynamics remain poorly understood. In this chapter, we investigate the contributions of interactions mediated by LC3's hydrophobic protein interaction surface and the ability of LC3 to undergo lipidation to the nuclear dynamics of LC3. The results presented in the chapter clarify the roles for LC3's hydrophobic protein interaction surface as well its lipid modification in controlling the ability of LC3 to enter and exit the nucleus and suggest that soluble LC3 is associated with high molecular weight complexes in both the cytoplasm and nucleus, but that this may not be entirely responsible for its localization in the nucleus. We also show that LC3's localization in the nucleus is physiologically relevant.

VI.1 Introduction

Autophagy is a major catabolic lysosomal degradation pathway in cells. A distinctive intermediate in the autophagy pathway is the formation of a double membrane vesicle called the autophagosome, and is responsible for sequestering cytoplasmic materials. The formation of autophagosomes occurs in the cytoplasm, but it is increasingly evident that several key proteins in the autophagy pathway may have important functions in the nucleus [266]. More work needs to be done to investigate the functions of autophagy proteins in the nucleus.

Surprisingly, LC3, a protein that participates in autophagosome formation and cargo selection, was reported to be in the nucleus [120, 121]. Given that LC3 is primarily thought to function in the cytoplasm where autophagosomes form, this discovery raises the possibility that nuclear LC3 may have currently unknown functions in the autophagy pathway. A small number of studies have begun to examine LC3's potential functions in the nucleus. It was shown that LC3 interacts with the nuclear tumor suprresor TP53INP1 and influences cell death by autophagy [122]. The interaction of LC3 with a TP53INP1 family member called DOR, also a nuclear protein, functions in the dual regulation of autophagy and thyroid hormone receptor transcription [123–125]. Recent studies suggest nuclear LC3 may also regulate signaling via interactions with ERK signaling cascade components [126].

In previous studies GFP-LC3 was shown to be enriched in the nucleus by fluorescence microscopy [121]. However, it is unclear if the localization of LC3 in the nucleus is physiological, or if it may be due to an artifact of transient overexpression or due to the GFP tag itself [173]. Although, prediction software showed that LC3 may have an active nuclear export signal, it appears that LC3 does not utilize CRM1 mediated active nuclear export to cross the nuclear envelope. Furthermore, transport of LC3 between the cytoplasm and nucleus was significantly slowed compared to GFP, suggesting that LC3 was either being specifically retained in the nucleus or was part of a complex that is too large to cross the nuclear envelope by passive diffusion [121]. Previous diffusion based studies showed that, in the cytoplasm, a single soluble LC3 is associated with a 500 kDa complex [164]. In addition, nuclear LC3 diffuses much more slowly than expected for a monomer suggesting that it may also be bound to a large complex or may be reversibly binding to DNA [121]. Furthermore, the diffusional mobility of the cytoplasmic pool of soluble LC3 is altered upon disruption of the hydrophobic protein binding interface of LC3, but not its lipidation [164]. The composition and function of these LC3-associated complexes is not entirely clear, but may be related to regulation of autophagy. However, it is currently unknown if LC3 associates with similar or different complexes in the nucleus, or if the association of LC3 with these putative complexes regulate the nucleo-cytoplasmic trafficking of the protein.

Here, we investigate the contributions of interactions mediated by LC3's hydrophobic protein interaction surface and its lipid modification site to LC3's intranuclear mobility, and its nucleocytoplasmic mobility. Our results identify an important role for protein-protein interactions in controlling the ability of LC3 to enter and exit the nucleus and suggest that although soluble LC3 exists in similar complexes in both the cytoplasm and nucleus, this may not be the complete mechanism responsible for maintaining its nuclear localization.

VI.2 Results and Discussion

VI.2.1 Endogenous LC3 is in the nucleus

The nuclear localization of LC3 was recently questioned, as it was speculated that nuclear GFP-LC3 may be an artifact of transient overexpression or the GFP label itself [173]. One study showed evidence for endogenous LC3 in the nuclear fraction [120], but this study lacked proper controls for the various fractions which leaves the question open for debate. In order to confirm that the localization of LC3 in the nucleus is physiological, we set out to determine if endogenous LC3 is in the nucleus of HeLa cells using subcellular fractionation to isolate nuclear and cytoplasmic fractions.

Nucleocytoplasmic fractionation experiments showed that like GFP-LC3, endogenous LC3 is in fact localized in the nucleus (Figure VI.1). This finding suggests that the localization of LC3 in the nucleus is physiological relevant, and may have important implications for autophagy regulation or possibly an autophagy

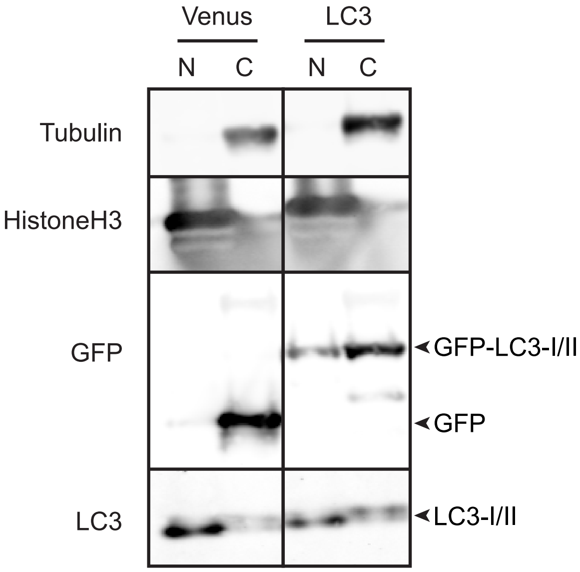

Figure VI.1: Both endogenous LC3 and Venus-LC3 are localized in the nuclear compartment. HeLa cells expressing either Venus or Venus-LC3 were subjected to subcellular fractionation. Nuclear (N) and cytoplasmic (C) fractions were blotted using antibodies against beta tubulin as a control for a cytoplasmic protein, histone H3 as a control for a nuclear protein, GFP for detection of both Venus and Venus-LC3, or LC3 for detection of endogenous LC3.

independent function of the protein.

The nature of LC3's localization in the nucleus remains a mystery. It was previously shown that it undergoes slow nucleocytoplasmic shuttling, but it is not under the control of CRM1 mediated active nuclear export [121]. In previous studies however, it was shown that LC3 interacts with the coregulator of thyroid hormone receptor, DOR, and with perturbations to the autophagy pathway the proteins can shuttle to the cytoplasm and stimulate autophagosome formation [125]. In addition it appears that starvation with Hank's balanced salt solution may also modulate the N/C ratio of LC3 [121]. Thus, we next sought to test whether the nuclear localization of LC3 is regulated by perturbations to the autophagy pathway directly by using either known activators or inhibitors. We addressed this by testing if the N/C ratio of LC3 changes after treatments with either rapamycin or chloroquine. We found that for both of these treatments there were no significant changes in LC3's N/C ratio after the 2 hour treatment ($p > 0.03$) (Figure VI.2). This suggests that the proteins N/C ratio may not be modulated by direct perturbation to the autophagy pathway.

Previous experiments by Drake et al. [121] showed that the N/C distribution and slow nucleocytoplasmic shuttling of LC3 may be regulated by binding to a large complex. The experiments described in chapter III showed that LC3 in fact associates with a large complex, and that the LC3(R70A) mutant's ability to associate with the complex is disrupted. We next sought to extend our FRAP measurements of the mutants to the nuclear compartment to examine if these mutations play a role in regulating LC3's association with complexes there.

We performed FRAP measurements in the nucleus of HeLa cells under basal conditions, and after treatment with either chloroquine or rapamycin (Figure VI.3). The effective sizes of the constructs in the nucleus

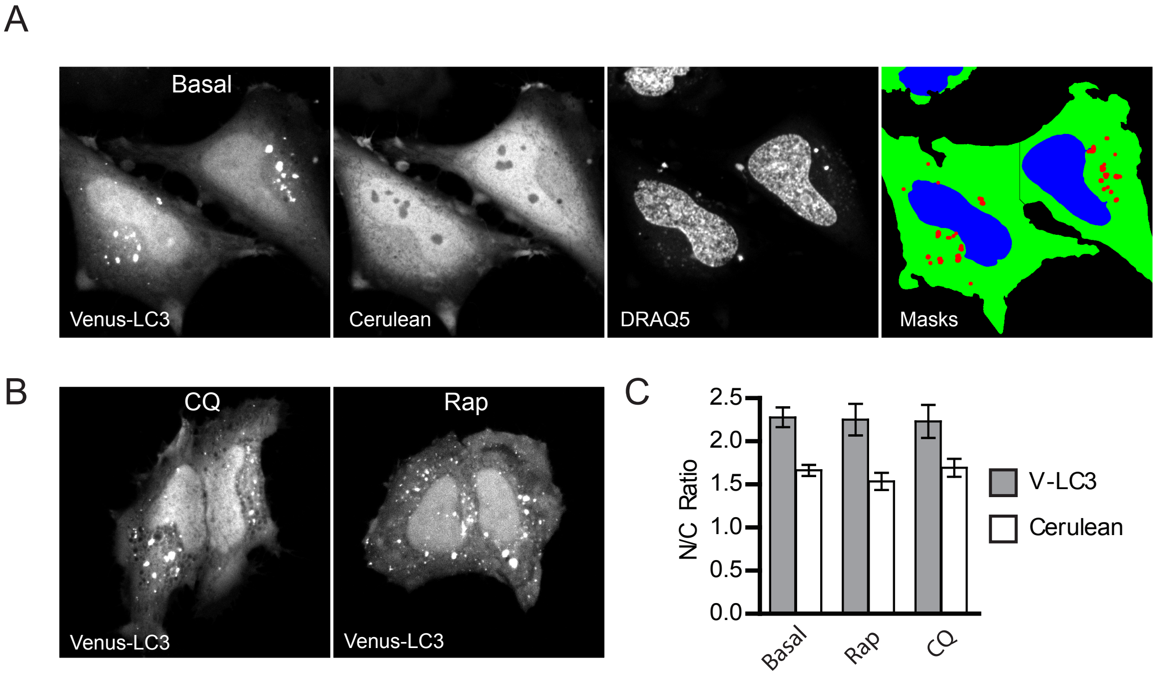

Figure VI.2: Activation or inhibition of autophagy with rapamycin or chloroquine does not change LC3's nucleocytoplasmic distribution. (A) An automated image analysis routine was used to quantify the nucleocytoplasmic distribution by creating masks for cytoplasm (green) using the Cerulean channel, nucleus (blue) using the DRAQ5 channel, and puncta (red) using the Venus channel for HeLa cells co-expressing Venus-LC3 and Cerulean under either (A) basal conditions, or (B) after incubation with 100 nM rapamycin or 100 µM chloroquine for 2 h. The cells were labeled with DRAQ5 as a marker for the nucleus, and imaged live using a confocal microscope. Scale bar is 10 µm. (C) Bar graph of the mean nucleocytoplasmic ratio. Error bars are 95 % confidence intervals. N values are the number of cells – 80 for basal; 30 for rapamycin; and 31 for chloroquine.

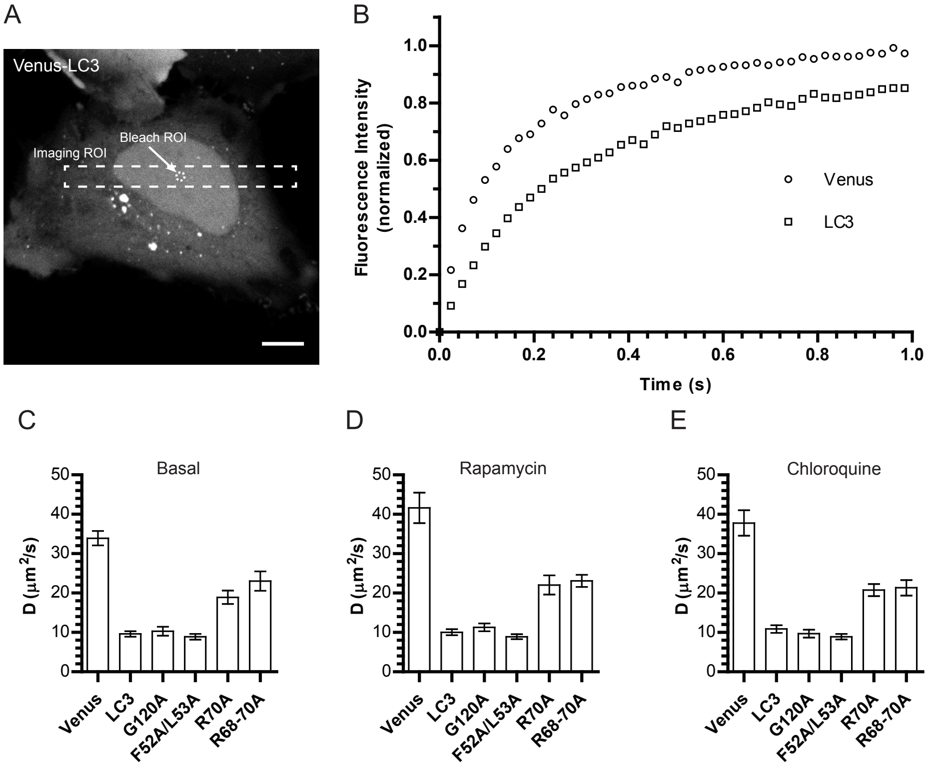

Figure VI.3: Disruption of LC3's hydrophobic protein interaction surface but not its lipid modification decreases LC3's effective hydrodynamic radius in the nucleus. (A) An example of the quantitative FRAP protocol that we carried out in the nucleus of live HeLa cells. The imaging ROI was reduced in size for speed, and the bleaching ROI was a 1 μm radius circle placed in the center of the nuclear compartment. (B) Average FRAP curves for Venus and Venus-LC3 from 10 cells, normalized between 0 and 1, were well fit by a single component diffusion model (data for G120A, F52A L53A, R70A, and R68-70A were similarly well fit by this model). The mean diffusion coefficients from FRAP experiments under (C) basal conditions, (D) after incubation with 100 nM rapamycin for 2 h, or (E) after incubation with 100 μM chloroquine for 2 h are displayed as bar graphs. The error bars are 95 % confidence intervals, and the $N > 20$ cells from at least two independent experiments.

were all larger than what was observed in the cytoplasm in chapter III; however, their values in the cytoplasm and nucleus and across treatments were strongly correlated (Figure VI.4). Notably, the increased diffusion of R70A suggests this mutation also disrupts its association with complexes in the nucleus, but mutations affecting LC3's lipidation have no affect on its diffusion. Thus, the nuclear and cytoplasmic complexes may be very similar in both compartments.

Previous studies demonstrated LC3 associates with RNA via its triple arginine motif (LC3 residues R68-R70) [118, 119]. This triple arginine region is overlapping with the R70A mutant that we examined in our own studies. This suggests that RNA is one possible component of the large LC3-associated complexes. In these studies we extended our analysis of LC3's diffusion to include a triple LC3 mutant LC3(R68-70A). Interestingly, this mutant's diffusion is similar to LC3(R70A) (Figure VI.3).

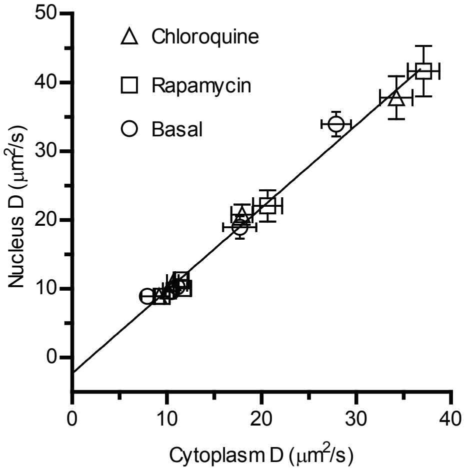

Figure VI.4: The diffusional mobilities of nuclear and cytoplasmic pools of LC3 are strongly correlated for both wild type and mutant forms of LC3. The diffusion coefficients for autophagosome independent LC3 in the cytoplasm are from Figure III.3 and the diffusion coefficients for LC3 in the nucleus are from Figure VI.4 shown here for comparison purposes. Linear regression between nucleus and cytoplasmic diffusion coefficients is shown.

With the knowledge that R70A likely disrupts LC3's association from complexes in both cytoplasm and nucleus, we now have a tool to test if LC3's slow nucleocytoplasmic transport is regulated by its association with large complexes. Transport of small proteins can occur via passive diffusion through nuclear pores, and the rate at which a protein passes through the pores by this mechanism is very sensitive to its hydrodynamic radius [170, 267–269]. We next examined if the nucleocytoplasmic transport rate of the LC3 mutants is altered by FRAP.

In this experiment, the entire nucleus was selectively photobleached (Figure VI.5A). Our results revealed that the nucleocytoplasmic transport kinetics of all of the mutants of LC3 are statistically within error of the wild-type protein (Figure VI.5B). Venus on the other hand recovered much faster, and its rate of nucleocytoplasmic transport was consistent with previous reports for GFP [170]. This suggests that the mechanism that regulates LC3's localization in the nucleus was not disrupted by mutations to LC3's hydrophobic protein interaction surface, or its lipid modification.

Our nuclear LC3 findings up to this point suggest that like cytoplasmic LC3, nuclear LC3 is also associated with large complexes, but that this may not be completely responsible for its nuclear localization. We next began to consider possible functions of nuclear LC3 by turning to the literature on known LC3 interacting proteins. Interestingly, it was shown that the LC3 interacting protein SQSTM1 associates with nuclear puncta colocalized with promyelocytic leukemia (PML) bodies after inhibition of CRM1 mediated active nuclear export, and it was proposed that the protein may be involved in degradation of nuclear protein aggregates [236]. Therefore, we hypothesize since LC3 interacts with SQSTM1, nuclear LC3 may also play a role in degradation of nuclear protein aggregates by functioning together with SQSTM1 and ubiquitin. In order to test this we next took a closer look at the subnuclear distribution of LC3.

Indeed, we found that LC3 localizes to nuclear puncta (Figure VI.6). These nuclear LC3 puncta colocalize

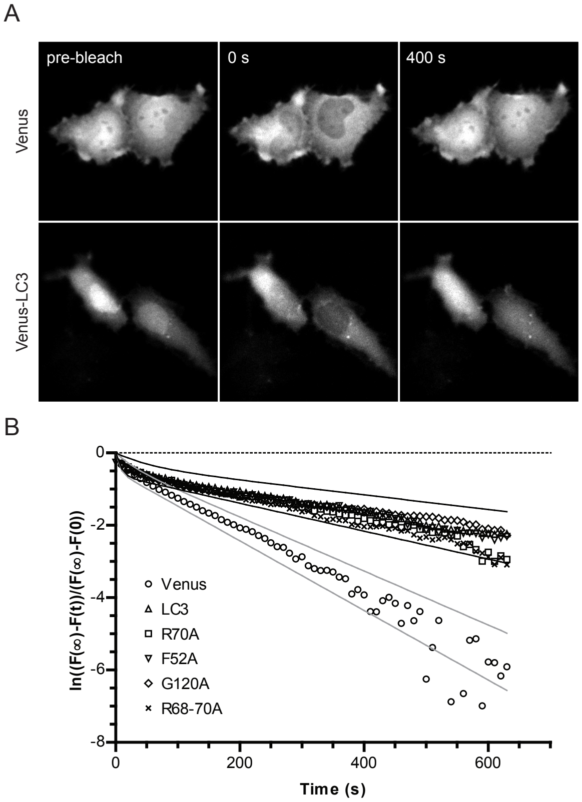

Figure VI.5: Disruption of LC3's hydrophobic protein interaction surface and disruption of its lipid modification does not change LC3's rate of nucleocytoplasmic transport. (A) An example of the quantitative FRAP protocol that we carried out to examine nucleocytoplasmic transport. The entire nuclear region was selectively photobleached using a user defined ROI, and the whole cell fluorescence intensity was used for normalization. Scale bar is 10 µm. (B) Average FRAP curves, from cells expressing Venus, Venus-LC3, Venus-LC3(G120A), Venus-LC3(F52A L53A), Venus-LC3(R70A), or Venus-LC3(R68-70A) were all well fit by a two phase exponential model. The fast component was consistent with intracompartmental diffusion, while the slow component was due to nucleocytoplasmic transport. Here we have transformed the data such that the slow exponential nucleocytoplasmic transport between constructs can be more easily compared. The solid gray lines are the 95 % confidence intervals for the fit to Venus, and the solid black lines are the 95 % confidence intervals for the fit to Venus-LC3.

with both SQSTM1 and ubiquitin puncta (Figure VI.6). These results point to a possible novel nuclear function for LC3 in nuclear quality control processes along with SQSTM1 and ubiquitin.

To our surprise, we also found that LC3 partitions into the nucleolar compartment (Figure VI.7A). We went on to test if the nucleolar localization of LC3 was sensitive to autophagy perturbations, but we found no noticeable differences after treatment with rapamycin or chloroquine, similar to the N/C ratio (Figure VI.7B).

LC3 does not have any known NLS or NES sequences. Given the large apparent size of the LC3-associated complexes it is surprising that LC3 is not excluded from both the nucleus and nucleolar compartments. It is thought that generally only small soluble proteins with radii less than 5 nm are able to passively diffuse in and out of the nucleus [267, 269]. However, the nuclear localization of some proteins is maintained not by means of binding to a chaperone for transport across the nucleus envelope, but by retention via affinity for nuclear components. In addition, the nucleolus does not have a membrane boundary, but is instead a dense meshwork of nucleic acid and protein. It is believed that proteins that localize in the nucleolus have an affinity for nucleolar components, and are thereby detained there, as opposed to chaperoned [270]. In addition, it is thought that proteins with a general affinity for RNA will partition into the nucleolus due to interactions with the large amount of ribosomal RNA in this compartment [271]. We hypothesized that LC3's nucleolar localization may depend on its triple arginine RNA binding motif.

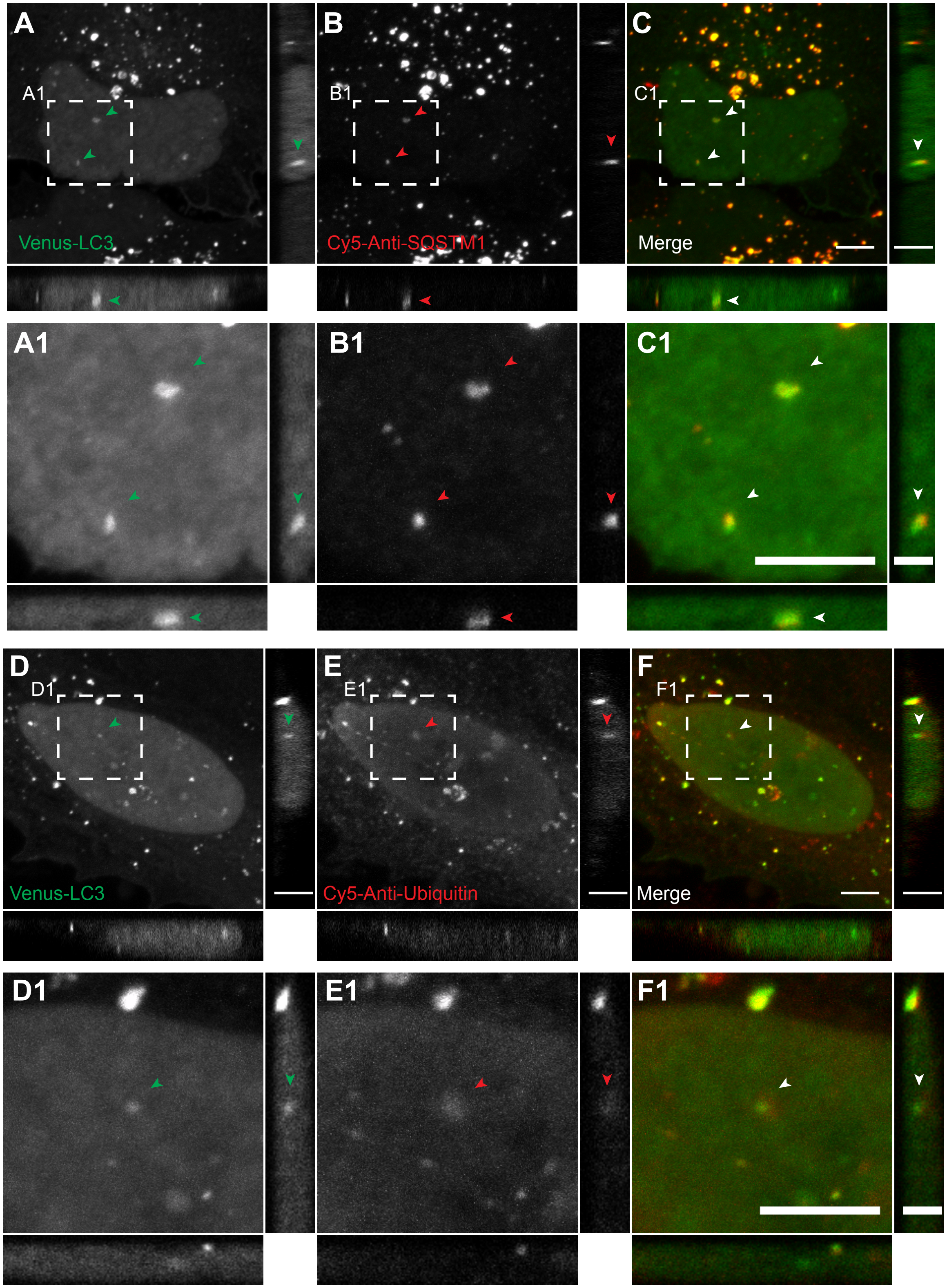

Figure VI.6: Venus-LC3 colocalizes with SQSTM1 and ubiquitin in nuclear puncta. Confocal z-stacks collected from fixed cells expressing Venus-LC3. Maximum intensity projections along with XZ- and YZ-sections of the fluorescence signal from Venus-LC3 (A,A1,D,D1); antibodies against SQSTM1 (B,B1); and antibodies against ubiquitin (E,E1). Merged pseudo colored images are shown in C,C1,F,F1. Arrowheads mark nuclear puncta.

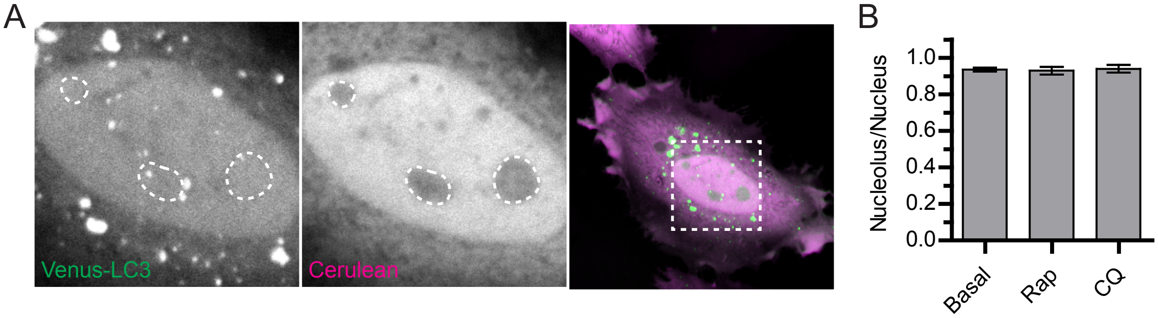

Figure VI.7: Nuclear LC3 partitions into the nucleolar compartment. (A) Confocal images of the nucleus of HeLa cells co-expressing Cerulean and Venus-LC3. Cerulean was used a control for protein that is excluded from the nucleolus. LC3 labeled puncta are visible in the nuclear compartment. (B) Autophagy was activated or inhibited by treatment with 100 nM Rapamycin or 100 µM chloroquine for 2 h, and the nucleolar ratio for Venus-LC3 was quantified by averaging across multiple nucleoli. Error bars are 95 % confidence intervals. N is the number of cells – 120 for basal; 36 for Rapamycin; and 45 for chloroquine.

Interestingly, mutations to the arginine residues R68-70 on LC3 completely abolish its nucleolar localization (Figure VI.8). This finding suggests LC3's ability to bind to RNA may regulate its localization to the nucleolus. Furthermore, the nature of nucleolar targeting sequences is not entirely clear, but some of these sequences appear to partially overlap with NLSs. Interestingly, we also saw a modest decrease in LC3's N/C ratio for the mutants with mutations to the triple arginine motif, but not mutations affecting its lipidation (data not shown). These results suggest that LC3's triple arginine motif may be a novel nucleolar detention sequence, and that LC3's general affinity for RNA may be responsible for its nuclear localization.

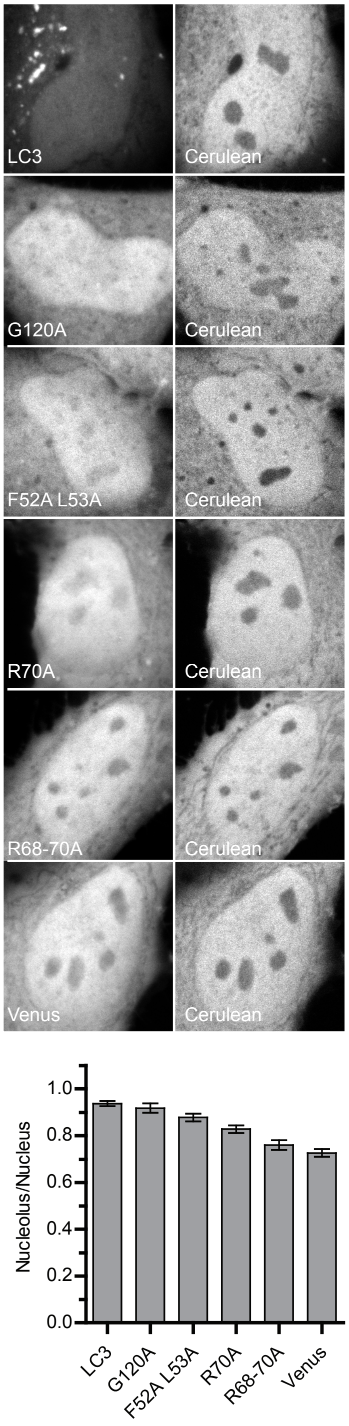

Figure VI.8: Mutations to LC3's triple arginine motif disrupt its ability to partition into the nucleolus. Example confocal images of the nucleolar compartment of HeLa cells co-expressing Cerulean as a control and Venus-LC3, Venus-LC3(G120A), Venus-LC3(F52A L53A), Venus-LC3(R70A), Venus-LC3(R68-70A), or Venus. The nucleolar ratios were quantified by averaging across all of the nucleoli in each cell, and across mulitple cells. Error bars are 95 % confidence intervals. N is the number of cells – 120 for LC3; 65 for G120A; 66 for F52A L53A and Venus; 62 for R70A; and 37 for R68-70A.

CHAPTER VII

Summary and Future Directions

The findings in this dissertation open up several new avenues for future research. This chapter outlines the ideas for these future directions, and a subset of the relevant preliminary findings are presented. Finally, the chapter ends with a brief summary of the major findings presented in this dissertation, and a discussion of their importance to the scientific community is given.

VII.1 Future Directions

VII.1.1 What is composition and function of the large LC3-associated complex?

LC3 is known to interact with a large network of proteins. Many of the LC3 interacting proteins are believed to form complexes. In our studies we showed that a single soluble LC3 interacts with a large $\sim 500\,\text{kDa}$ complex. The composition and function of these LC3-associated complexes remains unknown. We speculate that these complexes may be involved in the regulation of autophagy, as our results showed that autophagy perturbations modulate their size. For example, these complexes may correspond to a novel LC3-associated complex that functions as a scaffold in the assembly of the ULK complex. LC3 was already shown to play a role in the assembly of the ULK complex [44, 45]. Alternatively, the LC3-associated complex may function in targeting the Vps34 complex to the site of autophagosome formation, and thereby promote autophagosome maturation. Yet another possibility is that this complex may play an important role in coupling autophagosomes to the microtubule network when autophagy is upregulated. LC3 was recently shown to interact with FYCO1, which together with Rab7, functions in plus-end directed movement of autophagosomes along microtubules [59].

Our experiments revealed that the LC3 mutation, R70A, disrupts its association with the complex. This mutation was shown to disrupt interactions with at least 18 different proteins [9], and thus some of these proteins may be in a constitutive complex with LC3. The LC3(R70A) mutant is an important tool that can be leveraged in future studies directed at determining both the composition and function of the large LC3-associated complex. In previous studies it was shown that knockdown of all three LC3 subfamily members (LC3A, LC3B, and LC3C) disrupts autophagosome formation [80]. In the future, it would very interesting to construct a stable cell line expressing the siRNAs against endogenous LC3A, LC3B, and LC3C. Expressing either exogenous LC3B or LC3B(R70A) from Rattus norvegicus (siRNA resistant) would allow us to test if LC3's interaction with the $\sim 500\,\text{kDa}$ complex is required for autophagosome formation. This type of tool would also allow us to examine the composition of the complexes using a comparative proteomics approach by analyzing the components that co-immunoprecipitate (Co-IP) with LC3 from the LC3 expressing cell line compared to what co-IPs with LC3 from the LC3(R70A) cell line.

Our findings in chapter V raise some interesting possibilities for studying the nature of LC3-associated complexes formed in other contexts, for example, in the presence of over-expressed SQSTM1. Namely, our studies showed that when over-expressed with SQSTM1, LC3 associates with a substantially larger complex. In addition, since SQSTM1 homo-oligomerizes presumably there will be multiple LC3 proteins in this complex. Little is known about the mechanisms of selective targeting of autophagy cargoes [32], and it would be interesting to understand how the size, stoichiometry, and organization of the LC3-associated complexes change in response to changes in the levels of SQSTM1, as well as how these properties change in response to physiological modulators of selective autophagy such as metabolic stress.

VII.1.2 Does LC3 homo-oligomerize on autophagosomal membranes?

LC3 functions include contributing to membrane expansion and fusion events during the formation of the autophagosome [79]. LC3 was found to associate with autophagosome independent aggregates when transiently overexpressed [105, 130]. It was proposed that LC3 may non-specifically form aggregates [79, 105]. Furthermore, LC3's N-terminus promotes membrane tethering and hemifusion in *in vitro* liposome assays [93]. The energy for these fusion events was proposed to be contributed by the self-association of LC3's on opposing membranes via their N-termini [93]. Another LC3 family member, GABARAP, was shown to homo-oligomerize [107]. However, our studies revealed that autophagosome independent LC3 does not homo-oligomerize or aggregate, suggesting if homo-oligomerization of LC3 contributes to fusion events, they must be limited to the autophagosome membrane.

In the future it would be interesting to carry out detailed studies of the self-association properties of LC3 on autophagosomes by FRET and FPFA in living cells. In our studies we relied on a semiquantitative approach for the analysis of FRET microscopy data in cells, and our FPFA data for LC3 was collected in cell extracts where LC3 in autophagosomes was likely excluded [164, 165]. However, more advanced methods of analysis that takes donor:acceptor ratios as well as protein expression levels into account have the potential to reveal information about the stoichiometries of protein complexes by FRET microscopy in cells [242–244]. These methods may be able to shed additional light on the self-association properties of LC3 on autophagosome membranes in cells. In addition, FPFA experiments are capable of making spatially resolved measurements in cells using slight modifications of the experimental setup [176], or alternatively a slightly different extraction procedure could provide an enriched fraction of autophagosomes [39] for FPFA measurements *in vitro*.

Furthermore, there is some evidence to support the notion that members of the other ATG8 subfamilies

GABARAP and GATE-16 may have unique functions. For example, it was shown that although both LC3 and GATE-16 are essential for autophagosome formation, the LC3 subfamily contributes to membrane elongation, while the GATE-16 subfamily functions at a later stage of autophagosome maturation [80]. This points to a general need for our future efforts to be expanded to include analyses of GABARAP and GATE-16, as our unique assays may provide valuable information for determining what exactly the role of each ATG8 subfamily is in autophagy.

VII.1.3 High throughput characterization of LC3 interacting proteins in living cells

In chapters II and V we described several software tools to automate fluorescence based microscopy assays of LC3's N/C ratio, FRET with LC3 interacting proteins, and FRAP. These assays can be easily reformatted for high throughput analyses. A recently described program called Micropilot allows for automated acquisition of complex fluorescence microscopy imaging protocols using a standard LSM 510 microscope [152]. Thus acquisition of not only confocal images, but also FRAP and FRET data can now be automated. But the problem of how to collect very large, quantitative datasets goes hand-in-hand with the perhaps more challenging problem of data analysis. Automated data analysis is where the software programs that were presented in this dissertation will be especially useful. We developed a software program called FRAP-Toolbox that allows one to automatically analyze FRAP data sets using recently available quantitative FRAP models (http://www.fraptoolbox.com). We developed an algorithm called AbFRET that allows one the opportunity to automate the analysis of acceptor photobleaching FRET microscopy data (http://github.com/kraftlj/abFRET). We also developed an algorithm called LocalizeLC3 that makes it possible to automatically analyze images of GFP-LC3 in terms of the numbers of cytoplasmic and nuclear puncta, their intensity, and their size; it reports a statistic for the amount of scatter in the locations of puncta; and also reports the N/C ratio (http://github.com/kraftlj/LocalizeLC3). In the future these automated data analysis tools can be integrated with a high throughput system of data collection to enable fully automated high throughput screening for LC3 interacting proteins and complexes *in vivo*.

High throughput fluorescence-based assays for characterizing LC3 interacting proteins in living cells would open up the possibility to not only discover LC3 interacting proteins, but to also discover proteins that regulate LC3's association with complexes, as well as proteins that regulate its subcellular localization. Importantly, these studies could be subject to physiological perturbations to examine changes in the emergent properties of LC3. As a start, we used the LocalizeLC3 algorithm to analyze a recently published high-content-screen (HCS) of GFP-LC3 in response to autophagy perturbations rapamycin, and Hank's balanced salt solution, as well as a panel of siRNAs against LC3 interacting proteins provided to us by Dr. Christian Behrends [9]. This HCS consisted of analyzing over 1×10^5 confocal images. A preview of a subset of

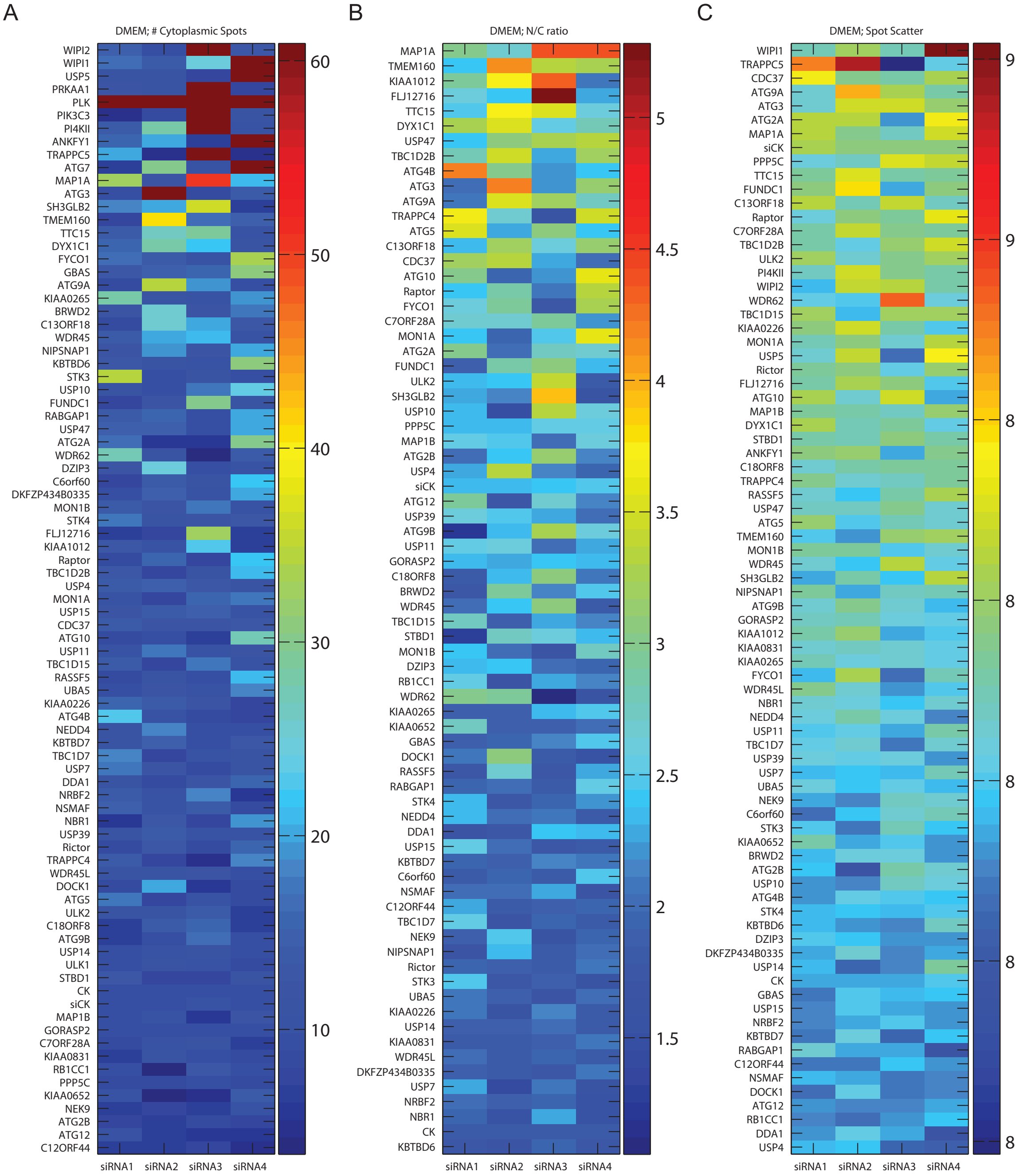

Figure VII.1: A preview of the results from the analysis of a high content screen of siRNAs against LC3 interacting proteins. The LocalizeLC3 automated image analysis routine was adapted to analyze the high content screen published by Behrends et al. [9]. A preview of the results are shown for the quantification of the numbers of cytoplasmic puncta (A), the nucleocytoplasic distribution (B), and the scatter in the location of the puncta (C) under basal conditions. The cells are U2OS cells stably expressing EGFP-LC3 incubated in complete DMEM media. The siRNAs for various LC3 interacting proteins were transiently transfected before fixation and imaging on an Opera high content screening confocal microscope. Each gene was targeted with at least 4 different siRNAs. The boxes are color coded according to the mean value of the particular statistic.

the results for: a) the number of cytoplasmic puncta, b) the N/C ratio, and c) the puncta scatter are shown in Figure VII.1. This study can be followed up in the future with experiments in living cells to verify some of the interesting findings of the HCS analyses. In addition, it would be interesting to determine if siRNA against particular genes that modulate either the N/C ratio, the number of puncta, or the puncta scatter statistics also disrupt LC3's association with the 500 kDa complexes. This would allow one to gain insights into the function and composition of the LC3-associated high molecular weight complexes.

VII.1.4 Size, stoichiometry, and organization of other autophagy related complexes

Up to this point we have focused almost exclusively on investigating the properties of LC3-associated complexes. This is justified by the fact that LC3 plays such a central role in the autophagy pathway. However, there are a number of other very interesting autophagy related complexes which deserve attention. Some of these other complexes include SQSTM1-associated selective autophagy complexes, the LC3 UBL conjugation complexes, and the signaling complexes ULK and Vps34. In the future, it would be interesting to investigate these other autophagy related complexes using FRAP, and FPFA in terms of their size, stoichiometry, and organization as we did for LC3 in chapter III. In collaboration with Dr. Steve Vogel's group at the NIH we have already collected some very interesting preliminary data on SQSTM1 where we found this protein diffuses as a homo-oligomer with multiple diffusion times. These experiments are expected to provide important details about the nature of SQSTM1-related selective autophagy complexes.

We also obtained FRAP data for several protein components in the ULK complexes and UBL conjugation complexes (Figure VII.2). As of now, these results are still a bit premature to interpret with great detail. For example, reports in the literature suggested that in yeast, newly synthesized ATG12 is immediately conjugated to ATG5. The formation of the ATG12-ATG5 covalent conjugate is constitutive, and there is virtually no free ATG12 [200]. If 100 % of ATG12 is conjugated to ATG5, their diffusion should be closer to identical. Instead, the FRAP results suggest that the apparent molecular weight of ATG12 is approximately 100 kDa - consistent with an ATG12-ATG5 conjugate, but the apparent molecular weight of ATG5 is much larger at about 500 kDa. Is all of ATG5 conjugated to ATG12, or is some ATG5 functioning elsewhere? It would be informative to examine ATG12 and ATG5 by western blot in order to determine how much of the conjugate is formed in HeLa cells. Notably, diffusion of ATG14 is very slow. ATG14 is thought to function as a component of the Vps34 complex and contributes to the regulation of autophagosome formation [40]. The diffusion coefficient of ATG14 is so slow in fact that it suggests it is most likely associated with membranes. This is very reasonable given the known function of Vps34 – it is a PI3K which is essential for generating PI3P at the phagophore membrane [40].

Our *in vivo* diffusion results are also important for understanding the effects of the intracellular envi-

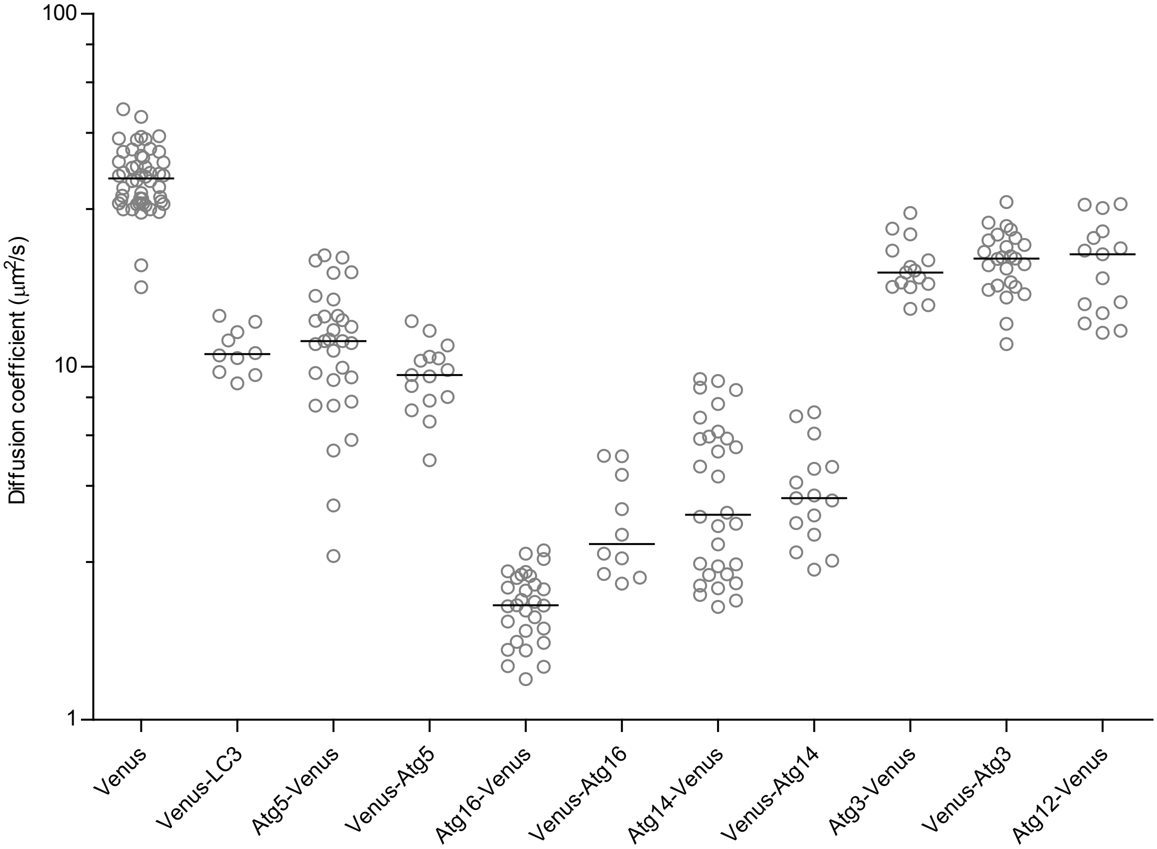

Figure VII.2: FRAP analyses of other autophagy related complexes. FRAP experiments were performed using a 1 µm radius circle placed in puncta independent regions of the cytoplasm of live HeLa cells. The diffusion coefficients from experiments across multiple cells are shown for protein compents of the autophagy UBL complexes (ATG5, ATG16, ATG12, ATG3), and a protein component of the Vps34 complex (ATG14). Horizontal lines represent the median. We are grateful for Mike Davidson's assistance preparing the fluorescently labeled ATG5, ATG16, ATG14, ATG3, and ATG12.

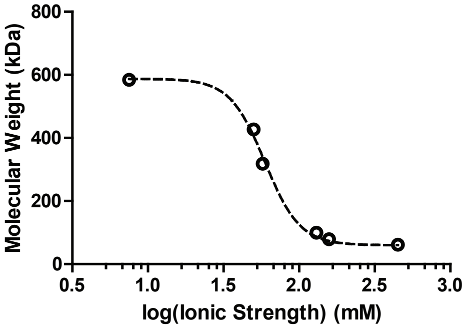

Figure VII.3: Effect of ionic strength on the effective size of soluble LC3 associated complexes *in vitro*. We prepared cytoplasmic extracts with varying ionic strengths by either dilution or addition of NaCl to the buffer. Shown in the plot are the experimental data points (open circles), along with a fit to a dose-response relationship (dashed line). The IC50 was about 60 mM, with a hill slope of about 3.7. The minimum molecular weight was constrained to the theoretical size of a Venus-LC3 monomer (45 kDa), and the theoretical maximum molecular weight at 0 mM ionic strength was about 590 kDa.

ronment on diffusion. There has been some controversy about the effects of the intracellular environment on the nature of molecular diffusion [272–275]. Our FRAP results show that the diffusion of proteins with radii in the range of 2 nm–6 nm are identical both *in vivo* and *in vitro* in solution. These results suggest that molecules of this size may not be heavily influenced by the crowded environment of the cell. The diffusion results that we obtained for the other autophagy related complexes extend the range of sizes of complexes that we have measured. They also extend the range of overall charge and hydrophobicity properties that we have examined. In the future, performing parallel studies on the *in vitro* diffusion of these complexes may contribute to our understanding of the effects of the intracellular environment on the diffusion of molecules. For these types of *in vitro* diffusion studies, it might also be interesting to examine how crowding agents [275], or reconstituted cytosol [276] affect the apparent size of autophagy related complexes *in vitro*.

As a final word of caution, we have come across at least one potential pitfall of performing diffusion experiments *in vitro*. In addition to the obvious point that labile complexes fall apart in a dilute solution, our studies also revealed that LC3-associated complexes were very sensitive to the concentration of salts in cell extracts (Figure VII.3). Therefore, a comparison of the results obtained *in vivo* with those obtained *in vitro* is helpful in screening for the optimal conditions of experiments.

Using the optimized salt conditions for LC3-associated complexes, we compared the results of our diffusion based estimate of molecular weight using the Stokes-Einstein relation to the classical method of sizing complexes by size exclusion chromatography. We subjected cytoplasmic extracts from HeLa cells expressing Venus or Venus-LC3 to size exclusion chromatography using a Superose 6 column. The FPLC fractions corresponding to sizes of 5 MDa all the way down to 5 kDa were collected and subjected to western blotting with antibodies against LC3, GFP, and various LC3 interacting proteins (Figure VII.4). To our satisfaction, we were able to obtain results which were consistent with our findings by diffusion. These results confirm that

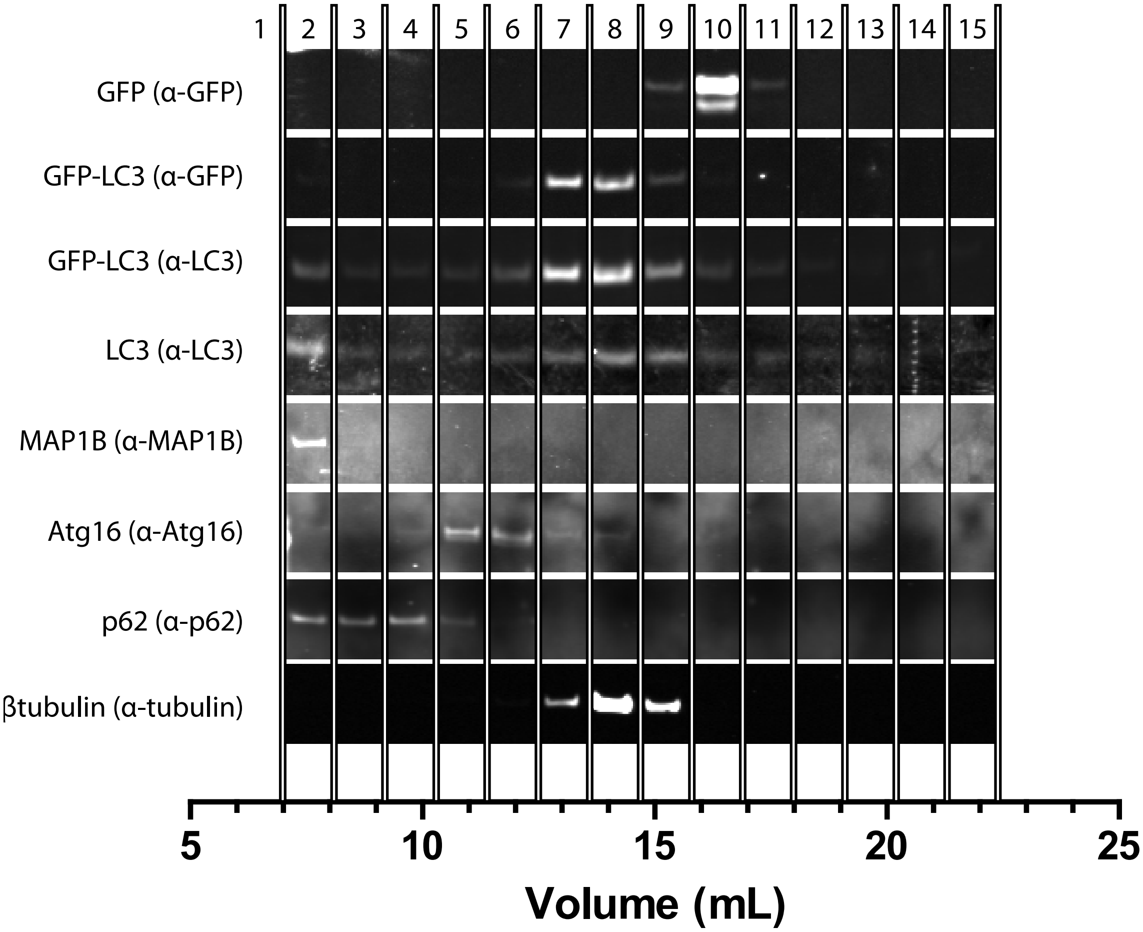

Figure VII.4: Size exclusion chromatography of autophagy related protein complexes. Cytoplasmic extracts from cells expressing Venus or Venus-LC3 were prepared and seperated according to their size and shape by FPLC gel filtration on a Superose 6, 10/300 GL 25 mL size exclusion column. The gel filtration fractions were subjected to SDS-PAGE, and western blotted using antibodies against GFP for detection of Venus and Venus-LC3; LC3 for detection of both Venus-LC3 and endogenous LC3; MAP1B; ATG16; SQSTM1; and beta tubulin.

with Venus as a control for a monomer, using the Stokes-Einstein relationship to estimate the hydrodynamic radius of a protein is a very reasonable first approximation.

VII.1.5 Does LC3 have a novel nuclear function?

Previous work highlighted LC3's surprising nuclear localization [121], but currently LC3's role in the nucleus and the nature of its localization there is unknown. In chapter VI we investigated the regulation of LC3's nuclear localization and nuclear dynamics in some detail using mutants of LC3 that had defects in their hydrophobic protein interaction surfaces, or their lipid modification. Our results suggested that soluble LC3 is associated with high molecular weight complexes in both the cytoplasm and nucleus, but that this may not be entirely responsible for its localization in the nucleus. We also show that LC3's localization in the nucleus is physiologically relevant.

There were some surprising and unexpected findings highlighted in the studies in chapter VI, such as, the findings that show LC3 associates with subnuclear structures. The LC3 associated nuclear puncta colocalized with the selective autophagy receptor SQSTM1 and ubiquitin. It was previously shown that after inhibition of CRM1 mediated active nuclear export, SQSTM1 colocalizes in nuclear puncta with promyelocytic leukemia (PML) bodies. It was proposed that SQSTM1 may be involved in degradation of nuclear protein aggregates [236]. Based on this evidence we hypothesize nuclear LC3 may also play a role in degradation of nuclear protein aggregates by functioning together with SQSTM1 and ubiquitin. However, we note that under basal conditions the bulk of Venus-LC3 is not associated with puncta.

We speculate that stress upregulates the formation of nuclear protein aggregates, which prompts ubiquitination and SQSTM1 association. Finally, LC3 would participate in the process by binding to SQSTM1 and targeting the complex for degradation by autophagy. Thus this model implies an entirely new mechanism for quality control of nuclear aggregates that are too large for the proteasome to degrade. In the cytoplasm, there are chaperones, proteasomes, as well as lysosomes to prevent misfolded proteins from accumulating, but in the nucleus there are only chaperones and proteasomes. If protein aggregates become too large for degradation by the proteasome they can still be degraded by the autophagy pathway [32]. However, currently, there are no known mechanisms to degrade very large aggregates that form in the nucleus via autophagy. An alternative hypothesis involves the known connections between LC3 and SQSTM1 and proteasomal degradation [70, 265]. LC3 may function together with SQSTM1 to target ubiquitinated nuclear aggregates for degradation via nuclear proteasomes. Thus these autophagy proteins may be involved in proteasomal degradation in the nucleus, and the nuclear puncta may correspond to the proteasome mediated degradation centers [277].

We found that LC3 also localizes to the nucleolus, and that this localization depends on LC3's triple arginine RNA binding motif. The nucleolar localization of LC3 may also be a very important clue as to what the function of nuclear LC3 may be. The nucleolus is a processing facility where ribosomal subunits are assembled, and there is evidence that ribosomal proteins are rapidly turned over in a proteasome dependent manner [278]. However, the nucleolus is devoid of proteasomes [279]. It is tempting to speculate that perhaps LC3 is somehow involved in regulating the assembly of ribosomal subunits via a mechanism that includes nuclear LC3 cycling in and out of the nucleolus to mediate ribosomal protein turnover via the proteasome. There is also evidence that the ATG8 homologue of LC3 in yeast functions in ribosome decay through selective autophagy [77].

In the future it would be interesting to examine LC3's RNA binding ability, and to test if the R70A mutant disrupts binding to RNA. This could be done using gel shift assays, or alternatively diffusion based methods could be used to test RNA binding by examining differences in the rate of diffusion after treating with RNase to digest all of the polymerized RNA. These results point to a novel nuclear function for LC3 in nuclear quality control processes. In the future it would be interesting to follow this up in at least two ways: a) to examine if nuclear puncta are disrupted in cells expressing the LC3 mutants in order to determine the structural nature of LC3's association with them; and b) to use the previously discussed stable LC3 knockdown cell line to test if these puncta require LC3 for their formation.

Does LC3 have a novel nucleolar detention sequence? A promising future direction would include ligating this region of LC3's sequence to the N-terminus of GFP to examine if it is a bonafide nucleolar detention sequence. In the future it will be important to test the potential models for LC3's nuclear function that were raised here. Experiments could be directed at tracking down what LC3 interacts with in the nucleus using a co-IP mass spectrometry approach similar to what was done in Behrends et al. [9]. We constructed a mutant of Venus-LC3 with a nuclear export signal attached to its N-terminus such that a relative comparison of nuclear and cytoplasmic LC3 interacting proteins could be examined using mass spectrometry. The stable LC3 knockdown cell line described above would be useful for these experiments. By identifying novel nuclear LC3 interacting proteins one may be able to gather some additional clues about the function of nuclear LC3.

VII.2 Summary

The cell is far from equilibrium, and its molecules undergo dynamic self-assembly to form ordered structures on a scale from nanometers to tens of microns [1]. Some proteins function as isolated monomeric enzymes continuously processing substrates into products, while many others function as very large, labile multicomponent complexes. Function (and dysfunction), patterns, and behaviors of a cell ultimately emerge from the collective behaviors of its molecules and assemblies. Emergent properties arise when numerous interacting components produce collective patterns or behaviors that are not attainable by the individual components themselves [2]. The autophagy pathway is an example of a metabolic process that displays stunning complexity, and that has exceptional relevance to human health and disease. Autophagy is a major catabolic pathway whereby cytoplasmic components including proteins, bacteria, and organelles are sequestered and degraded via the lysosome. LC3 is a central protein component in the autophagy pathway with functions in autophagosome membrane expansion, fusion, and autophagy substrate selectivity. LC3 interacts with a large number of proteins, but little is known about their physiological regulation, and whether LC3 interacts with these proteins in a binary fashion or if the proteins dynamically self-assemble to form multicomponent complexes.

VII.2.1 Novel findings related to autophagy protein LC3

In order to test if LC3 associates with complexes, we carried out quantitative *in vivo* diffusion measurements in chapter III in order to estimate its hydrodynamic radius. We found that the diffusion of LC3 was unaffected by either mutational disruption of its lipid modification or microtubule depolymerization. Brightness and homo-FRET analysis indicated LC3 does not homo-oligomerize. However, mutation of specific residues on LC3 required for binding other proteins and mRNA altered the effective hydrodynamic radius of the protein as well as its stoichiometry. We conclude that when not bound to autophagosomes, LC3 associates with a novel multi-component complex with an effective size of 500 kDa in the cytoplasm. These findings provided new insights into the nature of soluble LC3. We know that the effective size of the LC3-associated complexes increases in response to perturbations to the autophagy pathway, but the composition and function of these complexes remains to be determined.

In chapter IV we used FRET microscopy and FRAP to investigate the interactions of LC3 with ATG4B(C74A), a catalytically inactive mutant of the cysteine protease involved in lipidation and de-lipidation of LC3, as a model system to probe protein complex formation in the autophagy pathway. We found evidence that these proteins interact in live cells to form a complex which is consistent with the structure proposed by Satoo et al. [101]. The 2:1 complex formed between LC3 and ATG4B suggests a mechanism for regulation of LC3's lipid modification.

The site of autophagosome formation is in the cytoplasm, but surprisingly, LC3 is located in the nucleus as well, suggesting it may have a novel nuclear function. In chapter VI we investigated the mechanisms that retain LC3 in the nucleus and control its nuclear dynamics. We studied the contributions to these processes resulting from interactions mediated by LC3's hydrophobic protein interaction surface as well as its ability to undergo lipidation. These studies suggest that LC3 associated with large complexes in the nucleus as well, but that binding to these complexes may not be solely responsible for its nuclear localization. Importantly, our results raised several intriguing models for what LC3 might be doing in the nucleus and opened up several avenues for promising future research on the subject.

VII.2.2 New fluorescence microscopy based tools for studying biopolymers *in vivo*

Traditional studies rely on *in vitro* approaches to isolate the molecule before performing an analysis of structure and function, but these approaches are limited, because the function of a protein is highly dependent on its cellular context. Fortunately, new developments in fluorescence microscopy of GFP tagged proteins are making it possible to overcome these limitations. However, these approaches are currently not being widely used to their full potential for reasons that include a lack of easy-to-use analytical tools. In this dissertation, the fluorescence-based microscopy tools that were developed open up new possibilities to study the properties of biopolymers in the physiological context of a living cell.

Diffusion is fundamental to life. The diffusion of molecules over time is what is largely responsible for the transfer of material and information from one place to another at the scale of a cell. For the purposes of measuring diffusion in cells, FRAP is a widely available experimental method. FRAP has the potential to quantitatively measure diffusion coefficients [158]; however, the widespread use of this technology is currently limited by the requirement of experience in programming and mathematics for performing image analysis and non-linear curve fitting routines. In chapter II we presented a freely available software tool called FRAP-Toolbox for the automated analysis of FRAP data. The FRAP-Toolbox software tool promises to make quantitative FRAP more broadly available to the scientific community.

Finally, in chapter V we developed two additional fluorescence microscopy-based assays to probe for LC3 interacting proteins in living cells. To date, most LC3 interacting proteins have been identified using biochemical approaches. We describe three fluorescence microscopy-based assays that can be used to detect the interaction of specific proteins with LC3 in living cells. The first approach is astonishingly simple, as it consists of simple measurements of LC3's N/C ratio in the presence and absence of overexpressed SQSTM1. The analysis of these data was automated using a freely available software utility called LocalizeLC3. The second assay uses FRET microscopy to detect the close physical proximity of Cerulean- and Venus-tagged versions of LC3 with its interacting proteins. We also automated this approach by developing a freely available software utility called abFRET. Finally, we show that FRAP can measure decreases in the diffusional mobility of Venus-LC3 in the presence of overexpressed LC3 interacting proteins. We verified the specificity of these techniques by demonstrating that interactions of SQSTM1 with LC3B were inhibited by F52A and L53A mutations of LC3B's hydrophobic protein binding interface as reported by all three methods. Importantly, these assays take advantage of widely available technologies and offer a complementary approach to existing methods to detect protein interactions with LC3. They can also be readily adapted to characterize other protein complexes in the autophagy pathway.

BIBLIOGRAPHY

[1] Whitesides, G. M.; Ismagilov, R. F. *Science* **1999**, *284*, 89–92.

[2] Hazen, R. M.; Griffin, P. L.; Carothers, J. M.; Szostak, J. W. *Proc Natl Acad Sci U S A* **2007**, *104 Suppl 1*, 8574–8581.

[3] Klionsky, D. J. *Autophagy* **2008**, *4*, 740–743.

[4] Mizushima, N.; Levine, B. *Nat Cell Biol* **2010**, *12*, 823–830.

[5] Yang, Z.; Klionsky, D. J. *Nat Cell Biol* **2010**, *12*, 814–22.

[6] Tsukada, M.; Ohsumi, Y. *FEBS Lett* **1993**, *333*, 169–174.

[7] Harding, T. M.; Morano, K. A.; Scott, S. V.; Klionsky, D. J. *J Cell Biol* **1995**, *131*, 591–602.

[8] Thumm, M.; Egner, R.; Koch, B.; Schlumpberger, M.; Straub, M.; Veenhuis, M.; Wolf, D. H. *FEBS Lett* **1994**, *349*, 275–280.

[9] Behrends, C.; Sowa, M.; Gygi, S.; Harper, J. *Nature* **2010**, *466*, 68–76.

[10] Levine, B.; Mizushima, N.; Virgin, H. W. *Nature* **2011**, *469*, 323–35.

[11] Tsukamoto, S.; Kuma, A.; Murakami, M.; Kishi, C.; Yamamoto, A.; Mizushima, N. *Science* **2008**, *321*, 117–120.

[12] Kuma, A.; Hatano, M.; Matsui, M.; Yamamoto, A.; Nakaya, H.; Yoshimori, T.; Ohsumi, Y.; Tokuhisa, T.; Mizushima, N. *Nature* **2004**, *432*, 1032–1036.

[13] Mortensen, M.; Ferguson, D. J. P.; Edelmann, M.; Kessler, B.; Morten, K. J.; Komatsu, M.; Simon, A. K. *Proc Natl Acad Sci U S A* **2010**, *107*, 832–837.

[14] Ebato, C.; Uchida, T.; Arakawa, M.; Komatsu, M.; Ueno, T.; Komiya, K.; Azuma, K.; Hirose, T.; Tanaka, K.; Kominami, E.; Kawamori, R.; Fujitani, Y.; Watada, H. *Cell Metab* **2008**, *8*, 325–357.

[15] Gonzalez, C. D.; Lee, M. S.; Marchetti, P.; Pietropaolo, M.; Towns, R.; Vaccaro, M. I.; Watada, H.; Wiley, J. W. *Autophagy* **2011**, *7*, 2–11.

[16] Jung, H. et al. *Cell Metab* **2008**, *8*, 318–342.

[17] Elssser, A.; Vogt, A. M.; Nef, H.; Kostin, S.; Mllmann, H.; Skwara, W.; Bode, C.; Hamm, C.; Schaper, J. *J Am Coll Cardiol* **2004**, *43*, 2191–2199.

[18] Hein, S.; Arnon, E.; Kostin, S.; Schnburg, M.; Elssser, A.; Polyakova, V.; Bauer, E.; Klvekorn, W.-P.; Schaper, J. *Circulation* **2003**, *107*, 984–991.

[19] Knaapen, M.; Davies, M.; De Bie, M.; Haven, A.; Martinet, W.; Kockx, M. *Cardiovasc Res* **2001**, *51*, 304–312.

[20] Kockx, M.; De Meyer, G.; Muhring, J.; Jacob, W.; Bult, H.; Herman, A. *Circulation* **1998**, *97*, 2307–2315.

[21] Kostin, S.; Pool, L.; Elssser, A.; Hein, S.; Drexler, H.; Arnon, E.; Hayakawa, Y.; Zimmermann, R.; Bauer, E.; Klvekorn, W.-P.; Schaper, J. *Circ Res* **2003**, *92*, 715–724.

[22] Martinet, W.; Knaapen, M.; Kockx, M.; De Meyer, G. *Trends Mol Med* **2007**, *13*, 482–491.

[23] Nakai, A.; Yamaguchi, O.; Takeda, T.; Higuchi, Y.; Hikoso, S.; Taniike, M.; Omiya, S.; Mizote, I.; Matsumura, Y.; Asahi, M.; Nishida, K.; Hori, M.; Mizushima, N.; Otsu, K. *Nat Med* **2007**, *13*, 619–624.

[24] Levine, B.; Kroemer, G. *Cell* **2008**, *132*, 27–42.

[25] Brest, P.; Corcelle, E. A.; Cesaro, A.; Chargui, A.; Belaid, A.; Klionsky, D. J.; Vouret-Craviari, V.; Hebuterne, X.; Hofman, P.; Mograbi, B. *Curr Mol Med* **2010**, *10*, 486–502.

[26] Deretic, V. *Dig Dis* **2009**, *27*, 246–251.

[27] Kitada, T.; Asakawa, S.; Hattori, N.; Matsumine, H.; Yamamura, Y.; Minoshima, S.; Yokochi, M.; Mizuno, Y.; Shimizu, N. *Nature* **1998**, *392*, 605–608.

[28] Cavey, J. R.; Ralston, S. H.; Hocking, L. J.; Sheppard, P. W.; Ciani, B.; Searle, M. S.; Layfield, R. *J Bone Miner Res* **2005**, *20*, 619–624.

[29] Williams, A.; Sarkar, S.; Cuddon, P.; Ttofi, E. K.; Saiki, S.; Siddiqi, F. H.; Jahreiss, L.; Fleming, A.; Pask, D.; Goldsmith, P.; O'Kane, C. J.; Floto, R. A.; Rubinsztein, D. C. *Nat Chem Biol* **2008**, *4*, 295–305.

[30] Barnett, A.; Brewer, G. J. *J Alzheimers Dis* **2011**, *25*, 385–394.

[31] Chen, Y.; Klionsky, D. *J Cell Sci* **2011**, *124*, 161–170.

[32] Johansen, T.; Lamark, T. *Autophagy* **2011**, *7*, 279–375.

[33] Strmhaug, P. E.; Berg, T. O.; Fengsrud, M.; Seglen, P. O. *Biochem J* **1998**, *335 (Pt 2)*, 217–224.

[34] Fengsrud, M.; Roos, N.; Berg, T.; Liou, W.; Slot, J. W.; Seglen, P. O. *Exp Cell Res* **1995**, *221*, 504–519.

[35] Axe, E. L.; Walker, S. A.; Manifava, M.; Chandra, P.; Roderick, H. L.; Habermann, A.; Griffiths, G.; Ktistakis, N. T. *J Cell Biol* **2008**, *182*, 685–701.

[36] Hailey, D. W.; Rambold, A. S.; Satpute-Krishnan, P.; Mitra, K.; Sougrat, R.; Kim, P. K.; Lippincott-Schwartz, J. *Cell* **2010**, *141*, 656–667.

[37] Ravikumar, B.; Moreau, K.; Jahreiss, L.; Puri, C.; Rubinsztein, D. C. *Nat Cell Biol* **2010**, *12*, 747–757.

[38] Weidberg, H.; Shvets, E.; Elazar, Z. *Annu Rev Biochem* **2011**, *80*, 125–156.

[39] Ge, L.; Melville, D.; Zhang, M.; Schekman, R. *Elife* **2013**, *2*, e00947.

[40] Yang, Z.; Klionsky, D. *Curr Opin Cell Biol* **2010**, *22*, 124–131.

[41] Mercer, C. A.; Kaliappan, A.; Dennis, P. B. *Autophagy* **2009**, *5*, 649–662.

[42] Hara, T.; Takamura, A.; Kishi, C.; Iemura, S.-I.; Natsume, T.; Guan, J.-L.; Mizushima, N. *J Cell Biol* **2008**, *181*, 497–510.

[43] Jung, C. H.; Jun, C. B.; Ro, S.-H.; Kim, Y.-M.; Otto, N. M.; Cao, J.; Kundu, M.; Kim, D.-H. *Mol Biol Cell* **2009**, *20*, 1992–2003.

[44] Kraft, C.; Kijanska, M.; Kalie, E.; Siergiejuk, E.; Lee, S.; Semplicio, G.; Stoffel, I.; Brezovich, A.; Verma, M.; Hansmann, I.; Ammerer, G.; Hofmann, K.; Tooze, S.; Peter, M. *EMBO J* **2012**, *31*, 3691–3703.

[45] Alemu, E.; Lamark, T.; Torgersen, K.; Birgisdottir, A.; Larsen, K.; Jain, A.; Olsvik, H.; vervatn, A.; Kirkin, V.; Johansen, T. *J Biol Chem* **2012**, *287*, 39275–39290.

[46] Yan, Y.; Flinn, R. J.; Wu, H.; Schnur, R. S.; Backer, J. M. *Biochem J* **2009**, *417*, 747–755.

[47] Furuya, N.; Yu, J.; Byfield, M.; Pattingre, S.; Levine, B. *Autophagy* **2005**, *1*, 46–52.

[48] Furuya, T.; Kim, M.; Lipinski, M.; Li, J.; Kim, D.; Lu, T.; Shen, Y.; Rameh, L.; Yankner, B.; Tsai, L.-H.; Yuan, J. *Mol Cell* **2010**, *38*, 500–511.

[49] Fimia, G. M.; Stoykova, A.; Romagnoli, A.; Giunta, L.; Di Bartolomeo, S.; Nardacci, R.; Corazzari, M.; Fuoco, C.; Ucar, A.; Schwartz, P.; Gruss, P.; Piacentini, M.; Chowdhury, K.; Cecconi, F. *Nature* **2007**, *447*, 1121–1125.

[50] Takahashi, Y.; Coppola, D.; Matsushita, N.; Cualing, H. D.; Sun, M.; Sato, Y.; Liang, C.; Jung, J. U.; Cheng, J. Q.; Mul, J. J.; Pledger, W. J.; Wang, H.-G. *Nat Cell Biol* **2007**, *9*, 1142–1151.

[51] Liang, C.; Feng, P.; Ku, B.; Dotan, I.; Canaani, D.; Oh, B.-H.; Jung, J. U. *Nat Cell Biol* **2006**, *8*, 688–699.

[52] Matsunaga, K.; Saitoh, T.; Tabata, K.; Omori, H.; Satoh, T.; Kurotori, N.; Maejima, I.; Shirahama-Noda, K.; Ichimura, T.; Isobe, T.; Akira, S.; Noda, T.; Yoshimori, T. *Nat Cell Biol* **2009**, *11*, 385–396.

[53] Zhong, Y.; Wang, Q. J.; Li, X.; Yan, Y.; Backer, J. M.; Chait, B. T.; Heintz, N.; Yue, Z. *Nat Cell Biol* **2009**, *11*, 468–476.

[54] Fass, E.; Shvets, E.; Degani, I.; Hirschberg, K.; Elazar, Z. *Journal of Biological Chemistry* **2006**, *281*, 36303–36316.

[55] Jahreiss, L.; Menzies, F. M.; Rubinsztein, D. C. *Traffic* **2008**, *9*, 574–587.

[56] Kimura, S.; Noda, T.; Yoshimori, T. *Cell Struct Funct* **2008**, *33*, 109–122.

[57] Kchl, R.; Hu, X. W.; Chan, E. Y. W.; Tooze, S. A. *Traffic* **2006**, *7*, 129–145.

[58] Geeraert, C.; Ratier, A.; Pfisterer, S. G.; Perdiz, D.; Cantaloube, I.; Rouault, A.; Pattingre, S.; Proikas-Cezanne, T.; Codogno, P.; Pos, C. *J Biol Chem* **2010**, *285*, 24184–24194.

[59] Pankiv, S.; Alemu, E.; Brech, A.; Bruun, J.-A.; Lamark, T.; Overvatn, A.; Bjrky, G.; Johansen, T. *J Cell Biol* **2010**, *188*, 253–269.

[60] Lee, J.-Y.; Koga, H.; Kawaguchi, Y.; Tang, W.; Wong, E.; Gao, Y.-S.; Pandey, U. B.; Kaushik, S.; Tresse, E.; Lu, J.; Taylor, J. P.; Cuervo, A. M.; Yao, T.-P. *EMBO J* **2010**, *29*, 969–980.

[61] Gutierrez, M. G.; Munaf, D. B.; Bern, W.; Colombo, M. I. *J Cell Sci* **2004**, *117*, 2687–2697.

[62] Jger, S.; Bucci, C.; Tanida, I.; Ueno, T.; Kominami, E.; Saftig, P.; Eskelinen, E.-L. *J Cell Sci* **2004**, *117*, 4837–4848.

[63] Fader, C. M.; Snchez, D. G.; Mestre, M. B.; Colombo, M. I. *Biochim Biophys Acta* **2009**, *1793*, 1901–1916.

[64] Furuta, N.; Fujita, N.; Noda, T.; Yoshimori, T.; Amano, A. *Mol Biol Cell* **2010**, *21*, 1001–1010.

[65] Nair, U. et al. *Cell* **2011**, *146*, 290–302.

[66] Moscat, J.; Diaz-Meco, M. T.; Wooten, M. W. *Trends Biochem Sci* **2007**, *32*, 95–100.

[67] Bjrky, G.; Lamark, T.; Brech, A.; Outzen, H.; Perander, M.; Overvatn, A.; Stenmark, H.; Johansen, T. *J Cell Biol* **2005**, *171*, 603–614.

[68] Pankiv, S.; Clausen, T.; Lamark, T.; Brech, A.; Bruun, J.-A.; Outzen, H.; vervatn, A.; Bjrky, G.; Johansen, T. *J Biol Chem* **2007**, *282*, 24131–24145.

[69] Kirkin, V. et al. *Mol Cell* **2009**, *33*, 505–516.

[70] Gao, Z.; Gammoh, N.; Wong, P.-M.; Erdjument-Bromage, H.; Tempst, P.; Jiang, X. *Autophagy* **2010**, *6*, 126–137.

[71] Ding, W.-X.; Ni, H.-M.; Li, M.; Liao, Y.; Chen, X.; Stolz, D. B.; Dorn, G. W., 2nd; Yin, X.-M. *J Biol Chem* **2010**, *285*, 27879–27890.

[72] Geisler, S.; Holmstrm, K. M.; Skujat, D.; Fiesel, F. C.; Rothfuss, O. C.; Kahle, P. J.; Springer, W. *Nat Cell Biol* **2010**, *12*, 119–131.

[73] Kim, P.; Hailey, D.; Mullen, R.; Lippincott-Schwartz, J. *Proc Natl Acad Sci U S A* **2008**, *105*, 20567–20574.

[74] Lee, J.-Y.; Nagano, Y.; Taylor, J. P.; Lim, K. L.; Yao, T.-P. *J Cell Biol* **2010**, *189*, 671–679.

[75] Hanna, R.; Quinsay, M.; Orogo, A.; Giang, K.; Rikka, S.; Gustafsson, s. B. *J Biol Chem* **2012**, *287*, 19094–19104.

[76] Zheng, Y. T.; Shahnazari, S.; Brech, A.; Lamark, T.; Johansen, T.; Brumell, J. H. *J Immunol* **2009**, *183*, 5909–5916.

[77] Kraft, C.; Deplazes, A.; Sohrmann, M.; Peter, M. *Nat Cell Biol* **2008**, *10*, 602–610.

[78] Kim, J.-E.; You, D.-J.; Lee, C.; Ahn, C.; Seong, J. Y.; Hwang, J.-I. *Cell Signal* **2010**, *22*, 1645–1654.

[79] Shpilka, T.; Weidberg, H.; Pietrokovski, S.; Elazar, Z. *Genome Biol* **2011**, *12*, 226.

[80] Weidberg, H.; Shvets, E.; Shpilka, T.; Shimron, F.; Shinder, V.; Elazar, Z. *EMBO J* **2010**, *29*, 1792–1802.

[81] He, H.; Dang, Y.; Dai, F.; Guo, Z.; Wu, J.; She, X.; Pei, Y.; Chen, Y.; Ling, W.; Wu, C.; Zhao, S.; Liu, J. O.; Yu, L. *J Biol Chem* **2003**, *278*, 29278–29287.

[82] Egami, Y.; Kiryu-Seo, S.; Yoshimori, T.; Kiyama, H. *Biochem Biophys Res Commun* **2005**, *337*, 1206–1213.

[83] Zois, C. E.; Giatromanolaki, A.; Kainulainen, H.; Botaitis, S.; Torvinen, S.; Simopoulos, C.; Kortsaris, A.; Sivridis, E.; Koukourakis, M. I. *Biochem Biophys Res Commun* **2011**, *404*, 552–558.

[84] Ichimura, Y.; Kirisako, T.; Takao, T.; Satomi, Y.; Shimonishi, Y.; Ishihara, N.; Mizushima, N.; Tanida, I.; Kominami, E.; Ohsumi, M.; Noda, T.; Ohsumi, Y. *Nature* **2000**, *408*, 488–492.

[85] Geng, J.; Klionsky, D. J. *EMBO Rep* **2008**, *9*, 859–64.

[86] Tanida, I.; Ueno, T.; Kominami, E. *J Biol Chem* **2004**, *279*, 47704–47710.

[87] Tanida, I.; Sou, Y.-s.; Ezaki, J.; Minematsu-Ikeguchi, N.; Ueno, T.; Kominami, E. *J Biol Chem* **2004**, *279*, 36268–36276.

[88] Fujita, N.; Itoh, T.; Omori, H.; Fukuda, M.; Noda, T.; Yoshimori, T. *Mol Biol Cell* **2008**, *19*, 2092–2100.

[89] Mizushima, N.; Kuma, A.; Kobayashi, Y.; Yamamoto, A.; Matsubae, M.; Takao, T.; Natsume, T.; Ohsumi, Y.; Yoshimori, T. *J Cell Sci* **2003**, *116*, 1679–1688.

[90] Kabeya, Y.; Mizushima, N.; Ueno, T.; Yamamoto, A.; Kirisako, T.; Noda, T.; Kominami, E.; Ohsumi, Y.; Yoshimori, T. *EMBO J* **2000**, *19*, 5720–8.

[91] Kabeya, Y.; Mizushima, N.; Yamamoto, A.; Oshitani-Okamoto, S.; Ohsumi, Y.; Yoshimori, T. *J Cell Sci* **2004**, *117*, 2805–12.

[92] Xie, Z.; Nair, U.; Klionsky, D. *Mol Biol Cell* **2008**, *19*, 3290–3298.

[93] Nakatogawa, H.; Ichimura, Y.; Ohsumi, Y. *Cell* **2007**, *130*, 165–178.

[94] Weidberg, H.; Shpilka, T.; Shvets, E.; Abada, A.; Shimron, F.; Elazar, Z. *Dev Cell* **2011**, *20*, 444–454.

[95] Cherra, S.; Kulich, S.; Uechi, G.; Balasubramani, M.; Mountzouris, J.; Day, B.; Chu, C. *J Cell Biol* **2010**, *190*, 533–542.

[96] Lee, I. H.; Finkel, T. *J Biol Chem* **2009**, *284*, 6322–6328.

[97] Sugawara, K.; Suzuki, N. N.; Fujioka, Y.; Mizushima, N.; Ohsumi, Y.; Inagaki, F. *Genes Cells* **2004**, *9*, 611–618.

[98] Coyle, J. E.; Qamar, S.; Rajashankar, K. R.; Nikolov, D. B. *Neuron* **2002**, *33*, 63–74.

[99] Ichimura, Y.; Imamura, Y.; Emoto, K.; Umeda, M.; Noda, T.; Ohsumi, Y. *J Biol Chem* **2004**, *279*, 40584–40592.

[100] Shvets, E.; Fass, E.; Scherz-Shouval, R.; Elazar, Z. *J Cell Sci* **2008**, *121*, 2685–2695.

[101] Satoo, K.; Noda, N. N.; Kumeta, H.; Fujioka, Y.; Mizushima, N.; Ohsumi, Y.; Inagaki, F. *EMBO J* **2009**, *28*, 1341–50.

[102] Taherbhoy, A.; Tait, S.; Kaiser, S.; Williams, A.; Deng, A.; Nourse, A.; Hammel, M.; Kurinov, I.; Rock, C.; Green, D.; Schulman, B. *Mol Cell* **2011**, *44*, 451–461.

[103] Noda, N.; Satoo, K.; Fujioka, Y.; Kumeta, H.; Ogura, K.; Nakatogawa, H.; Ohsumi, Y.; Inagaki, F. *Mol Cell* **2011**, *44*, 462–475.

[104] Hong, S.; Kim, B.-W.; Lee, K.-E.; Kim, S.; Jeon, H.; Kim, J.; Song, H. *Nat Struct Mol Biol* **2011**, *18*, 1323–1330.

[105] Kuma, A.; Matsui, M.; Mizushima, N. *Autophagy* **2007**, *3*, 323–328.

[106] Tanida, I.; Yamaji, T.; Ueno, T.; Ishiura, S.; Kominami, E.; Hanada, K. *Autophagy* **2008**, *4*, 131–134.

[107] Pacheco, V.; Ma, P.; Thielmann, Y.; Hartmann, R.; Weiergraber, O. H.; Mohrluder, J.; Willbold, D. *J Biomol NMR* **2010**, *48*, 49–58.

[108] Nymann-Andersen, J.; Wang, H.; Olsen, R. W. *Neuropharmacology* **2002**, *43*, 476–81.

[109] Mann, S.; Hammarback, J. *J Biol Chem* **1994**, *269*, 11492–11497.

[110] Kouno, T.; Mizuguchi, M.; Tanida, I.; Ueno, T.; Kanematsu, T.; Mori, Y.; Shinoda, H.; Hirata, M.; Kominami, E.; Kawano, K. *J Biol Chem* **2005**, *280*, 24610–24617.

[111] Seidenbecher, C.; Landwehr, M.; Smalla, K.-H.; Kreutz, M.; Dieterich, D.; Zuschratter, W.; Reissner, C.; Hammarback, J.; Bckers, T.; Gundelfinger, E.; Kreutz, M. *J Mol Biol* **2004**, *336*, 957–1027.

[112] Pedrotti, B.; Islam, K. *Cell Motil Cytoskeleton* **1995**, *30*, 301–309.

[113] Faller, E. M.; Villeneuve, T. S.; Brown, D. L. *Molecular and Cellular Neuroscience* **2009**, *41*, 85–93.

[114] Sagiv, Y.; Legesse-Miller, A.; Porat, A.; Elazar, Z. *EMBO J* **2000**, *19*, 1494–1504.

[115] Nakamura, T.; Hayashi, T.; Nasu-Nishimura, Y.; Sakaue, F.; Morishita, Y.; Okabe, T.; Ohwada, S.; Matsuura, K.; Akiyama, T. *Genes Dev* **2008**, *22*, 1244–1256.

[116] Popovic, D.; Akutsu, M.; Novak, I.; Harper, J.; Behrends, C.; Dikic, I. *Mol Cell Biol* **2012**, *32*, 1733–1744.

[117] Zhou, B.; Rabinovitch, M. *Circ Res* **1998**, *83*, 481–490.

[118] Zhou, B.; Boudreau, N.; Coulber, C.; Hammarback, J.; Rabinovitch, M. *J Clin Invest* **1997**, *100*, 3070.

[119] Ying, L.; Lau, A.; Alvira, C. M.; West, R.; Cann, G. M.; Zhou, B.; Kinnear, C.; Jan, E.; Sarnow, P.; Van de Rijn, M.; Rabinovitch, M. *J Cell Sci* **2009**, *122*, 1441–1451.

[120] Karim, M. R.; Kanazawa, T.; Daigaku, Y.; Fujimura, S.; Miotto, G.; Kadowaki, M. *Autophagy* **2007**, *3*, 553–560.

[121] Drake, K.; Kang, M.; Kenworthy, A. *PLoS One* **2010**, *5*, e9806.

[122] Seillier, M.; Peuget, S.; Gayet, O.; Gauthier, C.; N'Guessan, P.; Monte, M.; Carrier, A.; Iovanna, J. L.; Dusetti, N. J. *Cell Death Differ* **2012**, *19*, 1525–1535.

[123] Sancho, A.; Duran, J.; Garca-Espaa, A.; Mauvezin, C.; Alemu, E. A.; Lamark, T.; Macias, M. J.; DeSalle, R.; Royo, M.; Sala, D.; Chicote, J. U.; Palacn, M.; Johansen, T.; Zorzano, A. *PLoS One* **2012**, *7*, e34034.

[124] Nowak, J.; Archange, C.; Tardivel-Lacombe, J.; Pontarotti, P.; Pbusque, M.-J.; Vaccaro, M.; Velasco, G.; Dagorn, J.-C.; Iovanna, J. *Mol Biol Cell* **2009**, *20*, 870–951.

[125] Mauvezin, C.; Orpinell, M.; Francis, V.; Mansilla, F.; Duran, J.; Ribas, V.; Palacn, M.; Boya, P.; Teleman, A.; Zorzano, A. *EMBO Rep* **2010**, *11*, 37–81.

[126] Martinez-Lopez, N.; Athonvarangkul, D.; Mishall, P.; Sahu, S.; Singh, R. *Nature Communications* **2013**, *4*.

[127] Noda, N.; Kumeta, H.; Nakatogawa, H.; Satoo, K.; Adachi, W.; Ishii, J.; Fujioka, Y.; Ohsumi, Y.; Inagaki, F. *Genes Cells* **2008**, *13*, 1211–1218.

[128] Amar, N.; Lustig, G.; Ichimura, Y.; Ohsumi, Y.; Elazar, Z. *EMBO reports* **2006**, *7*, 635–642.

[129] Ichimura, Y.; Kumanomidou, T.; Sou, Y.-s.; Mizushima, T.; Ezaki, J.; Ueno, T.; Kominami, E.; Yamane, T.; Tanaka, K.; Komatsu, M. *J Biol Chem* **2008**, *283*, 22847–22857.

[130] Shvets, E.; Elazar, Z. *Autophagy* **2008**, *4*, 1054–1056.

[131] Robbins, S. M.; Quintrell, N. A.; Bishop, J. M. *Mol Cell Biol* **1995**, *15*, 3507–3515.

[132] Lippincott-Schwartz, J.; Snapp, E.; Kenworthy, A. K. *Nat Rev Mol Cell Biol* **2001**, *2*, 444–456.

[133] Forster, T. *Die Naturwissenschaften* **1946**, *33*, 166–175.

[134] Stryer, L.; Haugland, R. P. *Proc Natl Acad Sci U S A* **1967**, *58*, 719–726.

[135] Lakowicz, J. R. *Principles of fluorescence spectroscopy*, 3rd ed.; Springer: New York, 2006; pp xxvi, 954 p.

[136] Day, R. N.; Davidson, M. W. *Bioessays* **2012**, *34*, 341–350.

[137] Thaler, C.; Koushik, S. V.; Blank, P. S.; Vogel, S. S. *Biophys J* **2005**, *89*, 2736–2749.

[138] Jacobson, K.; Derzko, Z.; Wu, E. S.; Hou, Y.; Poste, G. *J Supramol Struct* **1976**, *5*, 565(417)–576(428).

[139] Edidin, M.; Zagyansky, Y.; Lardner, T. J. *Science* **1976**, *191*, 466–8.

[140] Axelrod, D.; Koppel, D. E.; Schlessinger, J.; Elson, E.; Webb, W. W. *Biophys J* **1976**, *16*, 1055–69.

[141] Mai, J.; Trump, S.; Ali, R.; Schiltz, R. L.; Hager, G.; Hanke, T.; Lehmann, I.; Attinger, S. *Biophysical journal* **2011**, *100*, 1178–1188.

[142] Mller, J.; Chen, Y.; Gratton, E. *Methods Enzymol* **2003**, *361*, 69–92.

[143] Haustein, E.; Schwille, P. *Annu Rev Biophys Biomol Struct* **2007**, *36*, 151–169.

[144] Qian, H.; Sheetz, M.; Elson, E. *Biophys J* **1991**, *60*, 910–921.

[145] Jaqaman, K.; Loerke, D.; Mettlen, M.; Kuwata, H.; Grinstein, S.; Schmid, S.; Danuser, G. *Nat Methods* **2008**, *5*, 695–702.

[146] Saxton, M. *Biophys J* **1997**, *72*, 1744–1753.

[147] Mazerik, J. N.; Kraft, L. J.; Kenworthy, A. K.; Tyska, M. J. *Biophys J* **2014**, *106*, 649–658.

[148] Sprague, B. L.; Pego, R. L.; Stavreva, D. A.; McNally, J. G. *Biophys J* **2004**, *86*, 3473–95.

[149] Kang, M.; Day, C. A.; DiBenedetto, E.; Kenworthy, A. K. *Biophys J* **2010**, *99*, 2737–2747.

[150] Mller, P.; Rogers, K. W.; Jordan, B. M.; Lee, J. S.; Robson, D.; Ramanathan, S.; Schier, A. F. *Science* **2012**, *336*, 721–724.

[151] Mueller, F.; Mazza, D.; Stasevich, T. J.; McNally, J. G. *Curr Opin Cell Biol* **2010**, *22*, 403–411.

[152] Conrad, C.; Wnsche, A.; Tan, T. H.; Bulkescher, J.; Sieckmann, F.; Verissimo, F.; Edelstein, A.; Walter, T.; Liebel, U.; Pepperkok, R.; Ellenberg, J. *Nat Methods* **2011**, *8*, 246–249.

[153] Wang, L.; Chen, M.; Yang, J.; Zhang, Z. *Autophagy* **2013**, *9*, 65–78.

[154] Sprouse, R. O.; Karpova, T. S.; Mueller, F.; Dasgupta, A.; McNally, J. G.; Auble, D. T. *Proc Natl Acad Sci U S A* **2008**, *105*, 13304–13308.

[155] Braga, J.; Desterro, J. M.; Carmo-Fonseca, M. *Mol Biol Cell* **2004**, *15*, 4749–60.

[156] Sprague, B. L.; Müller, F.; Pego, R. L.; Bungay, P. M.; Stavreva, D. A.; McNally, J. G. *Biophysical journal* **2006**, *91*, 1169–1191.

[157] Mueller, F.; Wach, P.; McNally, J. G. *Biophys J* **2008**, *94*, 3323–39.

[158] Kang, M.; Day, C. A.; Drake, K.; Kenworthy, A. K.; DiBenedetto, E. *Biophys J* **2009**, *97*, 1501–11.

[159] Stasevich, T. J.; Mueller, F.; Brown, D. T.; McNally, J. G. *EMBO J* **2010**, *29*, 1225–1234.

[160] Montero Llopis, P.; Sliusarenko, O.; Heinritz, J.; Jacobs-Wagner, C. *Biophysical journal* **2012**, *103*, 1848–1859.

[161] Linkert, M. et al. *J Cell Biol* **2010**, *189*, 777–782.

[162] Benesh, A. E.; Nambiar, R.; McConnell, R. E.; Mao, S.; Tabb, D. L.; Tyska, M. J. *Mol Biol Cell* **2010**, *21*, 970–978.

[163] Cardarelli, F.; Tosti, L.; Serresi, M.; Beltram, F.; Bizzarri, R. *J Biol Chem* **2012**, *287*, 5554–5561.

[164] Kraft, L. J.; Nguyen, T. A.; Vogel, S. S.; Kenworthy, A. K. *Autophagy* **2014**, *10*.

[165] Kraft, L. J.; Kenworthy, A. K. *J Biomed Opt* **2012**, *17*, 0110081–01100812.

[166] Mizushima, N.; Sugita, H.; Yoshimori, T.; Ohsumi, Y. *J Biol Chem* **1998**, *273*, 33889–33892.

[167] Kaufmann, A.; Beier, V.; Franquelim, H. G.; Wollert, T. *Cell* **2014**, *156*, 469–481.

[168] Hanada, T.; Noda, N.; Satomi, Y.; Ichimura, Y.; Fujioka, Y.; Takao, T.; Inagaki, F.; Ohsumi, Y. *J Biol Chem* **2007**, *282*, 37298–37302.

[169] Maskey, D.; Yousefi, S.; Schmid, I.; Zlobec, I.; Perren, A.; Friis, R.; Simon, H.-U. *Nat Commun* **2013**, *4*, 2130.

[170] Wei, X.; Henke, V. G.; Strübing, C.; Brown, E. B.; Clapham, D. E. *Biophys J* **2003**, *84*, 1317–1327.

[171] Day, C. A.; Kraft, L. J.; Kang, M.; Kenworthy, A. K. *Current Protocols in Cytometry* **2012**, 2–19.

[172] Shintani, T.; Huang, W.-P.; Stromhaug, P.; Klionsky, D. *Dev Cell* **2002**, *3*, 825–837.

[173] Fujita, N.; Hayashi-Nishino, M.; Fukumoto, H.; Omori, H.; Yamamoto, A.; Noda, T.; Yoshimori, T. *Mol Biol Cell* **2008**, *19*, 4651–4660.

[174] Shpilka, T.; Mizushima, N.; Elazar, Z. *J Cell Sci* **2012**, *125*, 2343–2348.

[175] Kang, M.; Day, C.; Kenworthy, A.; Dibenedetto, E. *Traffic* **2012**, *13*, 1589–600.

[176] Nguyen, T.; Sarkar, P.; Veetil, J.; Koushik, S.; Vogel, S. *PLoS One* **2012**, *7*.

[177] Archuleta, T. L.; Du, Y.; English, C. A.; Lory, S.; Lesser, C.; Ohi, M. D.; Ohi, R.; Spiller, B. W. *Journal of Biological Chemistry* **2011**, *286*, 33992–33998.

[178] Vogel, S. S.; Thaler, C.; Koushik, S. V. *Sci STKE* **2006**, *2006*, re2–.

[179] Piston, D. W.; Kremers, G. J. *Trends Biochem Sci* **2007**, *32*, 407–14.

[180] Vogel, S. S.; Thaler, C.; Blank, P.; Koushik, S. V. In *FLIM Microscopy in Biology and Medicine*; Periasamy, A., Clegg, R. M., Eds.; Taylor & Francis: Boca Raton, 2010; pp 245–290.

[181] Lavalette, D.; Amand, B.; Pochon, F. *Proc Natl Acad Sci U S A* **1977**, *74*, 1407–1411.

[182] Koppel, D. *Biochemistry (Mosc)* **1974**, *13*, 2712–2719.

[183] Geng, J.; Klionsky, D. *Autophagy* **2010**, *6*, 144–147.

[184] Thaler, C.; Koushik, S.; Puhl, H.; Blank, P.; Vogel, S. *Proc Natl Acad Sci U S A* **2009**, *106*, 6369–6374.

[185] Chen, Y.; Mller, J.; Ruan, Q.; Gratton, E. *Biophys J* **2002**, *82*, 133–144.

[186] Verveer, P. J.; Bastiaens, P. I. *Histochem Cell Biol* **2008**, *130*, 833–43.

[187] Dehmelt, L.; Bastiaens, P. I. *Nat Rev Mol Cell Biol* **2010**, *11*, 440–52.

[188] Sung, M. H.; McNally, J. G. *Wiley Interdiscip Rev Syst Biol Med* **2011**, *3*, 167–82.

[189] Periasamy, A.; Day, R. N. *Methods Cell Biol* **1999**, *58*, 293–314.

[190] Demarco, I. A.; Periasamy, A.; Booker, C. F.; Day, R. N. *Nat Methods* **2006**, *3*, 519–24.

[191] Jares-Erijman, E. A.; Jovin, T. M. *Nat Biotechnol* **2003**, *21*, 1387–1395.

[192] Wouters, F. S.; Bastiaens, P. I. H.; Wirtz, K. W. A.; Jovin, T. M. *EMBO J* **1998**, *17*, 7179–7189.

[193] Gordon, G. W.; Berry, G.; Liang, X. H.; Levine, B.; Herman, B. *Biophys J* **1998**, *74*, 2702–2713.

[194] Chen, Y.; Lagerholm, B. C.; Yang, B.; Jacobson, K. *Methods* **2006**, *39*, 147–53.

[195] Goodwin, J. S.; Kenworthy, A. K. *Methods* **2005**, *37*, 154–64.

[196] Michelman-Ribeiro, A.; Mazza, D.; Rosales, T.; Stasevich, T. J.; Boukari, H.; Rishi, V.; Vinson, C.; Knutson, J. R.; McNally, J. G. *Biophys J* **2009**, *97*, 337–46.

[197] Reits, E. A. J.; Neefjes, J. J. *Nat Cell Biol* **2001**, *3*, E145–E147.

[198] Kim, S. A.; Heinze, K. G.; Schwille, P. *Nat Methods* **2007**, *4*, 963–73.

[199] Slaughter, B. D.; Schwartz, J. W.; Li, R. *Proc Natl Acad Sci U S A* **2007**, *104*, 20320–5.

[200] Ohsumi, Y. *Nat Rev Mol Cell Biol* **2001**, *2*, 211–6.

[201] Kirisako, T.; Ichimura, Y.; Okada, H.; Kabeya, Y.; Mizushima, N.; Yoshimori, T.; Ohsumi, M.; Takao, T.; Noda, T.; Ohsumi, Y. *J Cell Biol* **2000**, *151*, 263–76.

[202] Periasamy, A.; Clegg, R. M. *FLIM microscopy in biology and medicine*; Taylor & Francis: Boca Raton, 2010; pp xxix, 407 p.

[203] Periasamy, A.; Day, R. N. *Molecular imaging: FRET microscopy and spectroscopy*; The American Physiological Society methods in physiology series; Oxford University Press, Inc.: New York, New York, 2005; pp xv, 312 p.

[204] Rizzo, M. A.; Springer, G. H.; Granada, B.; Piston, D. W. *Nat Biotechnol* **2004**, *22*, 445–9.

[205] Koushik, S. V.; Chen, H.; Thaler, C.; Puhl, r., H. L.; Vogel, S. S. *Biophys J* **2006**, *91*, L99–L101.

[206] Hinow, P.; Rogers, C. E.; Barbieri, C. E.; Pietenpol, J. A.; Kenworthy, A. K.; DiBenedetto, E. *Biophys J* **2006**, *91*, 330–42.

[207] Delatorre, J. G.; Martinez, M. C. L.; Tirado, M. M. *Biopolymers* **1984**, *23*, 611–615.

[208] la Cour, T.; Kiemer, L.; Molgaard, A.; Gupta, R.; Skriver, K.; Brunak, S. *Protein Eng Des Sel* **2004**, *17*, 527–36, 1741-0126 (Print) Journal Article Research Support, Non-U.S. Gov't.

[209] Chen, Y.; Muller, J. D.; So, P. T.; Gratton, E. *Biophys J* **1999**, *77*, 553–67.

[210] Kenworthy, A. K. *Methods* **2001**, *24*, 289–96.

[211] Choi, A. M. K.; Ryter, S. W.; Levine, B. *N Engl J Med* **2013**, *368*, 651–662.

[212] Birgisdottir, Å. B.; Lamark, T.; Johansen, T. *J Cell Sci* **2013**, *126*, 3237–3247.

[213] Lamark, T.; Kirkin, V.; Dikic, I.; Johansen, T. *Cell Cycle* **2009**, *8*, 1986–1990.

[214] Ichimura, Y.; Komatsu, M. *Semin Immunopathol* **2010**, *32*, 431–436.

[215] Komatsu, M. et al. *Cell* **2007**, *131*, 1149–1163.

[216] Ishikawa-Ankerhold, H. C.; Ankerhold, R.; Drummen, G. P. C. *Molecules* **2012**, *17*, 4047–4132.

[217] Masi, A.; Cicchi, R.; Carloni, A.; Pavone, F. S.; Arcangeli, A. *Adv Exp Med Biol* **2010**, *674*, 33–42.

[218] Miyawaki, A. *Annu Rev Biochem* **2011**, *80*, 357–373.

[219] Zal, T. *Self Nonself* **2011**, *2*, 98–107.

[220] Grecco, H. E.; Verveer, P. J. *Chemphyschem* **2011**, *12*, 484–490.

[221] Sun, Y.; Wallrabe, H.; Seo, S.-A.; Periasamy, A. *Chemphyschem* **2011**, *12*, 462–474.

[222] Becker, W. *J Microsc* **2012**, *247*, 119–136.

[223] Brzostowski, J. A.; Meckel, T.; Hong, J.; Chen, A.; Jin, T. *Curr Protoc Protein Sci* **2009**, *Chapter 19*, Unit19.5.

[224] Chan, F. T. S.; Kaminski, C. F.; Kaminski Schierle, G. S. *Chemphyschem* **2011**, *12*, 500–509.

[225] Chen, Y.; Mauldin, J. P.; Day, R. N.; Periasamy, A. *J Microsc* **2007**, *228*, 139–152.

[226] Kaminski, C. F.; Rees, E. J.; Schierle, G. S. K. *Methods Mol Biol* **2014**, *1076*, 445–454.

[227] Piston, D. W.; Rizzo, M. A. *Methods Cell Biol* **2008**, *85*, 415–430.

[228] Sun, Y.; Day, R. N.; Periasamy, A. *Nat Protoc* **2011**, *6*, 1324–1340.

[229] Fitzpatrick, J. A. J.; Lillemeier, B. F. *Curr Opin Struct Biol* **2011**, *21*, 650–660.

[230] Lippincott-Schwartz, J.; Altan-Bonnet, N.; Patterson, G. *Nat Cell Biol* **2003**, *Suppl*, S7–14.

[231] Weiss, M. *Ann N Y Acad Sci* **2008**, *1130*, 21–27.

[232] Deschout, H.; Hagman, J.; Fransson, S.; Jonasson, J.; Rudemo, M.; Lorn, N.; Braeckmans, K. *Opt Express* **2010**, *18*, 22886–22905.

[233] Pucadyil, T. J.; Chattopadhyay, A. *J Fluoresc* **2006**, *16*, 87–94.

[234] Seiffert, S.; Oppermann, W. *J Microsc* **2005**, *220*, 20–30.

[235] Mazza, D.; Abernathy, A.; Golob, N.; Morisaki, T.; McNally, J. G. *Nucleic Acids Res* **2012**, *40*, e119.

[236] Pankiv, S.; Lamark, T.; Bruun, J.-A.; vervatn, A.; Bjrky, G.; Johansen, T. *J Biol Chem* **2010**, *285*, 5941–5994.

[237] Karpova, T.; McNally, J. G. *Curr Protoc Cytom* **2006**, *Chapter 12*, Unit12.7.

[238] Van Munster, E. B.; Kremers, G. J.; Adjobo-Hermans, M. J. W.; Gadella, T. W. J., Jr *J Microsc* **2005**, *218*, 253–262.

[239] Lamark, T.; Perander, M.; Outzen, H.; Kristiansen, K.; vervatn, A.; Michaelsen, E.; Bjrky, G.; Johansen, T. *J Biol Chem* **2003**, *278*, 34568–34581.

[240] Wilson, M. I.; Gill, D. J.; Perisic, O.; Quinn, M. T.; Williams, R. L. *Mol Cell* **2003**, *12*, 39–50.

[241] Itakura, E.; Mizushima, N. *The Journal of cell biology* **2011**, *192*, 17–27.

[242] Abdul Rahim, N. A.; Pelet, S.; Mofrad, M. R. K.; So, P. T. C.; Kamm, R. D. *Methods* **2014**, *66*, 208–221.

[243] Kofoed, E. M.; Guerbadot, M.; Schaufele, F. *J Biol Chem* **2010**, *285*, 2428–2437.

[244] Merzlyakov, M.; Hristova, K. *Methods Enzymol* **2008**, *450*, 107–127.

[245] Kenworthy, A. K.; Edidin, M. *J Cell Biol* **1998**, *142*, 69–84.

[246] Berney, C.; Danuser, G. *Biophys J* **2003**, *84*, 3992–4010.

[247] King, C.; Sarabipour, S.; Byrne, P.; Leahy, D. J.; Hristova, K. *Biophys J* **2014**, *106*, 1309–1317.

[248] Zacharias, D. A.; Violin, J. D.; Newton, A. C.; Tsien, R. Y. *Science* **2002**, *296*, 913–916.

[249] Padilla-Parra, S.; Tramier, M. *Bioessays* **2012**, *34*, 369–376.

[250] Pietraszewska-Bogiel, A.; Gadella, T. W. J. *J Microsc* **2011**, *241*, 111–118.

[251] Valentin, G.; Verheggen, C.; Piolot, T.; Neel, H.; Coppey-Moisan, M.; Bertrand, E. *Nat Methods* **2005**, *2*, 801.

[252] Mao, S.; Benninger, R. K. P.; Yan, Y.; Petchprayoon, C.; Jackson, D.; Easley, C. J.; Piston, D. W.; Marriott, G. *Biophys J* **2008**, *94*, 4515–4524.

[253] Elliott, A. D.; Gao, L.; Ustione, A.; Bedard, N.; Kester, R.; Piston, D. W.; Tkaczyk, T. S. *J Cell Sci* **2012**, *125*, 4833–4840.

[254] Devauges, V.; Marquer, C.; Lcart, S.; Cossec, J.-C.; Potier, M.-C.; Fort, E.; Suhling, K.; Lvque-Fort, S. *PLoS One* **2012**, *7*, e44434.

[255] Lin, X.; Li, S.; Zhao, Y.; Ma, X.; Zhang, K.; He, X.; Wang, Z. *DNA Cell Biol* **2013**, *32*, 220–227.

[256] Sprague, B. L.; McNally, J. G. *Trends Cell Biol* **2005**, *15*, 84–91.

[257] Anthony, N. R.; Berland, K. M. *PLoS One* **2014**, *9*, e90456.

[258] Duran, A.; Amanchy, R.; Linares, J. F.; Joshi, J.; Abu-Baker, S.; Porollo, A.; Hansen, M.; Moscat, J.; Diaz-Meco, M. T. *Mol Cell* **2011**, *44*, 134–146.

[259] Verschoor, A.; Srivastava, S.; Grassucci, R.; Frank, J. *J Cell Biol* **1996**, *133*, 495–505.

[260] MacIntosh, G. C.; Bassham, D. C. *Autophagy* **2011**, *7*, 662–663.

[261] Lykke-Andersen, J.; Bennett, E. J. *J Cell Biol* **2014**, *204*, 467–476.

[262] Duttler, S.; Pechmann, S.; Frydman, J. *Mol Cell* **2013**, *50*, 379–393.

[263] Pechmann, S.; Willmund, F.; Frydman, J. *Mol Cell* **2013**, *49*, 411–421.

[264] Groll, M.; Ditzel, L.; Lwe, J.; Stock, D.; Bochtler, M.; Bartunik, H. D.; Huber, R. *Nature* **1997**, *386*, 463–471.

[265] Seibenhener, M. L.; Babu, J. R.; Geetha, T.; Wong, H. C.; Krishna, N. R.; Wooten, M. W. *Mol Cell Biol* **2004**, *24*, 8055–8068.

[266] Fllgrabe, J.; Klionsky, D. J.; Joseph, B. *Nat Rev Mol Cell Biol* **2013**,

[267] Paine, P. L.; Moore, L. C.; Horowitz, S. B. *Nature* **1975**, *254*, 109–114.

[268] Terry, L. J.; Shows, E. B.; Wente, S. R. *Science* **2007**, *318*, 1412–6.

[269] Peters, R. *J Biol Chem* **1983**, *258*, 11427–11429.

[270] Audas, T. E.; Jacob, M. D.; Lee, S. *Cell Cycle* **2012**, *11*, 2059–2062.

[271] Emmott, E.; Hiscox, J. A. *EMBO Rep* **2009**, *10*, 231–238.

[272] Luby-Phelps, K. *Int Rev Cytol* **2000**, *192*, 189–221.

[273] Luby-Phelps, K. *Molecular Biology of the Cell* **2013**, *24*, 2593–2596.

[274] Swaminathan, R.; Hoang, C. P.; Verkman, A. S. *Biophys J* **1997**, *72*, 1900–7.

[275] Dix, J. A.; Verkman, A. *Annu. Rev. Biophys.* **2008**, *37*, 247–263.

[276] Sarkar, M.; Smith, A. E.; Pielak, G. J. *Proc Natl Acad Sci U S A* **2013**, *110*, 19342–19347.

[277] Dino Rockel, T.; von Mikecz, A. *J Struct Biol* **2002**, *140*, 189–199.

[278] Lam, Y. W.; Lamond, A. I.; Mann, M.; Andersen, J. S. *Current Biology* **2007**, *17*, 749???760.

[279] Rockel, T. D.; Stuhlmann, D.; von Mikecz, A. *J Cell Sci* **2005**, *118*, 5231–5242.